

The Hough Transform
as event filter
for the ANTARES neutrino
telescope

A simulation study

Die Hough-Transformation als Ereignisfilter
für das ANTARES Neutrino-Teleskop

Simulationsstudie

Der Naturwissenschaftlichen Fakultät
der Friedrich-Alexander-Universität Erlangen-Nürnberg
zur Erlangung des Doktorgrades Dr. rer. nat.



vorgelegt von
Horst Laschinsky
aus Deggendorf

The Hough Transform
as event filter
for the ANTARES neutrino
telescope

A simulation study

Die Hough-Transformation als Ereignisfilter
für das ANTARES Neutrino-Teleskop

Simulationsstudie

Der Naturwissenschaftlichen Fakultät
der Friedrich-Alexander-Universität Erlangen-Nürnberg
zur Erlangung des Doktorgrades Dr. rer. nat.



vorgelegt von
Horst Laschinsky
aus Deggendorf

Als Dissertation genehmigt von der Naturwissenschaftlichen Fakultät der Friedrich-Alexander-Universität Erlangen-Nürnberg.

Tag der mündlichen Prüfung: 29.06.2012

Vorsitzender der
Prüfungskommission: Prof. Dr. Rainer Fink

Erstberichterstatter: Prof. Dr. Uli Katz

Zweitberichterstatter: Prof. Dr. Gisela Anton

Contents

1	Zusammenfassung	5
2	Introduction	9
3	The ANTARES neutrino telescope	13
3.1	Why neutrino astronomy?	13
3.2	Neutrino detection	14
3.2.1	Neutrino nucleon reactions	14
3.2.2	Čerenkov neutrino telescopes	15
3.3	Overview of the ANTARES telescope	17
3.3.1	Basic detector layout	17
3.3.2	Detector strings	17
3.3.3	Optical modules and electronics	20
3.3.4	Determining the detector's position	21
3.3.5	Environmental data	22
3.3.6	Reconstruction of events and the need for a classification tool	23
4	Dealing with patterns - some theoretical remarks	25
5	Detecting ANTARES events	29
5.1	First approaches	29
5.1.1	Artificial neural networks	29
5.1.2	Principle Component Analysis	34
5.2	Analysis of geometric structures	36
5.2.1	Principle	36
5.2.2	Mathematics of moving hyperbolas	37
5.2.3	First pattern recognition results	42
5.3	Event detection using the Hough Transform	45

5.3.1	Introduction to the Hough Transform	45
5.3.2	Detection of straight lines using the Hough Transform	48
5.3.3	Detection of hyperbolas using the Hough Transform	48
5.3.4	Finding intersections	53
5.3.5	Determination of cut-off parameter	55
5.3.6	Elimination of random coincidences by comparing the angles of detected structures	58
5.3.7	Elimination of random coincidences by application of the nearest- neighbour strategy	58
5.3.8	SPE based pre-filter	58
6	Results	61
6.1	Application to Monte Carlo data	61
6.1.1	Analysis of the detection efficiency	62
6.1.2	Comparison to ANTARES standard trigger	69
6.2	Background only	71
6.3	Application to physical data	72
6.4	Summary of results	75
7	Conclusion and Outlook	83
	Appendix	87
A	Description of the event classification software	89
A.1	classify	89
A.2	get_points.pl	90
B	Results from the application to Monte Carlo data	91
C	Example results from real data	117

D	Investigations on correlated background photons	169
D.1	Introduction	169
D.1.1	The single photo electron peak	169
D.1.2	Correlated photons	170
D.2	Prototype Sector Line Data	171
D.2.1	The prototype sector line	171
D.2.2	Used data-sets	172
D.2.3	Data analysis	172
D.2.4	Results	173
D.3	Simulation study	174
D.4	Summary	175
E	The slow control system for acoustic particle detection	177
E.1	Acoustic particle detection	177
E.2	Acoustics within ANTARES	177
E.3	The Slow Control	178
E.3.1	Existing slow control system	179
E.4	Hardware	180
E.4.1	Constraints and selected hardware	180
E.5	The slow control protocol	181
E.5.1	Link layer of the slow control protocol	182
E.5.2	Application layer of the slow control protocol	183
E.5.3	The μ C-FPGA interface	186
E.5.4	FPGA update manual	188

1 Zusammenfassung

Das Ziel dieser Arbeit war es, eine Methode zur Erkennung von physikalisch relevanten Ereignissen in den Datensätzen des ANTARES Neutrinoobservatoriums zu entwickeln. Das ANTARES Neutrinoobservatorium ist ein Wasser-Čerenkov Detektor zum Nachweis kosmischer Neutrinos, der sich auf dem Meeresgrund vor der Küste von Toulon (Frankreich) befindet und das Meerwasser als Detektormedium verwendet. Bei den detektierten Ereignissen handelt es sich um Čerenkov Signaturen von hochenergetischen Endprodukten (i.A. geladene Leptonen und hadronische Schauer) aus schwachen Wechselwirkungen zwischen Neutrinos und Nukleonen im Detektormedium. Diese Signaturen äußern sich in Form von korrelierten Lichtsignalen, welche von Photomultiplier-Röhren detektiert werden und anschließend als Orts-Zeit-Informationen der gemessenen Čerenkov-Photonen vorliegen. Aufgrund der natürlichen Umgebung des Detektors sind diese Signale von optischem Untergrund aus verschiedenen Quellen überlagert und müssen vor der weiteren Verarbeitung erst aus diesen Rohdatensätzen extrahiert werden. Hierfür greift das ANTARES Standardverfahren auf die Suche nach Korrelationen in den Eingangsdaten zurück, welche sich aus der Lichtlaufzeit "echter" Signale ergeben. Da hierzu die Orts-Zeit-Informationen aller detektierten Photonen gegenseitig abgeglichen werden müssen und folglich die Anzahl an nötigen Vergleichen ungefähr quadratisch mit der Anzahl an Datenpunkten pro Datensatz skaliert (i.d.R. mehrere hundert bis tausend), handelt es sich um eine äußerst zeitaufwendige Strategie. Der in dieser Arbeit vorgestellte Algorithmus basiert hingegen auf einem modernen Mustererkennungsalgorithmus, welcher die Datensätze als Ganzes betrachtet und in Bezug auf die Anzahl an Datenpunkten nur eine lineare Zeitkomplexität aufweist. Dadurch wird bei (hinreichend kleinen) Datensätzen sogar eine Erkennung und Filterung der Daten in Fast-Echtzeit ermöglicht. Zudem sind die vorzunehmenden Analyseschritte bzgl. der einzelnen Datenpunkte voneinander unabhängig, wodurch der Algorithmus massiv-parallelisierbar wird. Somit kann die Erkennungsgeschwindigkeit je nach verwendeter Hardware im Prinzip beliebig gesteigert werden.

Bereits im Vorfeld wurden Untersuchungen zur zeitlichen Struktur des optischen Untergrundes im Detektormedium durchgeführt. Diese zielten auf den Nachweis möglicher Korrelationen auf Nanosekunden-Zeitskala der typischerweise als statistisch verteilt angenommenen Untergrundphotonen ab. Solche Korrelationen wären nicht nur bei der Auswahl geeigneter neuer Algorithmen zu beachten, sondern würden auch eine Gefahr für die bereits existierenden Filtermechanismen des ANTARES Neutrinoobservatoriums darstellen, da diese in der Regel auf der Annahme unkorrelierter Untergrundphotonen basieren. Leider konnten aufgrund der geringen Menge an zur Verfügung stehenden Daten keine endgültigen Schlussfolgerungen gezogen werden. Dennoch wurden in dieser Arbeit Hinweise darauf gefunden, dass derartige Korrelationen wirklich existieren könnten.

Zu Beginn der eigentlichen Arbeit wurden Standardverfahren, wie künstliche neuronale Netze oder Principal Component Analysis (Hauptkomponentenanalyse, auch Karhunen Loève Transformation genannt) untersucht. Aufgrund der Eigenschaften der ANTARES-Daten, vorrangig aufgrund ihrer schieren Menge und ihrer Diskretheit (im mathematischen Sinne), wurden diese Algorithmen wieder verworfen, da sich ihre Erkennungsrate nicht signifikant von Zufallstreffern unterschied. Beginnend mit Überlegungen über die geometrischen Eigenschaften der Signale, welche von Teilchen erzeugt werden, die den ANTARES Detektor passieren, wurde ein Datenfilter implementiert welcher die Hough-Transformation verwendet. Diese Methode wurde in den frühen sechziger Jahren entwickelt, um Spuren hochenergetischer Teilchen in Blasenkammern zu erkennen. Mehrere Verbesserungen wurden dieser Methode hinzugefügt, um den spezifischen Eigenschaften der ANTARES-Daten gerecht zu werden. Dadurch wurde die Menge an falsch erkanntem Untergrund reduziert und die Datenverarbeitung an sich beschleunigt. Der Algorithmus wurde angewandt auf a) Daten von Monte-Carlo-Simulationen, b) Daten, die noch während der Konstruktionsphase des ANTARES Detektors aufgenommen wurden, sowie c) reine Zufallsmuster. Die Ergebnisse der Analysen aller drei Klassen von Daten wurden mit den Ergebnissen des ANTARES Standard Triggers verglichen. Beim ANTARES Standard Trigger handelt es sich um eine zentrale Komponente der ANTARES Datenanalyse-Software, welche zur Erkennung physikalisch relevanter Ereignisse in dem vom ANTARES Detektor gelieferten Datenstrom dient und im Wesentlichen auf der anfangs erwähnten Suche nach Korrelationen von Lichtsignalen in den Eingangsdaten basiert.

Es wurde gezeigt, dass das in der Arbeit angewandte Mustererkennungsschema ein sehr vielversprechendes Verfahren ist, um eine verlässliche und echtzeitfähige neue Klasse von Datenfiltern und Triggern für den Detektor zu entwickeln. Abhängig von der Konfiguration der Mustererkennung und zusätzlichen Filterbedingungen wurden 80% bis 90% aller physikalischen Daten richtig erkannt. Der Anteil an falsch erkanntem Untergrund lag in allen Datensätzen unter 10%. Dieser Anteil konnte durch geeignete Schnitte und Filterbedingungen in der Nachbearbeitung der Ergebnisse noch weiter reduziert werden.

Der Vergleich der in dieser Arbeit entwickelten Methode mit dem ANTARES Standard Trigger zeigte bei der Ereignis-Identifikation eine Effizienzsteigerung um 100% bei deutlich verbessertem Zeitverhalten. Ein Vergleich der Effizienzen des ANTARES Standard Triggers und der Hough-Transformation für verschiedene Untergrundraten (basierend auf Monte-Carlo-Daten) ist in Abb. 1.1 dargestellt. Obwohl der Standard Trigger sich anfangs im Bezug auf den Untergrund unempfindlicher zeigte, konnte dieser Nachteil wiederum durch weitere Schnitte und Filterbedingungen in der Nachbearbeitung der Ergebnisse ausgeglichen werden.

Der neue Algorithmus bewies seine Stabilität auch bei der Anwendung auf echte Daten, die vom - zum Zeitpunkt der Analyse zur Hälfte fertig gestellten - ANTARES Detek-

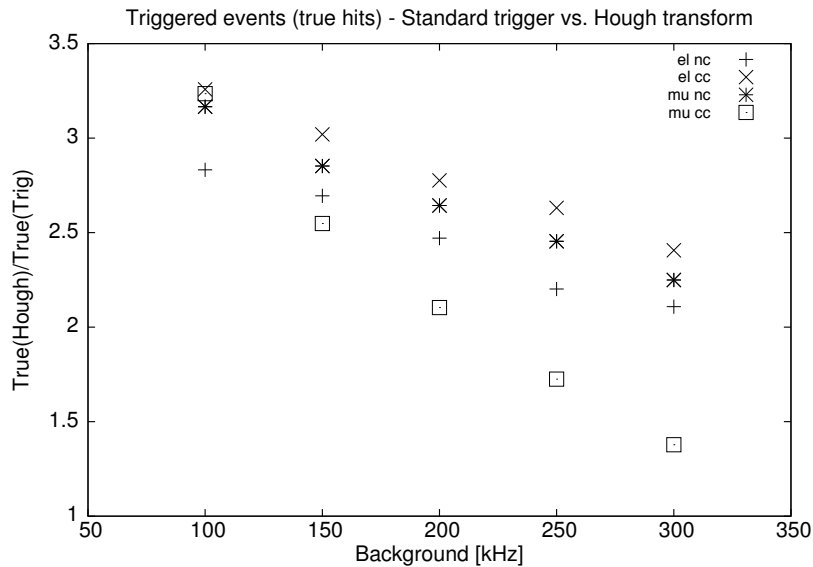


Figure 1.1: *Verhältnis der Anzahl der vom ANTARES Standard Trigger und von der Hough-Transformation gefundenen Ereignisse für alle vier untersuchten Ereignis-Klassen bei verschiedenen Untergrundraten (kHz pro Photomultiplier), basierend auf Ereignissen aus Monte-Carlo-Simulationen.*

tor in seiner Konstruktionsphase aufgenommen wurden. Wiederum wurde im Vergleich zum Standard Trigger in etwa die doppelte Menge an Ereignissen erkannt. Da - im Gegensatz zu den Monte Carlo Simulationen - natürlicherweise keinerlei Information über die Natur der Daten vorlag, wurde eine visuelle Analyse der Ergebnisse vorgenommen. Diese lässt vermuten, dass es sich bei den erkannten Ereignissen in der Tat um Signaturen hochenergetischer Teilchen handelt, in guter Übereinstimmung mit den vorhergehenden Ergebnissen.

Der in dieser Arbeit entwickelte Algorithmus stellt somit eine verlässliche, stabile und erweiterbare Methode zur Erkennung physikalisch relevanter Signale im Datenstrom des ANTARES Neutrinoobservatoriums dar. Aufgrund seines grundlegenden Funktionsprinzips, nämlich der Suche nach geometrischen Mustern innerhalb von in Ort und Zeit verteilten Datenpunkten, ist der vorgestellte Algorithmus relativ einfach auf andere Arten von Detektoren anpassbar, welche ihre Messwerte in der beschriebenen Form liefern. Zu nennen wäre hier in etwa der zur Zeit sich in Planung befindende Kubikkilometer-Detektor KM3NeT, oder aber auch die Experimente zum akustischen Nachweis von Teilchen, die im Rahmen des ANTARES Projektes durchgeführt werden. Insbesondere aufgrund seines Echtzeitverhaltens ergibt sich dabei die Möglichkeit, interessante Signaturen praktisch sofort zu erkennen und umgehend untersuchen zu können, und somit die Wahrscheinlichkeit der Erstentdeckung eines kosmischen Ereignisses durch das ANTARES Neutrinoobservatorium oder verwandte Projekte deutlich zu erhöhen.

2 Introduction

When Viktor Hess was the first to discover evidence of cosmic rays in 1912 he surely did not anticipate what widespread and evolving field of research this subject, which is today known as "astroparticle physics", would become a century later. Many new particles have since been found, and many new ways of detecting them have been developed. These discoveries and techniques not only made valuable and fruitful contributions to our current understanding of the universe, they also gave rise to new questions: How are the particles created? How are they accelerated to energies well beyond any imagination? Why do we detect highest energy particles on earth, in spite of the so called Greisen-Zatsepin-Kuzmin cut-off (GZK cut-off)[1, 2]? Are cosmic rays, at least partially, made up of unknown particles - maybe even of the long proposed dark matter? These questions cover a large range of topics of modern physics, from high energy particle physics to cosmology. And, moreover, the answers, if eventually found, may give evidence for (or definitely rule out) "physics beyond the standard model", which is one of the most active fields of research nowadays, proposing theories as different as Modified Newtonian Dynamics (MOND)[3], super symmetry[4] or loop quantum gravity[5].

This work's topic is that of neutrino astronomy, which is one of the many different subtopics of astroparticle physics. Moreover, it is one of today's most active fields of research with large detectors in operation or currently being built all over the world. Due to the special properties of neutrinos, especially their capability to propagate through even dense matter almost without being absorbed, sophisticated detectors and filter algorithms have to be developed in order to detect them properly. This work deals with the latter problem concerning the ANTARES neutrino telescope which, at the time of writing, was still under construction but partially already in operation.

The ANTARES neutrino telescope is a water Čerenkov detector which uses the water of the Mediterranean Sea as detector medium for the detection of cosmic neutrinos. Due to the natural environment, the experiment suffers from one main disadvantage, namely the lack of controllable laboratory conditions. The physical events recorded by the detector are superimposed by a large amount of background signals, mainly originating from two sources: bioluminescence and Čerenkov photons from the radioactive decay of ^{40}K , which is an omnipresent isotope in sea water. This background noise cannot be neglected, since, if not filtered out, it has a heavy influence on the event detection and reconstruction tasks. Moreover, the detector records many events, which do not contain any physical data at all but consist of background only. The ANTARES detector therefore is equipped with an event filter ("trigger") in order to decide between data sets with background only and those which contain neutrino signatures. Furthermore, suppression of background noise in data sets with neutrino signatures is an another important task. The standard event filter, however, is based on the search

for correlations in the recorded signals, which is a complicated and time consuming task. Thus, the ANTARES detector uses the "all data to shore" strategy. All data recorded by the detector are sent to the control room, where they are processed by a computer farm executing the event filter algorithms. The necessity to run this filter in real time imposes severe constraints on the complexity of the filter software and thus reduces the filter efficiency. It was the goal of this work to provide a new filter approach with reduced demand of computing power and improved efficiency.

The first idea was to use an artificial neural network in order to distinguish between background-only and physically relevant events. After several approaches, this strategy was abandoned, as the structure and the amount of the event data could not be analysed properly with these networks. The next ansatz was to use "Principal Component Analysis", a well known strategy used in image recognition. Unfortunately, the discreteness and "sharpness" (compared to a smooth, true-colour image) of the ANTARES data caused this algorithm also to fail. The method, which finally was successful, was to search for geometrical patterns which are caused by the correlated signals from physical data. Such patterns are expected if the data are plotted in a suitable coordinate system. It turned out, that the geometrical structures resulting in these plots were conic sections. Thus, an algorithm, based on the Hough Transform, was developed. This algorithm allows for recognising these geometrical structures in real time, even if the input data are heavily distorted by background noise. Moreover, the applied algorithm is not only able to detect structures from physical data, but also allows for efficient filtering of background noise, resulting in pure physical data. Using this new strategy allows for extracting this pure physical data almost instantly after an event was recorded. This helps not only to save memory but also yields the possibility to quickly react on interesting events, without waiting for complete analysis.

Prior to the actual tasks, some investigations of the temporal structure of the optical background were done. These investigations aimed at the evidence for correlations on nanosecond timescale of background photons, which typically are considered to be distributed statistically. Such correlations, if they do exist, are on the one hand necessary input for the development of new algorithms. On the other hand, they may as well spoil the existing data filters of the ANTARES software. Unfortunately, due to the small amount of data, no definite conclusion could be drawn. However, the results imply that such correlations might exist.

After an introduction to the ANTARES neutrino telescope and neutrino astronomy as such in chapter 3, chapter 4 provides a short overview on the theory of pattern recognition. A mathematical introduction to the Hough Transform as well as its application to ANTARES data are presented in chapter 5. Chapter 6 shows the results of using this new strategy for analysing ANTARES data as well as of comparing it to the existing standard algorithms. The algorithms are applied to both data from Monte Carlo simulations as well as "real" data recorded during the construction phase of the

ANTARES detector. In chapter 7 the results are summarised and ideas for further development of the algorithm are presented. The details concerning the investigation of possible correlations of background photons can be found in appendix D.

Appendix A describes the usage of the software which implements the algorithm developed in this work. Appendices B and C show the results from the application of this software as well as the ANTARES standard trigger to Monte Carlo data and real data, respectively. Appendix E gives an overview of the software and wiring for control of the sensors for acoustic particle detection. A large fraction this control system has been developed as side project to this work.

3 The ANTARES neutrino telescope

3.1 Why neutrino astronomy?

Neutrino astronomy is a quite modern and evolving field of research within the wide area of astrophysics (or astroparticle physics, in particular). For several reasons, neutrinos are ideal messengers from outer space, carrying information about lots of different kinds of nuclear interactions which take place in the universe:

- They carry neither electric nor colour charge and are subjected to weak interaction only (apart from gravitative interaction, which can be neglected)[6]. Thus, they can cross large regions of space, even if these are filled up with dense matter, almost without being absorbed. Moreover, they are not deflected, neither by electric nor by magnetic fields. Back-tracing their track directly reveals the region of their origin.
- Their mass is almost zero (current upper limit: < 2 eV[7]), thus they are ultra relativistic particles with their speed being almost the speed of light. This allows to search for correlations between optical and neutrino observations to identify their source or e.g. to get more precise estimates of neutrino masses by comparing their arrival time to that of light from high-energetic events[8].
- Moreover, neutrinos may be signatures of new physics, as they may be created not only by well known "standard" nuclear interactions, but also by the annihilations of neutralinos for instance, one possible realisation of super-symmetric matter[9].

These examples - and there are many more - show that neutrino astronomy is a very important and highly interesting field of science, especially when it leads to fundamental questions proposed by our modern theories. Unfortunately, due to exactly these special properties which make them that interesting and important, neutrinos are very hard to detect and their properties are still much more difficult to investigate. As they only interact weakly, they can in principle not be detected directly but only by the products resulting from a weak interaction with "normal" matter. Due to the weakness of this interaction¹, these reactions occur only rarely. In order to get statistically significant results, a possible neutrino detector thus has to contain a large amount of some medium in which the weak interactions can take place. The ANTARES neutrino telescope uses the water of the Mediterranean Sea as detector medium in which the products of neutrino nucleon interactions result in secondary particles emitting Čerenkov light, which is subsequently detected by an array of photomultiplier tubes.

¹The relative coupling strength of the weak interaction is about 10^{-14} that of the strong interaction and about 10^{-12} that of the electromagnetic interaction[10]

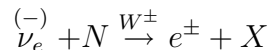
3.2 Neutrino detection

3.2.1 Neutrino nucleon reactions

Since neutrinos are subjected to weak interaction only, the reactions are restricted to only two basic types: *charged current* and *neutral current* reactions, depending on the type of vector boson mediating the interaction (W^\pm or Z^0 boson). A further subdivision of the event types originates from the so called flavour of the incident neutrino: electron (ν_e), muon (ν_μ) or tau (ν_τ) neutrino. According to the conservation of flavour, the type of neutrino has a direct influence on the type of the secondary particle. At the time of writing of this work, no software allowing to reliably simulate ν_τ interactions and their end products did exist. Thus only four types of events were analysed in this work, which are now described in more detail (for further information, see e.g. [6]):

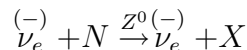
- Electronic² charged current events

A charged vector boson W^\pm mediates the interaction between a nucleon N and an electron (anti-)neutrino $\nu_e^{(-)}$, possibly creating a hadronic shower X :



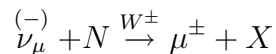
- Electronic neutral current events

A neutral vector boson Z^0 mediates the interaction between a nucleon N and an electron (anti-)neutrino $\nu_e^{(-)}$, possibly creating a hadronic shower X :



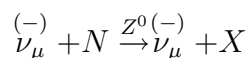
- Muonic charged current events

A charged vector boson W^\pm mediates the interaction between a nucleon N and a muon (anti-)neutrino $\nu_\mu^{(-)}$, possibly creating a hadronic shower X :



- Muonic neutral current events

A neutral vector boson Z^0 mediates the interaction between a nucleon N and a muon (anti-)neutrino $\nu_\mu^{(-)}$, possibly creating a hadronic shower X :



²The term *electronic* in this sense shall refer to the electrons which take part in the reaction, in contrast to muons which are part of a *muonic* event.

The basic difference between the signatures of charged and neutral current events is the presence or absence of an electron or muon track. Fig. 3.1 illustrates this in detail. Apart from the shower products, which occur at both types of events, only the charged current reaction yields a single charged lepton as reaction product. In case of a neutral current reaction, the resulting lepton is again a neutrino, which can not be detected. The shower only extends up to a few meters within water and thus can be treated

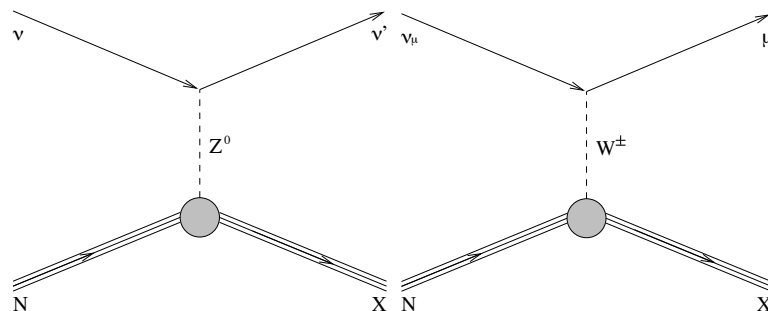


Figure 3.1: *Feynman graphs of neutral (left) and charged (right) current neutrino-nucleon interactions. The only observable signature of a neutral current reaction is the resulting hadronic shower (X), while a charged current reaction additionally produces a charged lepton (in this case a muon μ).*

as point-like compared to the ANTARES detector volume. Due to this property, it is invisible to the detector if the reaction itself took place outside the observed volume, but must not be neglected otherwise. The track of the muon however reaches up to several ten kilometres and thus is a reliable signature of a muonic charged current reaction, even if this reaction itself took place far outside the observed detector volume. Basically, an electronic charged current reaction also yields an electron track. But due to the small mass of the electron, it is likely to quickly lose a large part of its energy in form of bremsstrahlung, resulting in a track too short to be resolved by ANTARES[11].

It should be noted here, that the observable final states of electronic and muonic neutral current events are exactly the same. However, the ANTARES Monte Carlo simulation software allowed for simulating both event types separately, thus they will also be distinguished in the rest of this work.

3.2.2 Čerenkov neutrino telescopes

Fig. 3.2 depicts the basic principle of a Čerenkov neutrino telescope like ANTARES. A neutrino, which has passed through the Earth, weakly interacts with some nucleon within or at least in the vicinity of the observed volume. The product of this interaction

is a hadronic shower³ as well as maybe a secondary particle (the exact result depends on the type of reaction, as has been shown in the previous section). The shower components, as well as the secondary particle propagate through the water with a speed higher than that of light in water. Thus they emit Čerenkov radiation[12] in a cone shaped manner which is then to be sensed by the photomultiplier tubes. The

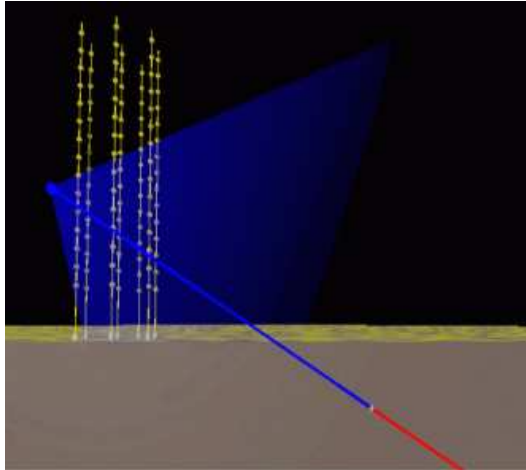


Figure 3.2: *Basic detection principle of the ANTARES neutrino telescope. Taken from [13].*

apex angle φ of this Čerenkov light cone is given by

$$\cos \varphi = \frac{1}{\beta n} \quad (3.1)$$

with β being the well known relativistic factor v/c (v the speed of the particles, c the speed of light in vacuum) and n the refractive index of the surrounding media[14]. Since, in case of ultra relativistic particles, $\beta \approx 1$ and, for sea water, $n \approx 1.3$ [10], the apex angle of the products of neutrino-nucleon interactions in the interesting energy range of $> 10\text{GeV}$ calculates to

$$\varphi \approx 42^\circ. \quad (3.2)$$

This fixed value then allows to reconstruct the shape of the light cone and thus the direction of the shower axis and/or particle track from photomultiplier data. Since at these energy ranges, there is a momentum transfer of almost 100% between the reaction partners, the direction of the shower axis and the particle track is virtually identical to the direction of the track of the incident neutrino.

³In case of a tau neutrino it could also be an electromagnetic shower, caused by the decay of the generated tau. But, as mentioned, this reaction has not been regarded in this work due to the lack of a suitable simulation software.

3.3 Overview of the ANTARES telescope

In this section a short overview of the ANTARES neutrino telescope is presented. Much more information about the detection principle as well as the newest results can be obtained from the project's web page [13]. For details on the technical design, see the ANTARES Technical Design Report (TDR)[15], on which this chapter is based.

3.3.1 Basic detector layout

The ANTARES neutrino telescope (Astronomy with a Neutrino Telescope and Abbyss environmental RESEarch) is a water Čerenkov detector currently built⁴ in 2400m depth near La Seyne sur Mer at the coast of Toulon, France. It is the research project of a Europe-wide collaboration of currently (March 2008) 24 research institutes⁵ (19 particle physics institutes, 1 astronomy institute, 4 sea science institutes) from seven European countries (see fig. 3.3).

Located in the Mediterranean Sea, the ANTARES telescope is not only a major research project "just around the corner" of the member institutes, it is also complementary to the two existing large neutrino telescopes in the Antarctic, AMANDA and IceCube. Together with these two telescopes, 100% of sky coverage in "neutrino light" is reached. Fig. 3.4 depicts the regions in the sky which are in the field of view of a neutrino telescope located in the Mediterranean, as well as some known interesting neutrino sources. In contrast to AMANDA and IceCube, the ANTARES detector also allows to investigate neutrinos from the galactic centre, which is not in the fields of view of the Antarctic telescopes. Additionally, due to a large overlap of the regions observed by all three projects, observed signals can be compared and cross checked.

3.3.2 Detector strings

The ANTARES detector consists of 12 so called *strings*⁶, which are anchored to the seabed at distances of approx. 60 m next to each other in an octagonal shape (see fig. 3.5). An ANTARES detector string consists of 25 storeys which are connected by electromechanical cables (EMCs) at distances of 14.5 m each, thus forming an in-

⁴At the time of this writing, about 90% of the detector have been deployed successfully

⁵A continuously updated list of the collaboration's members can be found at [16].

⁶The detector strings are quite often also called "lines". This work strictly uses the term "string" when referring to such a detector component (except for proper names like "Sector Line"), because later in this work, the term "line" will be used in a completely different meaning when it comes to pattern recognition.

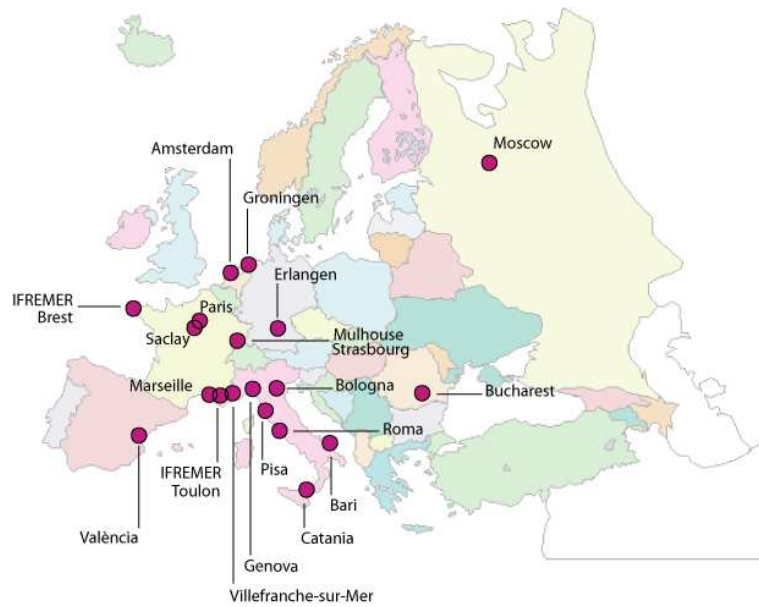


Figure 3.3: Members of the ANTARES collaboration at the time this work was written. Taken from [13].

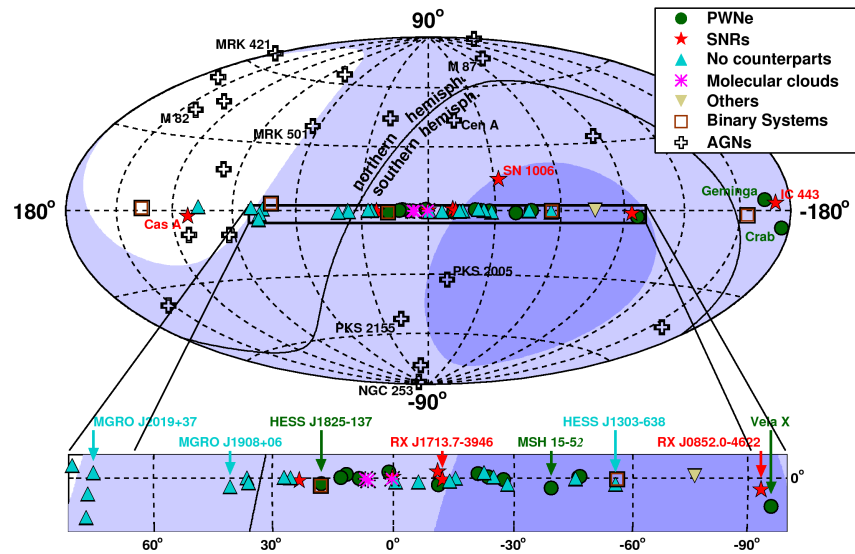


Figure 3.4: Regions of the sky which are in the field of view of a neutrino telescope located in the Mediterranean, like ANTARES. The white area is never in the field of view of ANTARES the dark blue area always. AMANDA/IceCube observes the region north of the "northern hemisphere" border. The centre of the map corresponds to the galactic centre. The image also shows certain interesting neutrino sources. The figure has been taken from [17].

strument of a total length of 350 m⁷. Each string is anchored to the seabed by the so called *bottom string socket* (BSS) and held in upright position by a buoy attached to its top. The BSS mainly consists of a heavy weight assuring that the string remains on its position on the sea floor, a release mechanism which can be activated by a special acoustic signal in order to recover the string for maintenance, and a titanium container called *string control module* (SCM) containing electronics for string control and data collection. The electromechanical cable is not only responsible for the mechanical stability of the system, it also establishes the electrical connection between the individual electronic components for power supply and data distribution tasks. All 12 detector strings are attached to the *junction box* (JB) which collects the data and transmits them to the control room at the coast of La Seyne sur Mer. Power is also supplied to the detector through the electromechanical cable by a special coast station, called *power hut*.

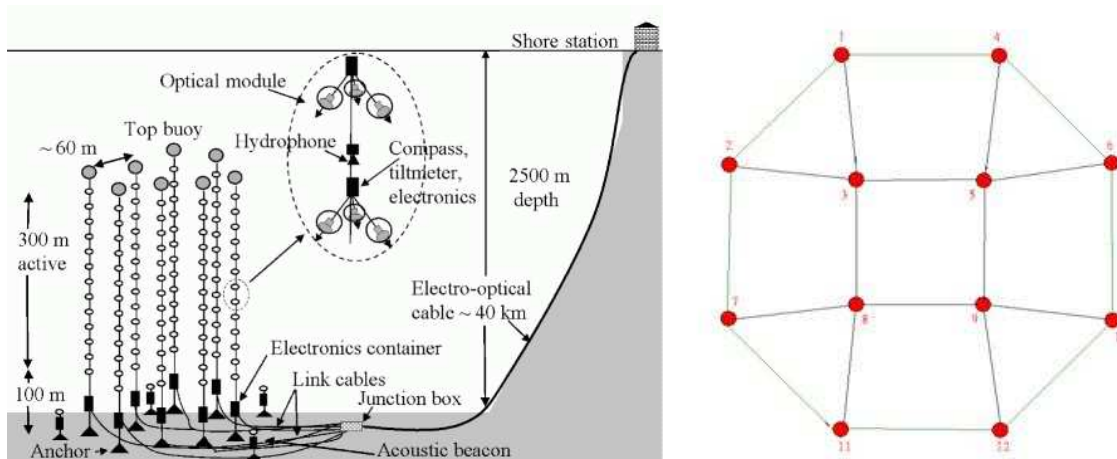


Figure 3.5: Schematic 3D representation of the ANTARES detector and the arrangement of the 12 strings on the seabed. Taken from [13].

Each storey consists of a mechanical structure made of titanium, called *optical module frame* (OMF). This frame houses three *optical modules* (OMs) as well as a hollow titanium cylinder containing the electronics for the control of the modules and for gaining physical and calibration data. These electronics's containers are referred to as *local control modules* (LCMs). Fig. 3.6 shows two storeys prior to their deployment.

The storeys of a string are combined into so called *sectors*, containing five storeys each, so that there are five sectors per string. Within each sector, one LCM is responsible for collecting and pre-processing data from all five storeys. This dedicated LCM is called *master local control module* (MLCM).

⁷Actually, the total length of a string is 450m, as there are additional 100m of uninstrumented EMC below the bottom storey.

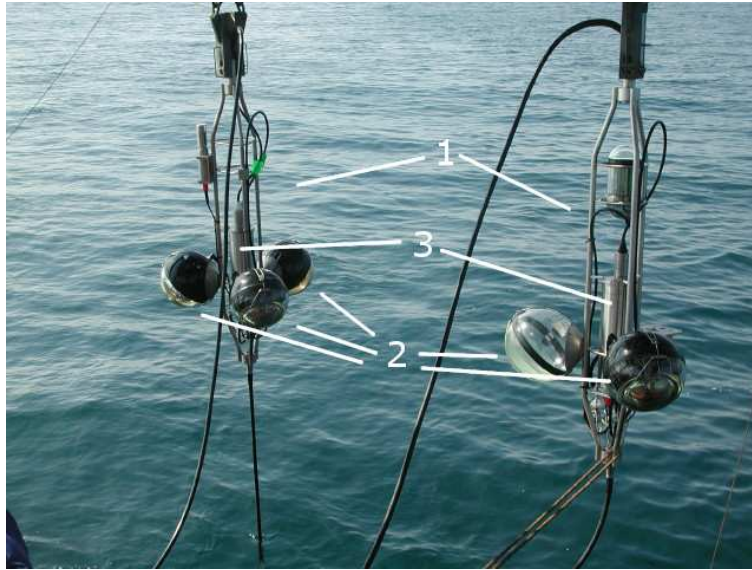


Figure 3.6: Two storeys of an an ANTARES detector string (MILOM, March 2005) prior to their deployment. The optical module frames (1) with optical modules (2) as well as the LCM containers (3) are clearly visible. Taken from [13].

Some of the storeys are additionally equipped with special sensors to get calibration or positioning information, like for example hydrophones (basically under-sea microphones), tilt-meters or LED beacons, see below.

3.3.3 Optical modules and electronics

An optical module of the ANTARES detector consists of a 10" *photomultiplier tube* (PMT) which is placed within a pressure resistant glass sphere. The glass sphere also contains some of the electronics necessary to properly operate the PMT as well as a mesh of wire made of mu metal⁸ in order to shield the PMT from the magnetic field of the earth. The back half of the sphere is coated with black colour to ensure that only photons from within about 95° with respect to the OM's axis are detected. Fig. 3.7 shows a picture of an optical module.

The signal from the PMT is read out and time stamped by a so called *analogue ring sampler* (ARS), a special integrated circuit which is part of the LCM electronics⁹. There are two modes of operation for the ARS chip, the *single photo electron* (SPE) mode and the *waveform* mode. In SPE mode, the PMTs signal is integrated over a certain (configurable) interval of time. In waveform mode, the signal is sampled with

⁸A special alloy with high magnetic permeability, which allows to insulate from magnetic fields.

⁹There are two ARS chips per PMT which alternately process the data in order to overcome their intrinsic dead time.

high temporal resolution in order to allow investigation of its time development. The data are then transmitted via the MLCM, the SCM and the JB to the control room in La Seyne sur Mer, where they are stored for later examination.

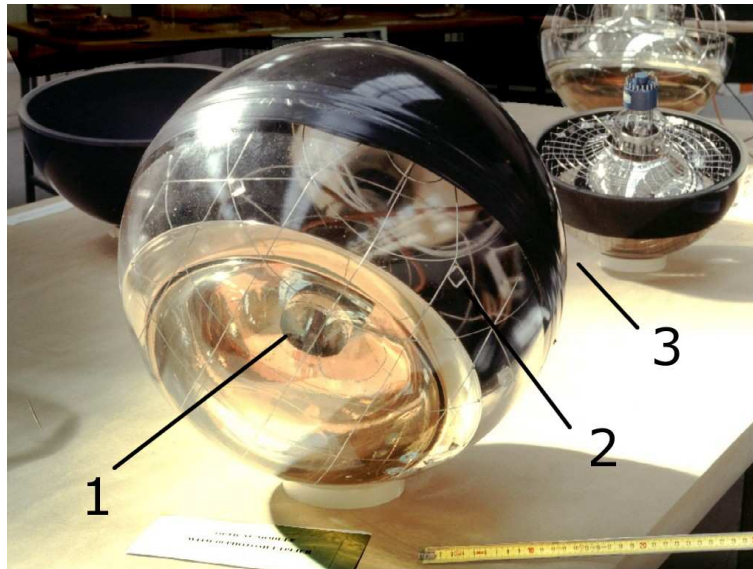


Figure 3.7: *An optical module as used in the ANTARES detector. The photomultiplier tube (1) and the mesh of mu metal (2) within the pressure resistant glass sphere are clearly visible. The back half of the sphere is coloured black (3) in order to allow light to enter the sphere from front direction only. Taken from [13].*

3.3.4 Determining the detector's position

In order to allow precise reconstruction of the events, exact knowledge of the detector's position and shape as well as exact temporal synchronisation of the different components is absolutely mandatory. In order to get the position information, some of the LCMs are equipped with compasses and tilt-meters, as well as with hydrophones which record the signals of acoustic beacons located on well defined positions on the sea floor. Synchronisation of the system's clocks is achieved by LED beacons situated on some of the LCM containers which emit flashes of light at well known points in time which are then detected by the PMTs. The combination of these these systems allows to determine the position and heading of each optical module to better than 10 cm and 5° , respectively.

3.3.5 Environmental data

A special 13th string, the so called *instrumentation line* (IL), contains electronics and sensors for the measurement of environmental data. Examples of the signals collected by the instruments of this string are water transparency, salinity or seismological information. On the one hand, these data are used for the neutrino detection capabilities (e.g. to determine the speed of sound in water, which is a necessary information for the acoustic positioning system). On the other hand, these data are also shared with sea science institutes for interdisciplinary studies. Additionally, the IL is equipped with sensors for acoustic particle detection, a side project of the Erlangen (Germany) group of the ANTARES collaboration (for some more details on this topic, see chapt. E and the references cited there). Fig 3.8 depicts a schematic representation of the IL and the various sensors it contains.

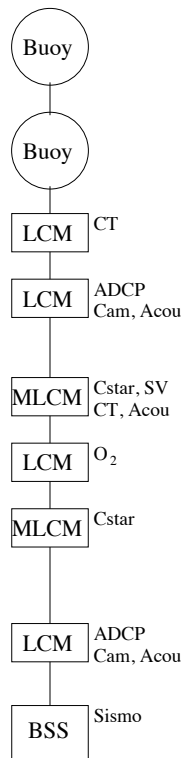


Figure 3.8: Schematic representation of the ANTARES instrumentation line and its sensors collecting environmental data: Conductivity and temperature (CT), water velocity (ADCP), water transparency (Cstar), sound velocity (SV), oxygeniety (O_2) and seismological data (Sismo). Storeys 2, 3 and 6 contain equipment for acoustic particle detection (Acou), with storeys 2 and 6 being also equipped with cameras (Cam) monitoring the surrounding water area.

3.3.6 Reconstruction of events and the need for a classification tool

The event reconstruction strategies for ANTARES data are based on the strategy to fit a cone with appropriate parameters through the hits which are believed to belong to an event. The axis of the cone then defines the path along which the lepton propagated through the water. Due to the almost perfect momentum transfer, this axis is virtually identical to the axis of the originating neutrino.

It is mandatory for this algorithm, that appropriate filter strategies remove all interfering background hits from the data before the algorithm is applied. Mainly two phenomena contribute to possible background noise:

- Bioluminescence
- Čerenkov photons from radioactive decay (mainly ^{40}K)

While the background noise from bioluminescence usually results in photon rates high above the baseline rate¹⁰ (and thus can either easily be filtered out or renders the corresponding data set unusable), Čerenkov light from radioactive decay is a more problematic background noise. Due to its omnipresence and uniform distribution in time and space, this background noise has a high potential of overriding the filter strategy by creating random coincidences resembling the signature of real events.

The "classical" approach to differentiate between background noise and real events, which is in principle also used by most of the ANTARES data filters (see e.g. [18, 19, 20]), is based on comparing the position and time information of all hits. Only those hits are then interpreted as physically relevant, for which the measured values correspond to the limits imposed by the speed of light (the *causality* condition). This strategy, however, suffers from the large disadvantage of being extremely time consuming, as the required amount of computing time increases approximately with the square of the number of hits present in the data set¹¹. This disadvantage is tried to be overcome by the "all-data-to-shore" strategy. This means that all data measured by the ANTARES detector are transferred to the coast station where they are stored for later analysis.

¹⁰The baseline rate is the mean rate of photons per second and PMT when no "extraordinary" events take place, see also chapt. D.

¹¹Not all of the actual track fitting and reconstruction algorithms use the raw coordinates of the hits as input parameters. Many of them use pre-estimates of which hits belong to a track as well as sophisticated considerations on the geometrical properties of the signals for performing the actual filtering task. However, the principal problem remains, as is also stated in chapt. 5 of [18]: "However, if we compute the time per reconstructed track the factor is reduced to ≈ 4 [author's note: as explained in the same paper, previous algorithms had a factor of ≈ 8 here, thus the term "reduced to"], as the number of reconstructed tracks is increased by a factor ≈ 2 ."

Obviously, a more efficient way is desirable here, not only to save memory space but also to analyse the data in near time to be able to quickly react on interesting events.

Thus, a different filter strategy has been developed in this work, which is based on a pattern recognition algorithm. Within this strategy, not single hits are compared to each other, but the whole set of hits in an event. An "event" in this context means a set of data which is defined by the hits detected in a certain time interval of measurement. It does not necessarily contain physically relevant data.

The strategy, which will be explained in detail in the following chapters, uses the fact that correlated signals from a Čerenkov light cone significantly differ from the signals of background noise. The pattern of these signals is tried to be recognised in near real time, so that the relevant information is immediately available for further investigation, whereas events containing only background noise can freely be discarded or stored for closer analysis at later time, respectively.

4 Dealing with patterns - some theoretical remarks

This chapter, which is mostly an English summary of selected sections from [21], provides some theoretical background on the topic of pattern recognition and classification, a broad field of science with almost as much different strategies and approaches as there are problems to solve. It mainly shall put the language used when talking about pattern recognition on a more mathematical fundament. Most of the terms used in this topic are taken from common language and keep their "intuitive" meaning. Thus, the rest of the work can be understood without knowledge from this chapter. The reader interested in the mathematical concepts behind the topic, however, may find some basic information here and, especially, in the referenced literature.

In order to give a precise formulation of "pattern classification" or "pattern recognition", the term "pattern" has to be defined first. But to do so, two further definitions are necessary beforehand.

Definition 1 *The environment E is the set of all physically measurable quantities ${}^\rho b(x)$:*

$$E = \{ {}^\rho b(x) | \rho = 1, 2, \dots \}$$

Obviously, due to the - in general - infinite amount of measurable quantities ${}^\rho b(x)$, a real measuring instrument will never be able to perceive the complete environment as a whole. Such a real instrument will rather observe only a subset of the environment, consisting of carefully selected quantities ${}^\rho f(x)$ which serve as input to (normally quite specialized) sensors. Such a subset is called an *issue*.

Definition 2 *An issue Ω is a subset of the environment E which consists of certain, selected quantities which can be measured by suitable sensors.*

If one sensor is enough in order to get all desired information, the issue is defined by

$$\Omega = \{ {}^\rho f(x) | \rho = 1, 2, \dots \} \subset E$$

If n sensors are required to measure all relevant quantities, the definition extends to

$$\Omega = \{ {}^\rho f_1(x_1), \dots, {}^\rho f_n(x_n) | \rho = 1, 2, \dots \} \subset E$$

Note that in this case, x_1 to x_n are in general vectors of different lengths.

These two terms now allow for defining the term *pattern*:

Definition 3 *The elements of Ω , that is the quantities ${}^\rho f_i(x_i)$, are called **patterns**.*

Pattern recognition can now be seen as mapping from a certain pattern to a suitable formal description. One special realisation of pattern recognition is **pattern classification**. In this case, the formal description is the *class* the pattern belongs to, which, in the most simple form, is just a unique ID, for example a number or a letter.

Definition 4 *The classes Ω_κ result from splitting the set Ω into k subsets Ω_κ , $\kappa = 1, \dots, k$ such that*

- $\Omega_\kappa \neq \emptyset$
- $\Omega_\kappa \cap \Omega_\lambda = \emptyset$, $\lambda \neq \kappa$,
- $\bigcup_{\kappa=1}^k \Omega_\kappa = \Omega$

Now all necessary definitions have been made in order to give a precise definition of *pattern classification*:

Definition 5 **Pattern classification** *is the mapping from one pattern, which is regarded independently from other patterns, to exactly one class Ω_κ of k possible classes. Under certain circumstances, some additional information about the location of the pattern, the translation t and rotation R with respect to some predefined coordinate system may be part of the classification's result, yielding the triplet $(\Omega_\kappa, t_\kappa, R_\kappa)$.*

For practical purposes some postulates are needed which will allow for using the previous definitions for real world applications.

Postulate 1 *To gain information about a certain issue Ω , a **representative sample***

$$\omega = \{(^1 f(x), y_1), \dots, (^N f(x), y_N)\} \subset \Omega$$

exists. Here, $^i f(x)$ is the i -th pattern and y_i some additional information belonging to it.

When creating such a sample, it is very important, that it only contains patterns belonging to the interesting issue. Additionally, it is important, that the sample is **representative**, because the pattern classification algorithm should not only be applicable to elements of ω but to (at least almost) all elements of Ω . The latter problem is called the problem of **generalisation** of observations.

The additional information y_i can be realised in many different ways, depending on the exact nature of the problem. Some examples are:

- $y_i \in \{-1, 1\}$: used in case of only one class. The pattern either belongs to it or not.
- $y_i \in \{1, \dots, k\}$: used in case of several classes. The pattern belongs to exactly one of k possible classes.
- $y_i = \emptyset$: No additional information at all.

In order to classify a certain pattern, two more, quite self explanatory postulates are required:

Postulate 2 *Each pattern possesses certain features which are characteristic for the class it belongs to.*

Postulate 3 *The features of all patterns of the same class form a quite compact area within the feature space. The areas belonging to different classes are quite disjoint. This is called **hypothesis of compactness**.*

Postulates 2 and 3 also help to determine the *similarity* of patterns. Two patterns are said to be **similar** to each other, when their features differ only slightly.

Although being quite self-evident, the concept of similarity has to be treated carefully. Consider for example the three statements:

1. The object is five meters long, of green color and has four wheels.
2. The object is five meters long, of yellow color and has four wheels.
3. The object is five meters long, of green color and has four helms.

Although the objects described in statements 2 and 3 both differ in only one property compared to the object described in statement 1, the object of statement 2 intuitively is more similar to that of statement 1 than the one described in statement 3. To account for this difference in similarity, usually some kind of **weighting** is introduced which allows to prefer some features to some others when evaluating the similarity of patterns.

Now, all terms concerning pattern recognition and classification used in the rest of this work (and even some more) have been defined. For further information on the topic, see e.g. [22] for the topic in general, or [23, 24] for the application of pattern recognition techniques in the areas of image recognition and astrophysics.

5 Detecting ANTARES events

5.1 First approaches

As explained in chapter 3.2.1, a typical event consists of a point-like shower and possibly a main secondary particle propagating through a large part of the detector. Čerenkov light emitted by both the shower and the secondary particle, spreads through the detector volume on the surface of a cone, thus illuminating the photomultiplier tubes in a correlated fashion. These correlated hits are then supposed to lead to certain patterns which significantly differ from patterns created by uniformly distributed background photons.

Several different approaches have been taken in the course of this work in order to recognise the signals of physical events and separate them from background noise. Before a detailed introduction to the successful strategy is given, two other methods will be presented and it will be explained why they did not prove to be suitable enough for the task. The first approach used artificial neural networks. Secondly, Principal Component Analysis was applied for projecting the input data to a description which could more easily be processed.

5.1.1 Artificial neural networks

Artificial neural networks (ANNs) are facilities which simulate the behaviour of animal nervous cells in order to reproduce their capabilities concerning pattern recognition and classification. There exists a vast amount of literature on this topic, though, which covers the wide range from basic introductions[25] over interesting real world applications[26] to pure mathematical theory[27].

The animal nervous system consists of some millions to many billions of nervous cells which are interconnected in a certain way, as depicted in fig. 5.1. Each cell, called *neuron*, consists of a cell body, named *soma*, with a long tail, the so called *axon*. The body of the cell is equipped with some thousands of smaller tails which split into even more branches, called *dendrites*. The functional principle of "learning" and "recognising patterns" is, that an electrical signal¹ spreads along the dendrites towards the cell body and from there further on along the axon. Each axon ends in special compartments, the so called *synapses*, which connect the axon to the dendrites or the somas of the

¹The exact biochemical process which creates and conducts these signals shall not be explained further, as it leads too far away from the topic of this work. It can be looked up in almost any introductory work to modern biology, see e.g. [28].

Input 1	Input 2	Output
0	0	0
0	1	1
1	0	1
1	1	0

Table 5.1: *Truth table of the XOR function.*

neighbouring cells. Within the synapse, the electrical signal is converted into a chemical signal by emitting chemical substances, the *neuro transmitters*. The latter cross the *synaptic gap* (which is a small gap between the synapse's cellular membrane and that of the connected neuron). By another biochemical process, the neuro transmitter creates again an electrical signal in this subsequent neuron, restarting the same procedure. Using a system of biochemical feedback reactions, the strength of the newly created electrical signal depends (loosely speaking) on the amount and biochemical type of reactions per time interval. The synaptic interconnection is thus either strengthened or weakened, depending on the history of past signals. Having different input patterns with a common similarity, this said similarity will lead to a strengthening of a certain bunch of interconnections (those synapses which are "accessed" by each pattern due to the common similarity), whereas other interconnections are weakened (because they are activated only randomly). This, finally, results in the fact, that similar patterns, which are perceived by some "input" neurons (e.g. some sense organ) will yield similar (or even the same) electrical signals in the corresponding "output" neurons (which are then, e.g., connected to muscular cells). The neural network has thus learnt to recognise patterns and react in the same, characteristic way to different patterns which have a common similarity. Fig. 5.2 depicts the principle of learning for the classical example of the so-called XOR function. The XOR function is a simple logical function with two inputs and one output, which adheres to the truth table 5.1. It is used throughout the literature to explain the principle of (artificial) neural networks.

The above mentioned characteristic power of biological networks, to *generalise* common features of different input patterns and to project them onto one and the same output reaction is tried to be simulated by artificial neural networks (ANNs). The basic structure of an ANN is the same as in its biological counterpart. It consists of three parts:

- An array of "perceiving" input cells
- One or more layers of interconnected cells
- An array of output cells

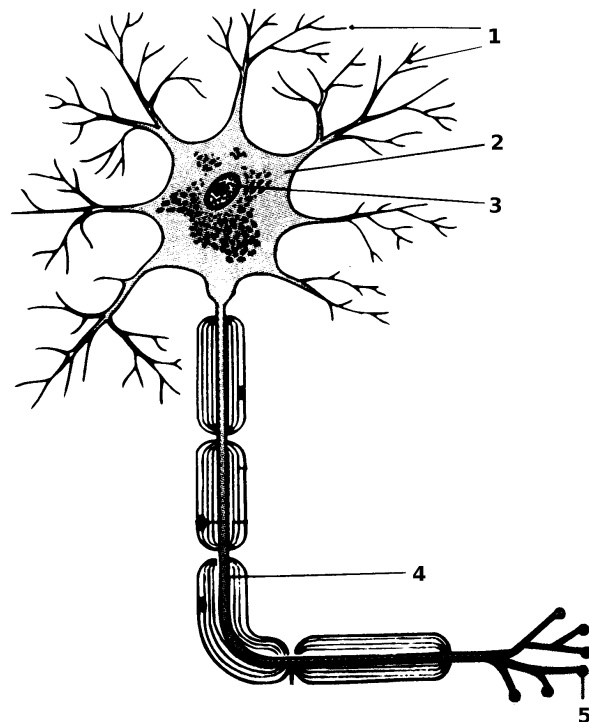


Figure 5.1: *Schematic drawing of a neuron. 1: Dendrites, 2: Soma, 3: Cell nucleus, 4: Axon, 5: Synapses. The drawing is taken from [28].*

Each "cell" is basically just a numerical variable. Its content symbolises its amount of "activity". This activity is propagated to some or all of the connected cells. Certain weights assigned to each of the connections determine the influence of the cells activity on the activity of the subsequent cells. The principle of learning patterns can now be summarised as follows:

- A certain pattern is presented to the input layer and the expected reaction (the activities in the output layer) is predefined.
- The pattern is propagated through the network by multiplying the activity of each cell for which this activity exceeds a fixed, predefined threshold, with the weight of the interconnections and adding the result to the activity of the subsequent cells.
- The result in the output layer is compared to the expectation value and the difference is fed back to the weights by a so-called *back-propagation algorithm*. These weights are then adjusted so that the output pattern becomes more similar to the expected result.

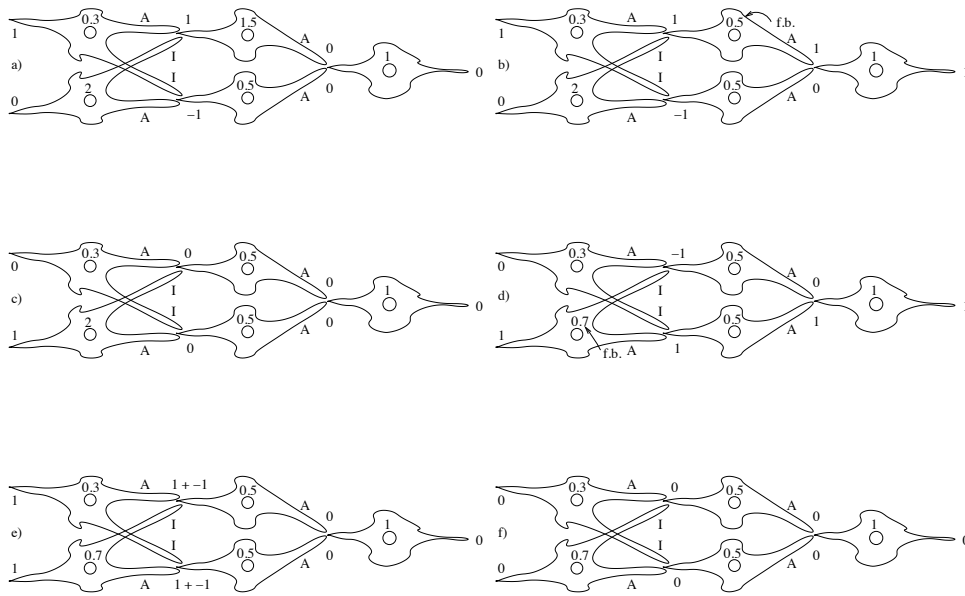


Figure 5.2: A simple three layered neural network for calculating the XOR function (table 5.1). The numbers next to the axons and dendrites represent the conducted activity (in arbitrary units). The numbers within the cell bodies show the threshold value the activity must reach in order to create a new signal. The dendrites labeled with "A" are "amplifying", i.e. they will create a new activity of value 1 in the subsequent neuron. The dendrites with label "I" are "inhibiting", they will create a signal -1.

a) The thresholds in the neural network are initially set to arbitrary values. A (1,0) pattern presented to the input neurons yields the wrong value 0. b) The wrong value is fed back to the neural network (f.b.) and the threshold of the upper intermediate neuron is adjusted. The network now yields the correct value 1. In a living organism, this feedback is achieved e.g. by a pain receptor which is connected to the system by additional neurons (these are not depicted for reasons of simplicity). c) A (0,1) pattern is represented to the network, and again the wrong value 0 is created at the output layer. d) Again, the threshold is adjusted by some feed-back mechanism (f.b.) (that of the lower input neuron this time) so that the correct value 1 is calculated. e) and f) The network now also computes the correct values for input patterns (1,1) and (0,0). It has learned to distinguish between the two pattern classes "both input neurons sense the same value" and "both input neurons sense different values".

For an exact calculation of the XOR function, the threshold values of the two input neurons need to be 0.5 both. This would be achieved by further iterations of the above procedure.

The series of pictures is based on the artificial neural network presented in [29].

This sequence is repeatedly applied for a large set of input patterns, the *training set*, until the difference between the actual result and the expected result is below a certain threshold for each pattern. If this training procedure has been completed and a new pattern is presented to the network, which is similar to a pattern of the training set, the same distribution of output activities will be reached. The network has thus learnt to map similar patterns to the same output values - it has *generalised* the structure of similar patterns. This capability can then be used for recognition or classification issues.

The main problem with neural networks is the large consumption of computing time. Even for the simplest realisations, for example networks based on so-called McCulloch-Pitts neurons[30], the amount of necessary computations roughly increases with the product of the number of all cells. As there have to be at least as many cells in the input layer as there are different input quantities (of whatever nature they may be) and considering that the number of cells must not differ too much from layer to layer for reasons of numerical stability, the input data should not contain too many of these quantities. This fact usually requires carefully designed pre-processing of the patterns to be analysed by the network.

Concerning ANTARES data, the basic quantities an event consist of are the signals of all PMTs with nanosecond temporal resolution. Considering a typical duration for an event of $1\mu\text{s}$, this leads to approximately 10^6 data points - too much for the naive approach to use a single input cell for each PMT at each nanosecond.

Several investigations to reduce the amount of data were done:

- Perform binning: treat the three PMTs of one storey as one unit and reduce the temporal resolution.
- Only take those PMTs which actually measured a signal and encode the time in the input cell's activation.
- Only take those signals into account with an SPE value above a certain threshold.

None of the data reduction strategies led to promising results, as they

- either removed too much necessary information,
- the resulting amount of data was still too large
- or they were not applicable in case of background noise, because due to random coincidences, the SPE value was no longer a suitable filter criterion

Another major problem generally arose from the correct construction of the training set. A well known story, which circulates the Internet for quite a time now (see e.g. [31]) tells about a neural network used for military purposes. This network should distinguish between images containing military equipment (tanks, aircrafts etc.) and images without showing such devices. After successfully training the network, it completely failed in its task when being applied to new, unknown images. The reason, which was found later, was that all images from the training set which contained military equipment were taken on a cloudy day, while those without the equipment were taken on a sunny day. The network had thus learnt to decide between different weather conditions but has completely ignored the devices which were present in the images. Although this story has never been confirmed officially and could quite probably be a hoax only, it nevertheless shows the principal problem: The patterns from the training set have to be chosen with extreme care in order to only differ significantly in the features which have to be recognised. Any other differences must occur uniformly distributed over the whole training set and must not correlate with the "interesting" features. Concerning ANTARES data, collecting events which fulfil these requirements is a very time consuming and error-prone task. There is a high variation in both the signatures of physical events as well as in the distribution and strength of the background noise.

All in all, these problems eventually led to a mean detection rate of approx. 70%, even when analyzing only such events which did contain pure physical data without background noise. This detection rate is not significantly better than it were on pure random decisions (which, by definition, would still "detect" 50% of all events). Thus the usage of ANNs was abandoned again and a different strategy was taken into consideration.

5.1.2 Principle Component Analysis

The second investigated pattern recognition algorithm was *Principal Component Analysis* (PCA), a statistical method invented in 1901 by Karl Pearson[32] and later generalized by Kari Karhunen and Michel Loève[33, 34]. To a certain extent PCA is comparable to a low pass filter. It takes a set of "training data" (i.e. a set of data with a common property which is to be recognised) and "smooths out" features which show a large variation from sample to sample, leaving only those features which are common to the whole training set. Subsequently, unknown data are analysed for the aforementioned features and, in case they are found, the unknown datum is considered similar to the training set.

The basic strategy can be summarised in the following way (for an introduction into PCA based on geometrical instead of algebraic considerations, see [35]):

- Prepare a set of training data $x_i, i \in \{1 \dots n\}$. Each datum has to be present as vector (if this is not the case, for example if the data are provided as an image of size $x \times y$, this requirement can be achieved simply by concatenating the columns of the image, resulting in one large column of length $x \cdot y$).

- Calculate the *average vector*

$$c = \frac{1}{n} \sum_{i=1}^n x_i.$$

- Calculate the *covariance matrix*

$$A = \frac{1}{n} \sum_{i=1}^n (x_i - c)(x_i - c)^T.$$

- Calculate the eigenvectors e_i of A .
- Select those eigenvectors with the k largest eigenvalues.
- For a new, unknown pattern y , calculate

$$y' = c + \sum_{i=1}^k e_i^T (y - c) e_i.$$

This projects y into a subspace of the eigenspace of the training data.

After the projection of the unknown pattern into the eigenspace of the training data, the similarity between y and the x_i s has to be determined. Several possibilities exist for realising this task, the most common of which are:

- Determine how "well" y is reconstructed by the k major eigenvectors e_i (which represent an *incomplete* basis of the eigenspace) by comparing y' to y (e.g. by calculating the difference of the Euclidean lengths). If y' is "similar enough" to y , it is also considered to be similar to the x_i s.
- Compute the mean Euclidean distance between y' and the x_i 's (which are derived from the x_i s the same way as y' is from y). If this mean distance is smaller than a certain threshold, y is considered "similar" to the x_i s.

As already mentioned in the introduction, the PCA is some kind of low pass filter: the remaining principal components (the y' s) indicate those features which are common to the input data. These are exactly those features, which do not vary much from

sample to sample. Unfortunately, this is the main disadvantage when trying to apply this method to ANTARES data. Due to the discreteness of the data and its large variety from event to event, the important features are encoded in the "high frequency" components of the event pattern. These, however, are those parts of the data which are effectively removed by the PCA, leaving only a smoothed representation of the uniform background noise.

5.2 Analysis of geometric structures

The strategy, which finally proved applicable, was to analyse the geometrical distribution of the detector data in a suitable coordinate system. This strategy shall now be presented in detail.

5.2.1 Principle

In order to get an idea on how the data actually "looked like", the space/time information of the arrival of light was plotted into a discrete coordinate system, with the x-axis being the time and the y-axis the space coordinate. Since the PMTs are numbered in a straight forward way along each string, starting with number 1 for the uppermost PMT of line 1 to number 900 for the lowest PMT of line 12, this PMT ID could directly be used as y coordinate. Each hit detected by a certain PMT at a certain time t contributed to the coordinate system as point at the corresponding PMT/ t coordinates.

As depicted in 5.3, the pattern resulting from a cone traversing a detector string is expected to consist of points lying on either a line or a hyperbola, depending on the angle of impact.

As illustrated, a light cone traversing the detector in an exactly horizontal manner yields a hyperbola opened to the right and if the impact angle is smaller than the apex angle of the light cone, the resulting pattern is that of a straight line. If the impact angle is somewhere between the apex angle and 90° finally, the signature is again a hyperbola, but its shape becomes distorted by the vertical component of the movement (for a detailed analysis, see section 5.2.2). So each particle traversing the detector in an angle greater than the apex angle of the cone will "draw" a (distorted) hyperbola opened to the right with its semi major axis parallel to the t axis into the t/PMT diagram.

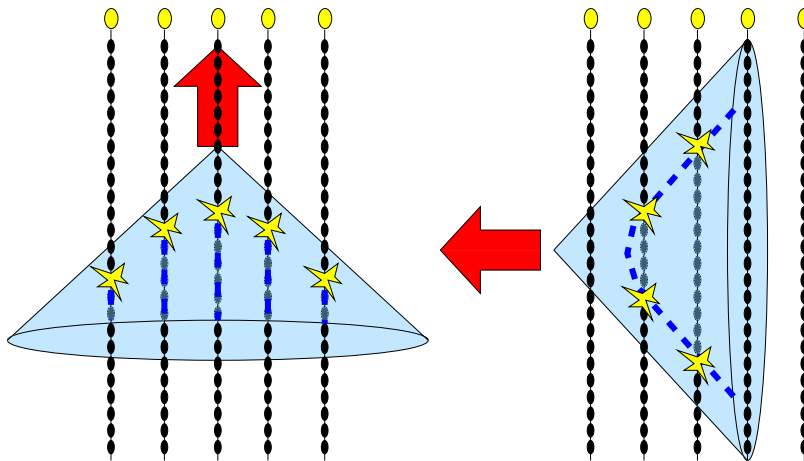


Figure 5.3: A light cone propagating through an array of strings. Left side: If the angle between the axis of the cone and the strings is smaller than the apex angle (i.e., the cone comes from "below"), each photomultiplier tube on a certain string is illuminated one after the other in equal intervals of time, leading to straight lines in an PMT/ t diagram (dashed blue lines). Right side: In cases of angles greater than the apex angle of the light cone (the cone comes from "the side"), the trajectory of the string can be seen as a plane yielding a hyperbola, which is mapped into the PMT/ t diagram.

Fig. 5.5 and fig. 5.6 depict the result of the mapping into a coordinate system for a typical shower-only and a typical muon-only event, respectively². The geometric structures, lines and (in this case only weak) hyperbolas, are clearly visible³.

5.2.2 Mathematics of moving hyperbolas

This section contains a mathematical analysis of the results obtained empirically in the previous section. It shall put the results on a more fundamental basis and will help to understand certain features of the detected neutrino signatures.

To calculate the shape which is created in an PMT/ t diagram by the light cone crossing a detector string in an arbitrary impact angle, it is enough to only consider the conic

²The data are taken from Monte Carlo simulations with a reduced detector size of only 12 storeys per line, thus the photomultiplier ID only counts up to 500 instead of 900. The reason was, that these data could then also be visualised on the ANTARES model, a 1:100 facsimile of the ANTARES detector, which proved quite well as 3D event display. This reduction of storeys, however, had no influence on the pattern recognition strategy described here.

³As can easily be seen, different event types yield remarkably different point densities. This is a direct consequence of the different shapes of light emitted by a point like shower event compared to a spatially extended muon track. This difference of the population density of the conic sections could be used not only to detect but even to classify a detected event.

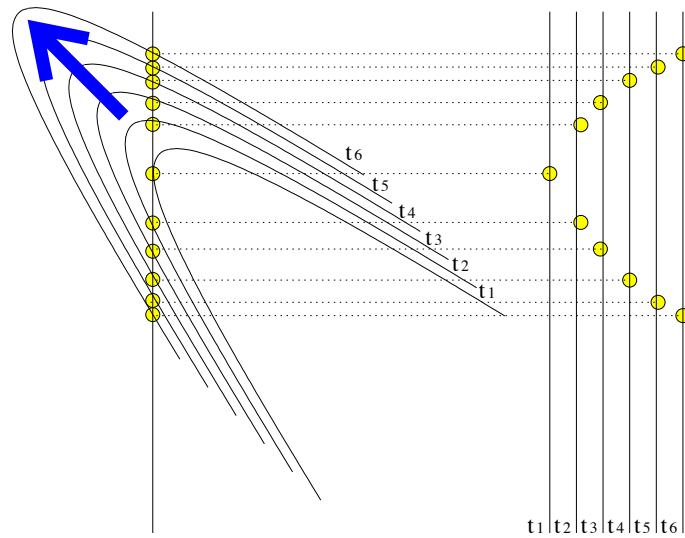


Figure 5.4: A light-cone crossing one detector string at an arbitrarily chosen angle somewhere between its apex-angle and 90° . Only the conic section (hyperbola resulting from the section between the plane defined by the moving cone and the string) is shown on the left hand side for different, equidistant times t_1 to t_6 . The right hand side shows the resulting signature in an PMT/ t diagram. It has the basic shape of a hyperbola opened to the right, however the shape may be distorted, depending on the impact angle, see section 5.2.2.

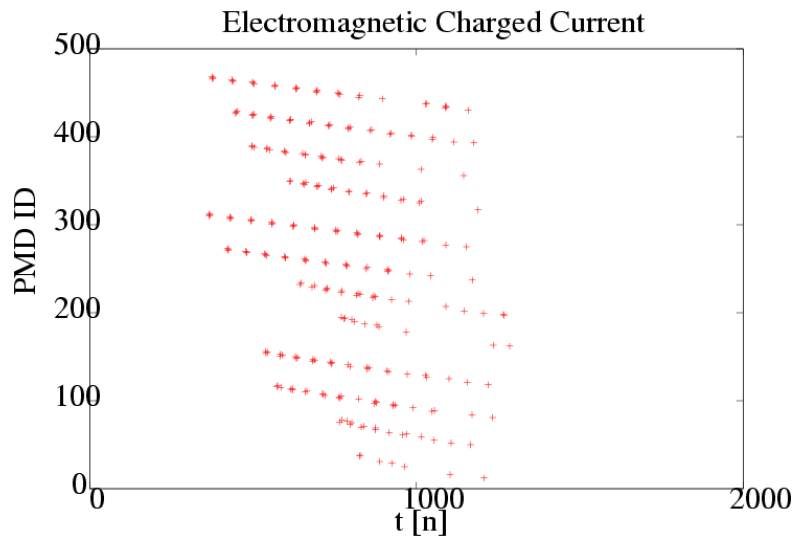


Figure 5.5: Data from a shower event, mapped into a PMT/ t diagram

section which results from the string intersecting the cone. For those events with an impact angle being larger than the apex angle of the light cone, this conic section will always be a hyperbola, as already mentioned in this work. To simplify things further,

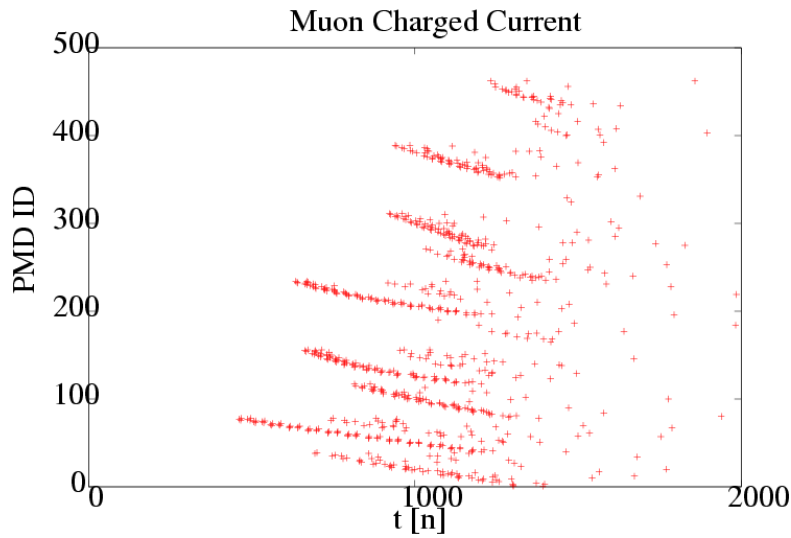


Figure 5.6: *Data from a muon event, mapped into a PMT/t diagram.*

it is assumed, that the string which is crossed by the hyperbola resides at the origin of the coordinate system and lies parallel to the plane spanned by the branches of the hyperbola. In this case it is sufficient to calculate those locations on the string which are intersected by the branches of the hyperbola.

As known from basic geometry (see for example [36]), a so called "east-west-opening hyperbola" (meaning a hyperbola with its branches opened "to the left and right") centred at the origin of the coordinate system is defined by

$$\frac{x^2}{a^2} - \frac{y^2}{b^2} = 1 \quad (5.1)$$

where a and b denote the semi major and (imaginary) semi minor axis, respectively. These two values also define the slope s of the asymptotes to the hyperbola's branches with respect to the semi major axis: $s = \pm \frac{b}{a}$. The solution of this equation is given by

$$y = \pm b \frac{\sqrt{x^2 - a^2}}{a} \quad (5.2)$$

In order to get the equation describing a hyperbola situated anywhere in space and rotated about a certain angle θ , the coordinate transform

$$\mathbf{v}' = \mathbf{R}(\theta)(\mathbf{v} - \mathbf{v}_0) \quad (5.3)$$

has to be applied. Here \mathbf{v} is the original vector belonging to the points of the hyperbola,

$\mathbf{R}(\theta)$ is an orthogonal rotation matrix performing a rotation about an angle θ and \mathbf{v}_0 is the displacement vector with respect to the origin of the coordinate system:

$$\begin{pmatrix} x' \\ y' \end{pmatrix} = \begin{pmatrix} \cos \theta & \sin \theta \\ -\sin \theta & \cos \theta \end{pmatrix} \left(\begin{pmatrix} x \\ y \end{pmatrix} - \begin{pmatrix} x_0 \\ y_0 \end{pmatrix} \right) = \begin{pmatrix} (x - x_0) \cos \theta + (y - y_0) \sin \theta \\ -(y - y_0) \sin \theta + (x - x_0) \cos \theta \end{pmatrix} \quad (5.4)$$

Inserting this result into equ. (5.1) yields

$$\frac{((x - x_0) \cos \theta + (y - y_0) \sin \theta)^2}{a^2} - \frac{((y - y_0) \cos \theta - (x - x_0) \sin \theta)^2}{b^2} = 1 \quad (5.5)$$

Equ. (5.5) defines a hyperbola, which is centred at (x_0, y_0) and rotated about an angle θ (with respect to the x axis of the coordinate system) around its centre.

In order to let this hyperbola move through the coordinate system along its symmetry axis (semi major axis), x_0 and y_0 have to be replaced by

$$\begin{pmatrix} x_0 \\ y_0 \end{pmatrix} \rightarrow \begin{pmatrix} t \cos \theta \\ t \sin \theta \end{pmatrix} \quad (5.6)$$

where the real valued variable t parametrises the actual position of the hyperbola. In the physical case and for a suitable choice of units, t is just the time. The signs have been chosen in such a way, that for increasing values of t , the hyperbola moves along the direction of the cusp of its right branch (basically "to the left"). Thus

$$\frac{((x - t \cos \theta) \cos \theta + (y - t \sin \theta) \sin \theta)^2}{a^2} - \frac{((y - t \sin \theta) \cos \theta - (x - t \cos \theta) \sin \theta)^2}{b^2} = 1 \quad (5.7)$$

To compute where this hyperbola crosses a certain vertical line at a given time, first of all equ. (5.7) has to be solved with respect to y , resulting in

$$\begin{aligned} y &= \frac{1}{-b^2 + b^2 \cos^2 \theta + a^2 \cos^2 \theta} \\ &\times \left(-b^2 t \sin \theta - a^2 x \cos \theta \sin \theta - b^2 x \cos \theta \sin \theta \right. \\ &\left. \pm \sqrt{a^2 b^2 (2xt \cos \theta + x^2 + b^2 - b^2 \cos^2 \theta - a^2 \cos^2 \theta + t^2 \cos^2 \theta)} \right) \end{aligned} \quad (5.8)$$

Next, a point which defines the line the hyperbola is crossing has to be selected. Without loss of generality, $x = 0$ can be chosen, yielding

$$y = \frac{-b^2 t \sin \theta \pm ab \sqrt{b^2 - b^2 \cos^2 \theta - a^2 \cos^2 \theta + t^2 \cos^2 \theta}}{-b^2 + b^2 \cos^2 \theta + a^2 \cos^2 \theta} \quad (5.9)$$

Substituting

$$\begin{aligned} A &:= \sqrt{-b^2 + b^2 \cos^2 \theta + a^2 \cos^2 \theta}, \\ B &:= \frac{ab}{\sqrt{-b^2 + b^2 \cos^2 \theta + a^2 \cos^2 \theta}} \text{ and} \\ X &:= t \cos \theta \end{aligned} \quad (5.10)$$

yields

$$y = \frac{-b^2 t \sin \theta}{A^2} \pm B \frac{\sqrt{X^2 - A^2}}{A} \quad (5.11)$$

Comparing to equ. (5.2) it is obvious, that the second term of equ. (5.11) is again the solution of a hyperbola which lies parallel to the X -axis. Up to scaling factor of $\cos \theta$, this axis is identical to the t -axis.

Obviously, the first term of equ. (5.11) can be neglected if $b^2 t \sin \theta$ is small compared to A^2 . This is the case for small intervals⁴ of t , if either θ is small or b is small compared to A . Moreover, for $\theta \equiv 0$, equ. (5.11) equates to equ. (5.2), thus exactly reproducing the shape of the original hyperbola. In both cases, the resulting hyperbola is of the parallel-to- t type.

Another boundary effect occurs when the incidence angle equals the apex angle of the hyperbola. As stated in the beginning of this chapter, the slope s of the asymptotes is determined by the semi major and minor axes a and b as $s = \pm b/a$, which can also be written as

$$\tan \varphi = \frac{b}{a} \quad (5.12)$$

with φ the apex angle of the hyperbola. This leads to

$$\begin{aligned} a &= \gamma \cos \varphi \\ b &= \gamma \sin \varphi \end{aligned} \quad (5.13)$$

with γ being a real valued constant defining the hyperbola's radius of curvature.

Inserting (5.13) into the denominator of equ. (5.9), $-b^2 + b^2 \cos^2 \theta + a^2 \cos^2 \theta$, and setting $\theta = 90^\circ - \varphi$ (which means that the angle between the hyperbolas vector of movement and the vertical line equals its apex angle) yields

$$\begin{aligned} &-b^2 + b^2 \cos^2 \theta + a^2 \cos^2 \theta = \\ &= -\gamma^2 \sin^2 \varphi + \gamma^2 \sin^2 \varphi \cos^2 \theta + \gamma^2 \cos^2 \varphi \cos^2 \theta \stackrel{\theta=90^\circ-\varphi}{=} \\ &= -\gamma^2 \sin^2 \varphi + \gamma^2 \sin^4 \varphi + \gamma^2 \cos^2 \varphi \sin^2 \varphi = \\ &= -\gamma^2 \sin^2 \varphi + \gamma^2 \sin^2 \varphi (\sin^2 \varphi + \cos^2 \varphi) = \\ &0 \end{aligned} \quad (5.14)$$

⁴The zero point of t can always be chosen such, that it coincides with the point of "first contact" between the hyperbola and the line at $x = 0$. So only intervals of t have to be considered.

So in case of $\theta = 90^\circ - \varphi$ equ. (5.9) diverges, which can easily be understood concerning the ANTARES detector: if the light cone intersects the string in an angle equal to its apex angle, the light front hits the whole string at the same time. This, in turn, leads to a vertical line in the (PMT/t) diagram, which is a line with infinite slope.

5.2.3 First pattern recognition results

As already mentioned, due to the geometry of the ANTARES detector, points belonging to physical events are all situated on either lines or hyperbolas in PMT/t space. In a real world detector, these patterns are superimposed by signals from ^{40}K decay and bioluminescence, which can be treated as uniformly distributed (white) noise. The task therefore was to develop an algorithm which allowed to distinguish those points which were aligned on such geometrical structures from others which were uniformly distributed in the coordinate system. In order to investigate and prove the applicability of such a strategy, first tests were performed using a simple algorithm which could be described as "walk-through-and-remove":

1. Find the left most point in the coordinate system.
2. Look, if another point is located on the right hand side within a certain maximum distance d .
3. If no such point is found, remove the original point from the coordinate system and start from the beginning with the next left most point.
4. If such a point is found, fit a straight line through both points.
5. Walk along the line and look, if another point lies on (or next to) it within the distance d .
6. If no such point is found, remove the second point from the coordinate system and restart at step 2.
7. If such a point is found, restart from step 4 and repeat until no more points are found.
8. If the number of points found exceeds a certain threshold n , store the coordinates of all points on the line.
9. Remove the collinear points and start from the beginning.
10. Repeat the whole sequence until all points have been removed.
11. Report the stored coordinates as detected physical event.

Fig. 5.7 shows the application of this algorithm to a muonic charged current event from a Monte Carlo simulation (without background noise). The blue line is the line mentioned in step 4 above. It starts at the hit $t = 156$ and $PMT = 116$ and ends at the hit $t = 1792$ and $PMT = 421$. The line visualises the track through the data set which was taken by the algorithm. Thereby the points which were abandoned again due to not meeting the requirements on n or d were not included. Each point in the vicinity of the line is considered to belong to a linear structure and thus to be physically relevant.

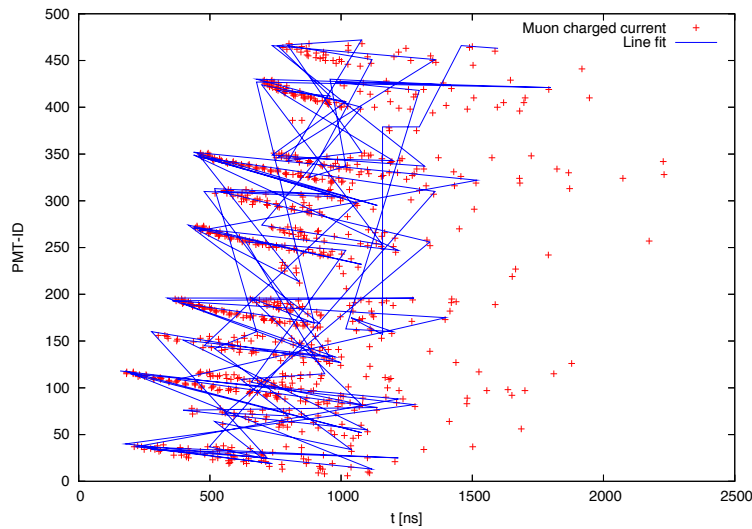


Figure 5.7: *Path along the hits from a muonic charged current event (blue line). The concentration of the blue line along the collinear point distributions is clearly visible.*

It is obvious, that the algorithm found the collinear point distributions in the coordinate system quite reliably. Thus, the basic strategy - namely searching for geometrical patterns - seemed to be a suitable approach for the detection of events. Unfortunately, the algorithm presented above is quite time consuming as the computing time roughly increases with the square of the total number of points in the coordinate system. Thus putting much effort in its improvement seemed inadvisable. Consequently, a better method for realising this task had to be found.

5.3 Event detection using the Hough Transform

Detecting geometrically distributed points among uniformly distributed background noise is exactly the problem for which the Hough Transform once was developed. Thus, it was this algorithm which finally was chosen for the pattern recognition task and proved to be successful.

In order to use the Hough Transform, a suitable parametric description of the shapes to be detected had to be found. In the following sections, first a general introduction to the Hough Transform is given, followed by the descriptions of the algorithms used for detecting straight lines and weak hyperbolas. It will also be explained, why the hyperbola detection was abandoned again (for a more detailed explanation see chapt. 5.3.3) and how this lack could be overcome by solely using the line detection algorithm. Next, it is shown how the intersections of the Hough Surfaces in the parameter space have been determined. Concerning this problem, an improvement of the "standard" Hough Transform was developed, which allowed for computing the cut-off value for successful detection prior to the analysis. This could then be used for detection of events even while the actual analysis is still ongoing. In the final sections, two improvements for elimination of random coincidences ("false positives") are shown, the "comparison of angles" and the "nearest-neighbour strategy".

5.3.1 Introduction to the Hough Transform

The Hough Transform is a simple means for the detection of geometric patterns in a set of points. It was originally developed by Paul V.C. Hough for the automatic recognition of straight lines in bubble chamber images [37] but can be used for the detection of any shape which can be expressed in parametric form. The basic principle is to map points from the original space, the *image space* I in a suitable way into the *parameter space* P , where "interesting" points yield intersections of hyper-surfaces. The localisation of these intersections in the parameter space then provides information about the position and the reliability of detected shapes. The exact realisation of the mapping thereby only depends on the shape to be recognised. In this section a short general introduction to the theory of the transform is given, mostly based on the argumentation of [38].

Theoretical background of the Hough Transform

Let $X = (x_1 \dots x_M)^T \in I$ be a point in the M dimensional image space I , $\Omega = (\omega_1 \dots \omega_N)^T \in P$ a point in the N dimensional parameter space P and f a parametric

function defining the Ω -dependent shape to be recognised. Then, each point in image space belonging to the shape determined by Ω fulfils, by definition, the condition

$$f(X, \Omega) = 0 \quad (5.15)$$

Now choosing a certain parameter value $\Omega_0 \in P$ leads to a subset $\tilde{X} \subset I$ of points in image space defined by the condition

$$\{\tilde{X} : f(\tilde{X}, \Omega_0) = 0\}. \quad (5.16)$$

On the other hand, choosing a certain point $X_0 \in I$ in image space determines a subset $\tilde{\Omega} \subset P$ of points in parameter space fulfilling

$$\{\tilde{\Omega} : f(X_0, \tilde{\Omega}) = 0\}. \quad (5.17)$$

This subset $\tilde{\Omega}$ describes an infinite amount of hyper-surfaces obeying the parametric constraint f which are passing through X_0 .

Let \hat{X} be a finite set of points satisfying the parametric constraint $f(x, \Omega_0) = 0, x \in \hat{X}$ for some Ω_0 . Then, equation (5.17) yields

$$\bigcap \Omega' = \Omega_0, \{\Omega' : f(x, \Omega') = 0\} \quad (5.18)$$

In other words, each of the points in \hat{X} leads to a certain hyper-surface in the parameter space. Each of these hyper-surfaces intersect at exactly one point, Ω_0 , with the number of intersections corresponding to the number of points on the shape in question, $|\hat{X}|$. Thus, the problem of finding points on a shape has been reduced to the problem of finding intersections of hyper-surfaces in the parameter space. The following explicit example should clarify the strategy of the transform:

Example application of the Hough Transform

Suppose, the task is to find points on straight lines, as was the original intention of Paul V. C. Hough. The parametric constraint of points on a line is often given in the *slope-intersection-parametrisation*[36]

$$y(x) = mx + b \quad (5.19)$$

This parametrisation, which also Paul V. C. Hough used in his original work[37], defines a set $(x, y) \in I$ of points lying on a line with slope m which intersects the y -axis at point $(0, b)$.

The transform from image to parameter space is done by expressing the parameters as function of the variables. In the simple example presented here, equation (5.19) thus becomes

$$b(m) = y - mx \quad (5.20)$$

which, in this special case, is again the equation of a line. Now, let (x_0, y_0) , (x_1, y_1) and (x_2, y_2) be three points, all of them lying on a line with slope m_0 and intersecting the y -axis at $(0, b_0)$. Then, by equ. (5.20), each of these points defines a line in parameter space with the property, that all three lines intersect at exactly one point, (m_0, b_0) . The point of intersection thus yields the parameter representation of the line in image space, where the points are lying on,

$$y(x) = m_0x + b_0 \quad (5.21)$$

and the number of lines intersecting at (m_0, b_0) corresponds to the number of points lying on the line in image space, in this case three. An example with three points at coordinates $(2, 35)$, $(3, 30)$ and $(6, 15)$, which define a line with parameters $m = -5$ and $b = 45$, is depicted in fig. 5.8.

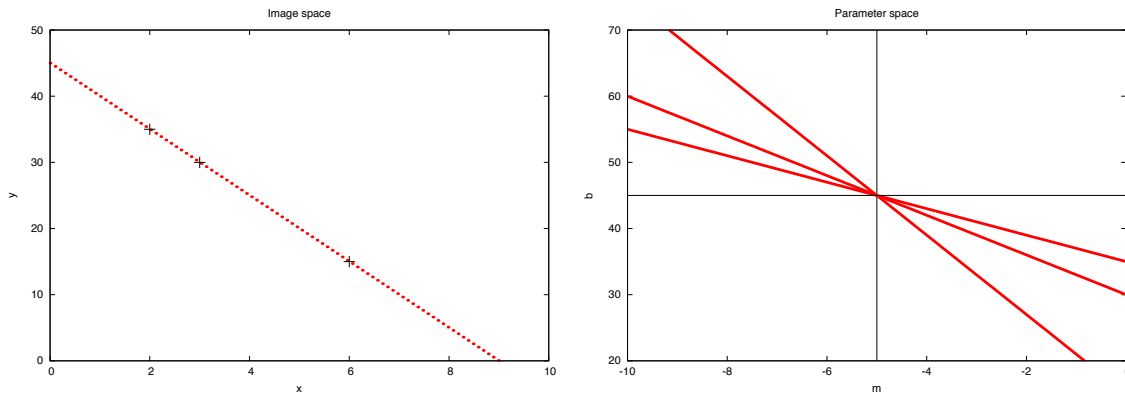


Figure 5.8: *Left side: Three points aligned on a line with slope -5 which intersects the y axis at $(0,45)$. Right side: Hough Transform of the points from the left image. The three lines have a common intersection at $(-5,45)$.*

A quite important problem is, that the Hough Transform detects any points in image space which satisfy the parametric constraint. This implies, that in case of high background noise, there is a high probability of several points satisfying the constraints by chance only. Thus it is mandatory to develop suitable strategies in order to distinguish between such random correlations and real signatures. The exact realisation of such an algorithm strongly depends on the properties of the data to be processed. Therefore, no generalised method can be given here. A special strategy, suitable for the needs to classify ANTARES data is presented in the remainder of this chapter.

Finally it is quite interesting to mention, that around of the time this work was written, an American team of neuro-scientists found some hints, that the human brain also uses a strategy similar to the Hough Transform in order to keep track of temporally extended events [39, 40].

5.3.2 Detection of straight lines using the Hough Transform

For straight lines, the situation seems to be quite clear, since a possible parametrisation has already been given in the previous section: $y(x) = mx + b \leftrightarrow b(m) = y - mx$. Unfortunately, this certain choice of the parametrisation of a line has the disadvantage of diverging in m for vertical lines. A common solution [41] to this problem is to choose a different parametrisation, called *normal parametrisation*, also known as *Hesse's normal form*:

$$y(x) = \frac{r}{\sin \theta} - x \cot \theta \leftrightarrow r(\theta) = x \cos \theta + y \sin \theta \quad (5.22)$$

Here, θ is the angle between the x -axis and the normal of the line through the origin of the coordinate system, and r is the length of this normal, see fig 5.9.

As a side effect this choice of parametrisation immediately yields the orientation of a detected line as "Hough coordinate". This can afterwards be used as criterion for discriminating between true events and random coincidences by comparing the angles of the lines, as, having already been mentioned, will be explained later.

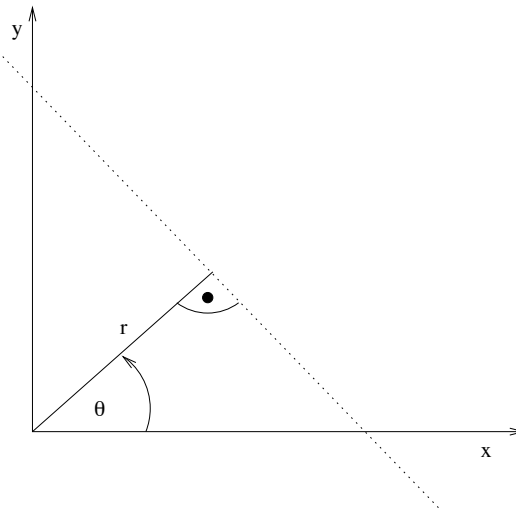


Figure 5.9: *Illustration of the normal parametrisation of a line*

5.3.3 Detection of hyperbolas using the Hough Transform

For hyperbolas, the situation is slightly more difficult. As derived in chapt. 5.2.2, events with an impact angle larger than the light cone's apex angle, create the signature of a distorted hyperbola, fulfilling the equation

$$y = \frac{-b^2(t - t_0) \sin \theta \pm ab\sqrt{b^2 - b^2 \cos^2 \theta - a^2 \cos^2 \theta + (t - t_0)^2 \cos^2 \theta}}{-b^2 + b^2 \cos^2 \theta + a^2 \cos^2 \theta} - y_0 \quad (5.23)$$

where a and b denote the semi major and semi minor axis, respectively, y_0 and t_0 denote the position of the hyperbola's centre and θ is the angle between the light cone's axis and the detector string.

This equation now consists of two coordinates, t and y , and five parameters, a, b, t_0, y_0 and θ . To get the associated Hough parametrisation, equ. (5.23) has to be solved for one of the parameters. In principle, it does not matter, which parameter to choose as the dependent and which ones as the independent Hough variables. However, as can be guessed from the general form of (5.23), solving the equation for example for t_0 leads to a more complicated equation, than for example solving for a . This more complicated equation will result in more computing time, in turn. As mentioned, solving for a yields:

$$a = \pm \frac{b(y \sin \theta - t + t_0 + y_0 \sin \theta)}{\sqrt{y_0^2 \cos^2 \theta + 2yy_0 \cos^2 \theta + y^2 \cos^2 \theta + b^2}} \quad (5.24)$$

Equation (5.24) describes four-dimensional hyper-surfaces in a five-dimensional Hough space. The shape and orientation of these hyper-surfaces is defined by the two parameters t and y .

Figure 5.10 visualises these hyper-surfaces for three arbitrarily chosen points at coordinates (80,6), (85,11) and (90,1). The parameter t_0 had been set to the fixed value $t_0 = 13$ and θ had arbitrarily been chosen as $\theta = 0$ in order to reduce the three-dimensional Hough planes to visualisable two-dimensional manifolds in a three-dimensional space. This choice could be made, because (distorted) hyperbolas can be drawn through any set of five points. Thus in case of only three points, two of the five parameters can be fixed to arbitrary values. The common intersection of the three planes at $a \approx 66$, $b \approx 10$ and $y_0 \approx 7$ is clearly visible in fig. 5.10, thus determining the parametrisation to these values⁵. As depicted in fig. 5.11, this parametrisation agrees very well with the data points chosen.

Unfortunately, the costs concerning memory consumption as well as computing time were much too high for real-time data analysis. Thus, only the straight line algorithm was used for further analyses. As will be shown later in the results chapter, this algorithm proved stable enough to correctly recognise the branches of the hyperbolas. Thus still most of the hits were detected, even at unfavourable angles of impact. The memory consumption in case of detecting hyperbolas shall now be explained in more detail.

⁵The coordinates are only approximate values, because for reasons of computing time, all calculations have been done with integral numbers. This, however, has no influence on the detection process itself.

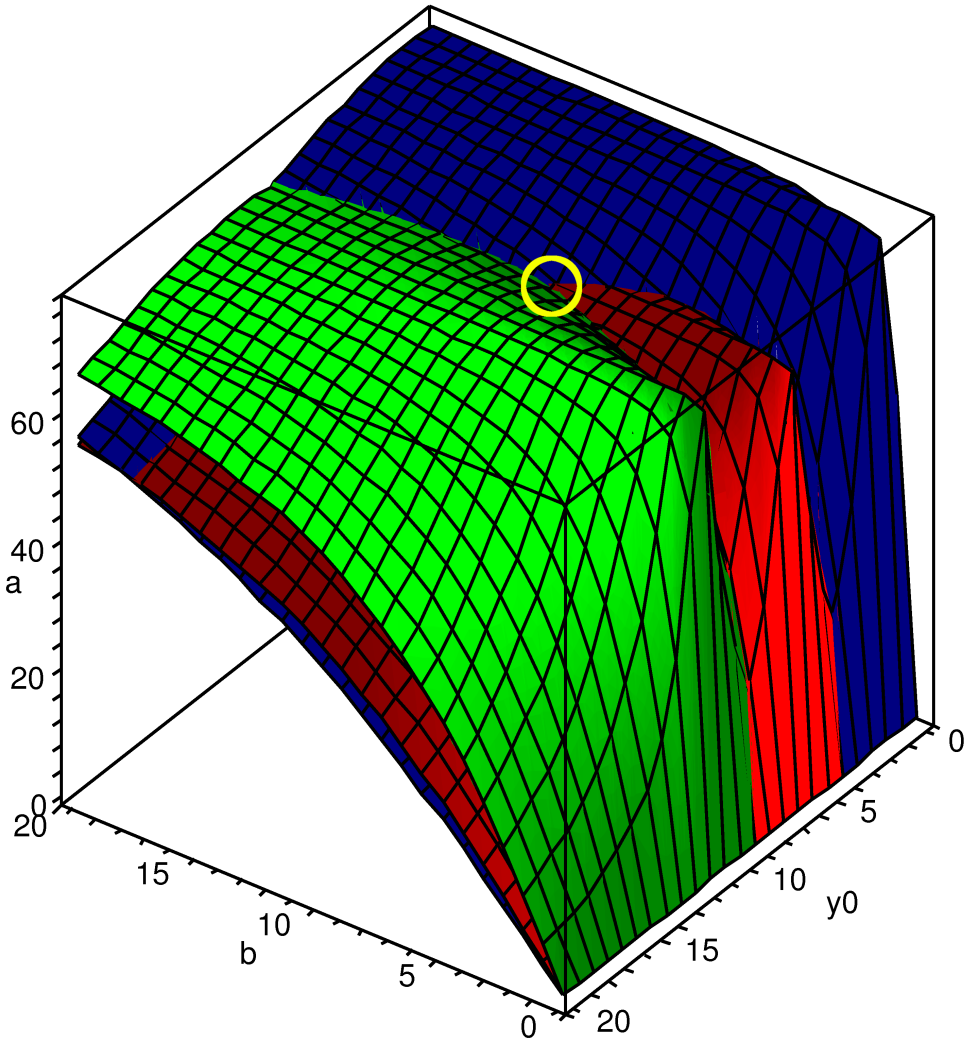


Figure 5.10: Three Hough planes corresponding to the data points $(80,6)$ (red), $(85,11)$ (green) and $(90,1)$ (blue) which intersect at $a \approx 66$, $b \approx 10$ and $y_0 \approx 7$ (yellow circle). θ had been fixed to 0 and t_0 to 13.

Memory consumption of the Hough Transform when applied to the detection of hyperbolas

The basic problem when trying to search for hyperbola shaped point distributions is the high dimensionality of the parameter space. For a unique parametrisation of a hyperbola, no matter if it is distorted or not, five parameters are necessary: The coordinates of the hyperbola's centre, t_0 and y_0 , the lengths of the semi major and the semi minor axis, a and b , and the rotation angle of the hyperbola, θ . These five parameters con-

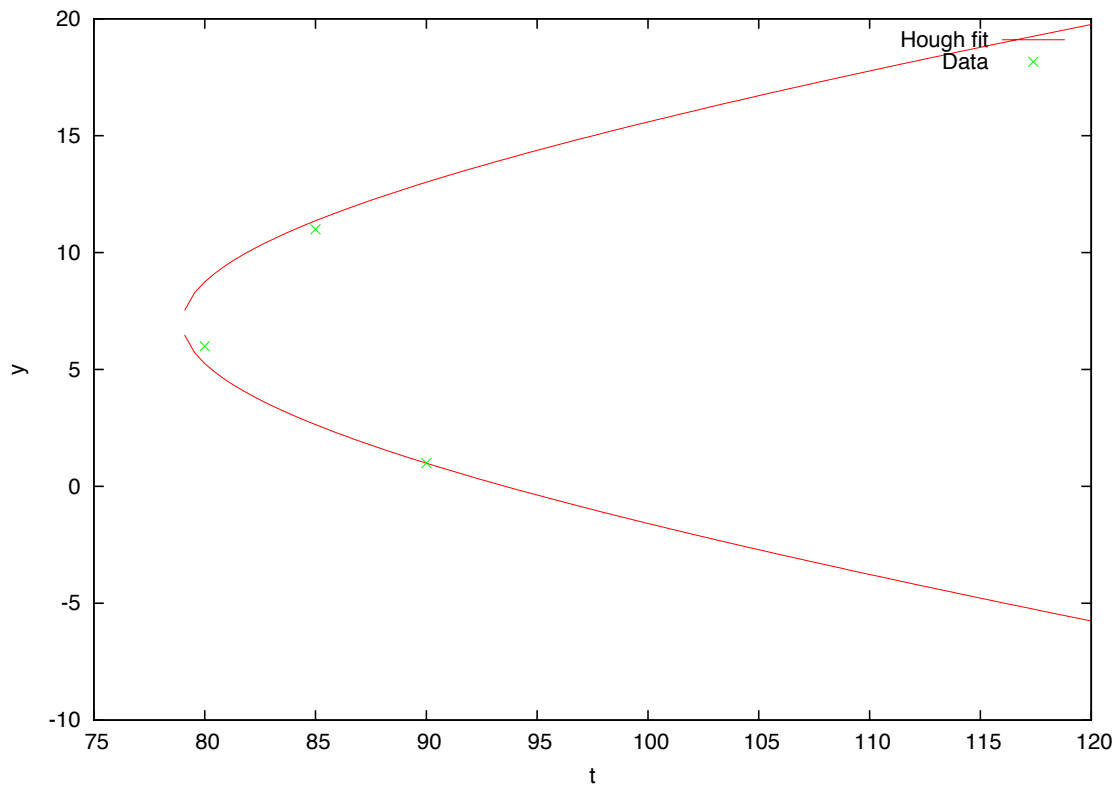


Figure 5.11: Three data points $(80,6)$, $(85,11)$ and $(90,1)$ and the corresponding hyperbola with parameters $t_0 = 13$, $y_0 = 7$, $a = 66$, $b = 10$ and $\theta = 0$. t_0 and θ had been fixed prior to the transform, a , b and t_0 have been determined by the Hough Transform.

sequently lead to a parameter space of five dimensions. Concerning ANTARES data, four of these five parameters cover a wide range of possible values. When signals from the whole detector are under investigation without binning, y_0 can take values between 1 and 900 and x_0 between 1 and 1000 (assuming a $1\mu s$ event with 1ns resolution). The same accounts for the values a and b . Since b/a defines the slope of the asymptotes of the hyperbola, both a and b can also take values between 1^6 and approx. 1000 in a discrete coordinate system. Only the angle θ is restricted to a set of 180 different values between -90° and 90° , because the choice of the coordinate system with the t axis being the time coordinate allows for "half-hyperbolas" only (those branches which are opened to the "right", i.e. to increasing values of time). Nonetheless, in this worst case concerning the amount of input parameters, the 5-dimensional Hough space has a size of approx. $2 \cdot 10^{14}$ cells, corresponding to a memory consumption of about 200 TB. The memory consumption can be reduced to approx. $2 \cdot 10^{11}$ cells (or 200 GB)

⁶In principle, a and b can also take the value 0, describing a hyperbola with either infinite ($a = 0$) or vanishing ($b = 0$) radius of curvature. But since both cases correspond to nothing else than straight lines, their recognition can fairly be left to the line-detection algorithm.

in case of binning and OM clustering. "OM clustering" means that the three OMs of one storey are treated as one single unit and "binning" means a reduction of the temporal resolution to the duration needed by light to cross the comparably bigger OM cluster (typically 5ns). Obviously, both values are unacceptable, thus analysing the whole image space at once is not feasible.

Fortunately, hyperbolas can only appear on single strings, therefore it is sufficient to search for them on a per string basis. In this case, the y_0 and b parameters only take values between 1 and 75 (or 1 and 25 in case of OM clustering), thereby reducing the amount of memory to approx. 1 TB or approx. 1 GB respectively.

Further reduction of memory usage can be achieved by a strategy derived from [42]: not all image space parameters are taken as Hough coordinates, but only a subset of them. All other parameters are taken as constants within the Hough Transform, while they are looped over outside the transform itself. Let, for example, a to e denote the number of possible values for five parameters of the parametric representation of a certain pattern. Then, instead of transforming an $a \times b \times c \times d \times e$ space, it is possible to loop over all possible values of d and e , thus performing $d \cdot e$ transforms of an $a \times b \times c$ space. Within each transform, possibly recognised candidates are stored for later examination and the memory is reused for the next transform. If for a , b and c those coordinates are selected which span over the smallest intervals of possible values, this will reduce memory consumption to $a \cdot b \cdot c$ bytes, although the computing time will increase about a factor of $d \cdot e$. Applying this strategy to ANTARES data would result in approx. 10^6 transforms with each transform consuming between 200MB in the worst and some kB in the best case.

Although the memory consumption is in an acceptable range when using the latter strategy, the computing time starts to exceed all practical limits in this case. Based on a mean computing time of approx. 100ms per event for the straight line algorithm, a mean time of approx. 1s seems reasonable for the three dimensional hyperbola transform as the parameter space has one dimension more than in the straight line algorithm and the computing time increases exponentially with the dimensionality. Looping over 10^6 combinations of external parameters would then result in a total computing time of 10^6 s per event, corresponding to approx. 12 days.

The calculations presented in this section show, that the Hough Transform in its primitive form is not applicable to detect hyperbolas in the data set. Several improvements and adaptations of the Hough Transform exist [43, 44, 45], though, which might overcome the problems mentioned here. Some closer analysis of these advanced algorithms seems advisable.

5.3.4 Finding intersections

After determining the parametrisation of the shape to be recognised, an algorithm suitable for finding the intersections of the hyper-surfaces in the parameter space had to be developed. The standard way, which is mentioned quite regularly in literature (see e.g. [41, 46]) can be summarised as follows:

- Initialise a memory region with zeros and use it as virtual coordinate system representing the Hough space.
- For each point in image space, calculate the shape of the hyper-surface in the Hough space and increase each point of the virtual coordinate system (and thus each memory cell) belonging to the hyper-surface by one.
- Search for local maxima in the virtual coordinate system.

Fig. 5.12 illustrates this in detail for the simple case of finding lines using the slope-intersection parametrisation. The basic procedure is the same for the normal parametrisation as well as the hyperbola parametrisation. In the latter, however, the Hough plane is a five dimensional manifold which leads to the mentioned unsuitable high consumption of memory and computing time when the maxima are searched for.

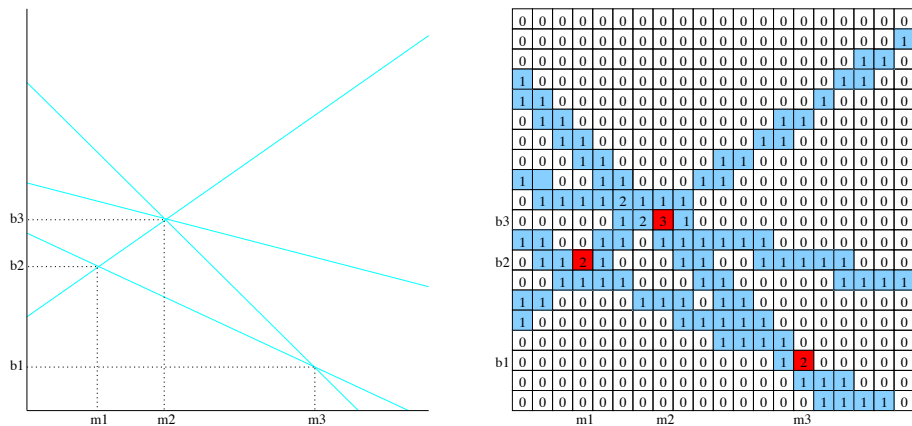


Figure 5.12: *The principle of finding intersections: Each line of the Hough plane (left) is "drawn" into a virtual coordinate system by increasing associated memory cells by one (right). Intersections of lines show up as local maxima (red squares). The indexes of these memory cells correspond to the coordinates in Hough space. In this case, the three intersections $(m1, b2)$, $(m2, b3)$ and $(m3, b1)$ have been found.*

In case of a priori knowledge of the cut-off parameter defining how many points have to be on the structure in question to be detected properly, the search for local maxima

can be performed parallel to "drawing" the hyper-surfaces into the virtual coordinate system: After each point drawn into the Hough space, the according memory cell is checked for exceeding the cut-off value. If this is the case, the corresponding parameter set is stored for later usage as parametric description of a detected structure. The memory cell is then tagged as "unusable" to prevent multiple detection of the same structure⁷. An algorithm for estimating this cut-off value is presented in the next section.

This strategy completely avoids the computing time for searching maxima. For the detection of hyperbolas, however, the amount of memory needed for analysis still stays beyond any practical limit. For the case of detecting lines, in contrast, this algorithm is quite suitable without further alterations, especially when using the normal parametrisation. A short assumption of the memory consumption for detecting lines shall follow now.

Memory consumption of the Hough Transform when applied to the detection of straight lines

Since the image space contains only positive coordinates in both time and space, θ is restricted to the interval between -90° and 180° - other lines with different angles will not be mapped to "existing" coordinates, as depicted in fig. 5.13.

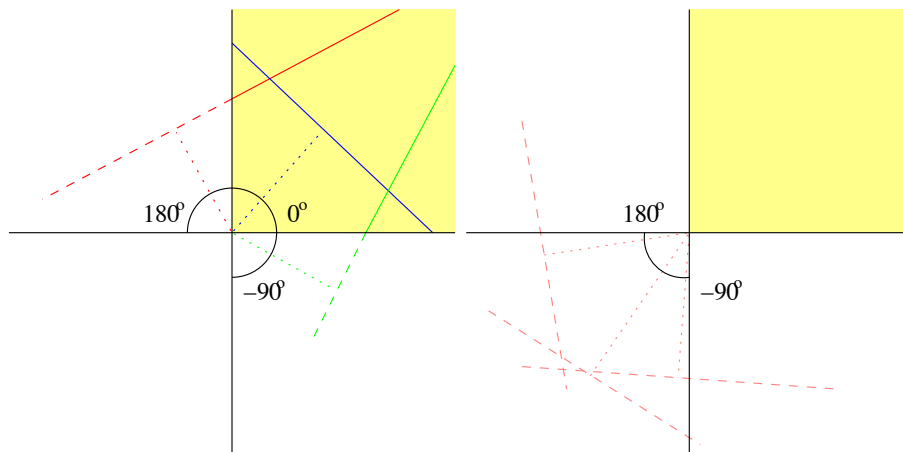


Figure 5.13: *Left side: Only lines with an angle θ of their normal between -90° and 180° correspond to lines in the physically relevant part of the coordinate system (yellow area). Right side: All other values for θ do not parametrise patterns belonging to physical events.*

⁷In the implementation used in this work, an array of signed variables was used for realising the Hough plane. To mark a cell as "unusable", it was set to the value -127, since a negative value obviously could not occur otherwise.

Further on, the largest value of r appears for lines starting at the origin of the coordinate system and passing through its top right corner. Assuming a temporal resolution of 1ns and a typical duration of $1\mu\text{s}$ for an event, this yields a maximum value for r of $r = \sqrt{900^2 + 1000^2} \approx 1300$ without binning and of only about $r = \sqrt{300^2 + 100^2} \approx 320$ when clustering all three OMs of one storey to one unit and perform binning of 10ns in time. Using an angular resolution of 1° and thus 270 possible angles for a line to pass through, the Hough plane takes a size of approx. 350 kB or approx. 86 kB of memory, respectively (assuming that one "cell" of the virtual Hough coordinate system requires one byte of storage space). When investigating data from each detector string separately, these values decrease even more, down to $r = \sqrt{75^2 + 1000^2} \approx 1000$ for the raw data and $r = \sqrt{25^2 + 100^2} \approx 100$ in case of binning and OM clustering, leading to a memory consumption of 270 kB or 27 kB, respectively.

5.3.5 Determination of cut-off parameter

As already mentioned in 5.3.1, the Hough Transform will detect **any** set of points aligned on a line. So, in cases of very high background noise, there is a high probability of several points being aligned on lines by chance only. Fortunately, this probability decreases approximately exponentially with the number of points positioned on the line. Therefore the number of points on the line can be used as cut-off parameter to decide between a "real" line drawn by a physical event and a "false" one based on a random coincidence. The strategy is to treat all points in an event as equally distributed background noise, calculate the number of lines L which are to be expected by k random coincidences and then choose that value of k as cut-off parameter for which L vanishes. The basic idea is, that due to their correlations, real events will lead to a number of collinear points which significantly exceeds the value expected by random coincidences only.

It is now described how this cut-off value is calculated. Considering a square coordinate system of size $n \times n$, the task is to compute the number of lines which are expected if N points are drawn randomly distributed into this coordinate system and k points are required to be on a line. Since a line can be drawn through any set of 2 points, this question is equivalent to the question of the probability of $k - 2$ points being situated on the line defined by the remaining 2 points multiplied by all different sets of k points among N .

For simplicity, it is assumed, that the the first two points are aligned horizontally. Fortunately, the algorithm derived from this assumption is also valid for almost all non horizontal lines as long as they are drawn into a *discrete square* coordinate system⁸.

⁸The precondition of discreteness is fulfilled by definition of the Hough Plane. The precondition of squareness is fulfilled by the properties of the ANTARES detector and a typical event: The ANTARES

As can easily be verified by counting, a horizontal line in a square, discrete coordinate system consists of exactly the same amount of pixels as e.g a diagonal one, as long as it either ends at opposite sides of the frame or starts at one of the corners, see fig. 5.14.

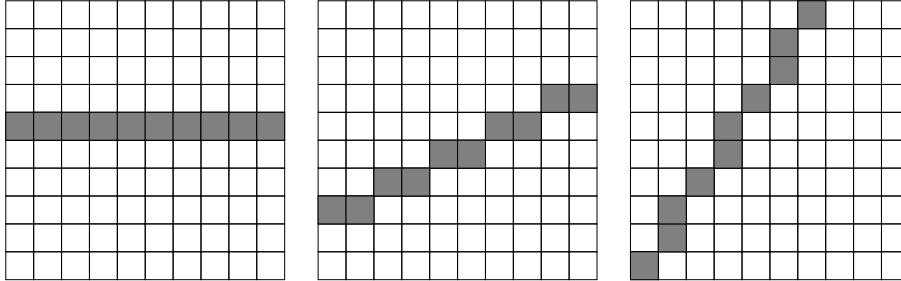


Figure 5.14: *Differently oriented lines in a discrete square coordinate system. As can easily be verified by counting, each line consists of exactly ten pixels, independent from its orientation.*

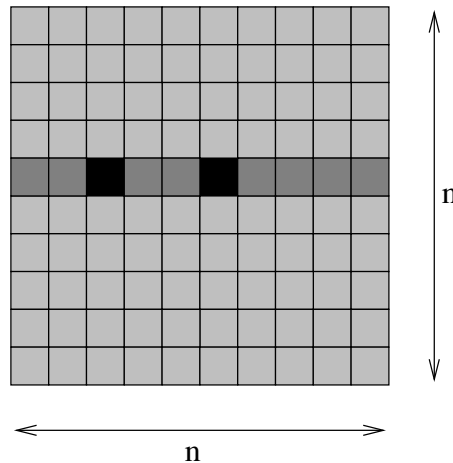


Figure 5.15: *A grid of $n \times n$ fields with two fields occupied (black squares). $n^2 - 2$ fields are still free (light and dark grey squares), with $n - 2$ of them aligned on the same line as the occupied ones (dark grey squares).*

Fig. 5.15 visualises the distribution of points used now for deriving the algorithm. In this coordinate system of size $n \times n$, 2 coordinates are "occupied" by a point. Since $n^2 - 2$ coordinates are still "free", the probability for the 3rd point to be drawn into a certain field is $\frac{1}{n^2 - 2}$. As there are $n - 2$ free fields which fulfil the requirement of collinearity, the probability for the 3rd point to become part of the line is thus $\frac{n - 2}{n^2 - 2}$. Subsequently, proposed that already three points are positioned on the line, the probability for the 4th point is $\frac{n - 3}{n^2 - 3}$ and, eventually, for the k th point it is $\frac{n - (k - 1)}{n^2 - (k - 1)}$. Consequently the

detector consists of 900 PMTs and a typical event lasts for about $1 \mu\text{s}$, which are 1000 ns at nanosecond temporal resolution.

probability for k random points being aligned on the same horizontal line by chance in a $n \times n$ grid is

$$p(k, n) = \binom{n-2}{n^2-2} \binom{n-3}{n^2-3} \cdots \binom{n-(k-1)}{n^2-(k-1)} = \prod_{i=2}^{k-1} \frac{n-i}{n^2-i} \quad (5.25)$$

To get the total number of lines L expected to be defined by k of N points, $p(k, n)$ must be multiplied by the number of unordered sets of k points among N , which is given by the binomial coefficient

$$\binom{k}{N} = \frac{N!}{(N-k)!k!}. \quad (5.26)$$

Thus,

$$L(N, n, k) = \frac{N!}{(N-k)!k!} \prod_{i=2}^{k-1} \frac{n-i}{n^2-i}. \quad (5.27)$$

Assuming $k \ll N$ and $k \ll n$ (from which follows $i \ll n \forall i$), yields

$$\frac{N!}{(N-k)!k!} \approx \frac{N^k}{k!} \quad (5.28)$$

and

$$p(k, n) \approx \left(\frac{1}{n}\right)^{k-2} \quad (5.29)$$

Since these conditions are always true for physical events due to the high amount of data points, these approximations are used instead of equ. (5.27) in this work for reasons of reducing computing time.

In order to take into account the contribution from lines that do not obey the constraints which were the basis for this estimation (ending on opposite borders and/or starting from a corner), the cut-off value k was increased by 1 before usage, leading to the following constraint:

$$L(N, n, k) = \frac{N^{k-1}}{(k-1)!} \left(\frac{1}{n}\right)^{k-3} \stackrel{!}{\approx} 0 \quad (5.30)$$

The correction value of 1 had been determined empirically by a set of tests with many different line configurations.

Equ. (5.30) was solved numerically for k for each event and the result was used to decide if a detected structure could be a candidate for a physical event.

5.3.6 Elimination of random coincidences by comparing the angles of detected structures

Although the estimation of the number of expected collinear points by random coincidences developed in the previous section allows a quite well suppression of background, there is still a finite probability, that more points than calculated are collinearly aligned by chance only. Fortunately, those lines which are passing through the points belonging to physical events are all parallel in the PMT/t diagram. This is because the Čerenkov light cone crosses each detector string with the same angle⁹. Thus, the θ parameter can be used for further reduction of randomly coinciding background hits.

The strategy used in this work is to take only those lines as physical signatures whose θ parameters mutually differ less than a certain threshold. In order to efficiently find those lines, first of all the lines are sorted by their θ parameter. Next, for each θ value, the number of "similar" angles is determined within the data set. "Similar" in this context means that the difference of the angles of a pair of lines lies within a predefined threshold. Then the lines are sorted according to these numbers of lines which fulfill the threshold condition. Finally those lines are taken as physically relevant, which are on top of the sorted list and whose θ parameter lies within the threshold value around their mean θ value.

5.3.7 Elimination of random coincidences by application of the nearest-neighbour strategy

Another filter strategy, which in the following is named "nearest-neighbour strategy" is motivated by the fact, that all hits belonging to physical events lie within compact areas of the image space while randomly coinciding background hits usually are situated anywhere inside the coordinate system, as shown in fig. 5.16. This allows to efficiently filter them out by only taking those hits into account which are not more than a certain distance apart, leading to a further decrease of the cut-off value.

Of course, both strategies will only help to suppress falsely recognised background hits but will not lead to an increase of true hits.

5.3.8 SPE based pre-filter

In order to remove a large part of the background noise prior to the application of the pattern recognition algorithm, a simple SPE (Single Photo Electron) based pre-filter

⁹Deviations from this assumption can of course appear due to movements of the detector strings caused by sea currents. These movements are considered small enough, though, to freely be neglected.

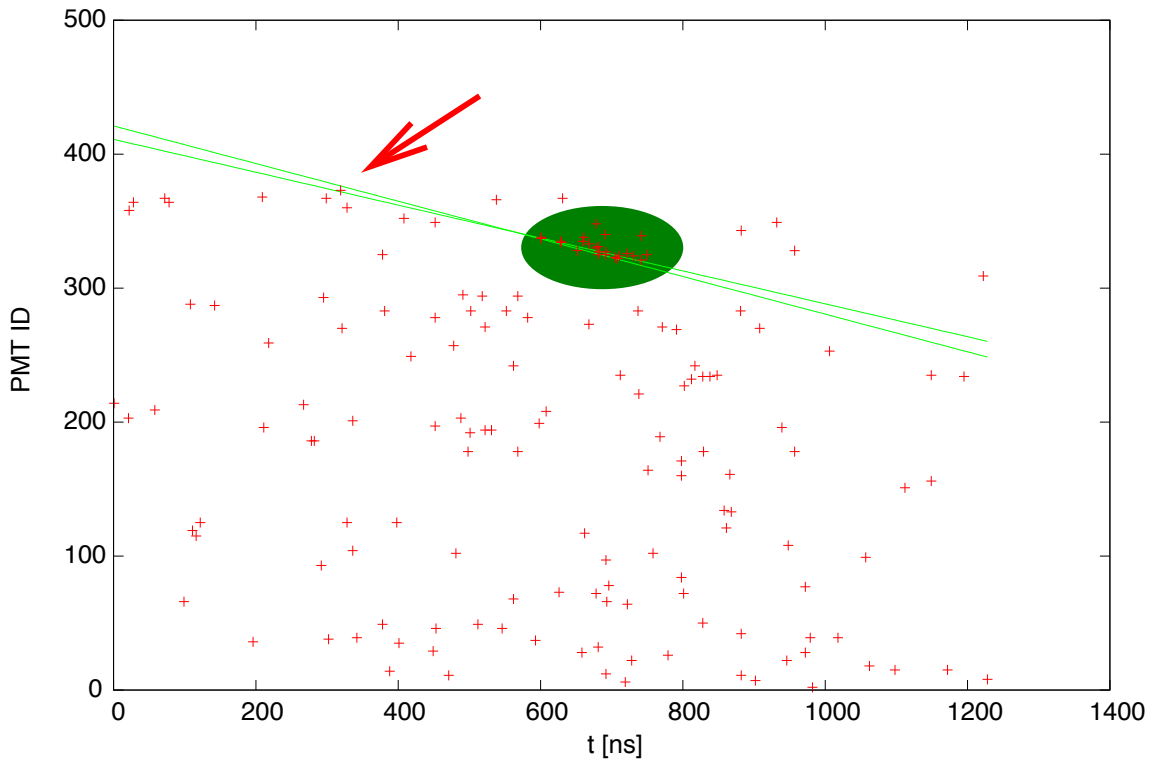


Figure 5.16: *Basic principle of the nearest-neighbour strategy. Hits of a physical event lie quite compact to each other (green area), while background hits are usually much more distinct, although they may also be collinear and thus are falsely detected as belonging to the event (red arrow).*

has been integrated into the pattern analysis package. To understand the idea behind this strategy, it is necessary to know, that the read-out electronics integrates the PMT signals over short periods of time with a default value of 25ns. Single photons hitting the PMT within this interval will thus lead to a much weaker signal than multiple photons which reach the PMT within this period. The basic idea was, that the uniformly distributed background yields hits largely distinct in time: at a background rate of e.g. 100kHz, photons will - by definition - arrive each $10\mu\text{s}$ in the mean. Thus they lead only to single hits within the integration window. Superluminal particles, in contrast, emit Čerenkov light at a much higher intensity, resulting in many photons reaching the PMTs within the integration interval. Background could therefore be suppressed by ignoring all hits with a signal corresponding to one photon only.

This pre-filter strategy has also been implemented in the event recognition package, although its impact has not been investigated further, since it is opposed by two main reasons:

- Too less hits in the input data spoil the algorithm for determining the Hough Transform cut-off (5.30), which is based on the assumption of the presence of background noise.
- It is not proven whether the background noise is indeed uniformly distributed and does not contain correlated photons of any kind. In fact, an analysis of the background noise, which was performed at the very beginning of this work (see chapt. D) gives rise to the assumption that such correlations do exist. If this is the case, these correlations are considered the more problematic phenomenon, as they have the capability to spoil any SPE based filter strategy.

As already mentioned and, moreover, at least for experimental purposes - the data recognition package offers the possibility to remove hits below a certain photon-per-time threshold prior to any other analysis. A very simple algorithm for determining a suitable cut-off has also been implemented. This algorithm reports that value as recommended threshold were the measured photon rates of 33% of all hits are below of. Since only the remaining hits have to be analysed, this leads to a heavy reduction of computing time but, on the other hand, has to be treated with much care, and should no be used in general, at least not for "production" use.

6 Results

The following chapter contains the results from the application of the Hough Transform based algorithm. In the first section, the algorithm was applied to data from Monte Carlo simulations. The patterns which have been recognised by the Hough Transform were then compared to the events which were actually present in the data sets. In the second section, the algorithm was applied to data sets containing background noise only. In the last section, the algorithm was eventually applied to real data which were recorded by the ANTARES detector in June 2007. In each section, the results from the Hough Transform algorithm were compared to the results from the ANTARES standard trigger. For the reason of readability, most of the plots contained in this chapter depict only summaries and general overviews on the results. More detailed plots to each of the data sets analysed in this chapter are shown in chapt. B and C.

6.1 Application to Monte Carlo data

This section summarises the results from the application of the Hough Transform algorithm to simulated ANTARES events from Monte Carlo runs. Several configurations of the Hough Transform algorithm have been tested (binning, single vs. multi string etc.) and the results have been compared to the results from applying the ANTARES standard trigger to the same Monte Carlo data sets.

All data in this section are based on these four different sets of event types¹:

- 354 electronic charged current events (*el_cc*)
- 282 electronic neutral current events (*el_nc*)
- 294 muonic charged current events (*mu_cc*)
- 291 muonic neutral current events (*mu_nc*)

The energies of the primary neutrinos lied within a range of $\approx 10^3$ to $\approx 10^6$ GeV for each set of events. All events were generated without background photons, which were added later as simple white noise. This allowed for comparing the recognised data to

¹These numbers of Monte Carlo events may seem quite low compared to usual applications of this technique, where thousands or even millions of data points are simulated. The reason for this is, that the focus of this work was initially based on the development of the Hough Transform algorithm on a mathematical level and the application to Monte Carlo data was added as "proof of concept" later. Nevertheless, the events have been chosen carefully in order to cover a wide range of possible input configurations. The results are therefore considered reliable.

the actual physical data, namely the simulated raw data before it was merged with background noise. Background photons were added in a range between 70 kHz and 300 kHz in steps of 10 kHz for each individual event. The boundary values of 70 kHz and 300 kHz have been chosen because they are the mean background rates at the ANTARES site in times of calm or extremely heavy sea conditions [47]. The interval of 10 kHz had been chosen arbitrarily.

Further on, the following naming conventions shall apply to all the plots and analyses in this work:

- *All hits*: All hits in the input data set, meaning physical hits as well as background noise.
- *Real hits*: Hits which belong to photons from the actual particle track(s), i.e. those from the original simulation without background noise.
- *Found hits*: All hits which were recognised by the Hough Transform as "belonging to an event".
- *True hits*: Hits which were recognised by the Hough Transform and indeed do belong to an event.
- *False hits*: Hits which were wrongly recognised by the Hough Transform but in fact were caused by background photons.

6.1.1 Analysis of the detection efficiency

In this section, the efficiency of the event recognition algorithm is analysed. In this context, "efficiency" refers to the amount of correctly or wrongly identified events (as function of certain parameters).

Whole detector without binning

The Hough Transform algorithm was applied to data sets from the whole detector without further modifications.

Figure 6.1 illustrates a typical example of the application of the line recognition algorithm to an electronic neutral current event. The incident neutrino had an energy of $1.1 \times 10^5 \text{ GeV}$ and the event contained background noise at a rate of 100kHz. The top left image shows the raw data, which was fed to the recognition algorithm. The top right image shows the lines, which the Hough Transform detected in the set. The cut-off for detecting a line was determined to be > 5 points per true line by applying

equ. 5.30, and only those lines were used for further processing, which differed in less than 5 degrees in their θ parameter. The threshold of 5 degrees had been determined empirically. The bottom left image shows the result of extracting the points "lying on the line", which were those points which had a distance of at most 2 pixels (in any direction) from the line, a value which, again, had been determined empirically. The bottom right image, eventually, shows the original data before adding background noise (the "real" hits).

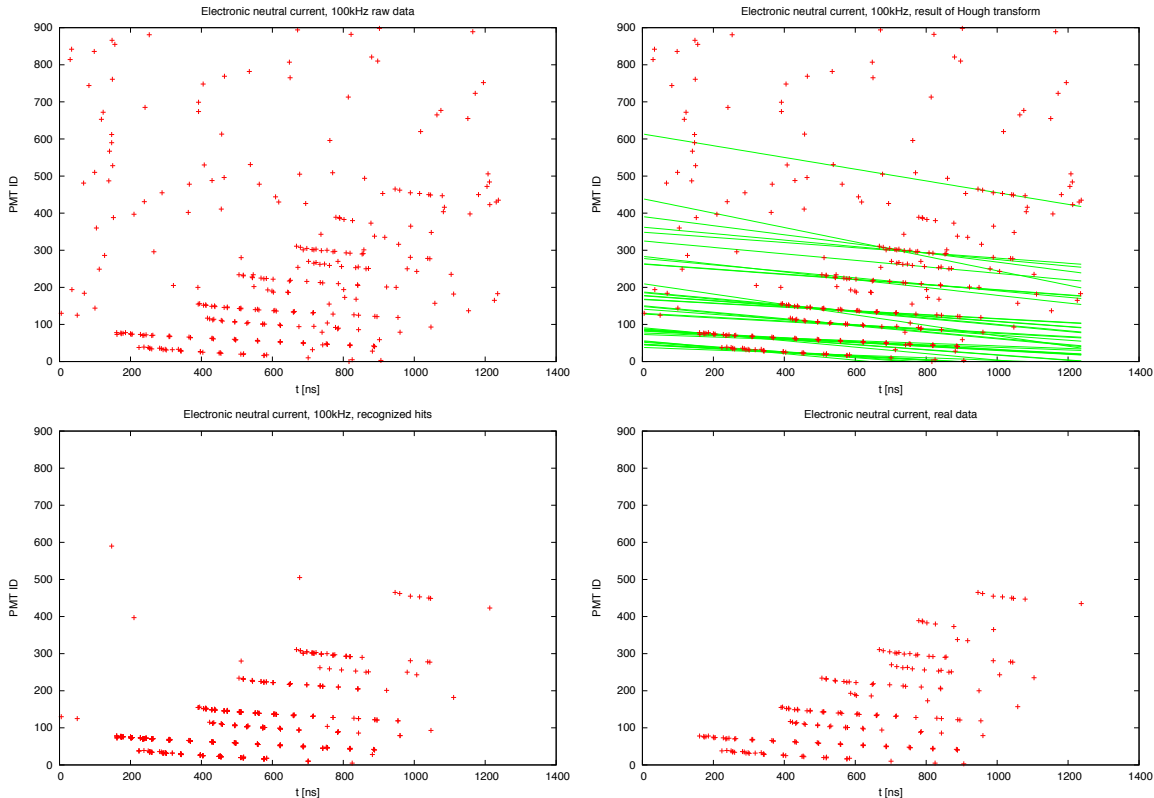


Figure 6.1: *Example of the detection of an electronic neutral current event at $1.1 \times 10^5 \text{ GeV}$ with 100kHz background noise. Top left: Raw data fed to the Hough Transform. Top right: Lines found by the Hough Transform. Bottom left: Hits extracted from raw data based on the Hough Transform's result. Bottom right: Original data without background noise.*

A very good agreement between the real data and the data recognised by the Hough transform (bottom images) is clearly visible. Although some of the real data were not recognised by the Hough Transform, it is quite pleasant, that only very few background hits were wrongly identified as physical hits. The latter is much more important, since a missing hit affects e.g. the track reconstruction - if at all - only slightly, compared to wrongly identified points at arbitrary positions and times.

In order to quantify "very good agreement", the results have been analysed in a more detailed way. For this analysis, the same set of events was used at different background

rates of 70kHz, 100kHz, 150kHz, 200kHz, 250kHz and 300kHz. The plots in this chapter show the results for electronic neutral current events at 150kHz background rate exemplary. As already mentioned, further plots belonging to this analysis are depicted in chapt. B.

Fig. 6.2 shows an example for the dependency of the number of found hits on the number of real hits at 150kHz background rate. A correlation of both numbers is clearly visible, which is a first hint that the Hough Transform algorithm was indeed working. In the mean, the fraction of found hits was in the 50-70% range. However, for a low amount of real hits (less than 25), the number of found hits exceeded the number of real hits present in the events. In this case, a large fraction of background hits has falsely been identified as physical. This result has also been confirmed by the analysis of false hits (figs. 6.5 and 6.6 below). The explanation for this phenomenon was that below 25 real hits (actually below 25 found hits, but as will be shown later, the numbers of both hits classes did not differ very much), the algorithm for calculating the cut-off value was no longer stable enough. In this region, the number of points being collinear by random coincidences became comparable to the number of real hits per recognised linear structure. Thus, the algorithm failed in predicting a reliable cut-off value. To be more precise, such a reliable cut-off value did no longer exist.

As can be seen from the other plots belonging to this analysis (chapt. B), the number of found hits stayed well within the 50-70% range (of real hits) for background rates below 150kHz, but started to decrease below 50% for higher rates. However, it stayed above 30% up to 300kHz background rate. The region where the number of found hits exceeded the number of real hits stayed stable below 25 real hits for the whole range of background rates. This is clear, since it is a mathematical effect of the cut-off calculation and thus quite independent from the actual data.

From fig. 6.3, which shows the number of true hits as function of real hits, it can be deduced, that up to 60% of all real hits have been detected correctly. The overall similarity of fig. 6.3 to fig. 6.2 (in both the shape of the plot as well as the scaling of the axes) suggests that most of the found hits were indeed true hits. This will also be confirmed by analyses later in this chapter. Considering the other plots concerning the true-to-real-hits dependency in chapt. B, a decrease of this ratio is visible for less than 25 real hits, in accordance with the previous results. Further on, these plots show that the fraction of true hits decreased below 50% for background rates above 150kHz, but still exceeded 30% at 300 kHz

As mentioned above, there is an obvious similarity between the plots which show the found-to-real-hits and those which show the true-to-real-hits ratios. In order to investigate if this similarity was purely artificial or if it was indeed based on a high detection efficiency of the Hough Transform method, the number of found hits have been compared to the number of true hits in the events (see fig. 6.4 as example).

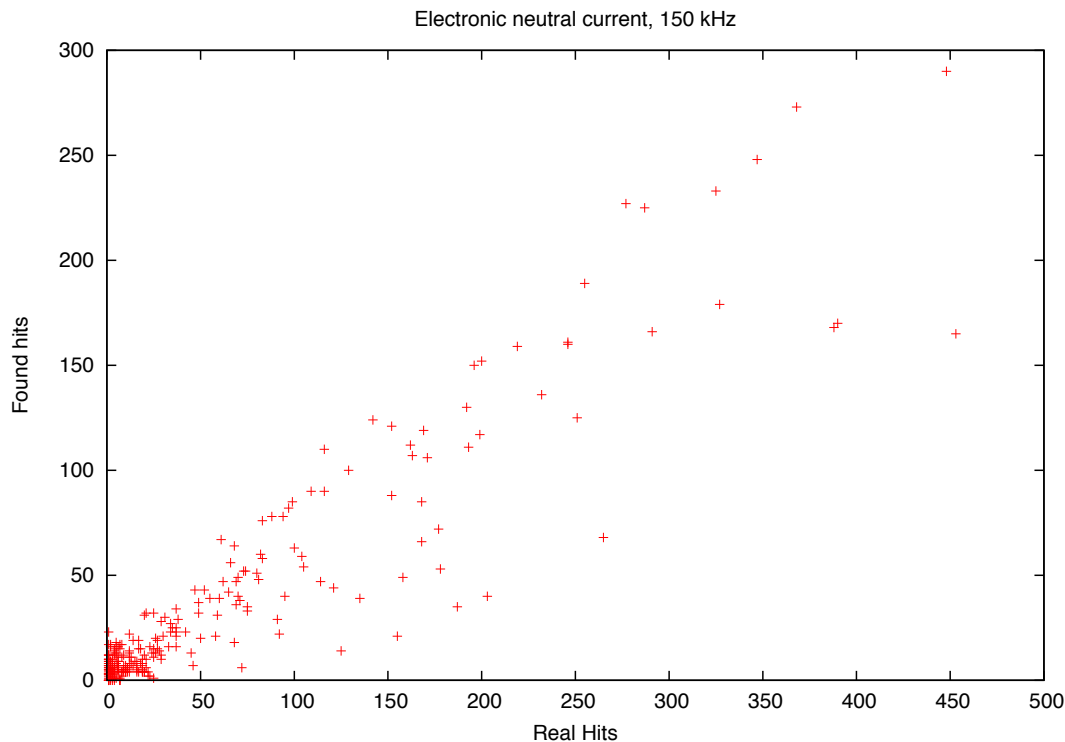


Figure 6.2: *Found hits as function of real hits for electronic neutral current events at 150kHz background rate.*

The linear dependency of these numbers is clearly visible above approx. 25 found hits, hence pointing out the intrinsic similarity of the two ratios. A linear fit to the plot has been performed to get quantitative values for the efficiency of the Hough Transform approach. It resulted in a true-to-found-hits ratio of 0.96 in the mean. This confirms the assumptions from the previous analyses, that most of the found hits ($\approx 96\%$) were true hits.

Table 6.1 summarises the results of the linear fits for all four event types at the investigated background rates. The plots belonging to this analyses are again contained in chapt. B. Up to 200kHz background noise, in the mean more than 95% of all detected hits are true hits, with still more than 90% in the range up to 300 kHz background noise.

By now, only the efficiency in terms of true hits has been discussed. Although the results already suggested a false positive rate of only approx. 10%, nevertheless further investigations were made, which aimed on the amount of false hits detected by the Hough Transform. Fig. 6.5 shows the number of false hits as function of found hits for electronic neutral current events at 150kHz background rate. Except for events with a very small number of found hits (which, again, is a consequence of the "25 real hits" boundary effect), the number of false hits stayed well below 10% of all detected

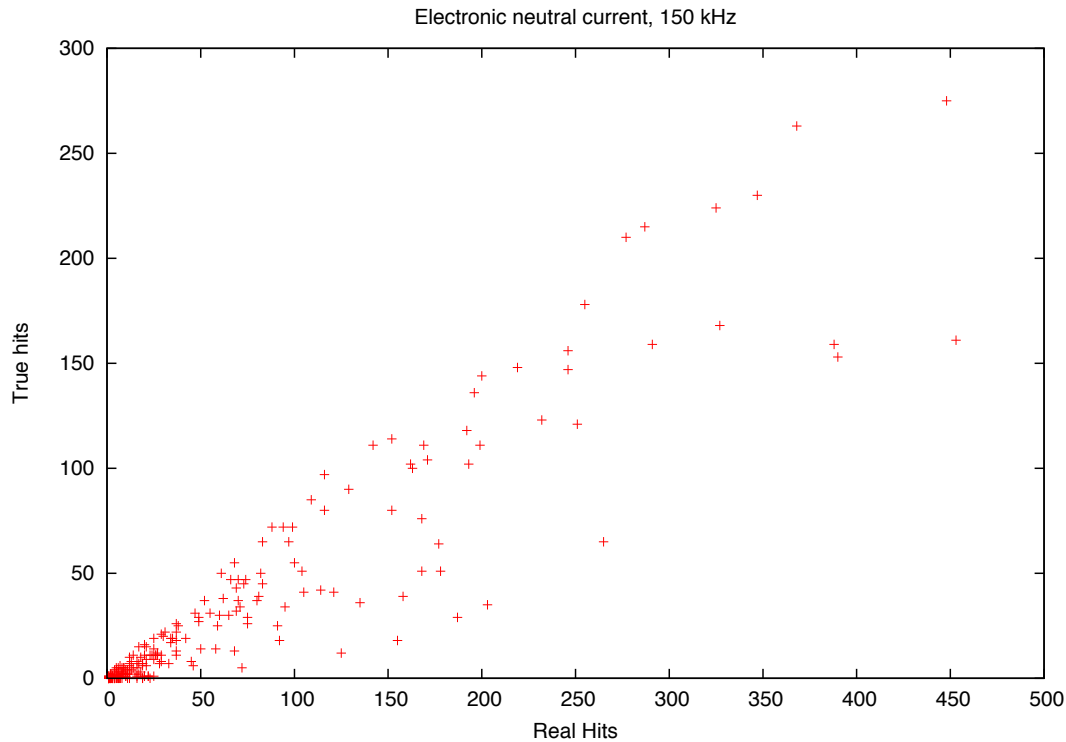


Figure 6.3: *True hits as function of real hits for electronic neutral current events at 150kHz background rate.*

hits, even up to 300 kHz background noise, as expected. Similar results were obtained for the other event types, which proved the overall stability of the Hough Transform approach. This behaviour has been confirmed by an analysis of the ratio of false and true hits as function of real hits, see fig. 6.6 for an example at 150kHz background rate. This ratio quickly dropped as the number of real hits exceeded the 25 landmark, reaching a stable ratio of about 10% within the analysed range of real hits, in good agreement with the previous results.

The results obtained so far lead to the conclusion, that the straight line Hough Transform in the mean detected up to 50% of all real hits in an electronic neutral current event at background rates up to 150 kHz and still up to 40% between 150 kHz and 300 kHz. The number of false hits stayed at a stable level of less than 10% if more than 25 real hits were contained in the processed event. Similar results have been obtained for electronic charged current and muonic neutral current events. Only for muonic charged current events, the overall detection rate was significantly smaller, and reached from approx. 20% for 300kHz to approx. 35% for 70kHz background rate only, see fig. 6.7. Fortunately, still more than 90% of all found hits were true hits for this event type as well, as stated in table 6.1.

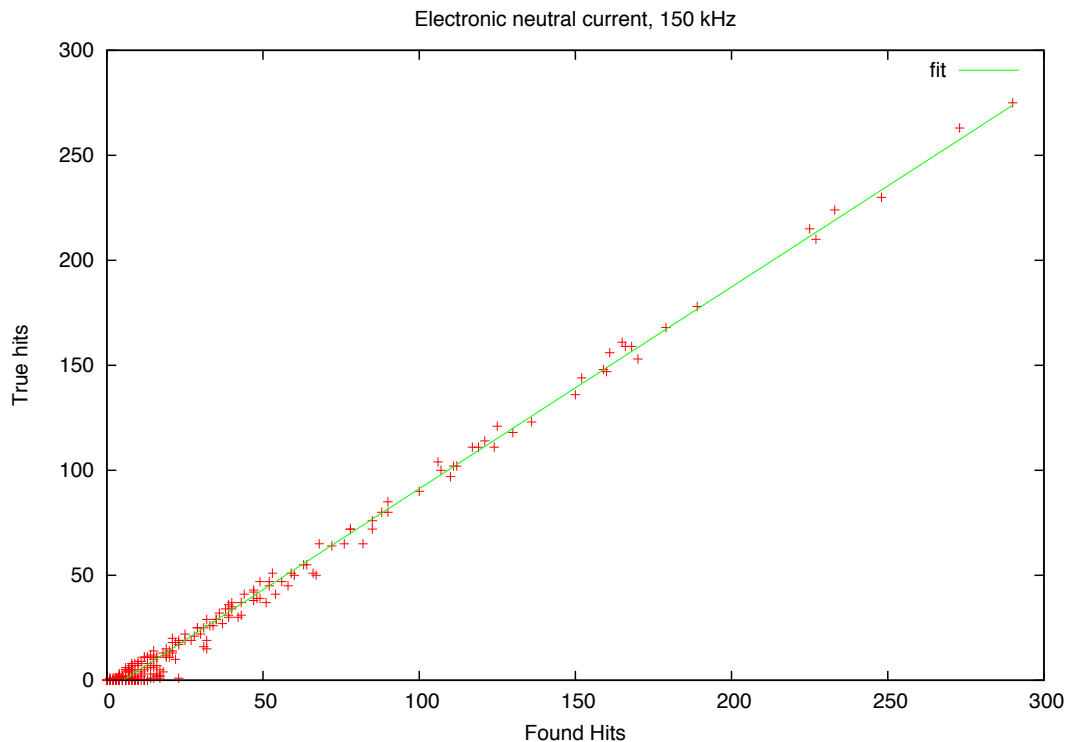


Figure 6.4: *True hits as function of found hits for electronic neutral current events at 150kHz background rate. The parameters a and b of the linear fit ($ax + b$, green line) have been determined to $a = 0.96$, and $b = -4.98$.*

Whole detector with cut

As stated above, the Hough Transform became unstable when less than 25 hits were found. Considering only these data sets for further analysis, which contained at least 25 found hits led to an increase of approx. 10% for all event types over the whole range of background noise, as depicted in fig. 6.8.

Whole detector with cut and binning

Further improvement could be achieved by binning the input data: The three optical modules of one storey were considered as one unit and the temporal resolution was decreased to units of five ns. This method was motivated by the fact, that for detecting geometrical structures, knowledge of the exact PMT was not necessary, although it is necessary for the reconstruction of the particle track. The temporal resolution of five ns was chosen because this is the approximate time which light needs in order to cross the diameter of one storey. Since the exact position of a particular PMT was no longer known after combining the data set of all three OMs of a storey to one mean value, this decrease in temporal resolution was acceptable.

Rate [kHz]	el_nc [%]	el_cc [%]	mu_nc [%]	mu_cc [%]
70	99	99	96	98
100	98	98	94	97
150	96	96	90	95
200	94	94	85	93
250	94	94	87	93
300	92	92	85	91

Table 6.1: *Percentage of true hits among found hits for different event types at different background rates.*

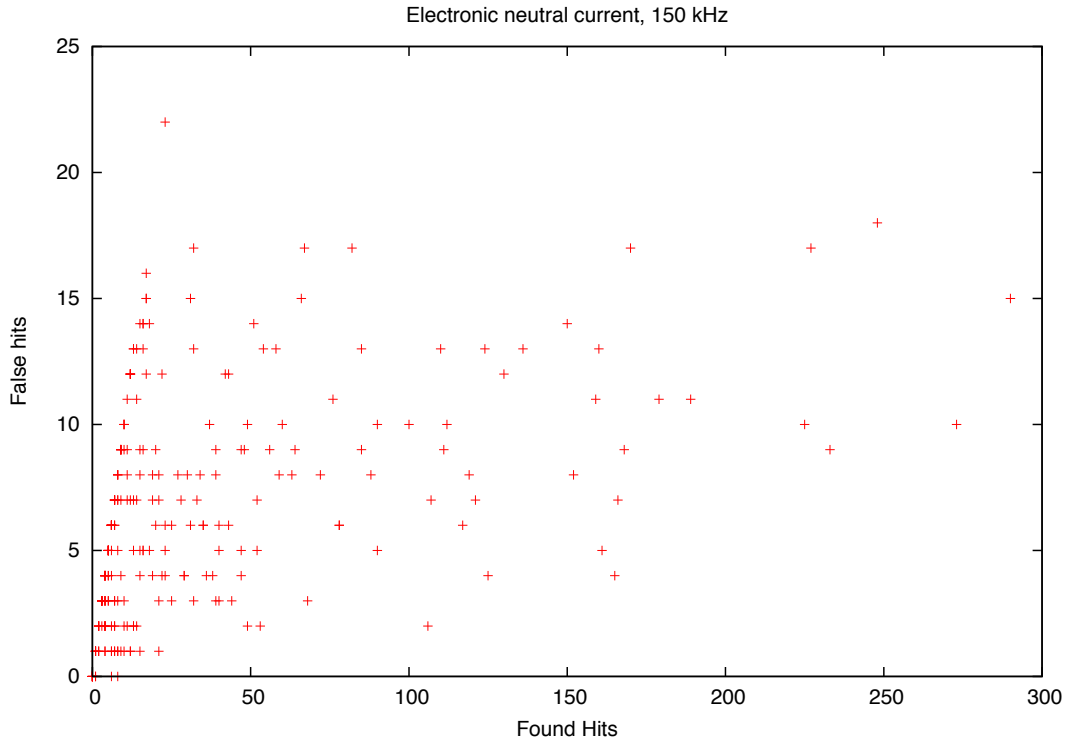


Figure 6.5: *False hits as function of found hits for electronic neutral current events at 150kHz background rate.*

Using this filter strategy additionally to the cut at 25 found hits led to correct identification of up to 75% of the hits belonging to el_nc, el_cc and mu_nc events, and up to 55% of the hits belonging to mu_cc events. Although the fractions dropped more quickly than in the analysis without binning, they stayed well above those values, thus leading to an overall improvement of detection efficiency (fig. 6.9).

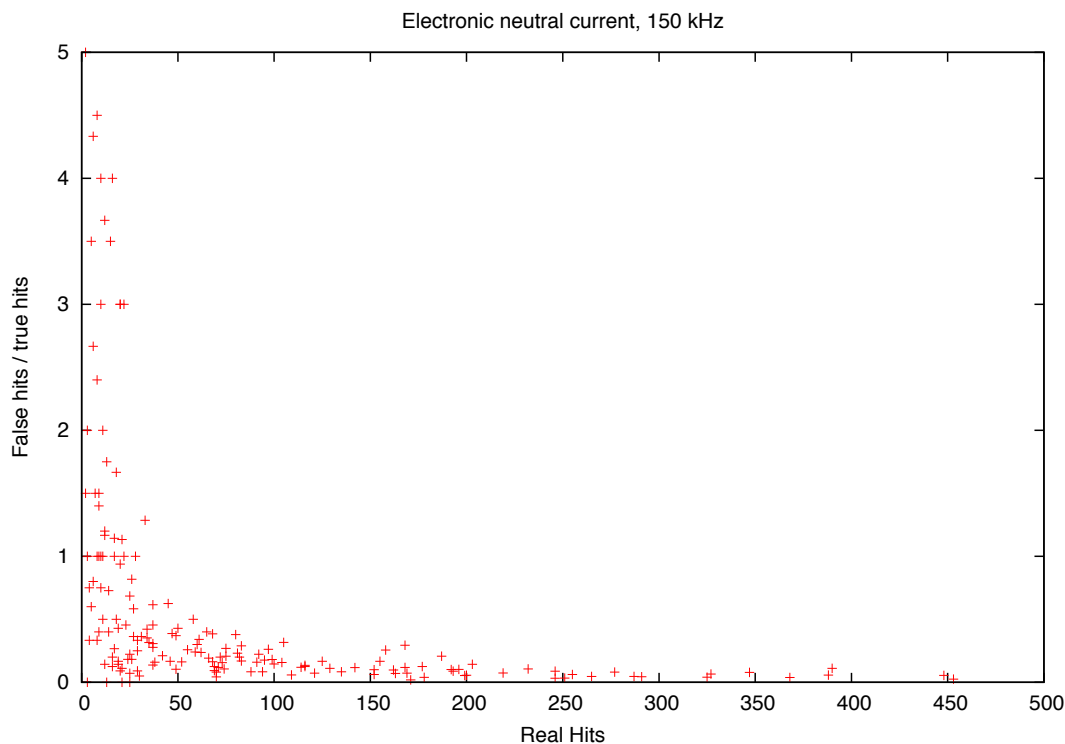


Figure 6.6: *Ratio of false and true hits as function of real hits for electronic neutral current events at 150kHz background rate.*

Single strings with cut and binning

As visualised in fig. 6.10, the best results in terms of the true-to-found hits ratio were achieved when the algorithm was applied to single strings only. In this case, random coincidences of hits between different strings were avoided. Such hits of course had no physical meaning but were nevertheless detected by the Hough Transform as collinear points and were thus reported as possible particle signatures. Eliminating these false candidates resulted in correctly identifying up to 80% of `el_nc` and `el_cc` events with a quite stable ratio within the whole range of background noise.

These results are quite promising, since up to now, no further pre-processing (as e.g. PE filtering) has been applied and only the straight-line algorithm has been used in order to extract physical data from background noise.

6.1.2 Comparison to ANTARES standard trigger

The ANTARES standard trigger uses (configurable) algorithms for evaluating tempo-spatial correlations between detected hits. In order to compare the efficiencies between the standard trigger and the pattern recognition approach, the same sets of Monte

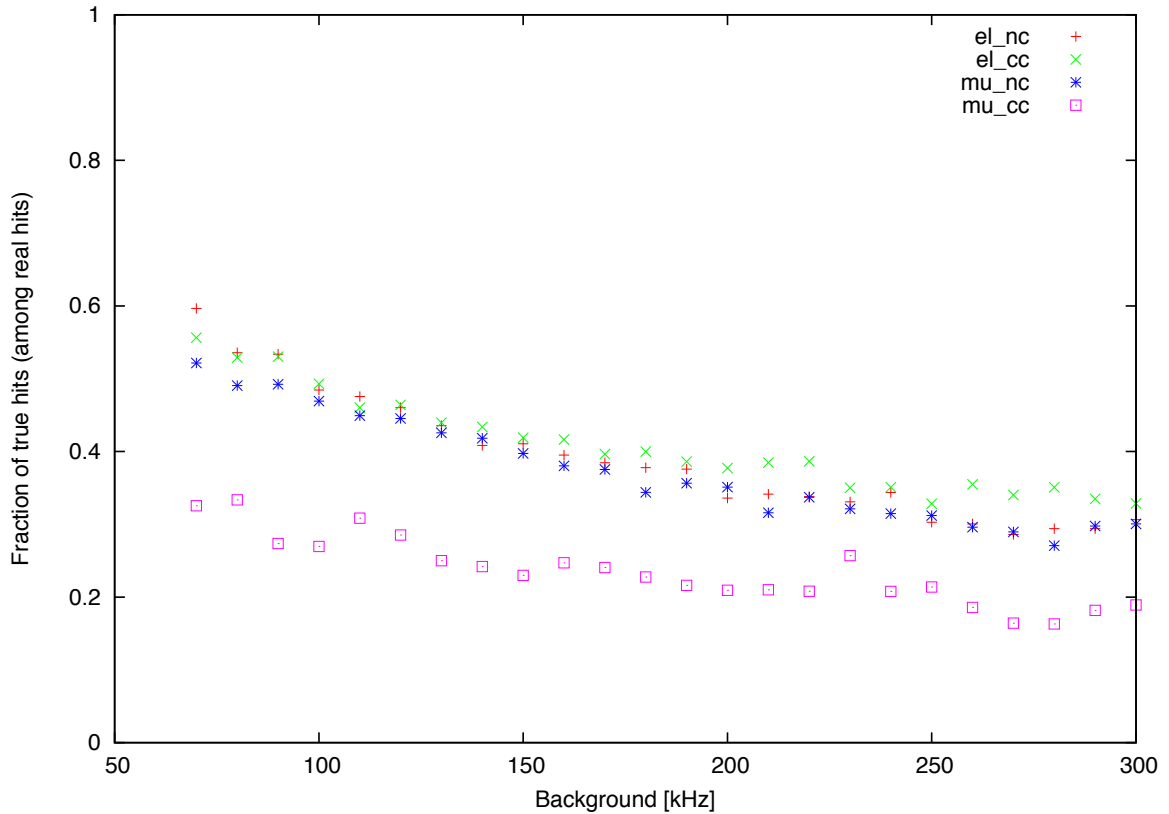


Figure 6.7: *Fraction of correctly identified hits as function of background noise for different event types.*

Carlo data as in the previous section had been fed to both algorithms as input data. Afterwards, the hits identified by both strategies have been compared to the raw data (real hits) as well to each other for each class of event. Fig. 6.11 shows a typical result for electronic neutral current data at 100kHz background rate. In three event classes, the Hough Transform method correctly identified about two to three times as much hits as the standard ANTARES trigger, even when the "worst" possible configuration was in use (whole detector without binning and cut-off). Only for muonic charged current events, the ratio between Hough Transform and ANTARES standard trigger dropped more quickly, but still stayed above 1 for 300kHz, hence the Hough Transform was still more efficient than the standard trigger for this event class as well. Fig. 6.12 and 6.13 show this in more detail.

This leads to the conclusion, that the trigger based on the pattern recognition method was in the mean at least twice as efficient as the standard ANTARES trigger for electronic charged and neutral current events as well as for muonic neutral current events, while offering comparable real time analysis and almost unlimited parallelisation capabilities. For muonic charged current events the overall efficiency was lower, but still exceeded that of the standard trigger.

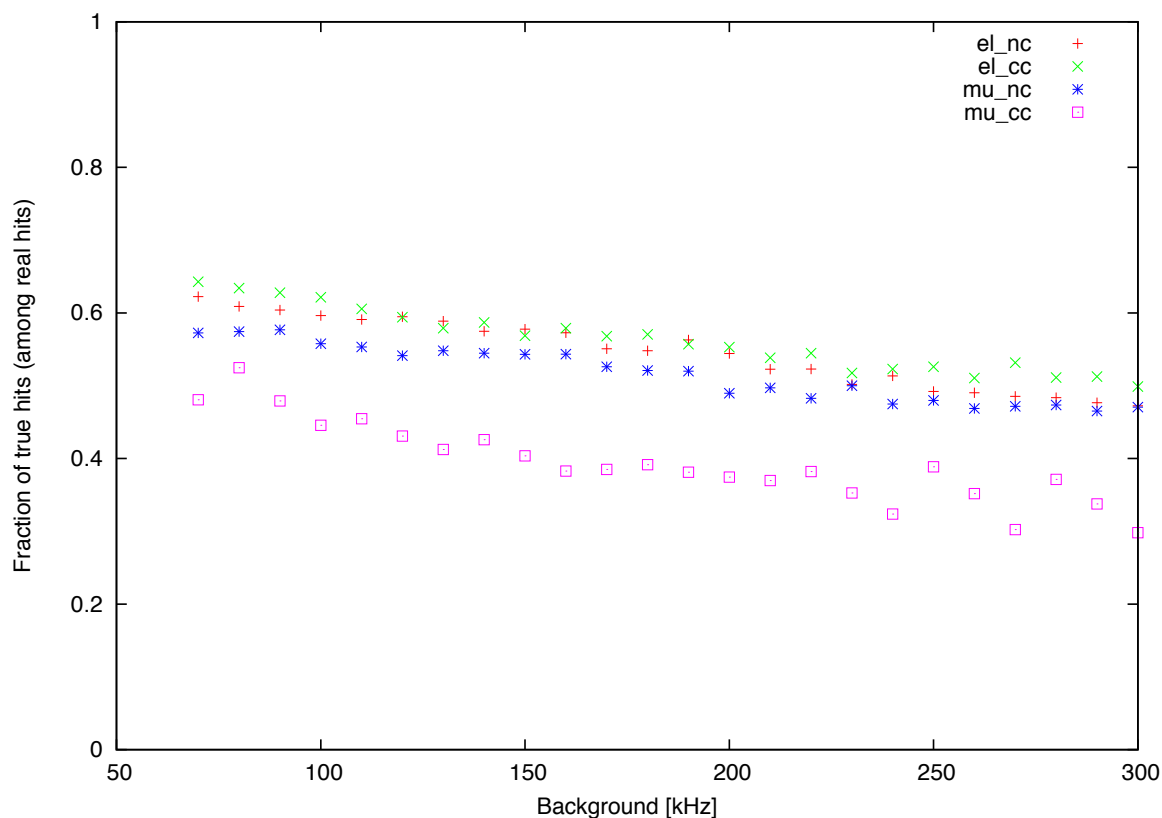


Figure 6.8: *Fraction of correctly identified hits as function of background noise for different event types after applying a cut at 25 found hits.*

6.2 Background only

Some further cross checks were done by applying the Hough Transform algorithm and the ANTARES standard trigger to several sets of events containing background only at rates between 100kHz and 300kHz at steps of 50kHz. Each set consisted of 500 events. The reason for this analysis was to get some information on the false positive rate of both algorithms. Table 6.2 lists the results obtained by both algorithms. Although the Hough Transform seemed to behave much worse than the standard trigger, none of the events exceeded the cut-off value of 25 found hits. The amounts of found hits dropped even more after the nearest-neighbour strategy was applied to the extracted hits. A value of 10 units maximum distance between two hits was used, which had been determined empirically. Thus, background could be efficiently suppressed by applying a suitable cut at ≈ 7 or ≈ 20 found hits, depending if the nearest-neighbour strategy was in use.

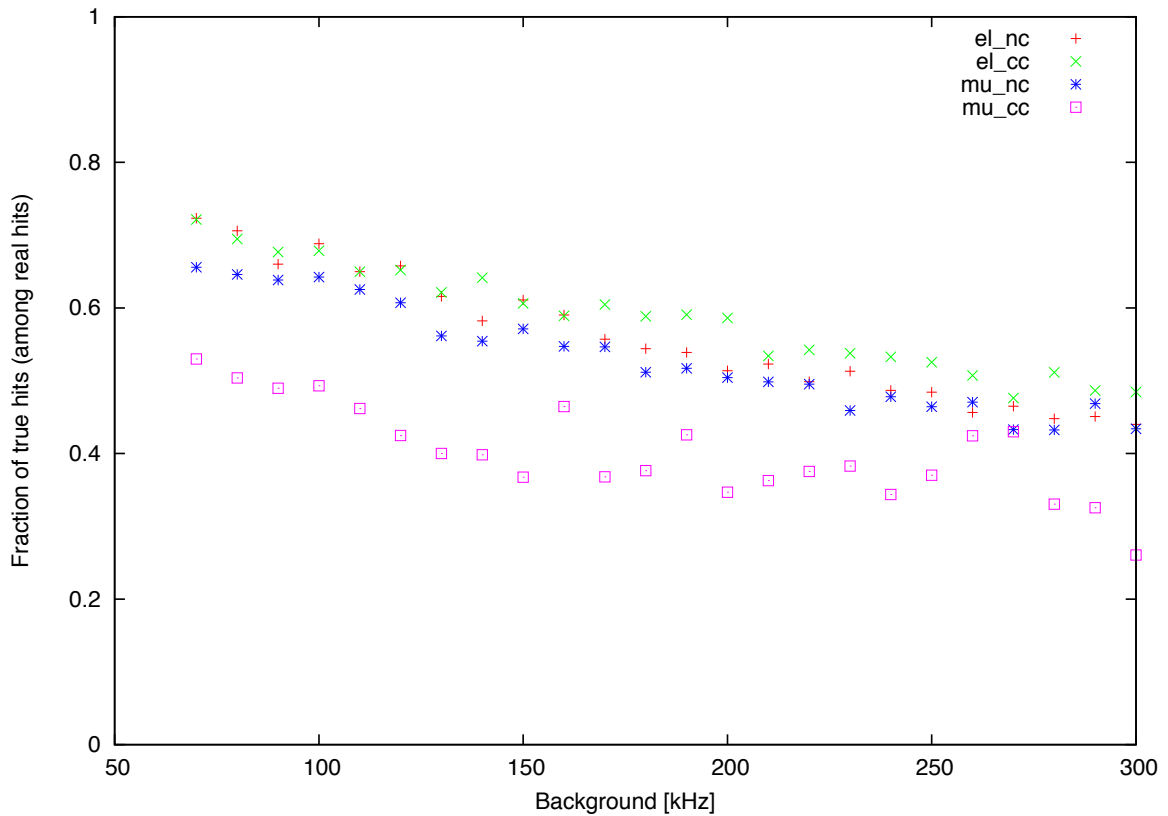


Figure 6.9: *Fraction of correctly identified hits as function of background noise for different event types after applying a cut at 9 found hits, OM clustering and binning with 5ns resolution.*

6.3 Application to physical data

In order to prove the stability of the Hough Transform algorithm under real world conditions, it was used to analyse real data which had been recorded during the construction of the ANTARES neutrino telescope. At the time of this analysis, 6 strings had been deployed with 5 of them already delivering physical data. These data, which had been recorded in May of 2007 (the data file had been chosen arbitrarily) were again analysed by both the ANTARES standard trigger and the Hough Transform analysis.

As illustrated in fig. 6.14, the Hough Transform again detected about three times as much hits as the ANTARES standard trigger. Since, in contrast to Monte Carlo data, there was no possibility in this case to decide between true and false hits, a visual inspection had been performed on a set of 50 events randomly selected from those used for fig. 6.14.

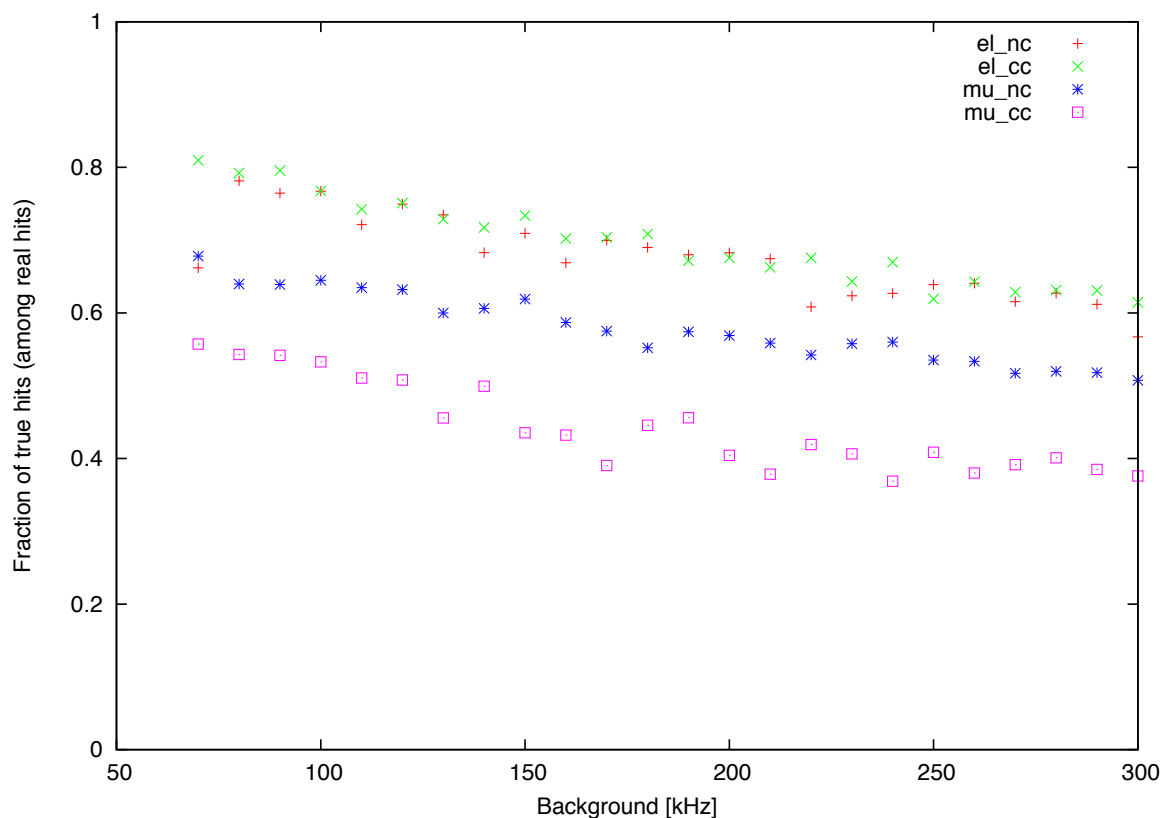


Figure 6.10: *Fraction of correctly identified hits as function of background noise for different event types after applying a cut at 9 found hits, OM clustering and binning with 5ns resolution to data from a single detector string.*

This inspection revealed three different result classes, which had to be distinguished:

1. Both triggers were similarly efficient
2. The ANTARES standard trigger was far more efficient than the Hough Transform method
3. The Hough Transform method was far more efficient than the ANTARES standard trigger

Item 1 could further be subdivided into "both methods found a similar number of events" vs. "both methods completely failed to detect an event", and items 2 and 3 could be subdivided into "both methods found the event but method A was far more efficient"² and "only method A found the event while method B either did not find it or reported an invalid result"³. This finally yielded six different result classes. An

²It has to be pointed out, that "efficient" in this context is to be understood as "according to the visual inspection, the triggered hits could indeed be physical hits".

³Similarly, "invalid" in this context is to be understood as "according to the visual inspection, it is quite improbable that the triggered hits are physical hits".

Rate [kHz]	ANT Tr	Hgh Tr	Hgh Max	Hgh NN	Hgh NN Max
100	0	1270	16	86	5
150	0	2270	17	98	6
200	0	1680	18	103	5
250	9	1187	13	92	4
300	44	772	13	48	3

Table 6.2: Total number of hits found by the standard ANTARES trigger (ANT Tr) and the Hough Transform (Hgh Tr) in background only events at different rates. Hgh Max is the maximum number of hits found for a single event. Hgh NN is the number of hits found after applying the nearest-neighbour filter strategy and Hgh NN Max the maximum number of hits found for a single event using this strategy.

example of each class is depicted in figs. 6.15 to 6.20 (the whole set of plots for all 50 events can be found in more detail in chapt. C).

In order to get some more objective information on the efficiency of the Hough Transform method compared to the ANTARES standard trigger, table 6.3 shows the classification of the physical data according to the result types just mentioned. Without regarding the subdivision of the event classes, both trigger types were of similar efficiency in 46% of all cases. The Hough Transform method was more efficient than the ANTARES standard trigger in 38% of all cases. Finally, the ANTARES standard trigger was more efficient than the Hough Transform method in only 16% of all cases, resulting in an overall increase of efficiency of the Hough Transform method of 22%. Including the results where both methods triggered on physical hits, but one method was more efficient than the other one, the Hough transform method had an overall detection success rate of 90%, whereas the ANTARES standard trigger had a success rate of only 80%.

Taking into account the number of individual hits which were correctly identified by both methods (instead of considering whole result classes only), the visual inspection of the plots hinted that the Hough Transform method was even twice as efficient as the ANTARES standard trigger, at least. This is in good agreement with the results from Monte Carlo data in the previous chapters.

It is necessary to stress here that the mapping of the events to the result classes and the analysis of "correctly identified hits" was surely subjective. There is much room for discussions if an event belonged to the class it has been assigned to and even more if a triggered hit was physical or if it was background only. Thus, table 6.3 as well as the statement in the preceding paragraph must not be seen as scientific fact but they nevertheless should be usable to get some hints on the behaviour of the Hough

Result class	No. of events
1	19
2	4
3	13
4	6
5	7
6	1

Table 6.3: *Number of events belonging to a particular result class. Class 1: Both trigger types detected a similar number of hits. Class 2: Both trigger types failed in detecting the event. Class 3: The Hough Transform method was more efficient than the ANTARES standard trigger. Class 4: The Hough Transform method detected the physical events, the ANTARES standard trigger did not detect the events. Class 5: The ANTARES standard trigger was more efficient than the Hough transform method. Class 6: The ANTARES standard trigger detected the physical events, the Hough Transform method did not detect the events.*

Transform compared to the ANTARES standard trigger. All in all, the analysis leads to the conclusion, that even under real world conditions, the Hough Transform method was about twice as efficient as the standard method - a quite promising result.

6.4 Summary of results

In this chapter it has been shown that the Hough Transform approach offers a promising new technology for event detection in raw ANTARES data. It proved to be more stable than the ANTARES standard trigger, especially in cases of high background noise, and the number of positive results exceeded that from the latter under almost all conditions. The number of false results was of the same order as (or even lower than) that of the standard trigger, thus no loss of information is to be worried about when using the presented new method. The above mentioned advantages have been proved by the analysis of Monte Carlo data as well as the analysis of real data, recorded by the then-existing ANTARES detector array. On academical level⁴, the implementation of the trigger algorithm is feasible without much effort and almost arbitrary speed-up can be gained by the application of suitable parallelisation techniques. Instead of waiting until some data recorded long ago will be finally analysed in off-line mode, true real-time extraction and analysis of physical hits of the ANTARES data stream would then become possible. This is an important advantage in occasion that it comes to

⁴Meaning that the actual integration of the Hough Transform method into the ANTARES data analysis software was not topic of this work. Some additional effort may become necessary here.

fast detection of (and reaction on) events. Since, at least in principle, a pre-fit of the declination parameter of the incident neutrinos is possible with the algorithm as well, reduction of the effort necessary for the final track fitting could be reached additionally. Both real-time analysis and track-pre-fit, may help ANTARES to be the first project to detect and analyse a new interesting cosmic event.

Another advantage arises from the fact that the Hough Transform method does not make any assumptions on the geometrical properties of the detector, apart from the requirement that the sensors are aligned in a vertical manner. It should thus in principle be possible to use the algorithm without any alterations for other, similar detectors (like e.g. the future KM3Net[17]), too. Even in case of a detector having a completely different shape and/or alignment of its sensors, one could easily adapt the parametrisation of the expected patterns on which the Hough Transform is based. Furthermore, as long as the signals from the detector behave as "single points in space and time", the algorithm could be used for completely different detector types as well (e.g. an acoustic particle detector, which reports single hits when a hydrophone detected a proper acoustic signal).

All in all, the Hough Transform method offers a new, fast, stable and very flexible approach for analysing data from ANTARES-like neutrino telescopes.

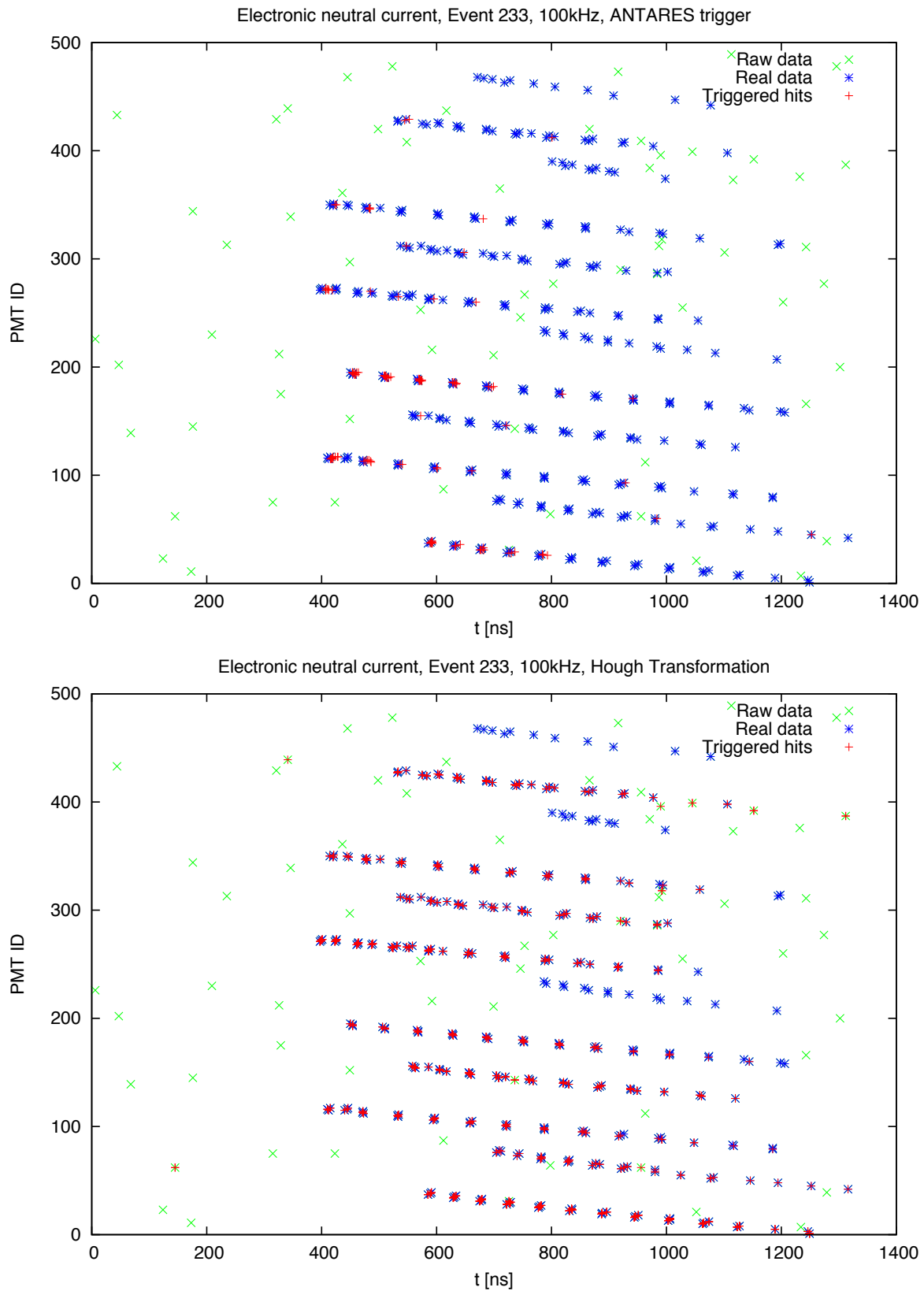


Figure 6.11: Results from standard ANTARES trigger (top) and Hough transform (bottom) applied to an electronic neutral current event. The Hough Transform method correctly identified about 3 times as much hits as the standard trigger (the small deviations in the positions between found hits and input data are a result from the integer arithmetic used for reasons of computing time).

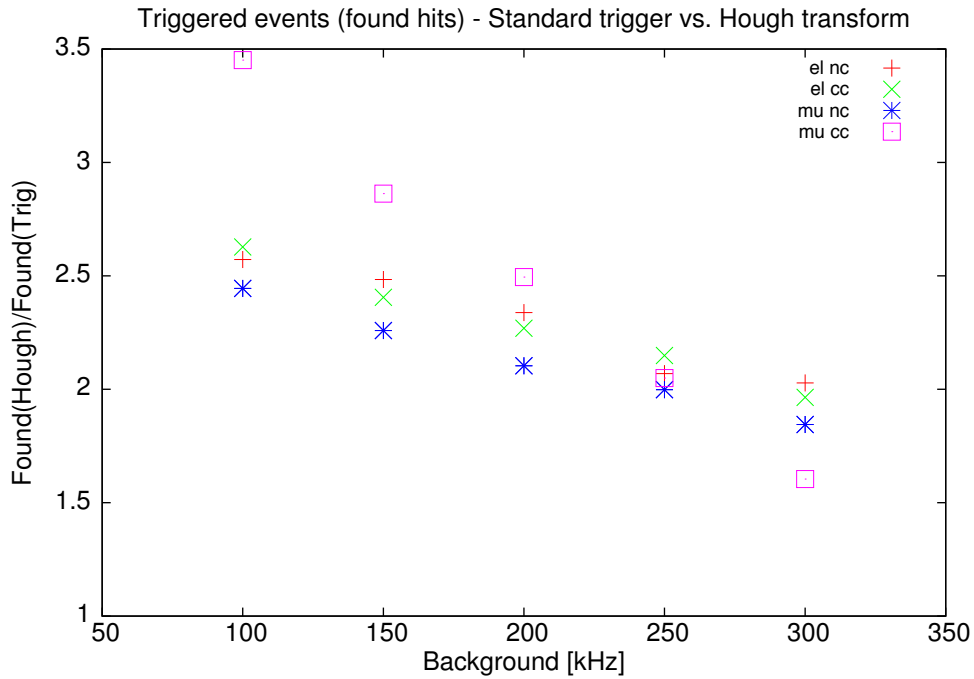


Figure 6.12: Ratio of hits found by the Hough Transform method and the ANTARES standard trigger at different background rates.

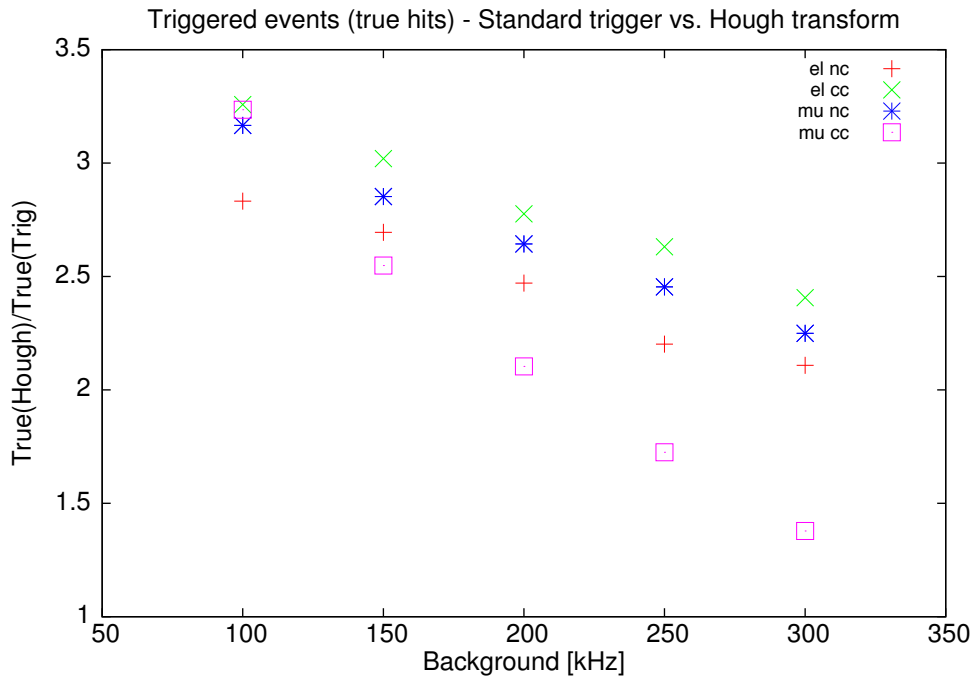


Figure 6.13: Ratio of true hits found by the Hough Transform method and the ANTARES standard trigger at different background rates.

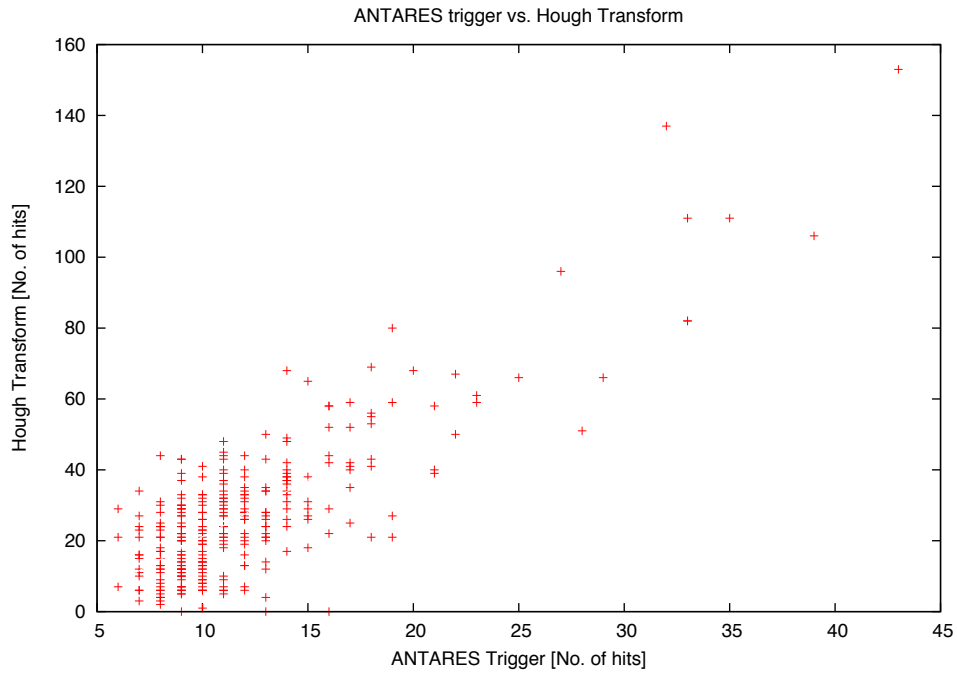


Figure 6.14: Number of hits found by the ANTARES standard trigger and the Hough Transform within the first 500 events of run 27955 (recorded on 29.05.2007).

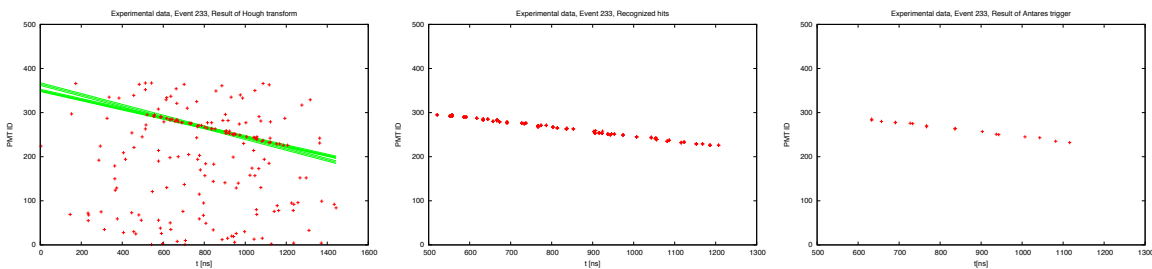


Figure 6.15: Raw data (left column), Hough Transform (mid column) and ANTARES trigger (right column) results of event 233 of run 27955 (recorded on 29.05.2007). Both trigger types were of similar efficiency.

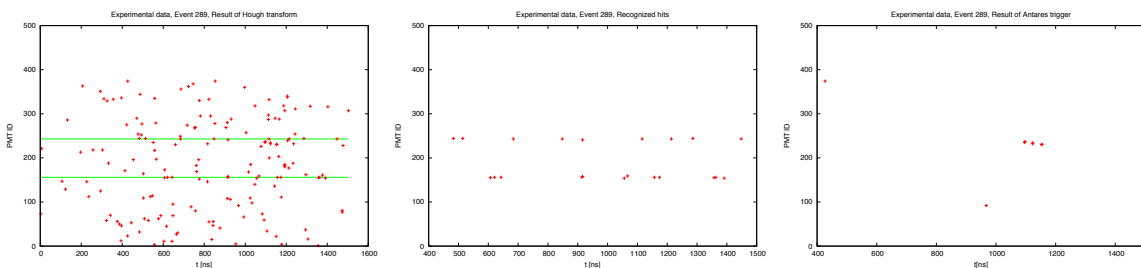


Figure 6.16: Raw data (left column), Hough Transform (mid column) and ANTARES trigger (right column) results of event 289 of run 27955 (recorded on 29.05.2007). Both triggers reported hits which apparently do not seem to be physical hits.

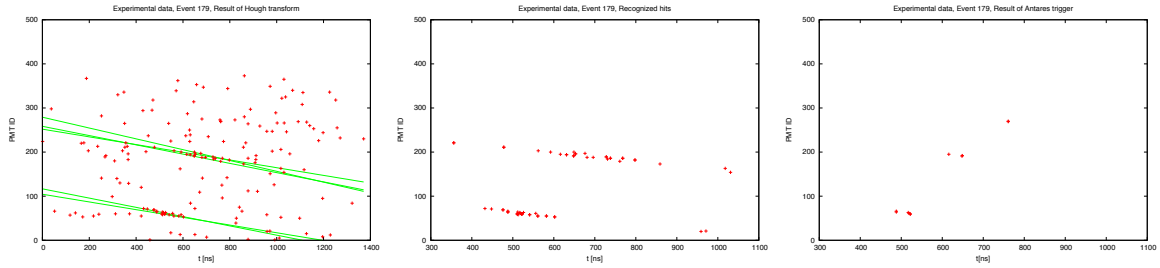


Figure 6.17: *Raw data (left column), Hough Transform (mid column) and ANTARES trigger (right column) results of event 179 of run 27955 (recorded on 29.05.2007). Both trigger types detected the events but the Hough Transform method was more efficient.*

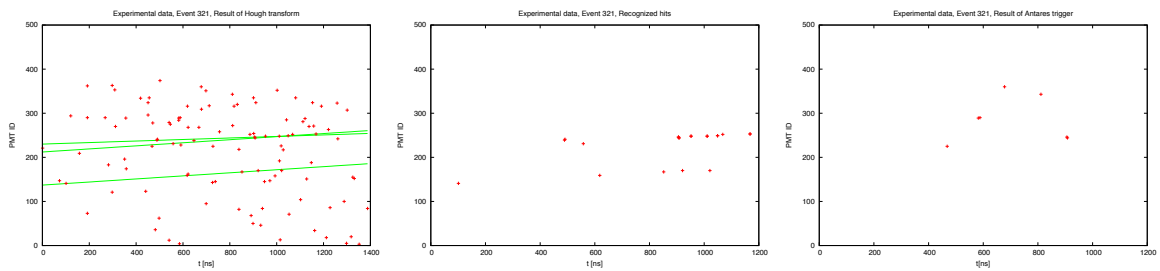


Figure 6.18: *Raw data (left column), Hough Transform (mid column) and ANTARES trigger (right column) results of event 321 of run 27955 (recorded on 29.05.2007). The Hough Transform method detected the event, the ANTARES standard trigger failed.*

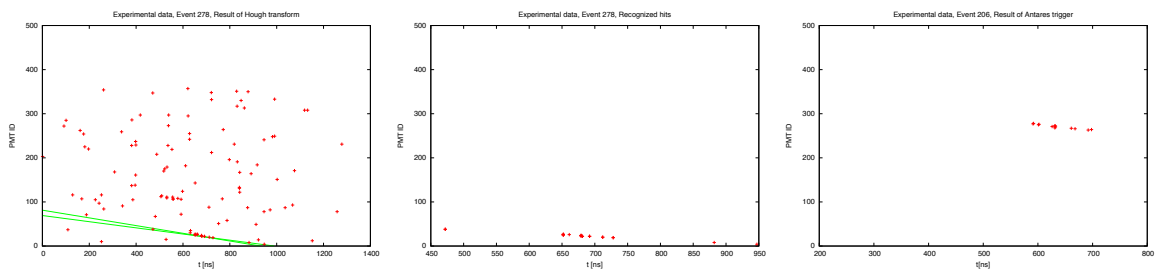


Figure 6.19: *Raw data (left column), Hough Transform (mid column) and ANTARES trigger (right column) results of event 278 of run 27955 (recorded on 29.05.2007). Both trigger types detected the events but the ANTARES standard trigger was more efficient.*

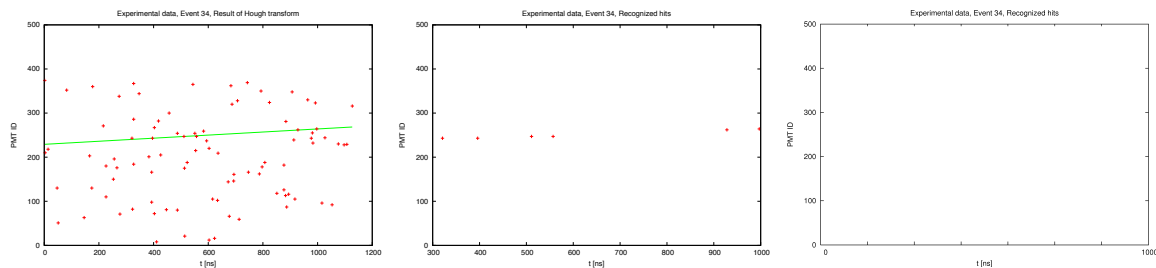


Figure 6.20: Raw data (left column), Hough Transform (mid column) results of event 34 of run 27955 (recorded on 29.05.2007). The ANTARES standard trigger detected the event, the Hough transform method failed (the event does not contain physical data, which has been correctly recognised by the ANTARES standard trigger, whereas the Hough Transform method falsely triggered on background hits).

7 Conclusion and Outlook

Several approaches have been taken in order to develop a new class of event detection algorithm for the ANTARES neutrino telescope. The aim was to find a strategy which uses elaborate pattern recognition techniques instead of the time consuming search for correlations in the input data.

Standard algorithms like artificial neural networks or Principal Component Analysis have been investigated. Because of the properties of the ANTARES data, especially their high amount and their discreteness (in the mathematical sense), these algorithms were abandoned, as their detection rate did not significantly exceed what would be expected from random choices. Finally, starting from considerations about the geometric properties of the signals which are caused by particles crossing the ANTARES neutrino telescope, a data filter strategy was established which uses the Hough Transform as core algorithm - a method developed in the early sixties for identifying particle tracks in bubble chamber images. Several improvements were added to this method to adopt the algorithm to properties inherent to ANTARES data and to reduce the amount of falsely recognised background noise as well as to speed up the detection process itself. The algorithm has been applied to data from Monte Carlo simulations, "real" data recorded during the construction phase of the ANTARES detector and purely random data. The results from analysing all three classes of data have been compared to results from the ANTARES standard trigger, which searches for correlations in the input data - loosely speaking - by comparing each data point to each other.

It has been shown that the pattern recognition technique presented in this work is a promising approach for developing a reliable and real time capable new class of data filter and trigger algorithms for the ANTARES detector. Treating the data delivered by the detector "as a whole" instead of searching for correlations between single data points resulted not only in a much less complex but also in a much more efficient detection system.

Depending on the configuration of the pattern recognition algorithm and on the presence of additional filter constraints, up to 80% to 90% of all physical hits present in the investigated data sets have been found. The amount of falsely identified background photons was less than 10% of the detected hits throughout all data. This rate of false positive results could be further reduced by the application of suitable cuts and constraints during the post-processing of the results.

Compared to the existing ANTARES trigger this newly developed strategy showed an increase in efficiency of about 100% while offering the same or even better real time capabilities due to the parallelisation properties of the algorithm. Although the standard trigger proved to be more resistant to background noise, this disadvantage

could be overcome by the application of certain constraints in the post-processing stage of the new technique.

The Hough Transform algorithm proved to be stable even when exposed to real data recorded by the then-semi-finished ANTARES neutrino telescope during its construction phase. Again about twice as much hits have been recognised as by the standard trigger. Due to the inherent lack of information about the nature of these hits, a visual inspection of the data was performed, which indicated that indeed most of the hits found by the Hough Transform based method were physical signatures. This finding is in good agreement with the previous results.

Regarding these results, the pattern recognition approach is worth further investigation. In the following, possible improvements of the algorithm are mentioned, which could be considered in future works:

- Particles with an incident angle larger than the apex angle of the Čerenkov light cone lead to hyperbolic instead of straight line signatures. Although branches of these hyperbolas are also recognised by the present implementation of the algorithm, their cusps are not. To solve this problem, a suitable extension of the recognition algorithm has to be developed, which should show a stability comparable to the straight line Hough Transform while still offering the possibility of real time analysis.
- The parametric descriptions, especially the angular information of the patterns, have so far only been used for background suppression purposes. In principle these data could also be used for track reconstruction tasks, at least to gain some estimates for the pre-fit stage of the existing reconstruction algorithms.
- Evaluating the spacial distribution of the hits by more sophisticated pattern recognition algorithms could help not only to extract events from background noise, but also to classify the flavour of the incident neutrino and the type of its reaction.

The mentioned improvements could - among many others - subsequently result in a data analysis package, which performs data filtering, track pre-reconstruction and event classification tasks in real time. The information could next be used to efficiently distinguish non-interesting from interesting data and to choose the perfect strategies for further investigation of the latter.

Moreover, as stated in chapt. 6.4, the algorithm presented in this work is not restricted to the ANTARES detector. Any detector for which the physical data are available as "points in space and time" and the expected signatures adhere to a parametric description may gain profit from the presented strategy. This especially applies to the

upcoming KM3NeT as well as the currently on-going experiment on acoustic detection of neutrino signatures in the ANTARES project.

All in all, the results obtained so far as well as the still open possibilities show that there is a high potential lying in this approach to help future astroparticle scientists to improve their work. The algorithm represents a reliable, stable and extendable method which reports significant physical data in (near) real-time. This provides ANTARES and related experiments the chance to be the first to discover interesting cosmic events. Let us take this opportunity together!

*Nihil tam difficile est, quin quaerendo investigari possit.*¹

¹Terenz, Heautontimorumenos

Appendix

A Description of the event classification software

The event classification software is split into two modules. One main program for feature extraction and one helper application which processes the result from the main program and reports the hits which were recognised as belonging to an event:

- **classify:** Preprocessing of data (noise reduction and binning) and feature extraction
- **get_points.pl:** Extract hits belonging to detected events

These programs will now be described in detail.

A.1 classify

Usage:

```
classify [-c] <file>
classify [-e] [-h] [-n] [-m] [-b <dt>] [-d <th>] [-t <thres>] [-l line]
        <file> <evt-nr>
```

This is the main program of the tool-chain, which it performs all the tasks concerning feature extraction. It is configurable using different command line options:

- **General information about event file**
 - **-c:** Prints the number of events in *file* minus one. The number of events is reduced by one, since they are internally counted starting from 0. So the output of the *-c* option can directly be used as *evt-nr* for subsequent analysis e.g. in a "num='classify -c ...; for i in 'seq 0 \$num';do ...; done" bash construct.
- **Modifiers:** These options influence the whole feature extraction process in the specified way.
 - **-b dt:** Performs OM clustering and binning: All three OMs of a storey are treated as one single unit and time is binned into intervals of *dt* ns.
 - **-d th:** Removes all hits with a PE amplitude less than *th*.

- **-l line:** Only analyses data from detector string *line* instead of the whole detector.
- **Feature extraction:** These options retrieve the selected information concerning event *evt-nr* of *file*. If more than one of them are specified, each output section is preceded by the line
OPTION *id*
where *id* is replaced by the letter defining the option, i.e. *e*, *h*, *t*, *n* or *m*. This helps to separate the various information in the output data.
 - **-e:** Prints the time, the PMT IDs and the PE amplitudes of each hit.
 - **-h:** Prints the contents of the Hough space cells. The output format is
 $r \theta N$
where N is the number of intersections within this cell and the other values are the parameters of the corresponding shapes according to chapt. 5.3.
 - **-t thres:** Like -h, but only prints those parameter values with $N > thres$. N is not printed.
 - **-n:** Prints the estimated cut-off for shapes based on random coincidences as described in chapt. 5.3.5.
 - **-m:** Prints the estimated SPE cut-off for suppression of background on SPE values, see 5.3.8.

A.2 get_points.pl

Usage:

```
get_points.pl <line> <tolerance> <houghfile> <datafile>
```

This tool prints the x and y position as well as the calculated y position (according to the line in Hough space) and the PE amplitude of those points in *datafile* which have a maximum distance *tolerance* to the line number *line*. *houghfile* is obtained via the *-t* option and *datafile* via the *-e* option of *classify*. These values can then be used e.g. as input to a data visualisation tool.

B Results from the application to Monte Carlo data

The figures in this chapter show the results from the application of the Hough Transform to Monte Carlo data. For each of the four event types, `el_n`, `el_cc`, `mu_nc` and `mu_cc`, the following plots are shown:

- A typical example for the event and the hits which were extracted by the Hough Transform
- The number of found hits as function of the number of real hits in the samples
- The number of true hits as function of the number of real hits in the samples
- The number of true hits as function of the number of found hits including a linear fit
- The number of false hits as function of the number of found hits
- The ratio of false to true hits as function of the number of real hits in the samples

Some of the plots for the `el_nc` data have already been shown in chapt. 6 but they are repeated here for reasons of completeness.

Each analysis was made at six different background rates of 70, 100, 150, 200, 250 and 300kHz. The plots show both a high reliability as well as a high stability of the Hough Transform algorithm over a wide range of background rates. Especially the overall fraction of > 0.9 of true hits to found hits proves applicability of the algorithm to ANTARES data.

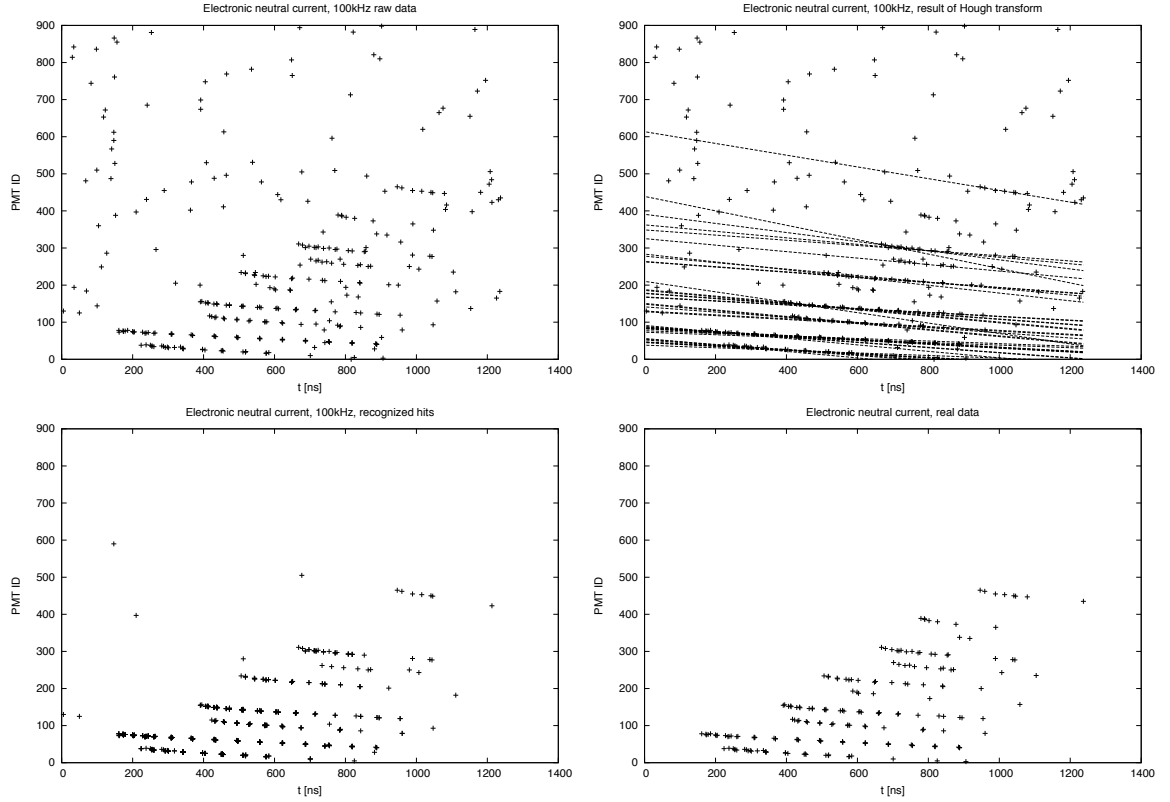


Figure B.1: Example of the detection of an electronic neutral current event at $1.1 \times 10^5 \text{ GeV}$ with 100kHz background noise. Top left: Raw data fed to the Hough Transform. Top right: Lines found by the Hough Transform. Bottom left: Hits extracted from raw data based on the Hough Transform's result. Bottom right: Original data without background noise.

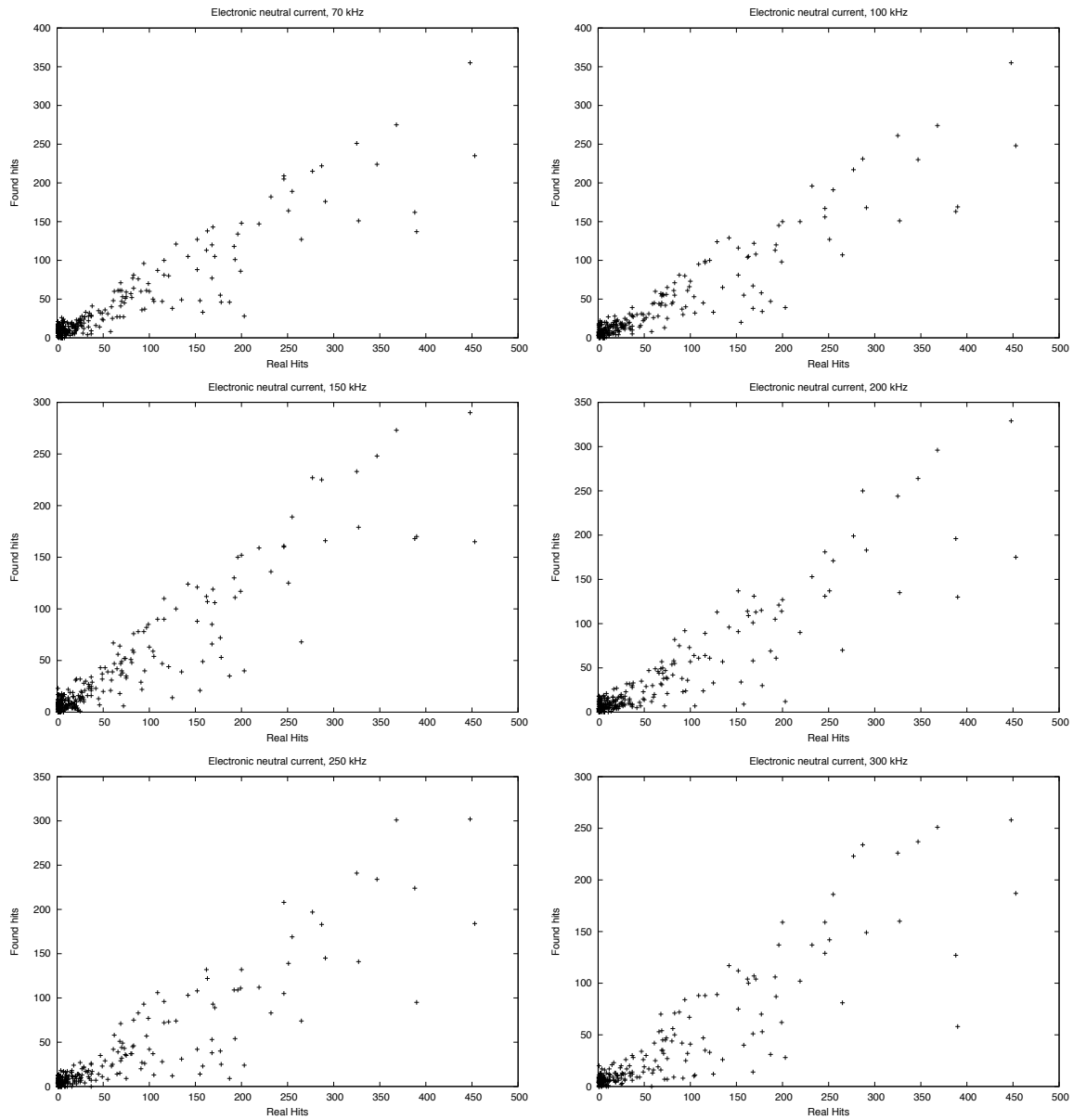


Figure B.2: Found hits as function of real hits for electronic neutral current events at different background rates.

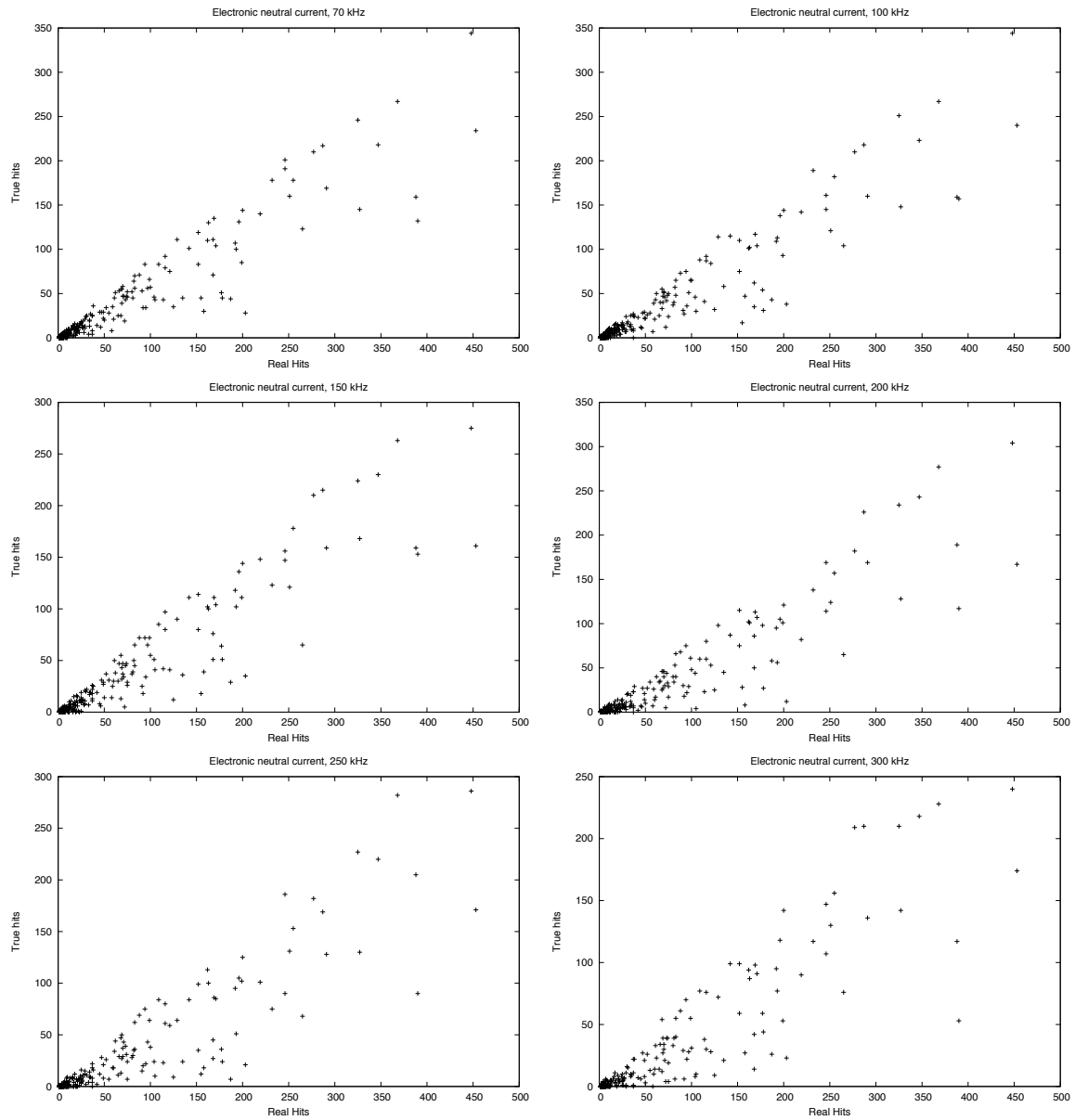


Figure B.3: *True hits as function of real hits for electronic neutral current events at different background rates.*

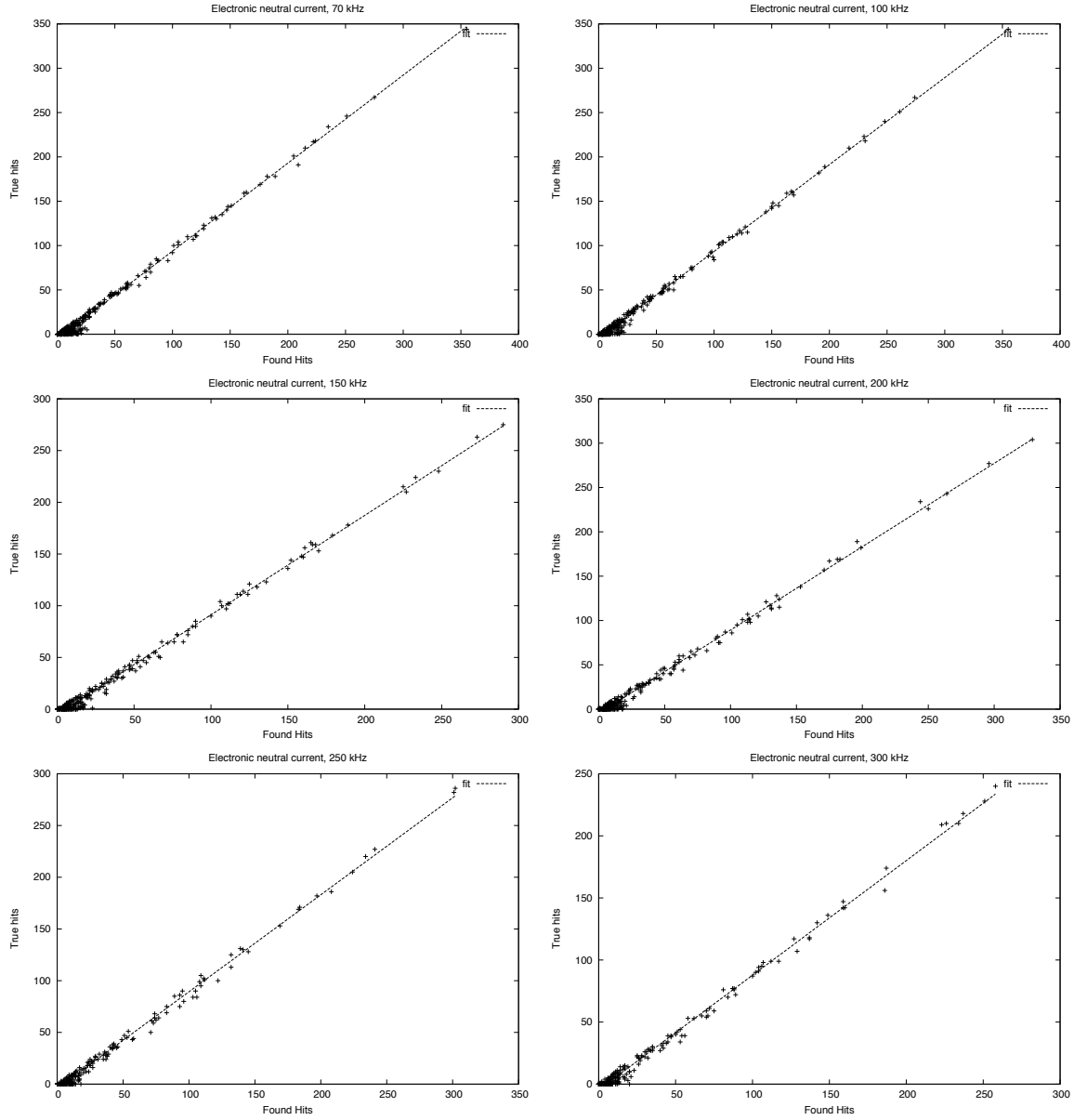


Figure B.4: True hits as function of found hits for electronic neutral current events at different background rates. The parameters a and b of the linear fit ($ax + b$, dashed line) have been determined to $a = 0.99, b = -5.52$ (70 kHz), $a = 0.98, b = -4.76$ (100 kHz), $a = 0.96, b = -4.98$ (150 kHz), $a = 0.94, b = -4.79$ (200 kHz), $a = 0.94, b = -4.51$ (250 kHz) and $a = 0.92, b = -4.65$ (300 kHz).

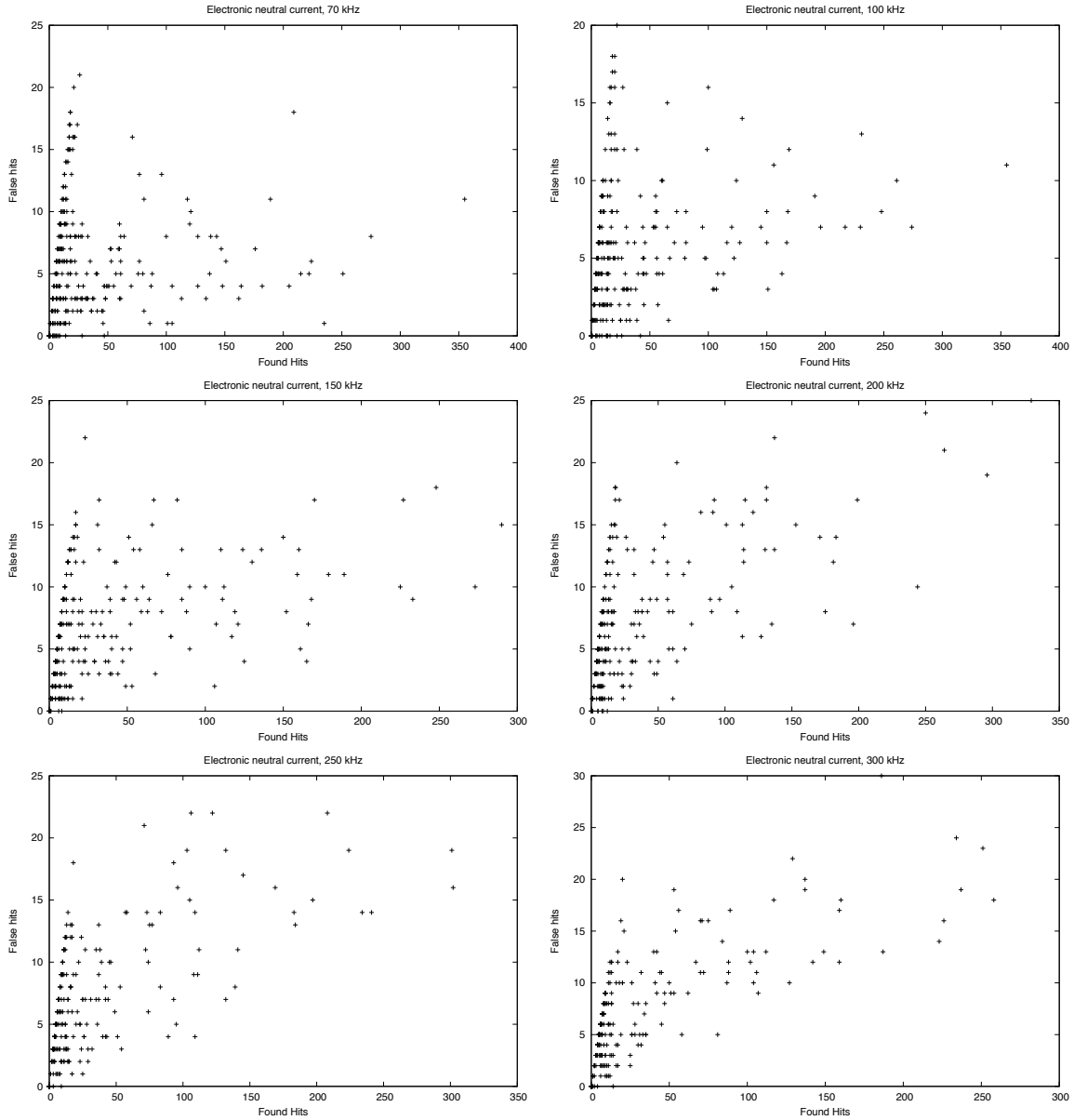


Figure B.5: *False hits as function of found hits for electronic neutral current events at different background rates.*

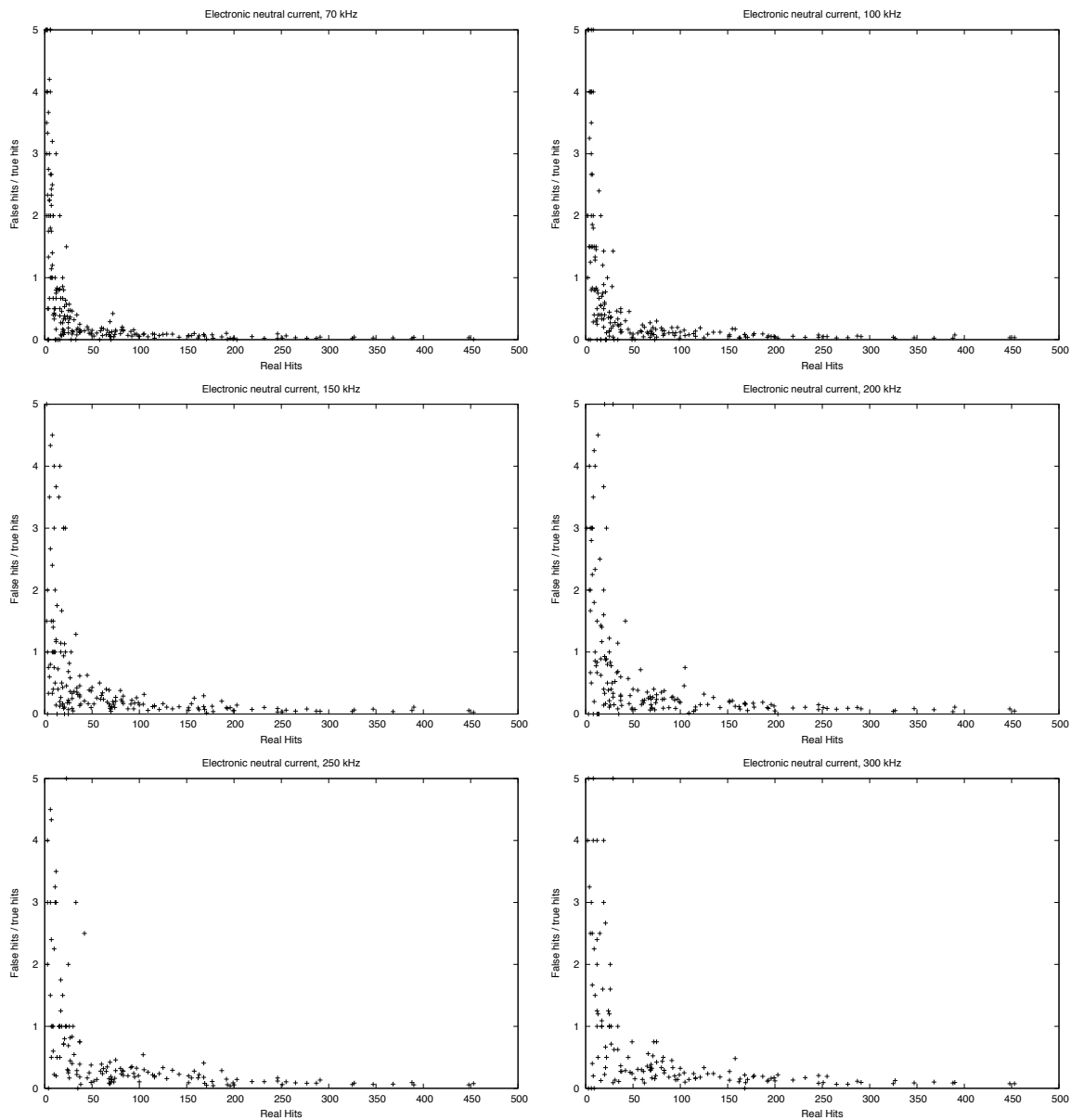


Figure B.6: Ratio of false and true hits as function of real hits for electronic neutral current events at different background rates.

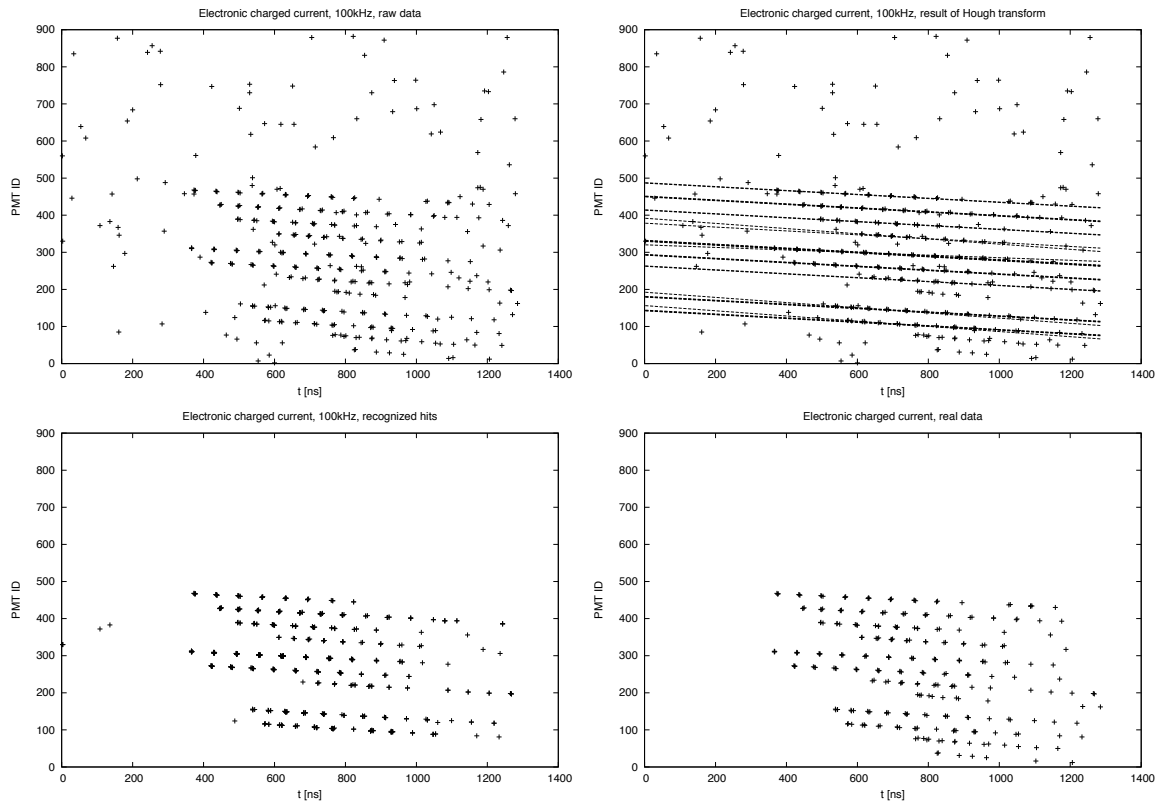


Figure B.7: *Example of the detection of an electronic charged current event at $1.3 \times 10^5 \text{ GeV}$ with 100kHz background noise. Top left: Raw data fed to the Hough Transform. Top right: Lines found by the Hough Transform. Bottom left: Hits extracted from raw data based on the Hough Transform's result. Bottom right: Original data without background noise.*

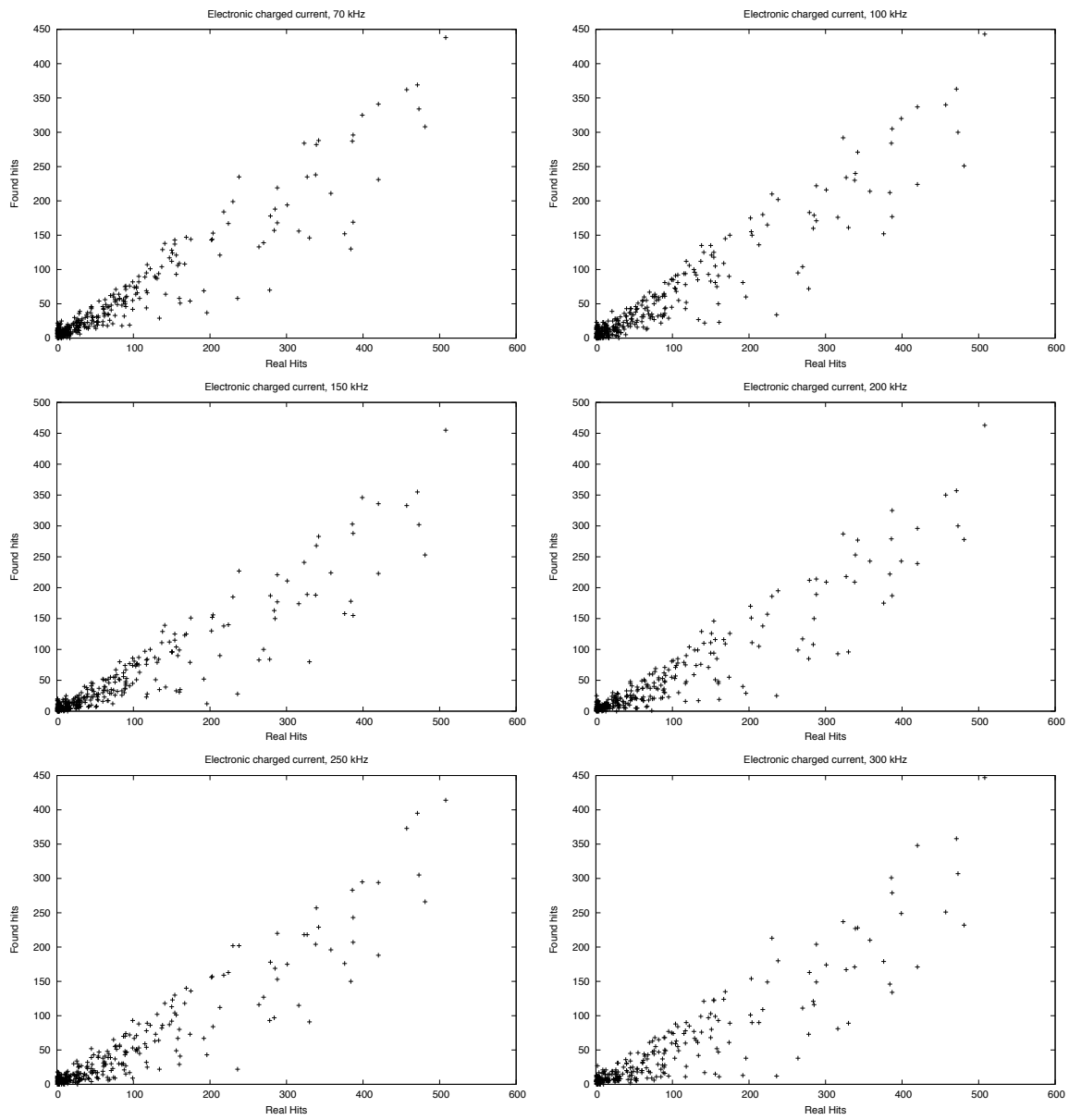


Figure B.8: *Found hits as function of real hits for electronic charged current events at different background rates.*

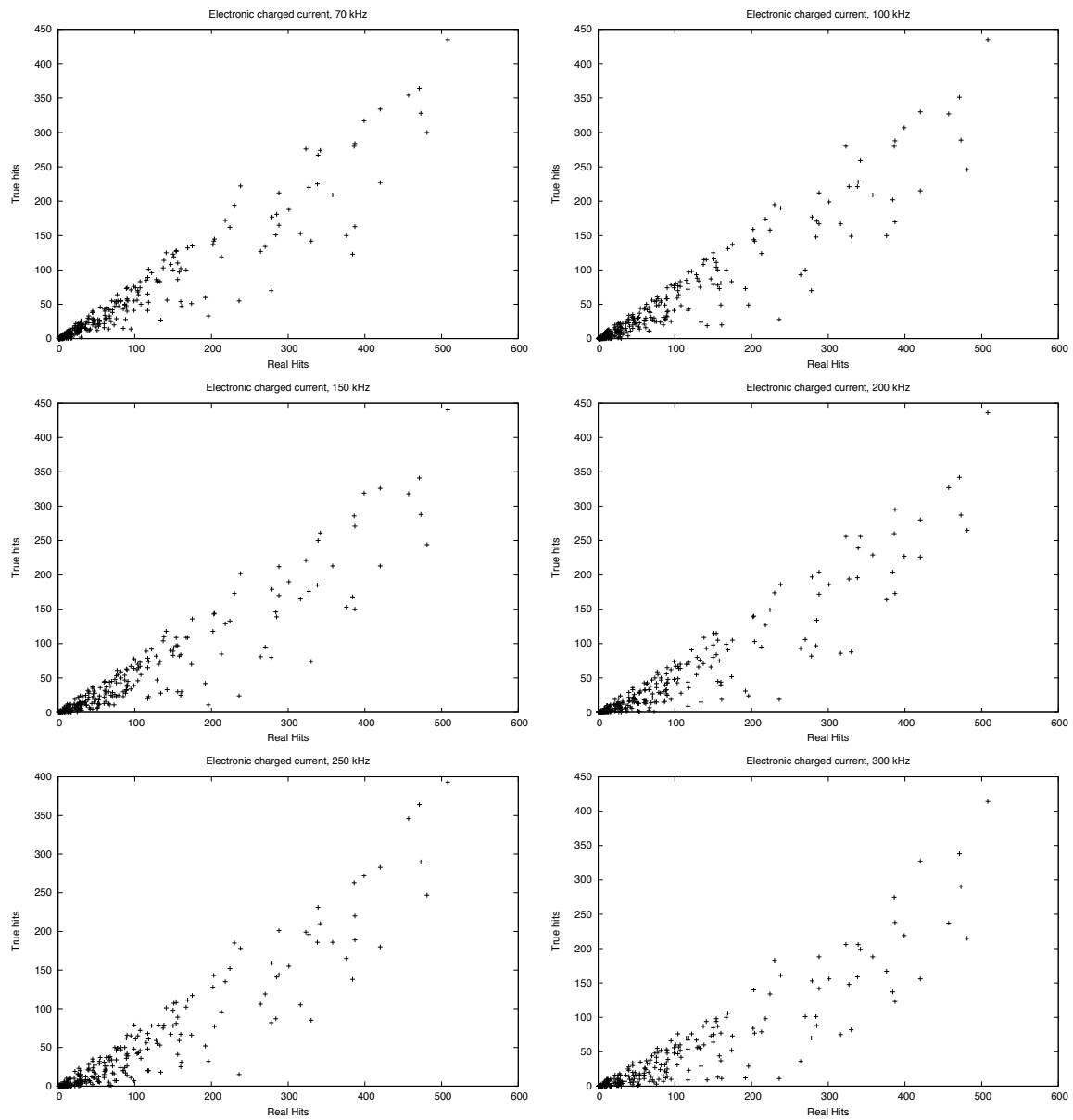


Figure B.9: *True hits as function of real hits for electronic charged current events at different background rates.*

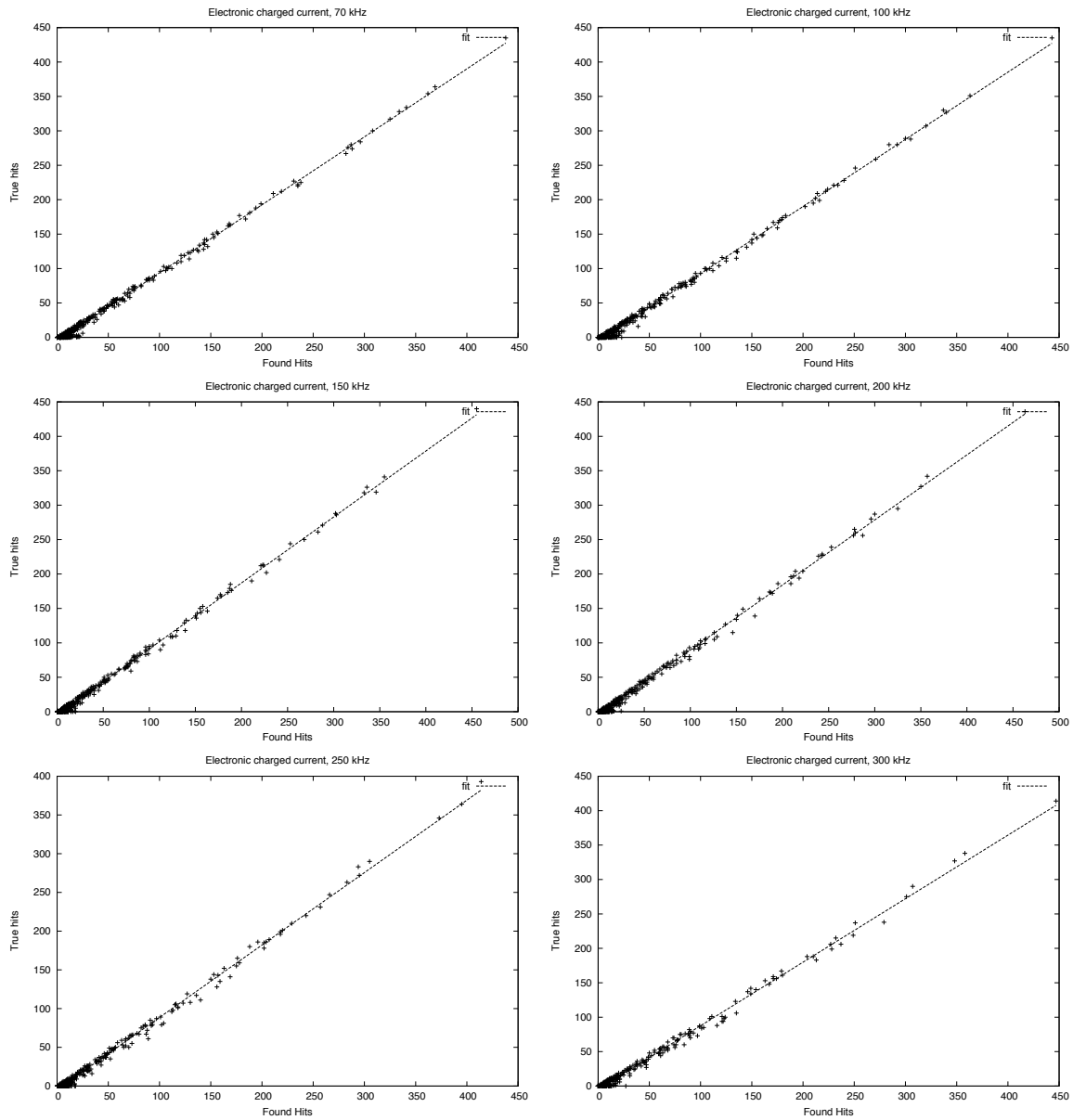


Figure B.10: True hits as function of found hits for electronic charged current events at different background rates. The parameters a and b of the linear fit ($ax + b$, dashed line) have been determined to $a = 0.99, b = -4.87$ (70 kHz), $a = 0.98, b = -5.05$ (100 kHz), $a = 0.96, b = -4.50$ (150 kHz), $a = 0.94, b = -4.78$ (200 kHz), $a = 0.94, b = -4.92$ (250 kHz) and $a = 0.92, b = -4.63$ (300 kHz).

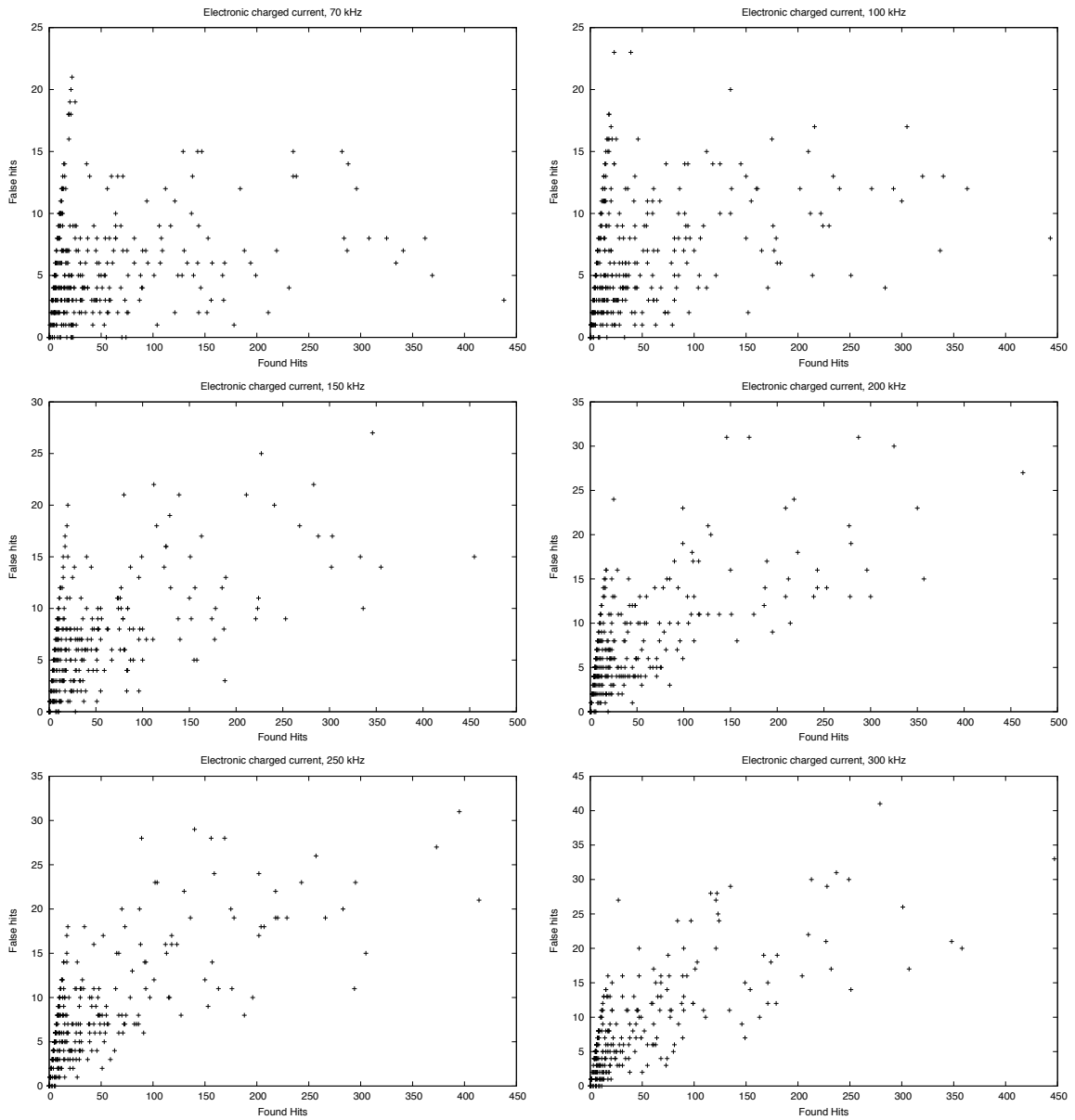


Figure B.11: *False hits as function of found hits for electronic charged current events at different background rates.*

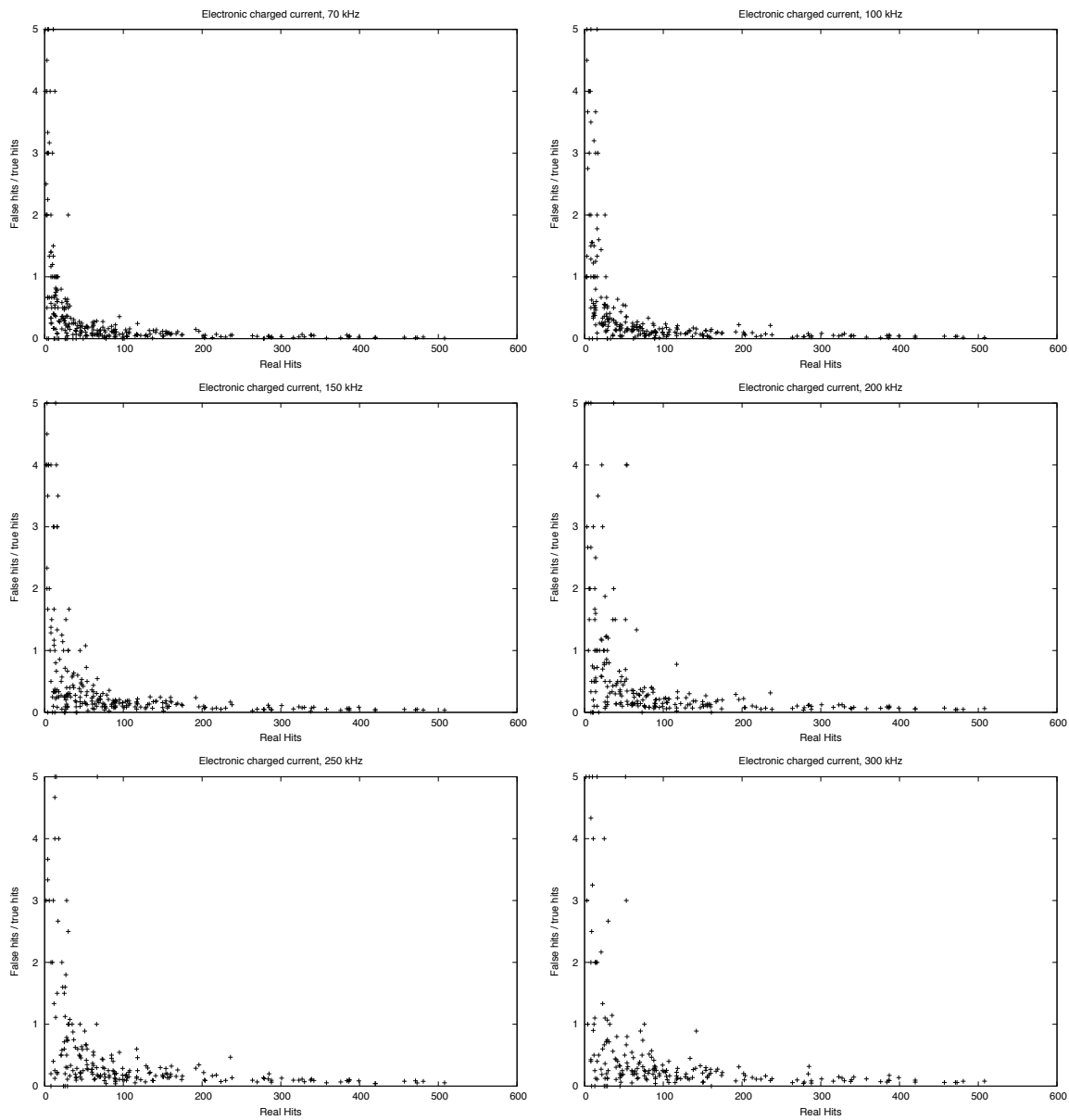


Figure B.12: *Ratio of false and true hits as function of real hits for electronic charged current events at different background rates.*

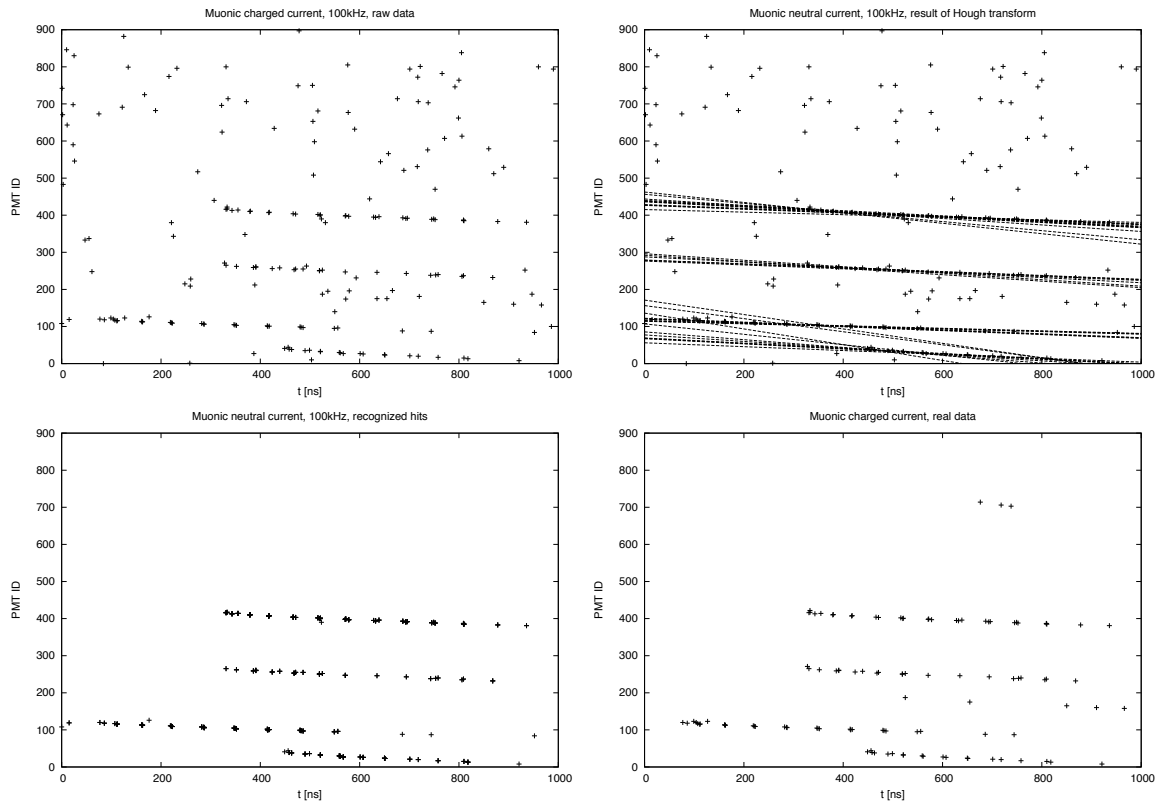


Figure B.13: *Example of the detection of a muonic neutral current event at $4.6 \times 10^4 \text{ GeV}$ with 100kHz background noise. Top left: Raw data fed to the Hough Transform. Top right: Lines found by the Hough Transform. Bottom left: Hits extracted from raw data based on the Hough Transform's result. Bottom right: Original data without background noise.*

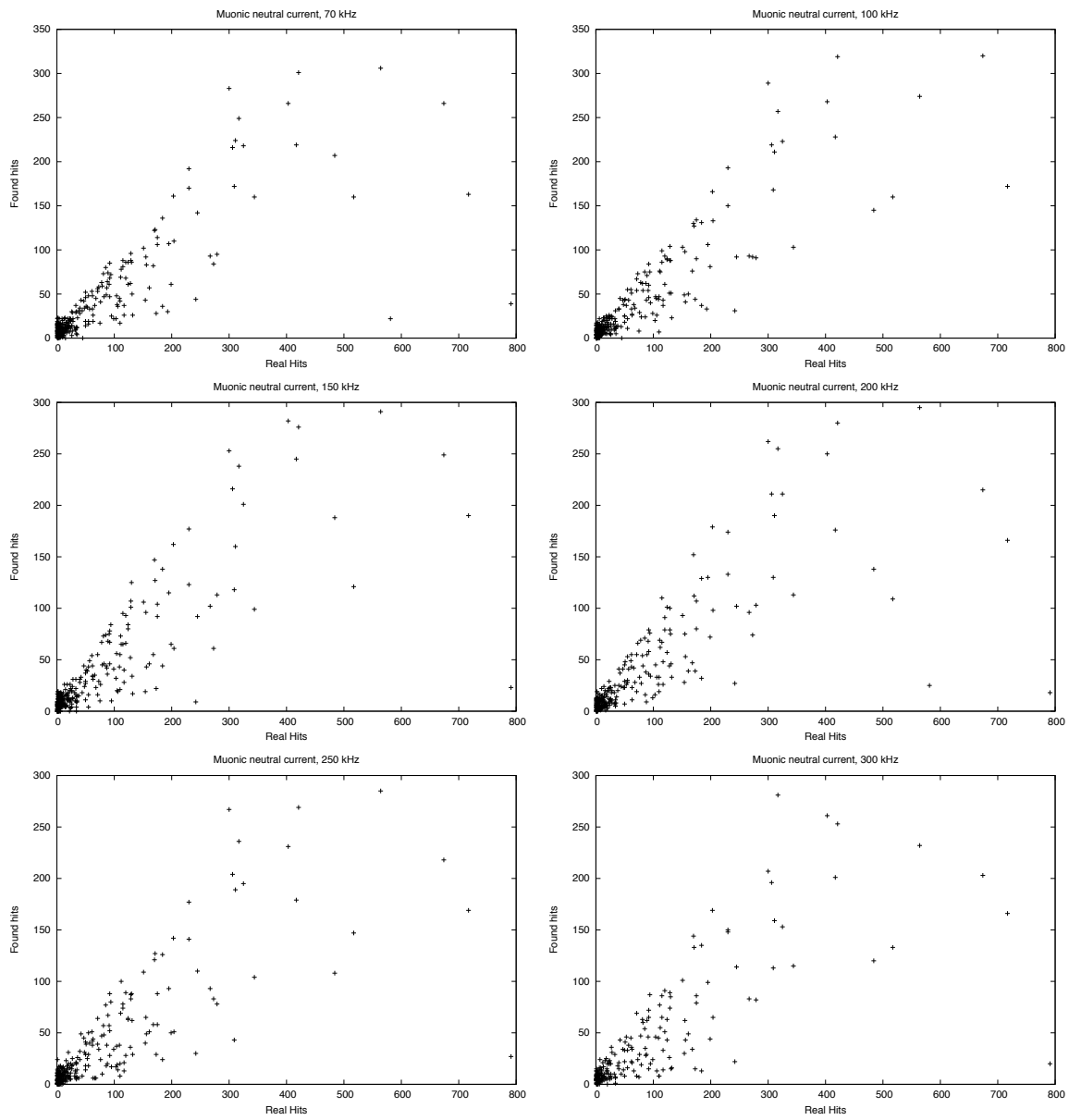


Figure B.14: *Found hits as function of real hits for muonic neutral current events at different background rates.*

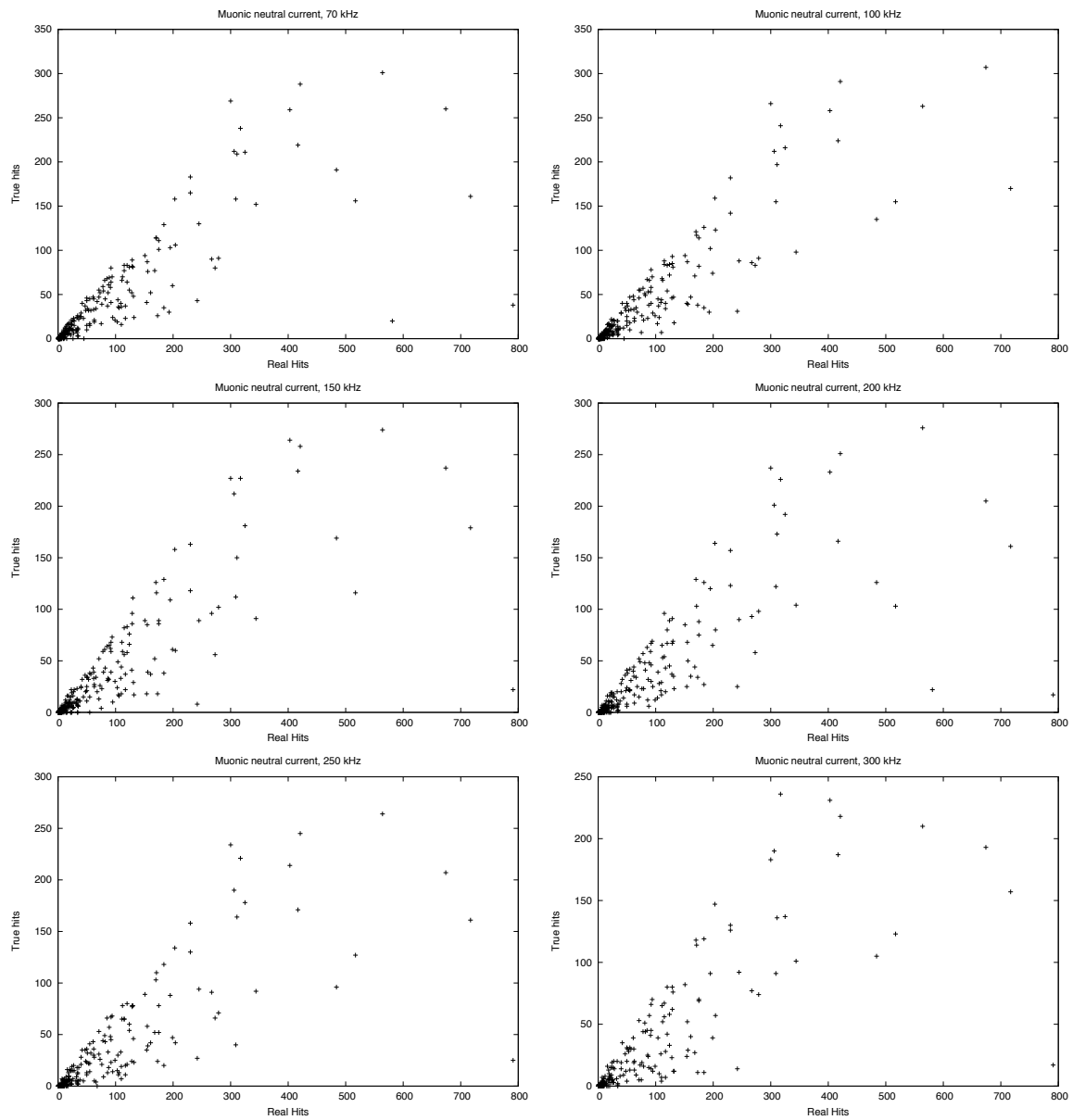


Figure B.15: *True hits as function of real hits for muonic neutral current events at different background rates.*

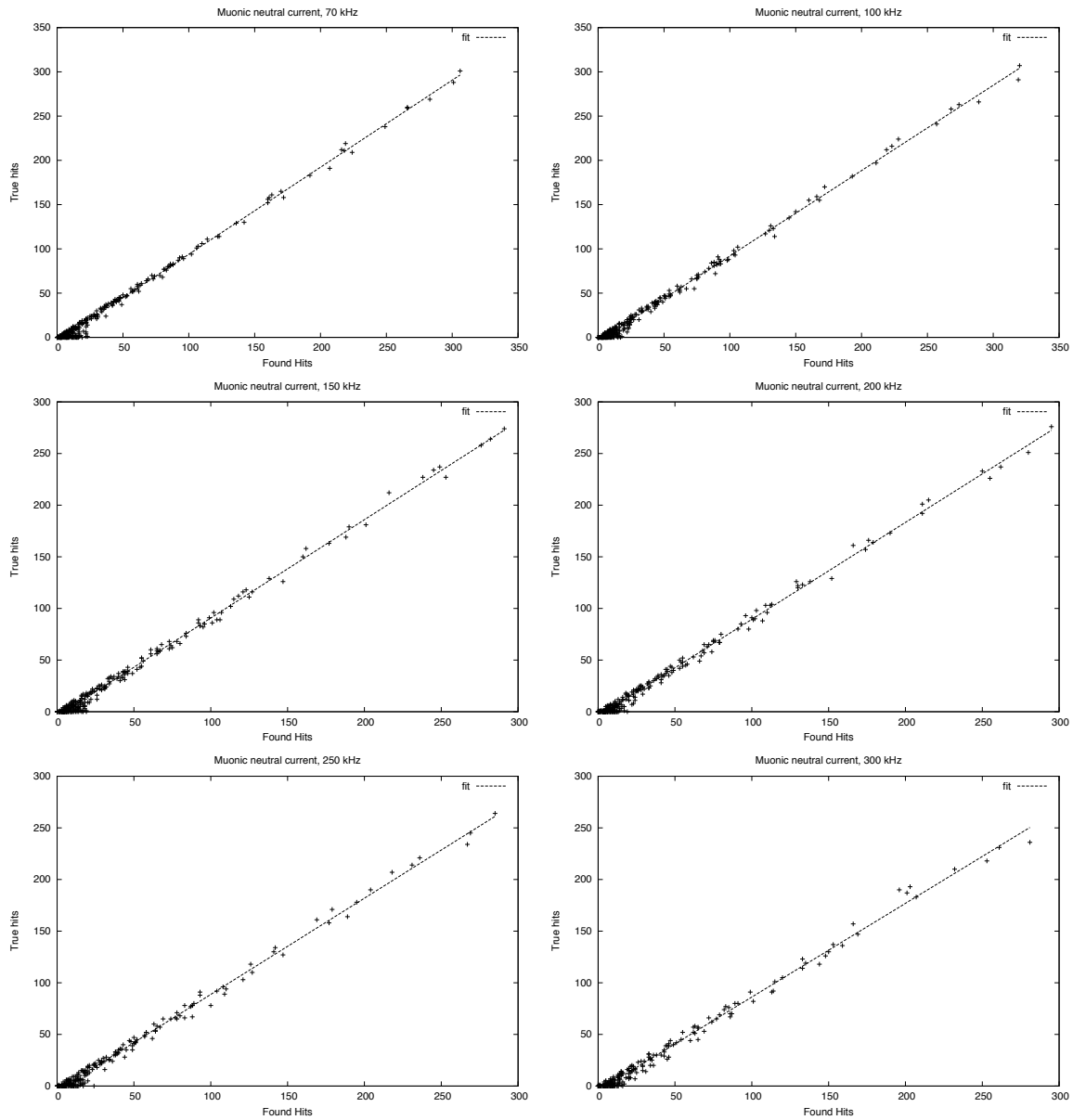


Figure B.16: True hits as function of found hits for muonic neutral current events at different background rates. The parameters a and b of the linear fit ($ax + b$, dashed line) have been determined to $a = 0.96, b = -4.69$ (70 kHz), $a = 0.94, b = -4.51$ (100 kHz), $a = 0.90, b = -4.41$ (150 kHz), $a = 0.85, b = -4.10$ (200 kHz), $a = 0.87, b = -4.75$ (250 kHz) and $a = 0.85, b = -4.43$ (300 kHz).

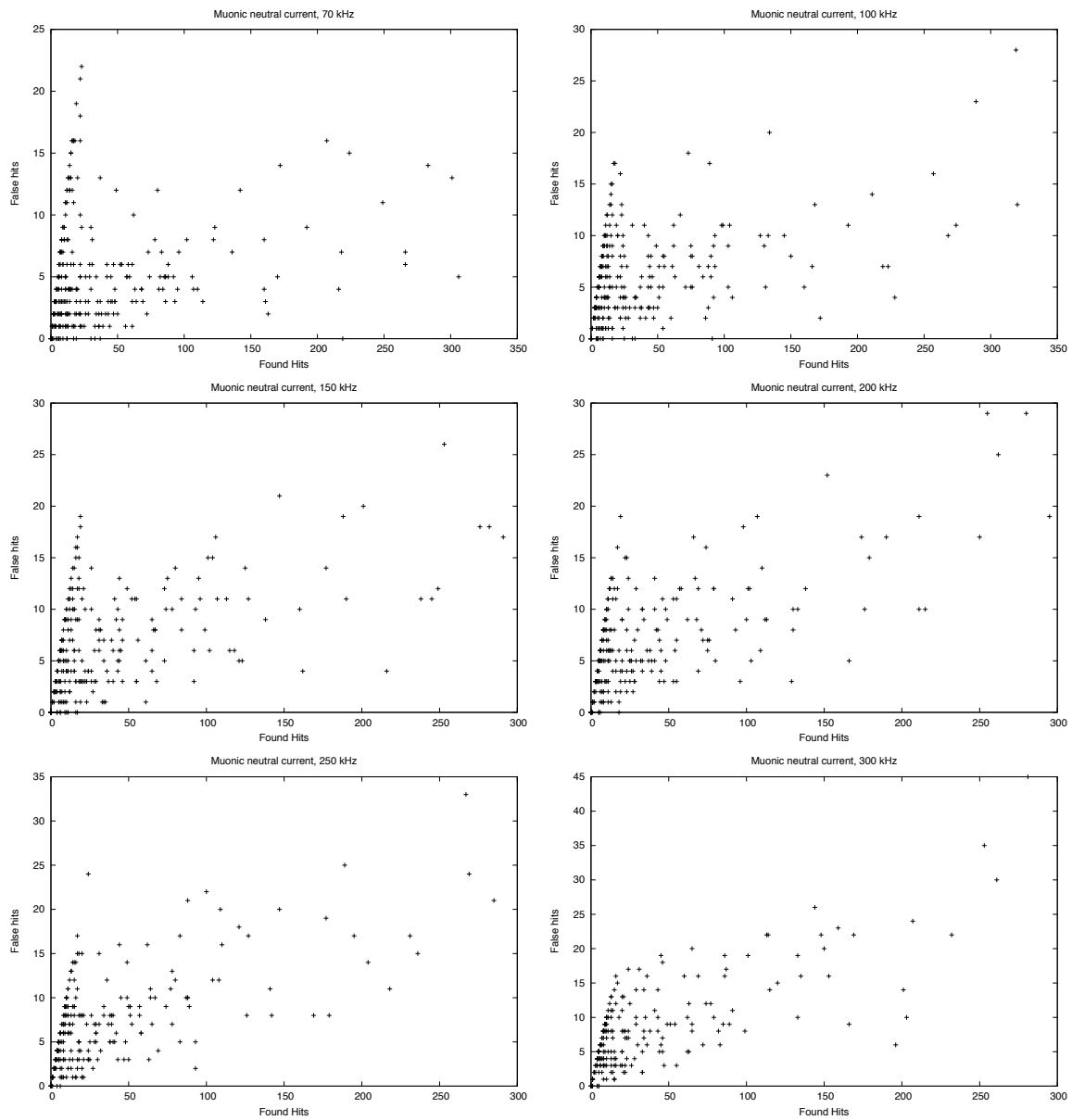


Figure B.17: *False hits as function of found hits for muonic neutral current events at different background rates.*

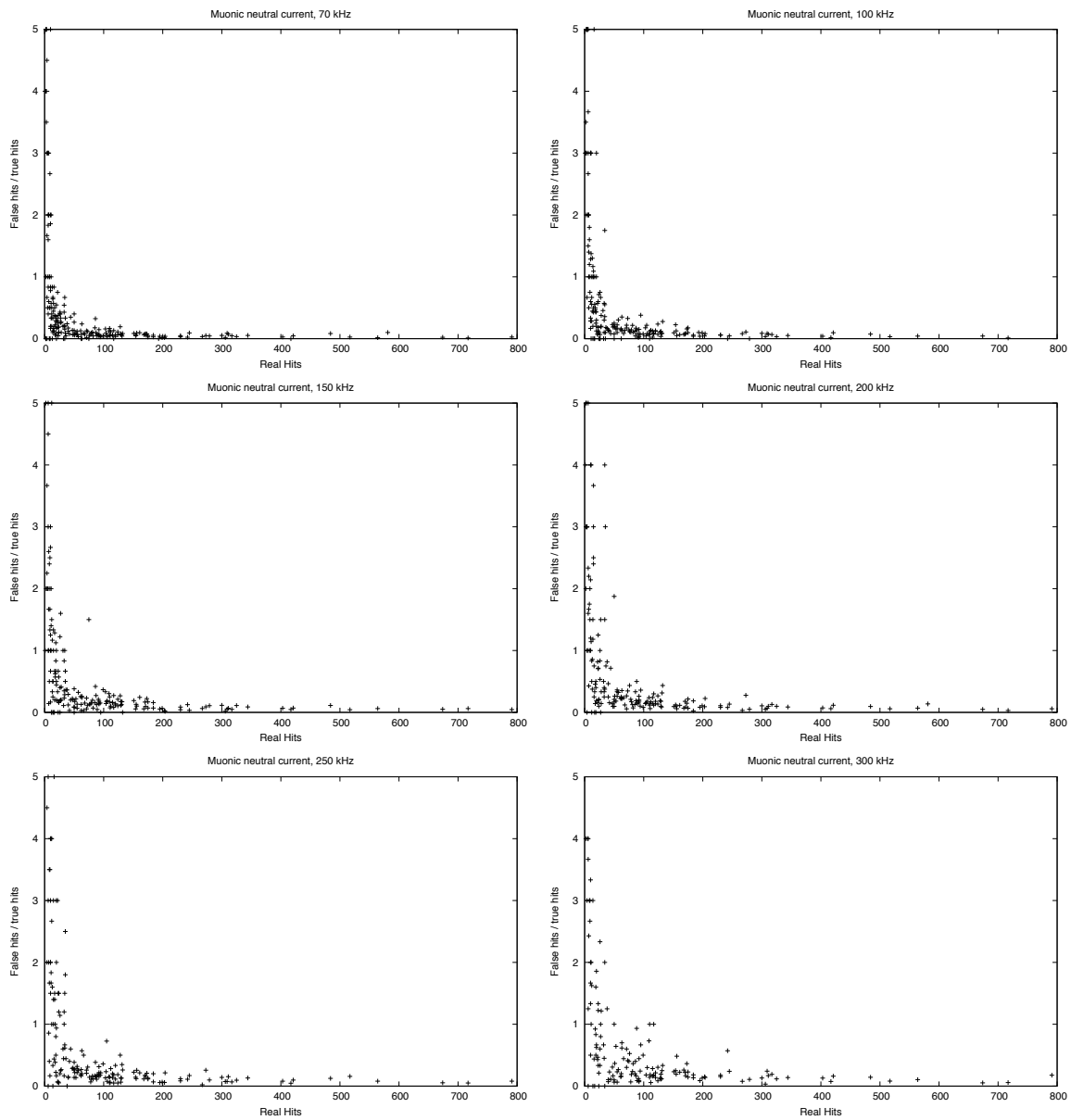


Figure B.18: *Ratio of false and true hits as function of real hits for muonic neutral current events at different background rates.*

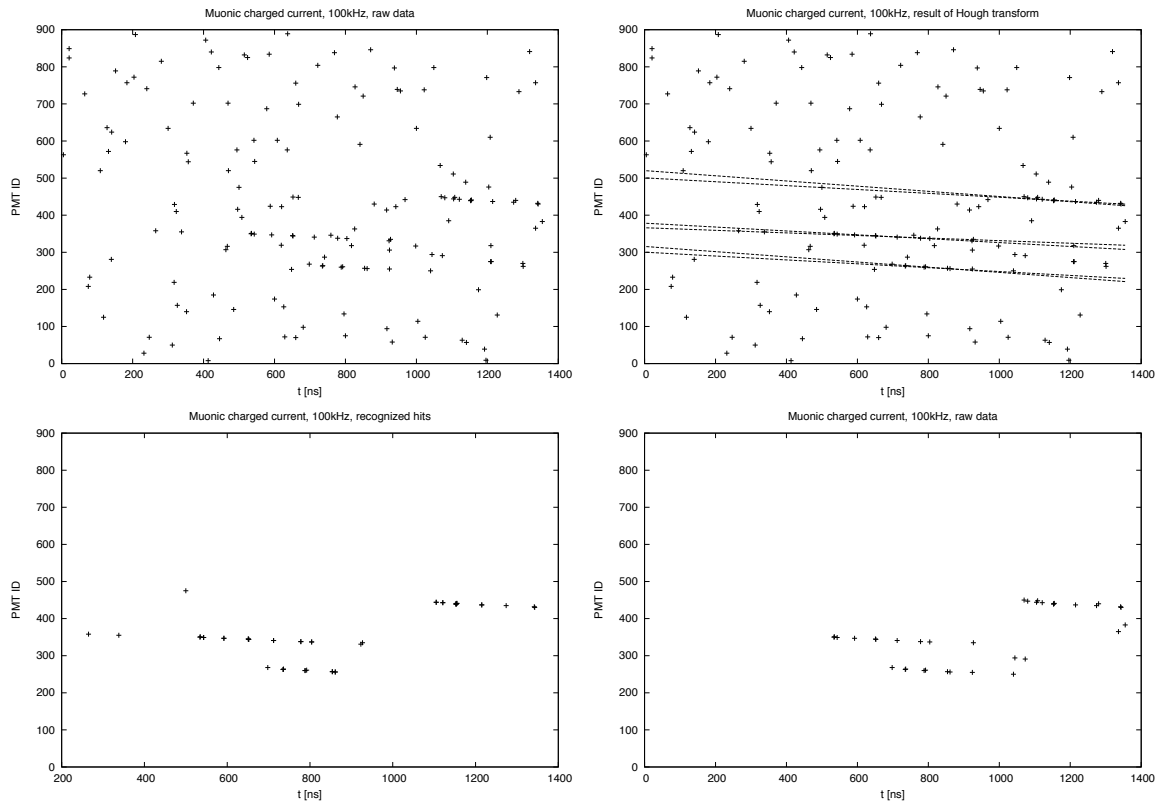


Figure B.19: *Example of the detection of a muonic charged current event at $3.0 \times 10^3 \text{ GeV}$ with 100kHz background noise. Top left: Raw data fed to the Hough Transform. Top right: Lines found by the Hough Transform. Bottom left: Hits extracted from raw data based on the Hough Transform's result. Bottom right: Original data without background noise.*

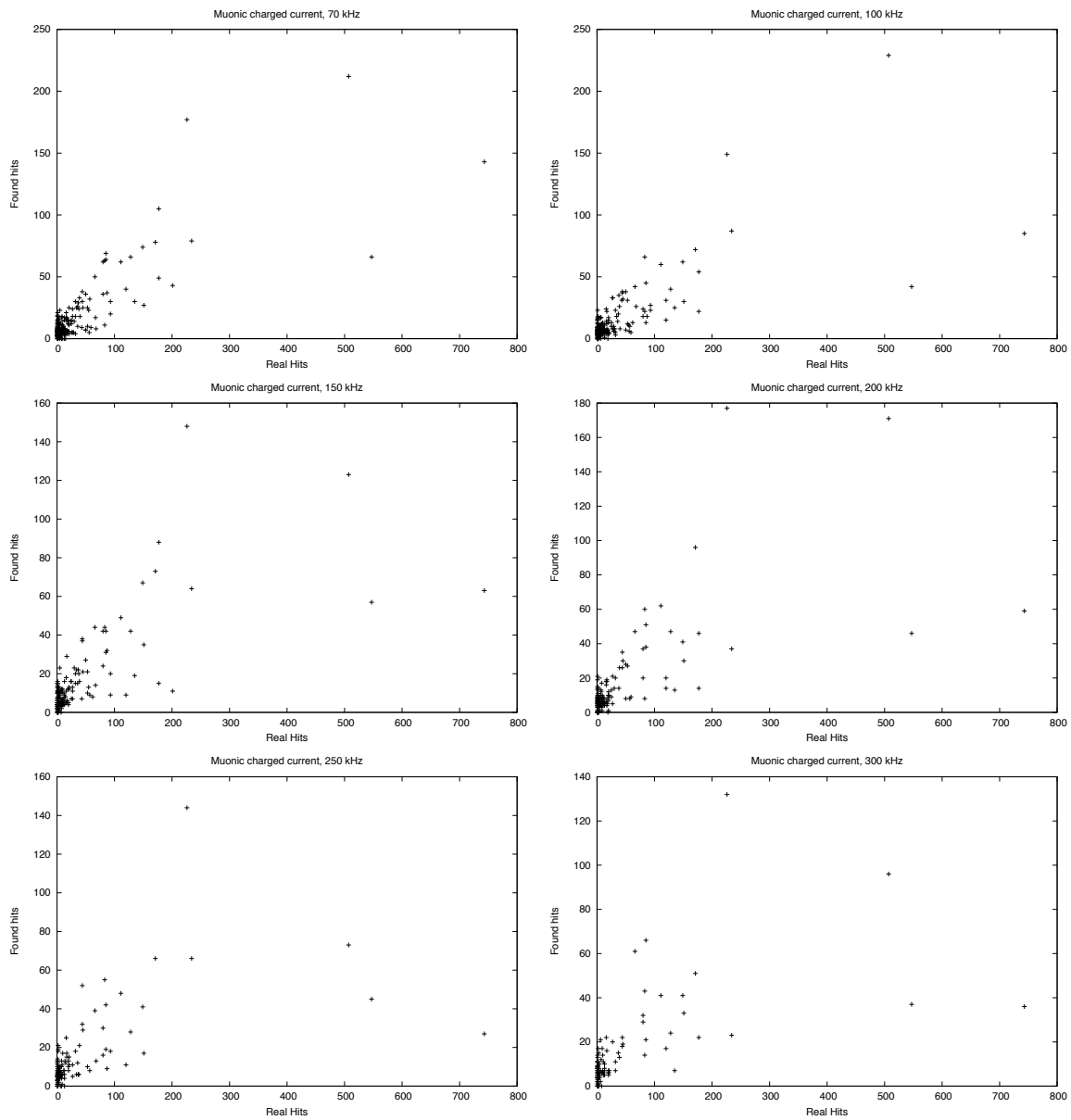


Figure B.20: *Found hits as function of real hits for muonic charged current events at different background rates.*

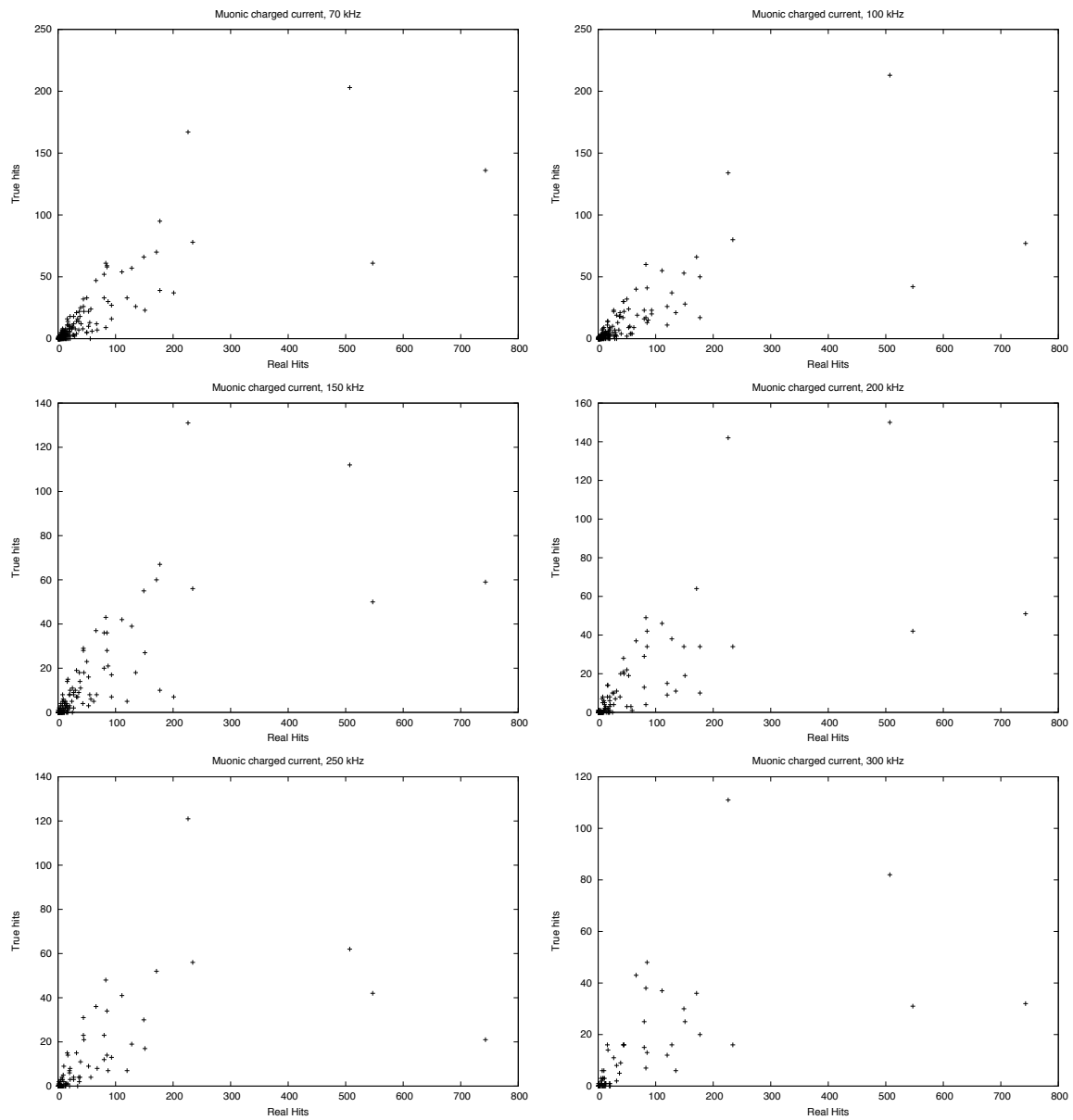


Figure B.21: *True hits as function of real hits for muonic charged current events at different background rates.*

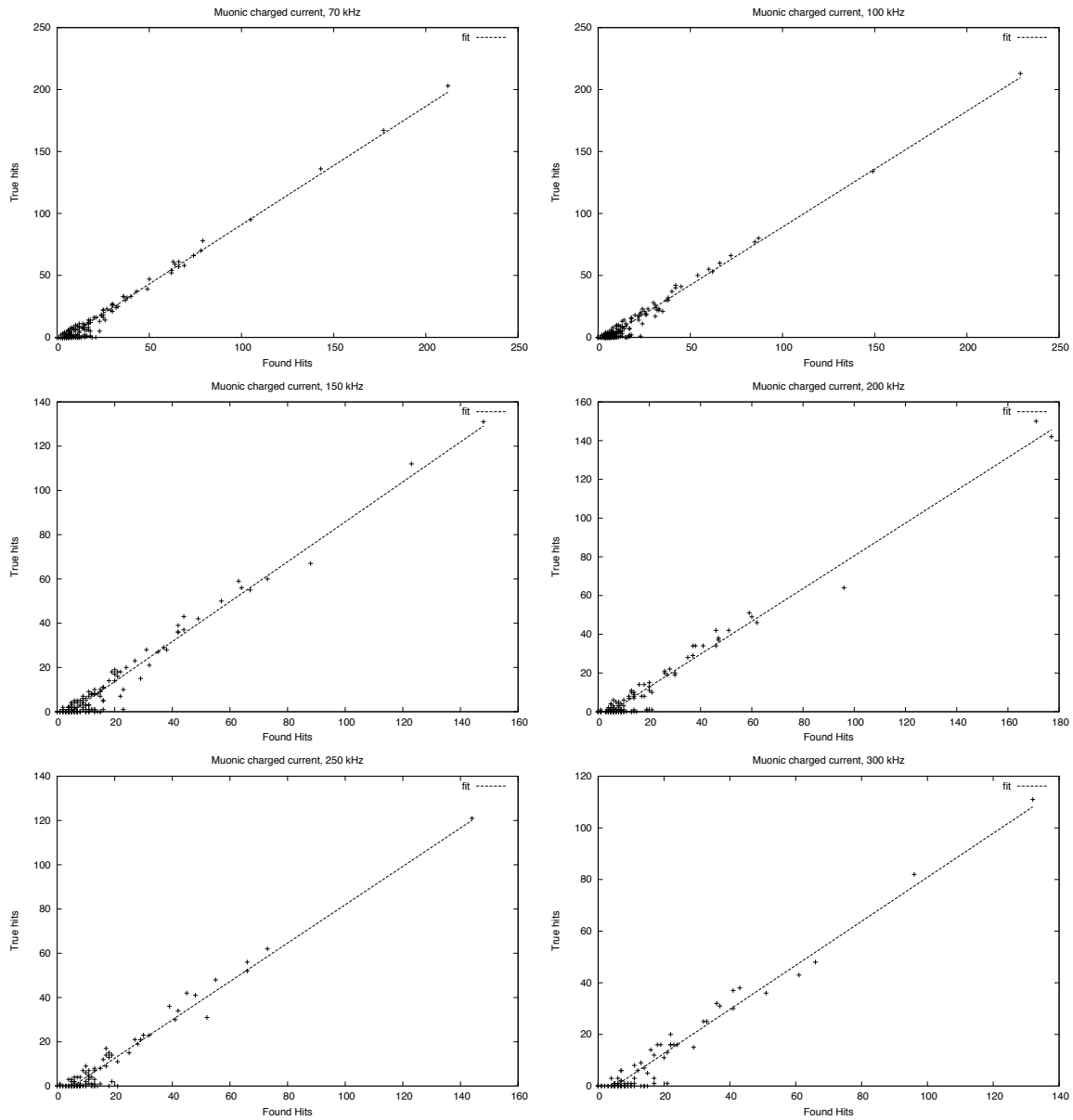


Figure B.22: True hits as function of found hits for muonic charged current events at different background rates. The parameters a and b of the linear fit ($ax + b$, dashed line) have been determined to $a = 0.98, b = -4.43$ (70 kHz), $a = 0.965, b = -4.31$ (100 kHz), $a = 0.95, b = -4.56$ (150 kHz), $a = 0.93, b = -4.44$ (200 kHz), $a = 0.93, b = -4.52$ (250 kHz) and $a = 0.91, b = -4.58$ (300 kHz).

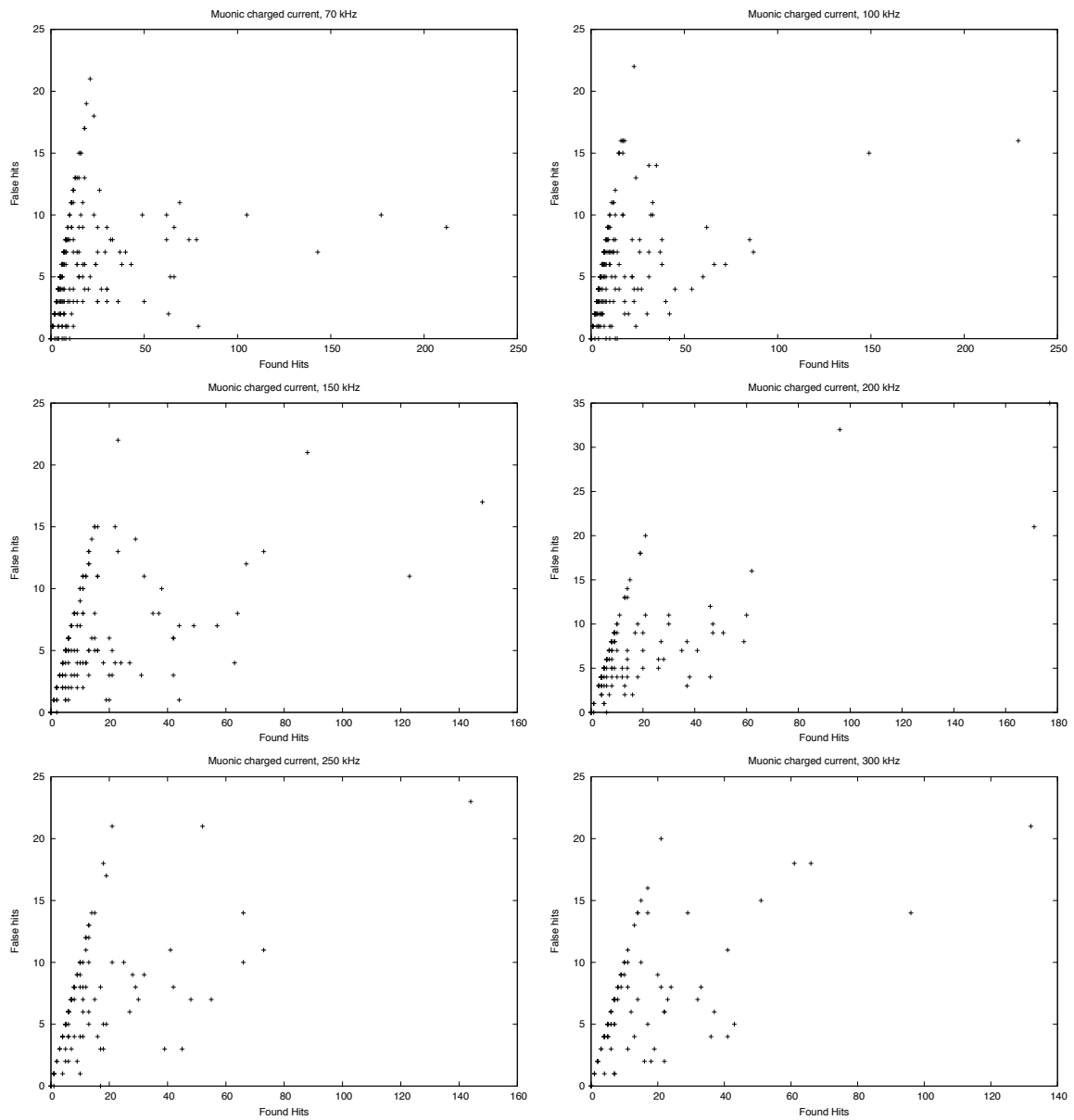


Figure B.23: *False hits as function of found hits for muonic charged current events at different background rates.*

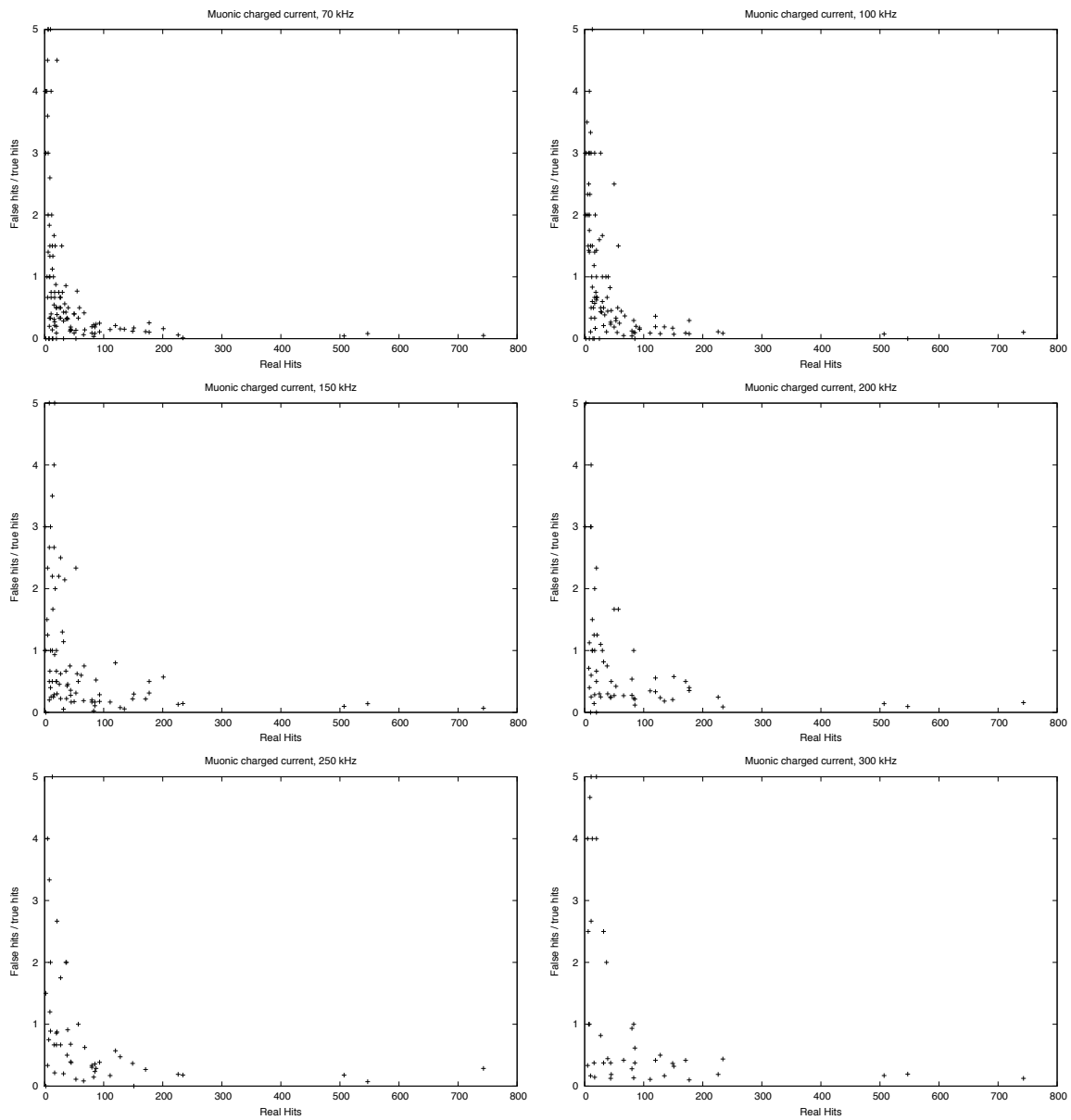


Figure B.24: *Ratio of false and true hits as function of real hits for muonic charged current events at different background rates.*

C Example results from real data

The following figures provide an overview of the analysis of real data recorded by the ANTARES detector, using the Hough Transform method or the standard ANTARES data filter, respectively. The top figure of each set shows the raw data including the lines which were detected by the Hough Transform. The second figure depicts the hits extracted by the Hough Transform. The bottom figure, eventually, illustrates the hits extracted by the standard ANTARES data filter. Only those plots contain data, where the corresponding algorithm detected an event. Additionally, the plots containing the Hough Transform and trigger results are rescaled to allow for a better comparison of the recognised hits. All 50 events were randomly selected from the data set of run 27995, recorded on May 9th 2007. The configuration of the Hough Transform algorithm was "whole detector without binning" but with a cut at 25 found hits. The angles of lines were required to mutually lie within a range of 5°, according to the filter strategy described in chapt. 5.3.6. Nearest-neighbour filtering was not used. The standard ANTARES data filter was used in its default configuration.

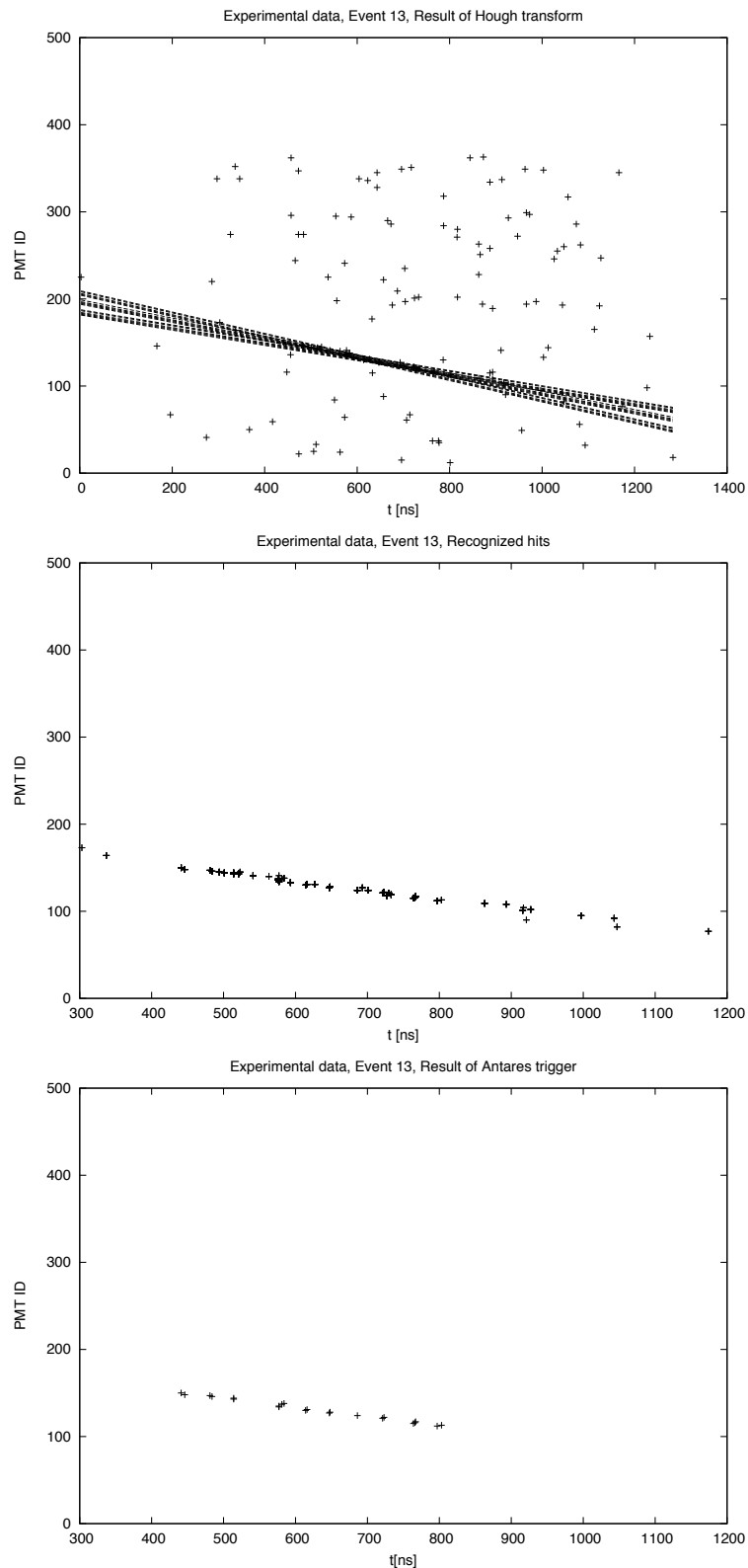


Figure C.1: Raw data (top), Hough Transform (mid) and ANTARES trigger (bottom) results of event 13 of run 27955 (recorded on 29.05.2007)

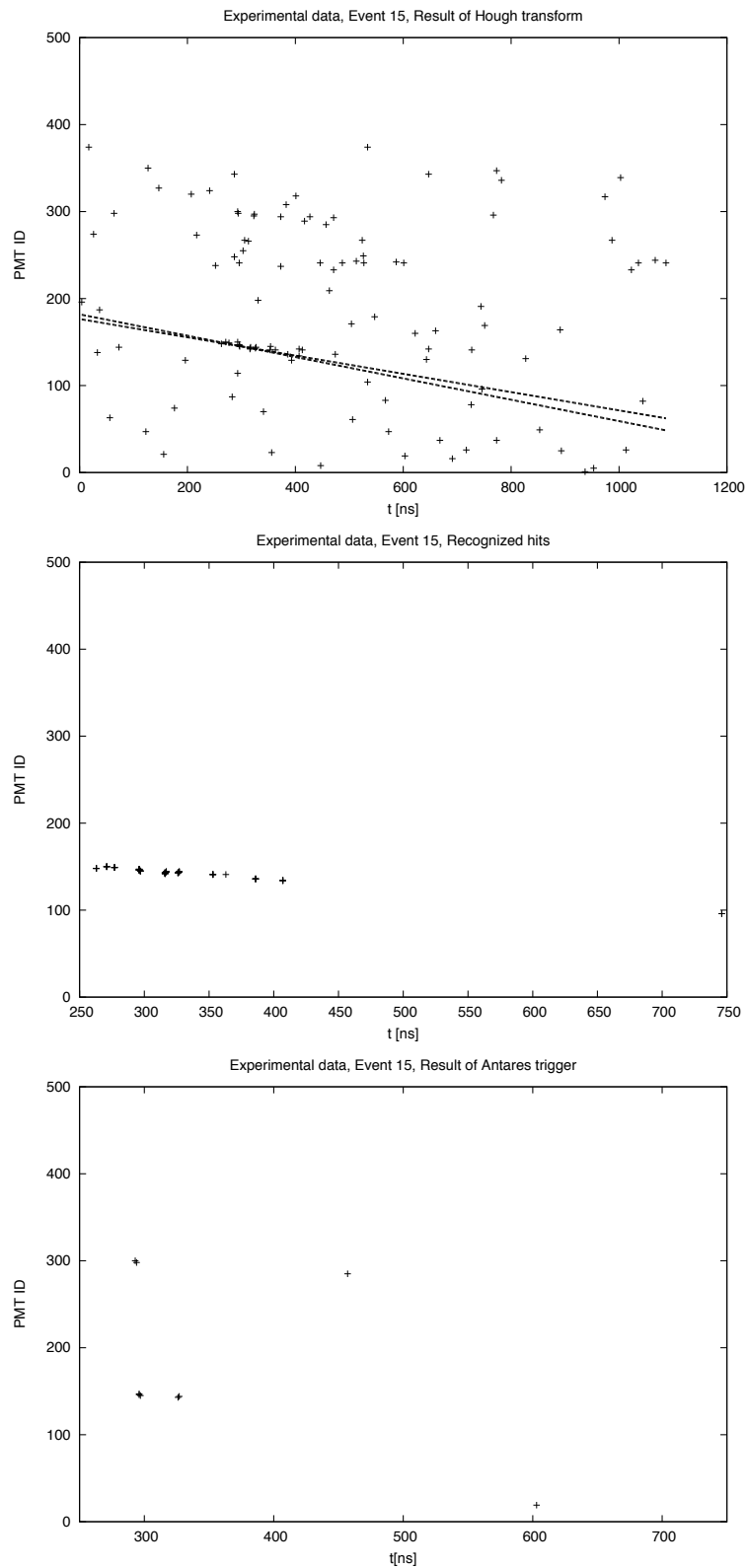


Figure C.2: Raw data (top), Hough Transform (mid) and ANTARES trigger (bottom) results of event 15 of run 27955 (recorded on 29.05.2007)

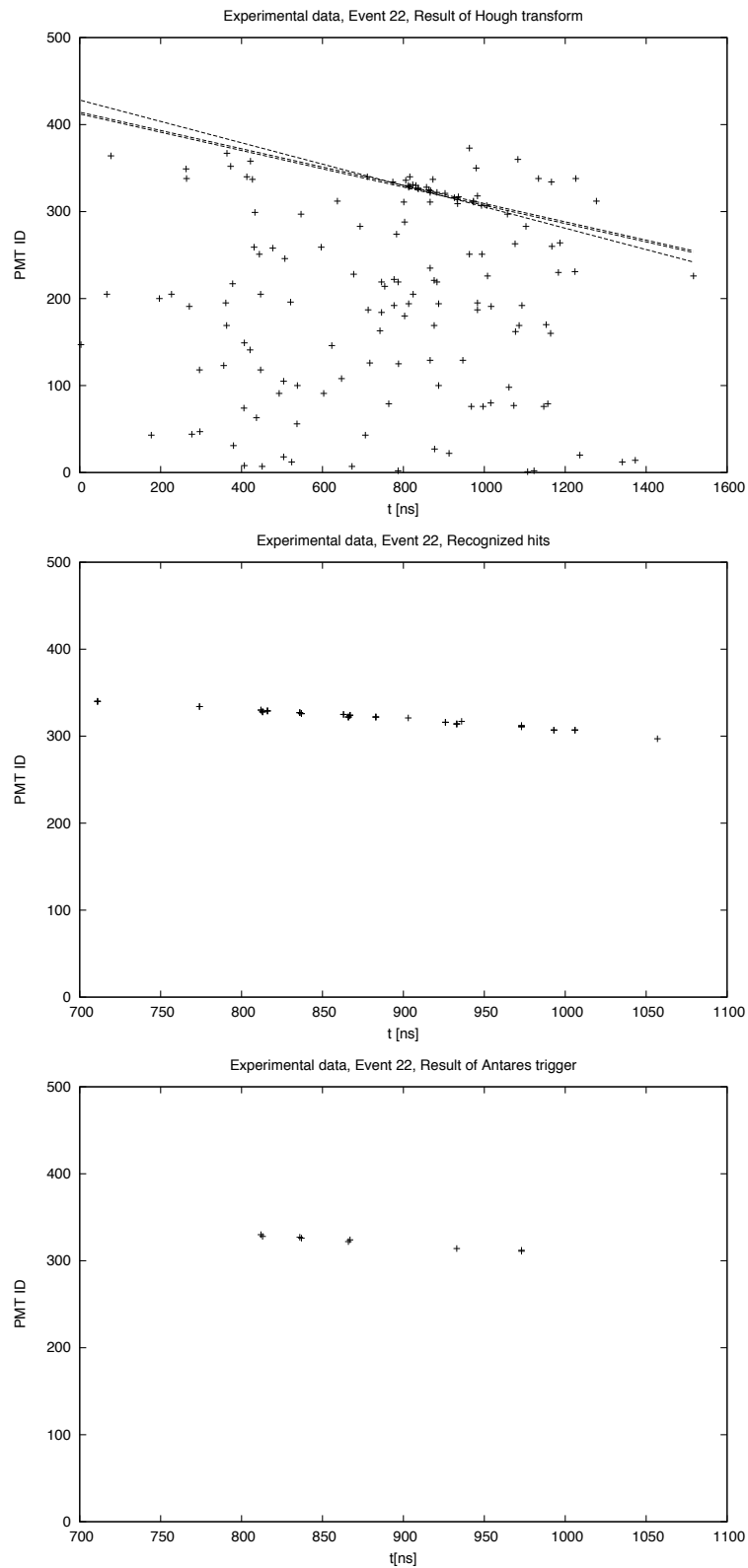


Figure C.3: Raw data (top), Hough Transform (mid) and ANTARES trigger (bottom) results of event 22 of run 27955 (recorded on 29.05.2007)

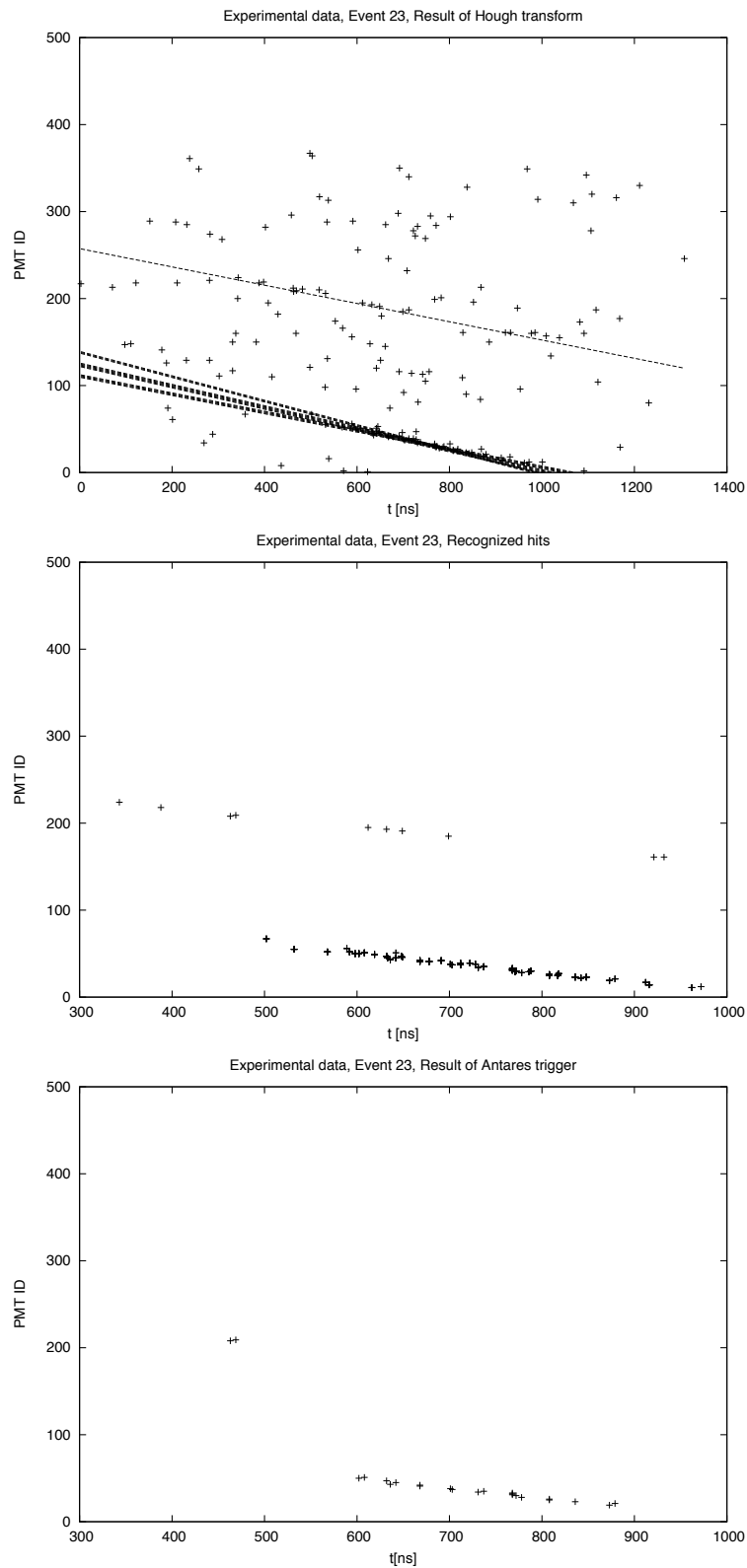


Figure C.4: Raw data (top), Hough Transform (mid) and ANTARES trigger (bottom) results of event 23 of run 27955 (recorded on 29.05.2007)

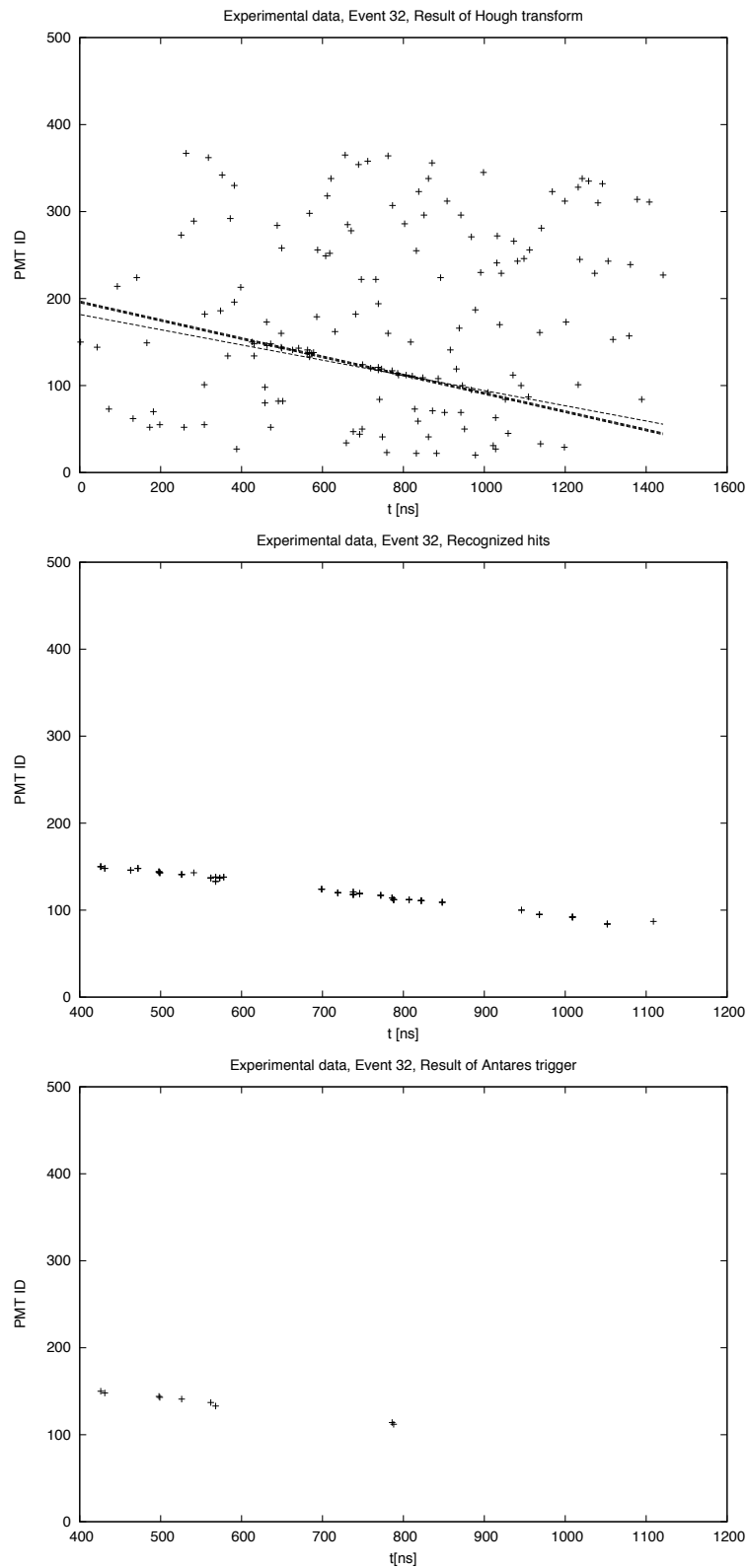


Figure C.5: Raw data (top), Hough Transform (mid) and ANTARES trigger (bottom) results of event 32 of run 27955 (recorded on 29.05.2007)

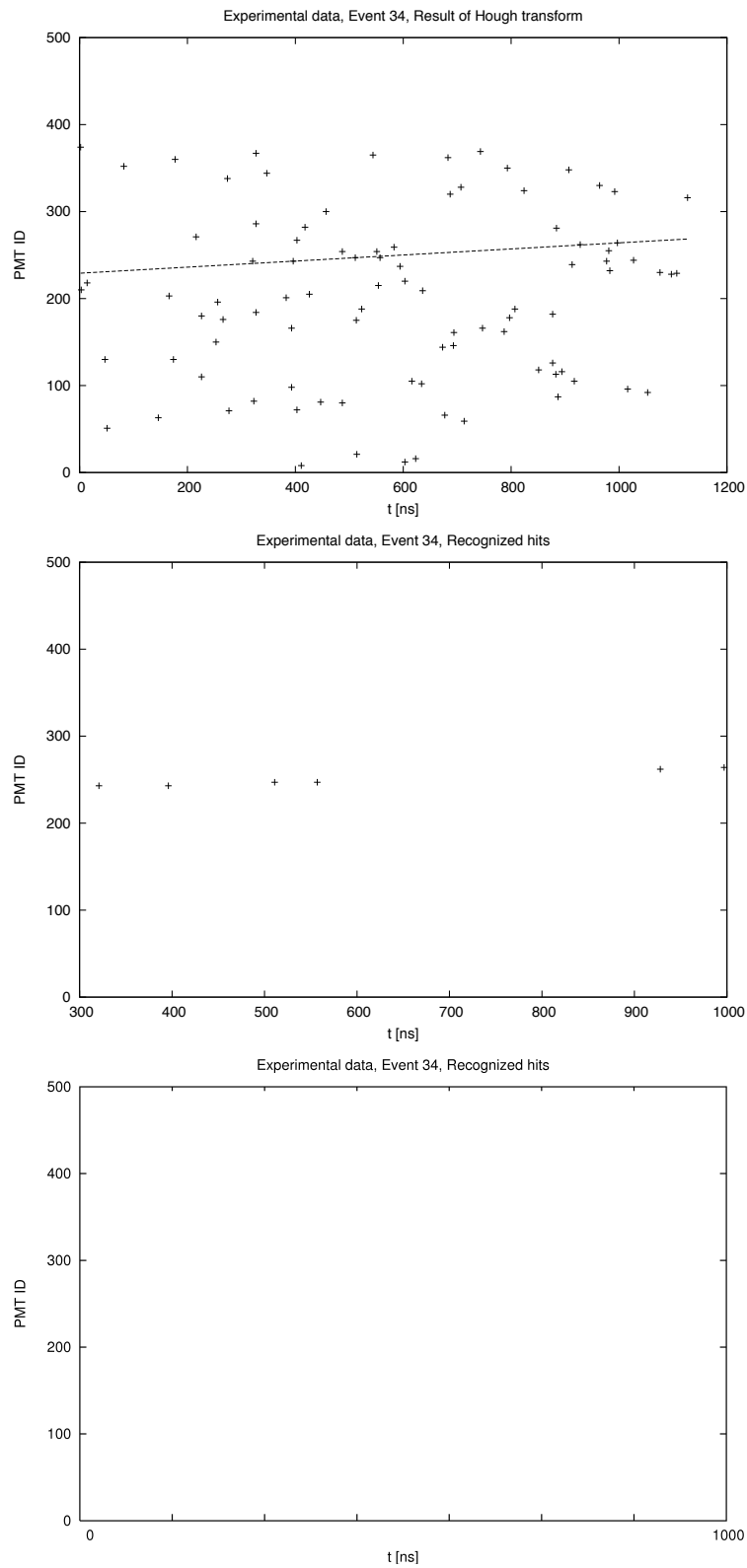


Figure C.6: Raw data (top) and Hough Transform (mid) results of event 34 of run 27955 (recorded on 29.05.2007). The ANTARES trigger did not detect the event.

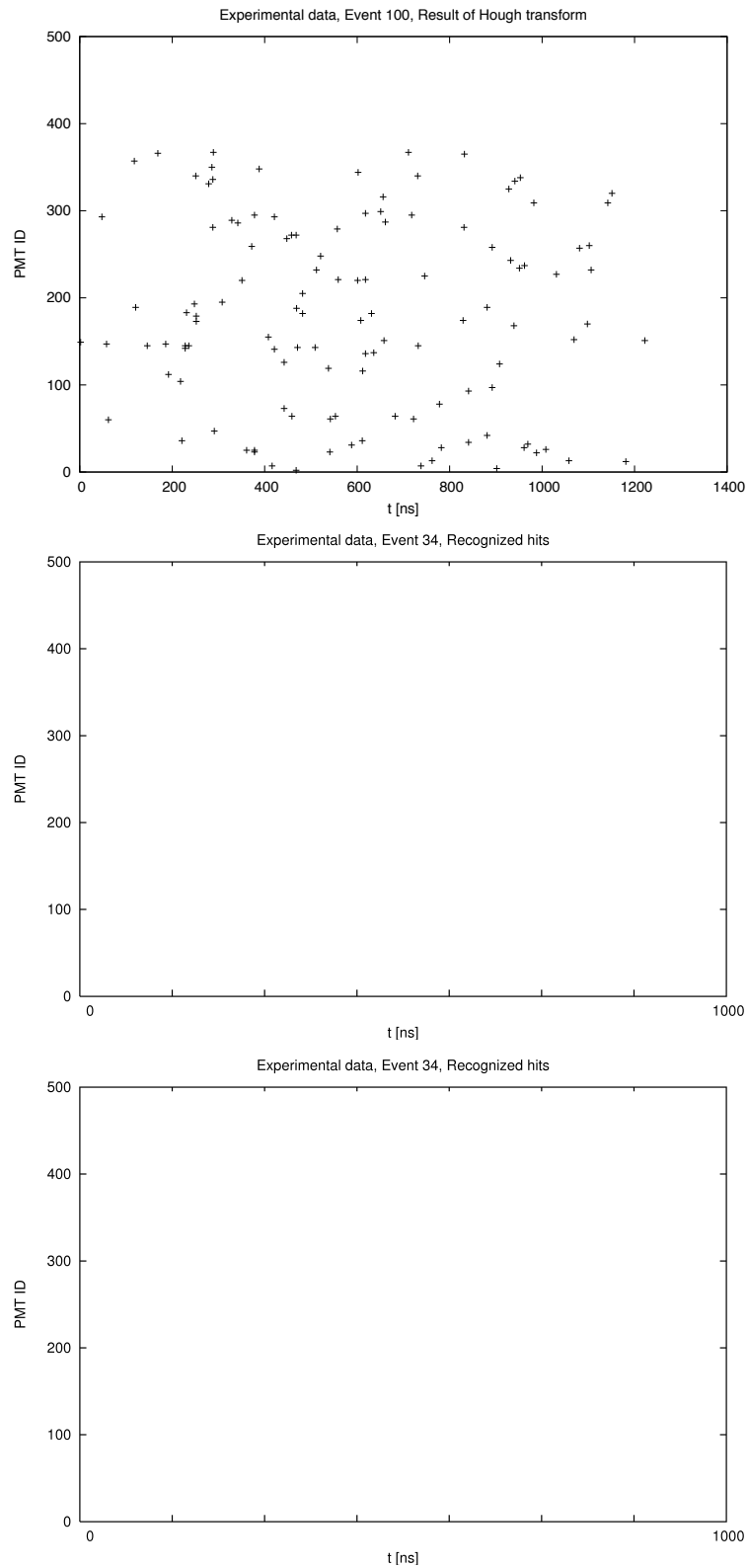


Figure C.7: Raw data of event 100 of run 27955 (recorded on 29.05.2007). Neither the standard trigger nor the the ANTARES trigger detected the event.

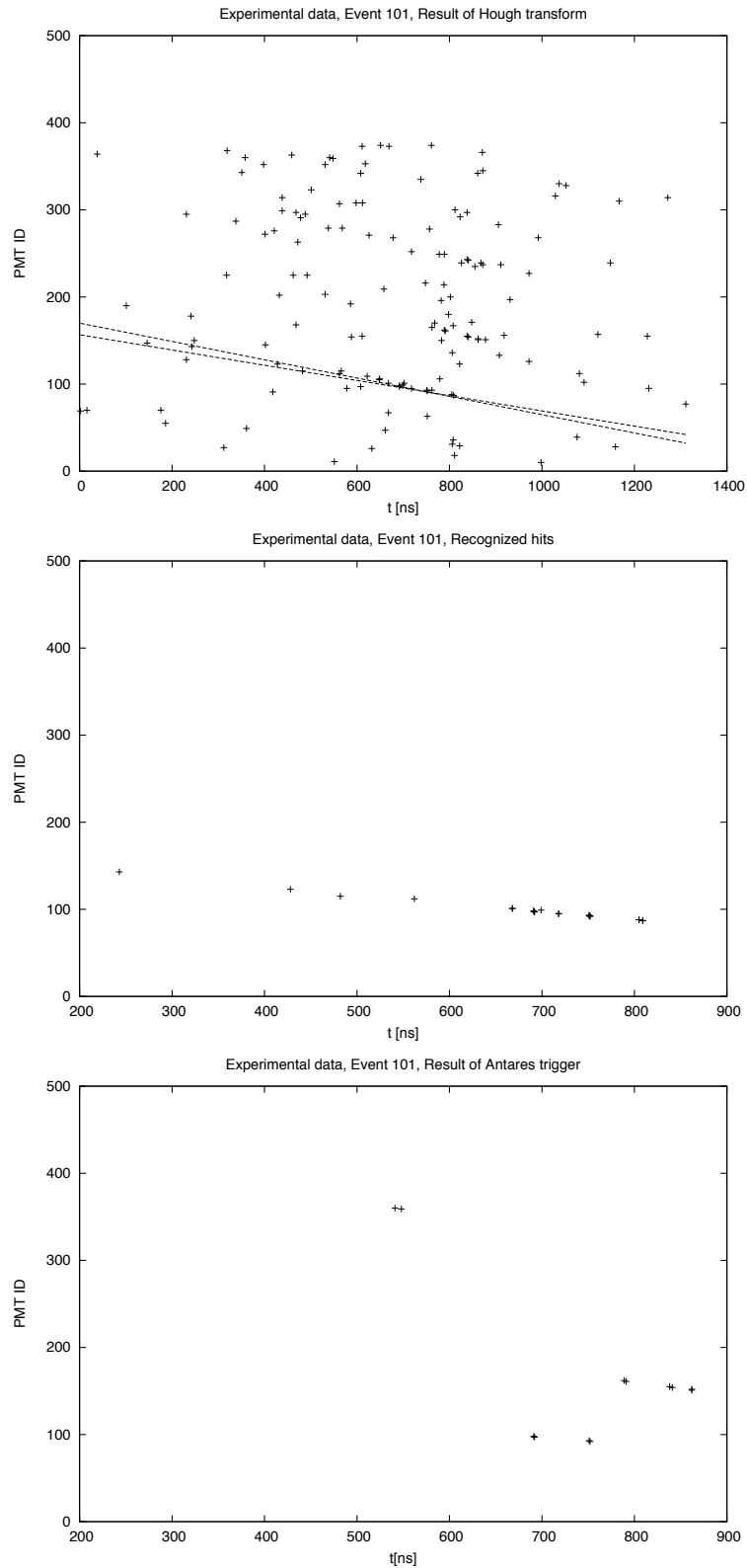


Figure C.8: Raw data (top), Hough Transform (mid) and ANTARES trigger (bottom) results of event 101 of run 27955 (recorded on 29.05.2007).

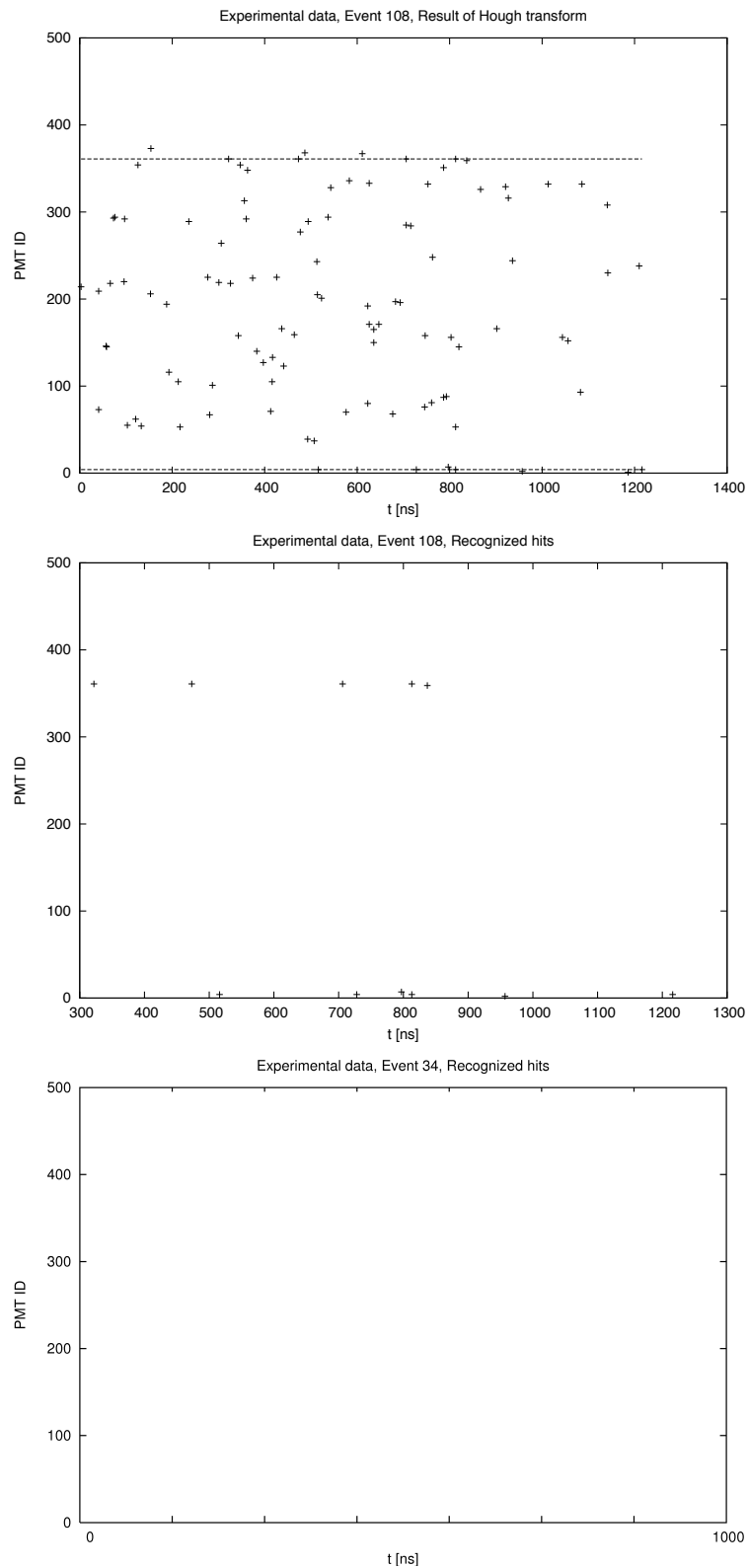


Figure C.9: Raw data (top) and Hough Transform (mid) results of event 106 of run 27955 (recorded on 29.05.2007). The ANTARES trigger did not detect the event

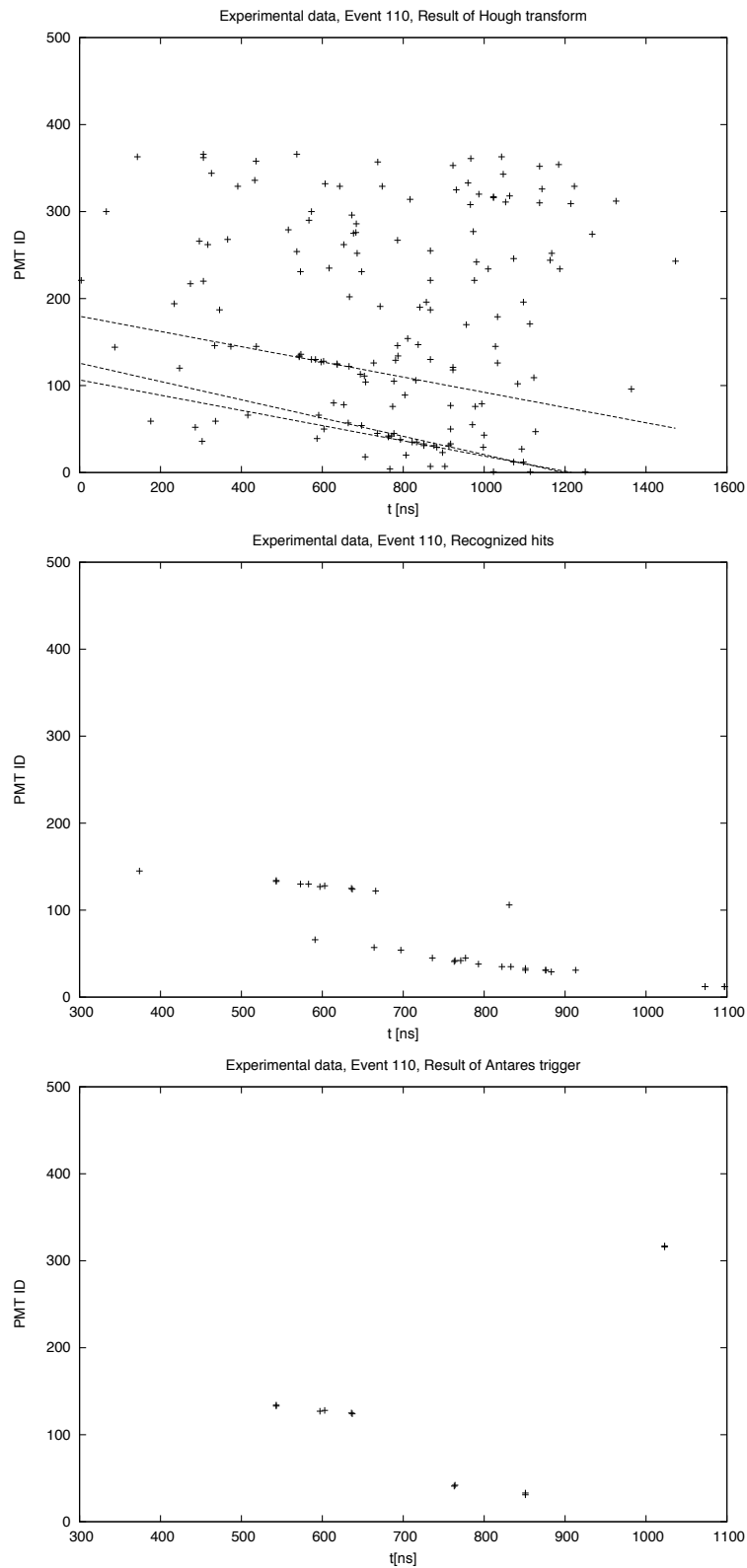


Figure C.10: Raw data (top), Hough Transform (mid) and ANTARES trigger (bottom) results of event 110 of run 27955 (recorded on 29.05.2007).

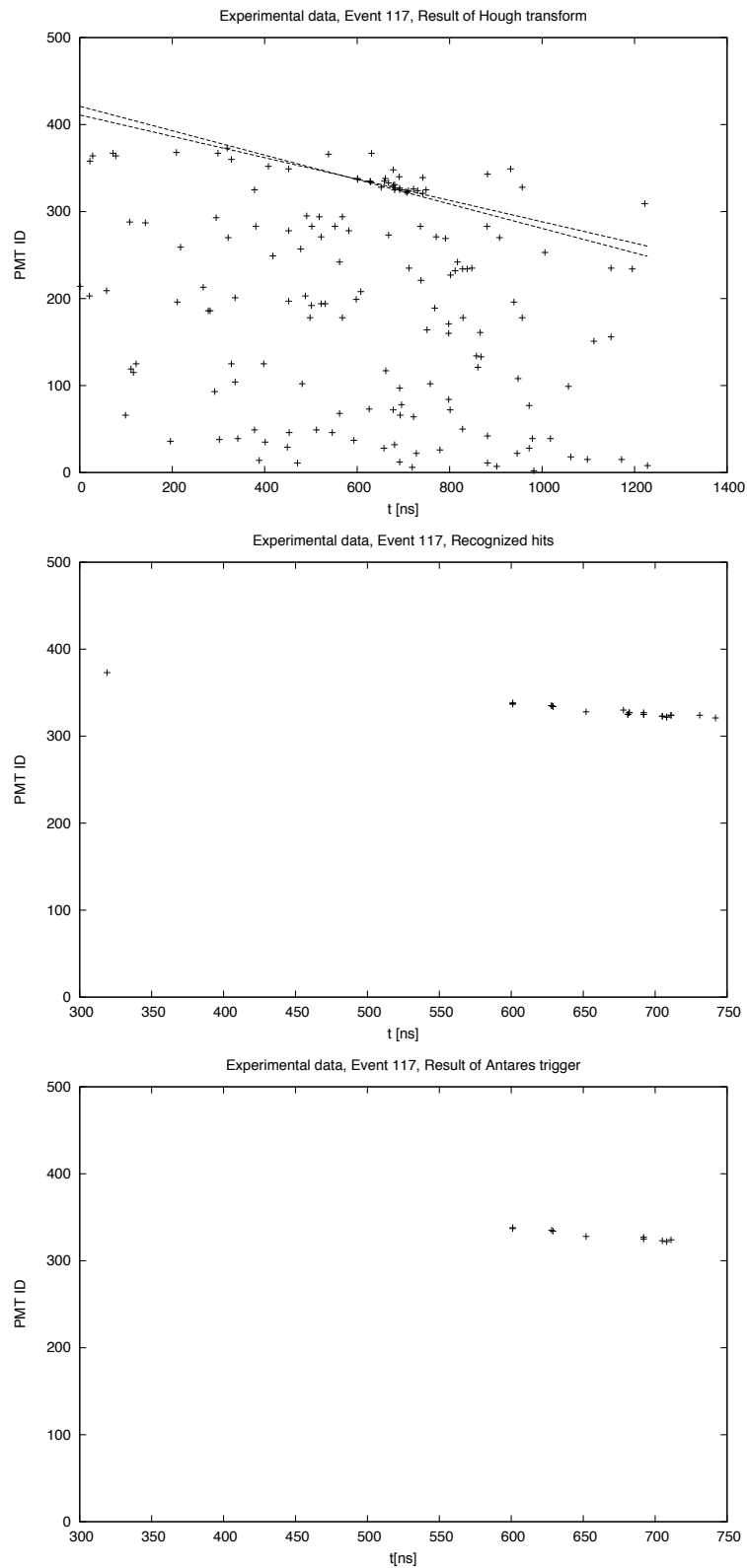


Figure C.11: *Raw data (top), Hough Transform (mid) and ANTARES trigger (bottom) results of event 117 of run 27955 (recorded on 29.05.2007).*

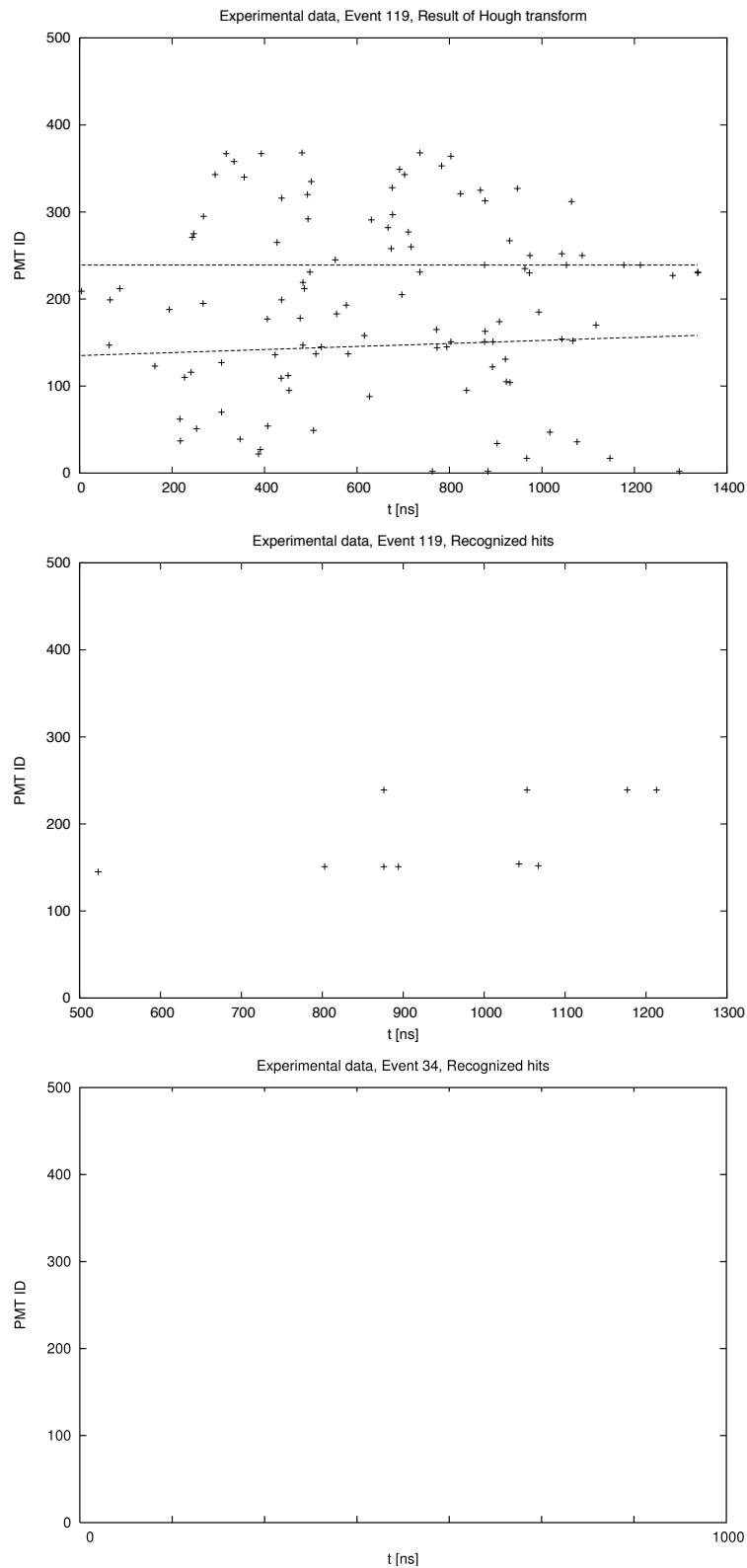


Figure C.12: Raw data (top) and Hough Transform (mid) results of event 119 of run 27955 (recorded on 29.05.2007). The ANTARES trigger did not detect the event

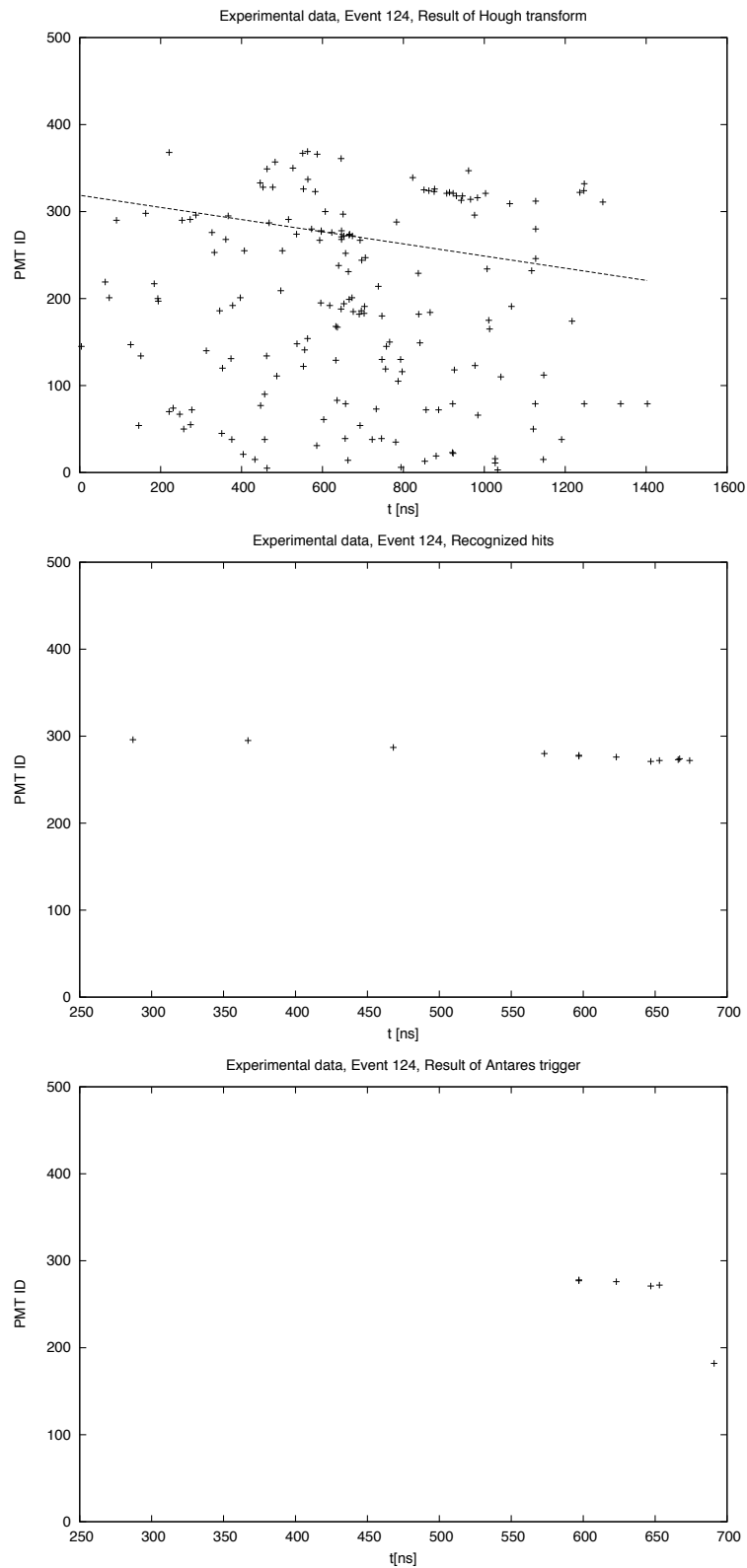


Figure C.13: *Raw data (top), Hough Transform (mid) and ANTARES trigger (bottom) results of event 124 of run 27955 (recorded on 29.05.2007).*

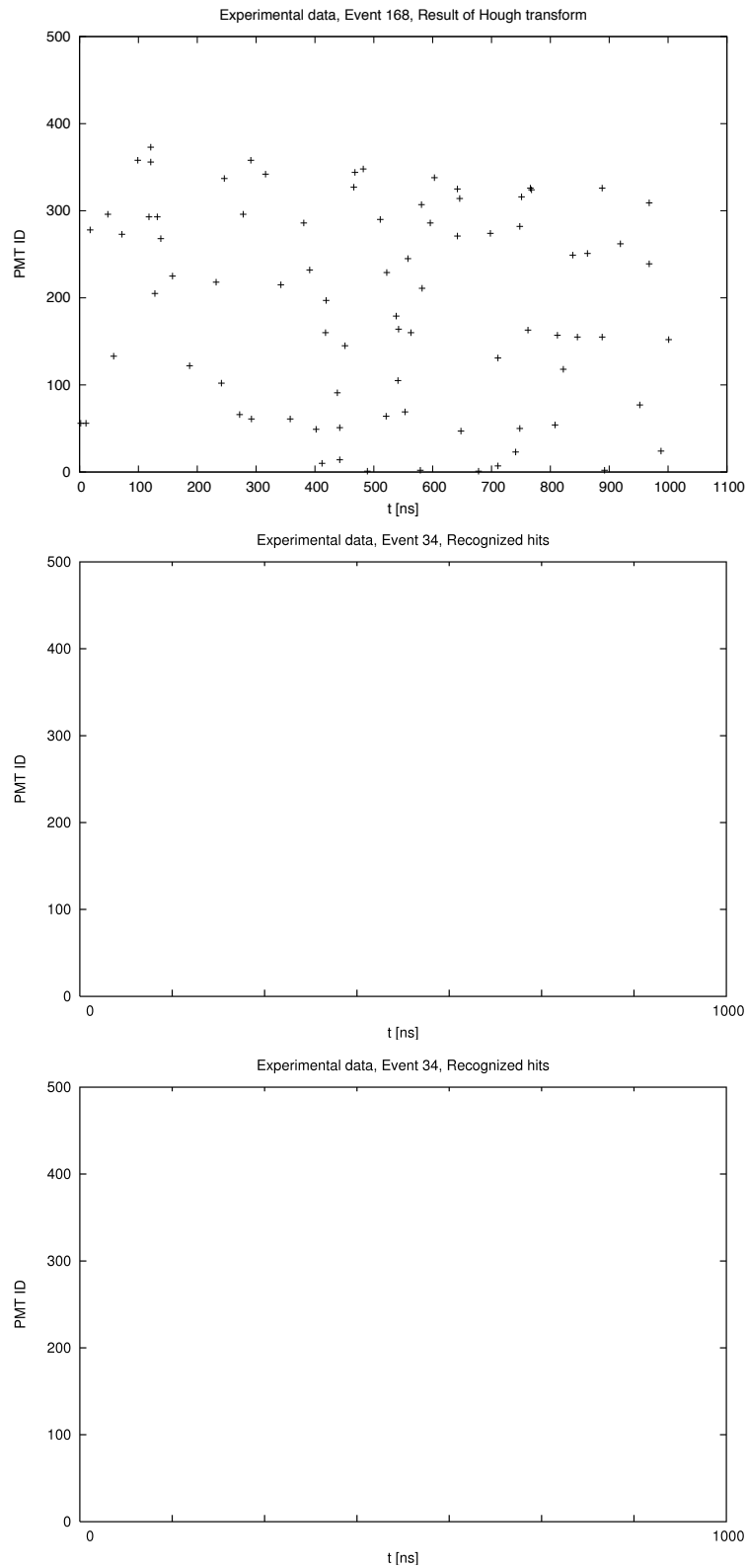


Figure C.14: Raw data of event 168 of run 27955 (recorded on 29.05.2007). Neither the standard trigger nor the the ANTARES trigger detected the event

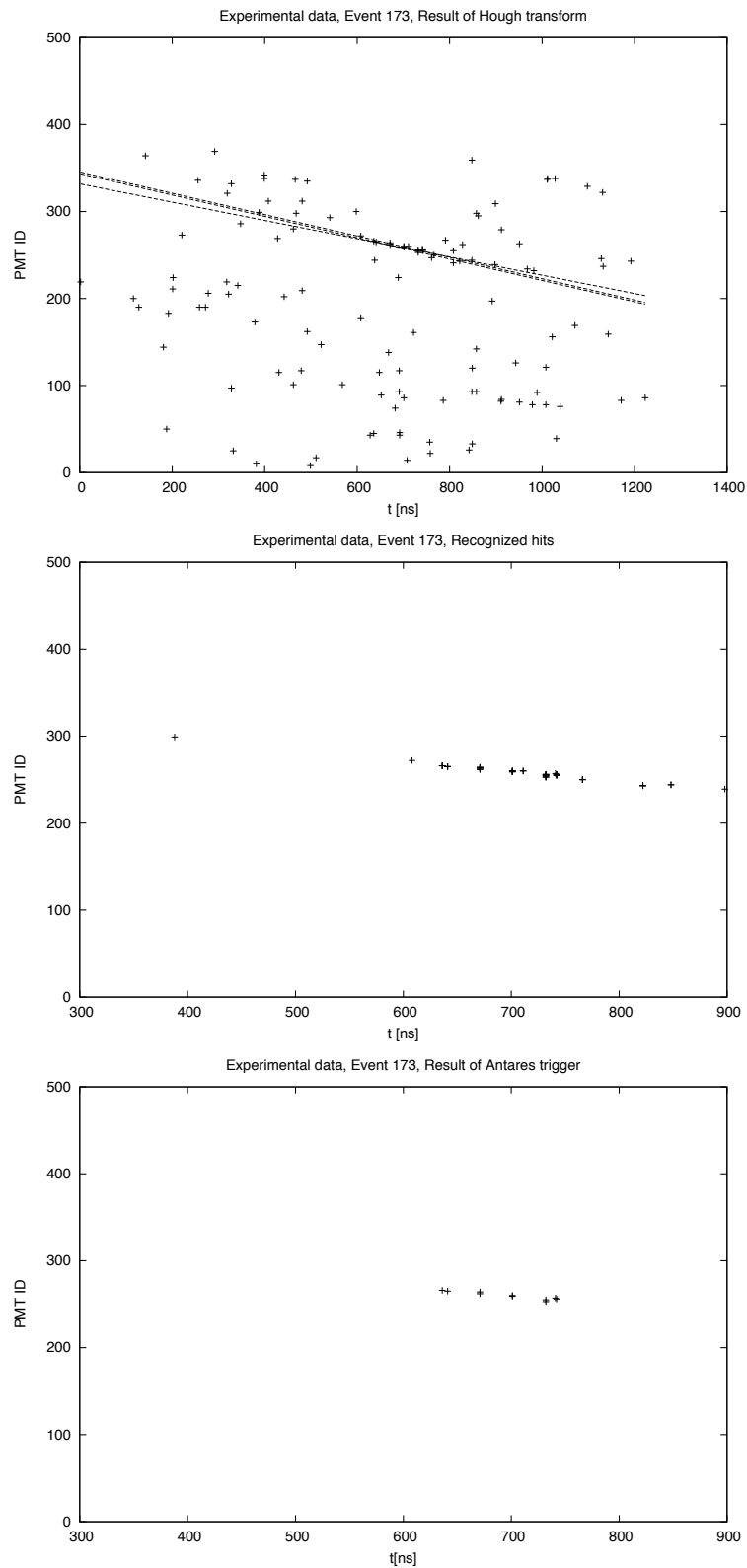


Figure C.15: *Raw data (top), Hough Transform (mid) and ANTARES trigger (bottom) results of event 173 of run 27955 (recorded on 29.05.2007).*

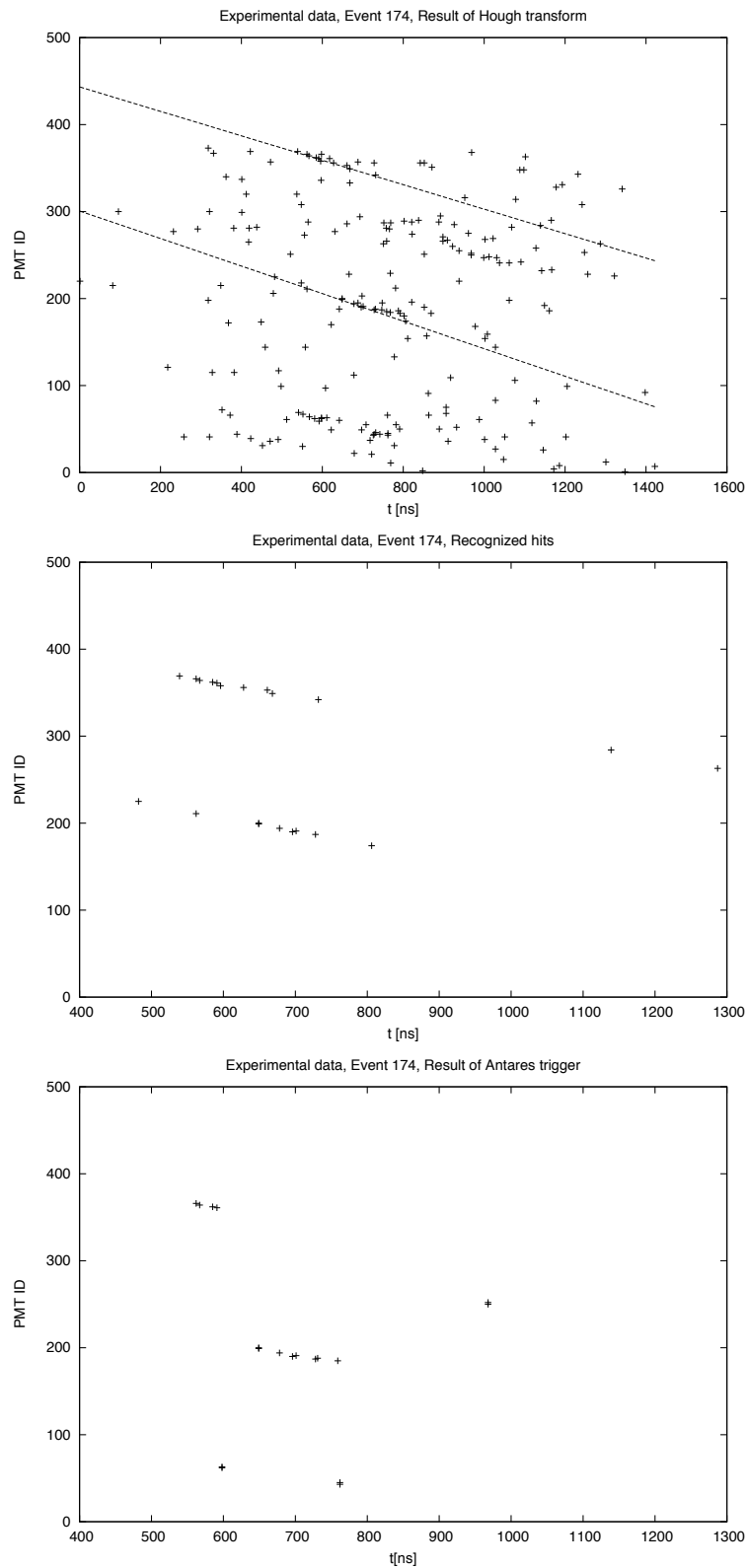


Figure C.16: Raw data (top), Hough Transform (mid) and ANTARES trigger (bottom) results of event 174 of run 27955 (recorded on 29.05.2007).

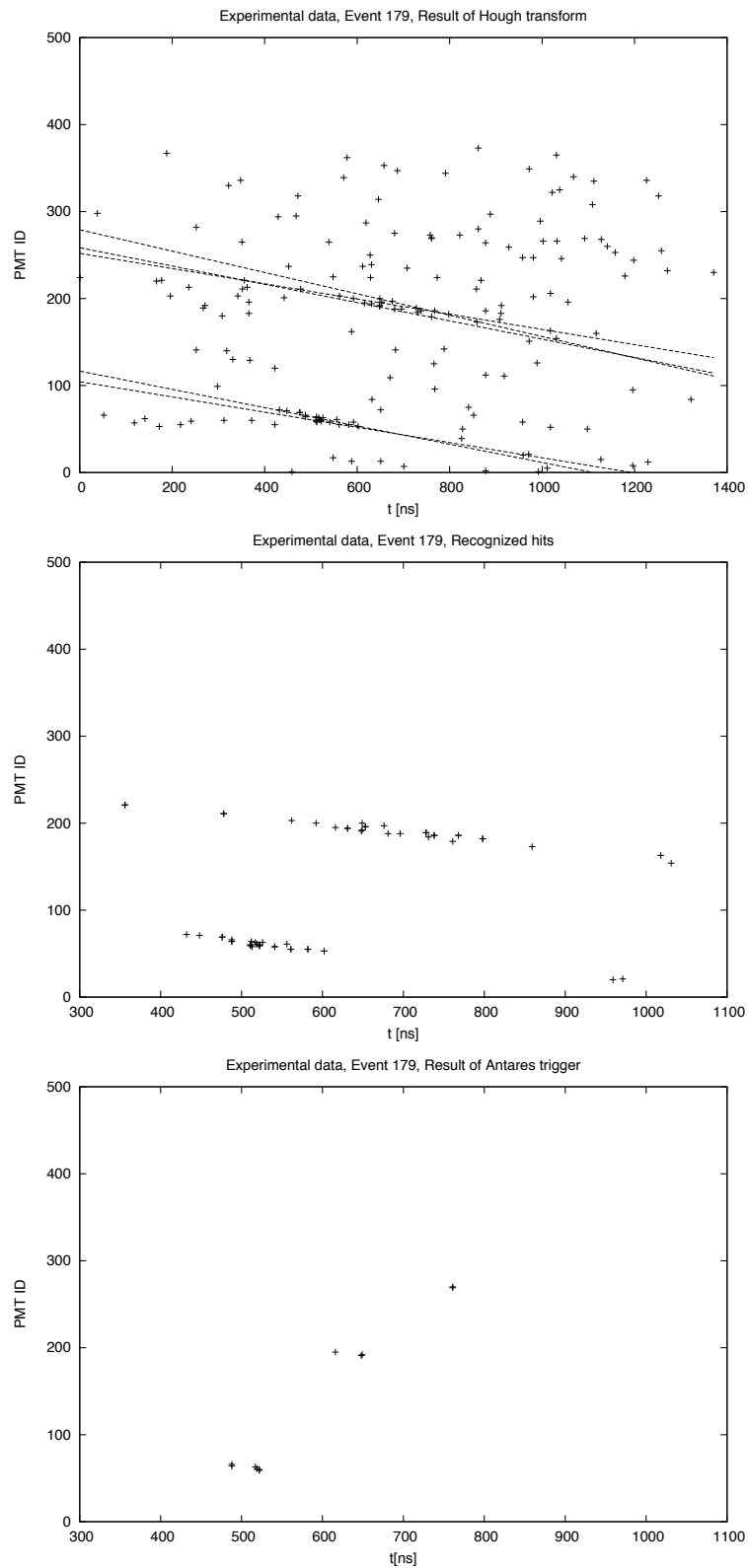


Figure C.17: Raw data (top), Hough Transform (mid) and ANTARES trigger (bottom) results of event 179 of run 27955 (recorded on 29.05.2007).

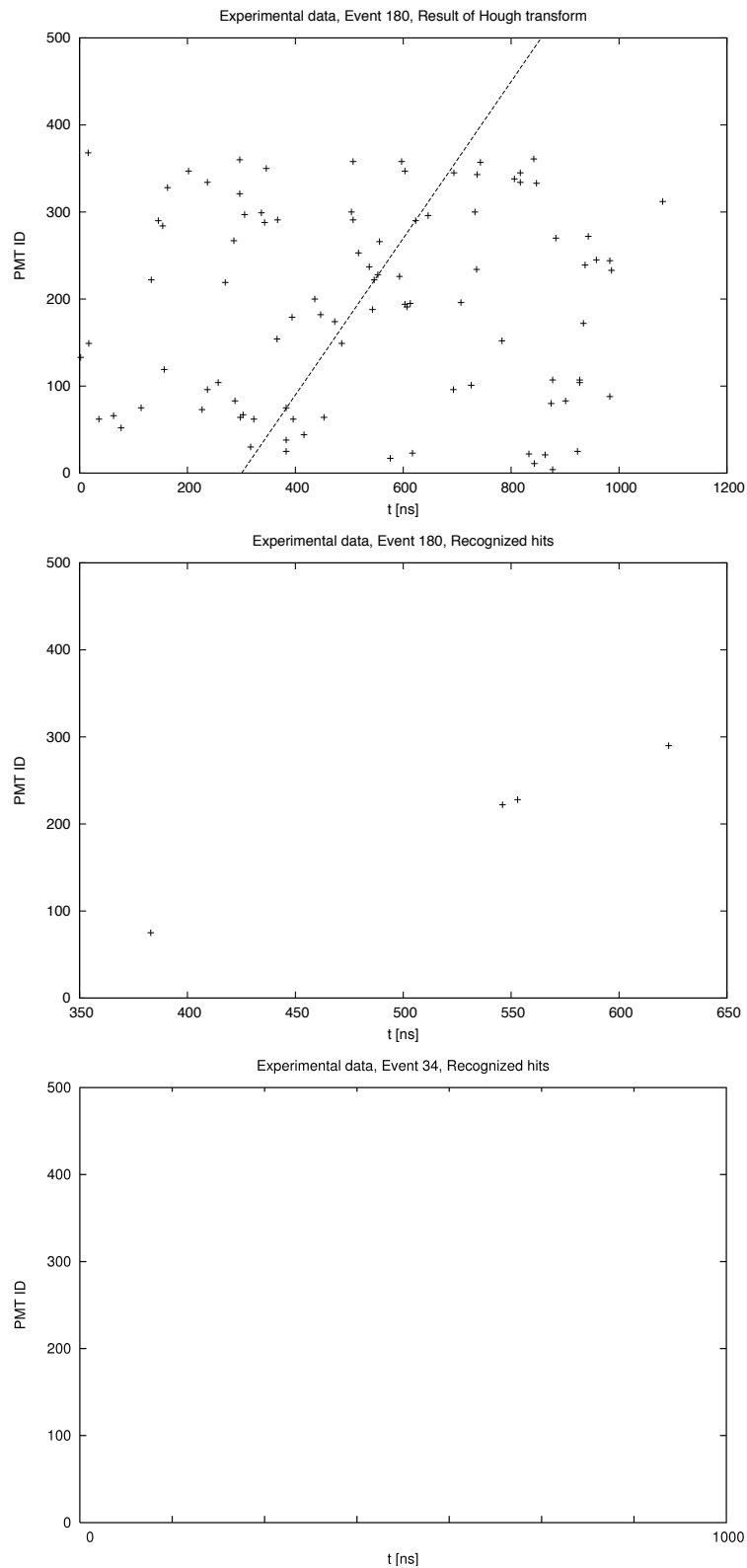


Figure C.18: Raw data (top) and Hough Transform (mid) results of event 180 of run 27955 (recorded on 29.05.2007). The ANTARES trigger did not detect the event.

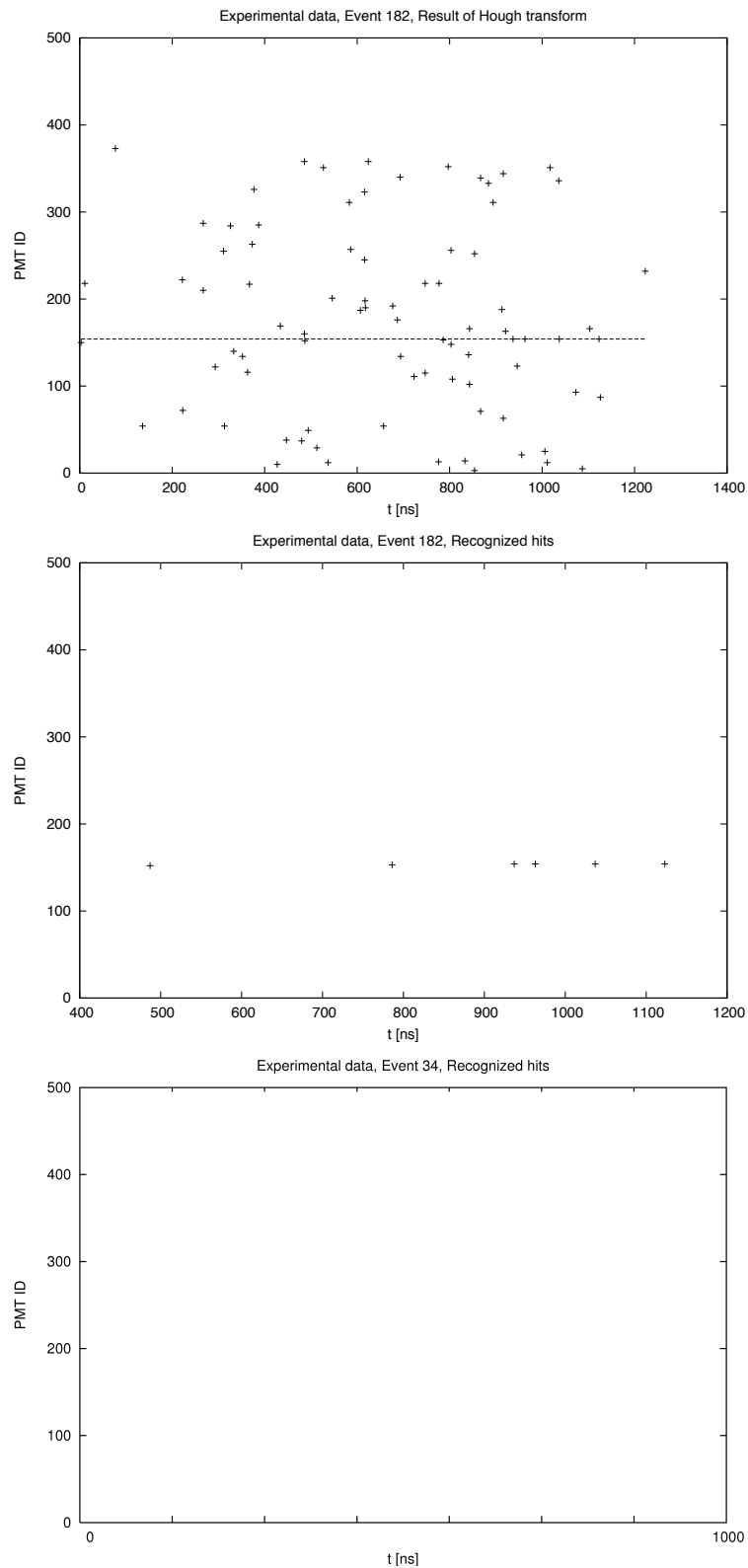


Figure C.19: Raw data (top) and Hough Transform (mid) results of event 182 of run 27955 (recorded on 29.05.2007). The ANTARES trigger did not detect the event.

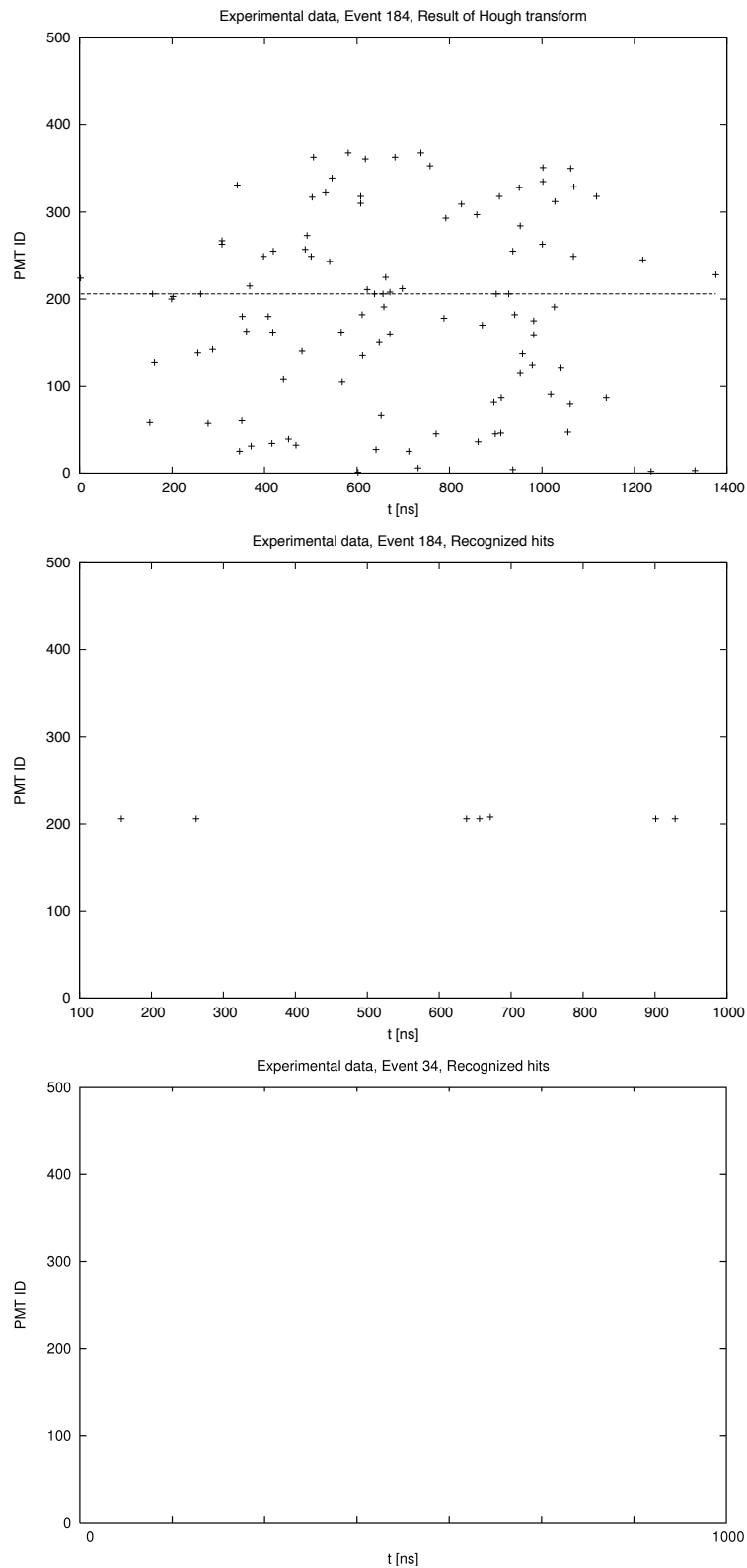


Figure C.20: Raw data (top) and Hough Transform (mid) results of event 184 of run 27955 (recorded on 29.05.2007). The ANTARES trigger did not detect the event.

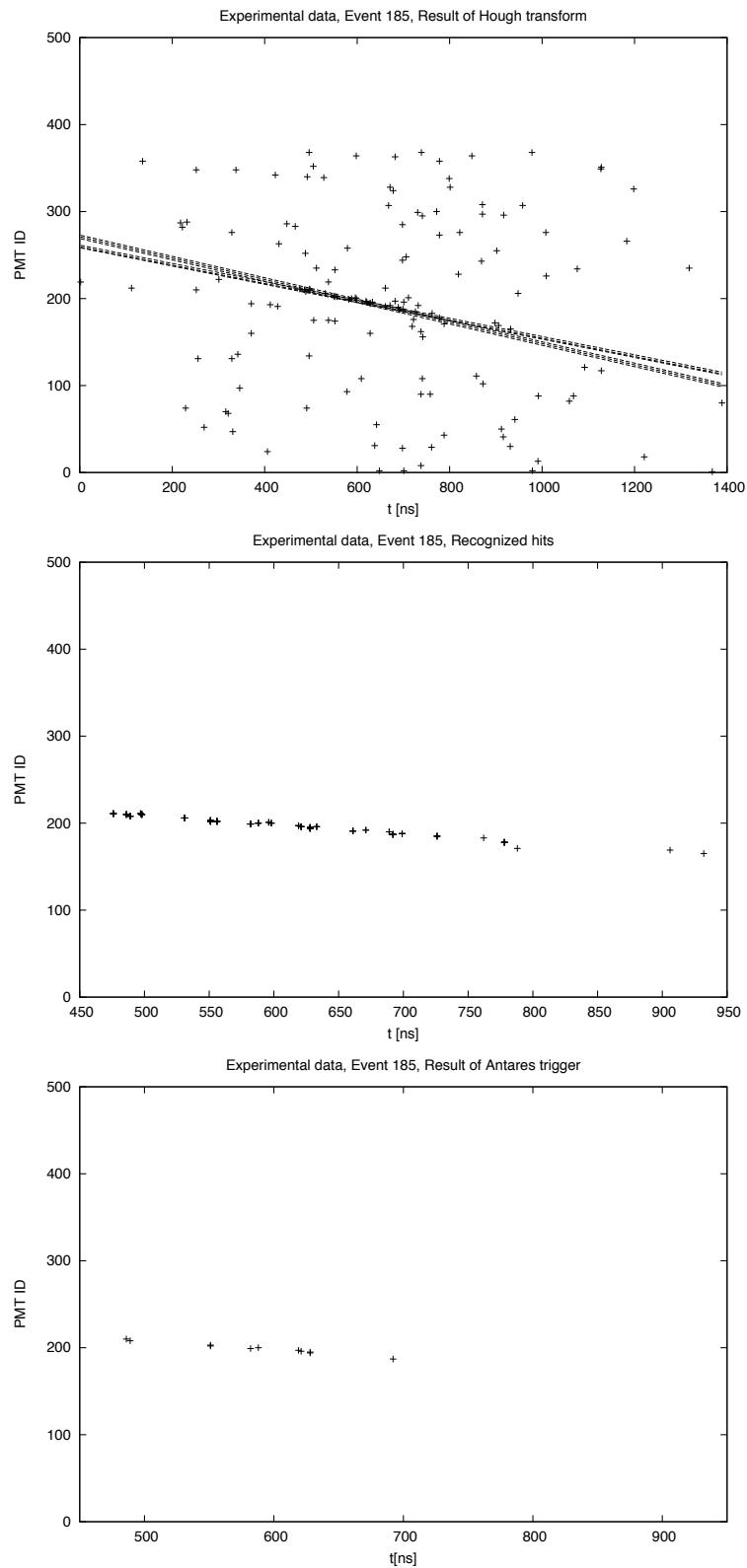


Figure C.21: *Raw data (top), Hough Transform (mid) and ANTARES trigger (bottom) results of event 185 of run 27955 (recorded on 29.05.2007).*

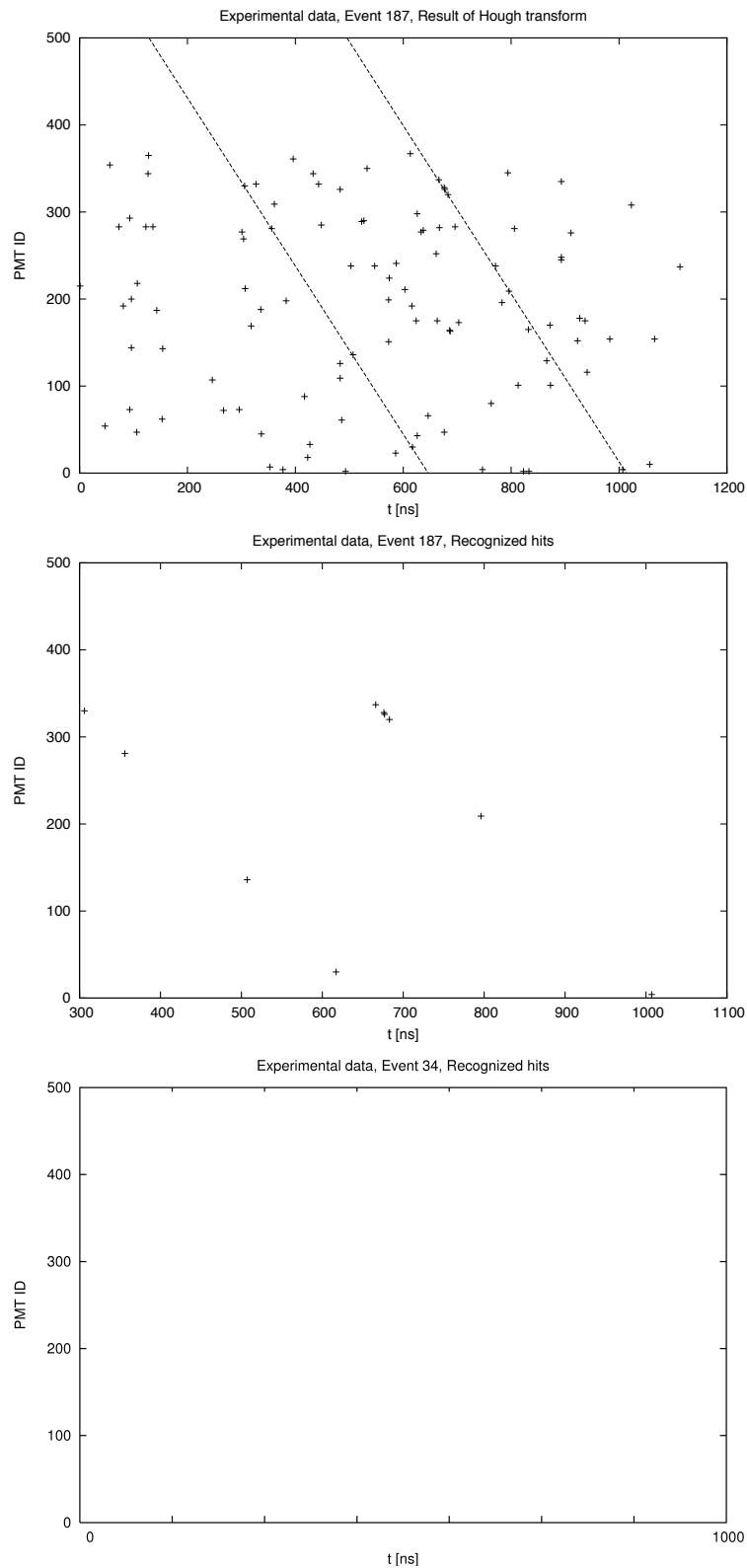


Figure C.22: Raw data (top) and Hough Transform (mid) results of event 187 of run 27955 (recorded on 29.05.2007). The ANTARES trigger did not detect the event.

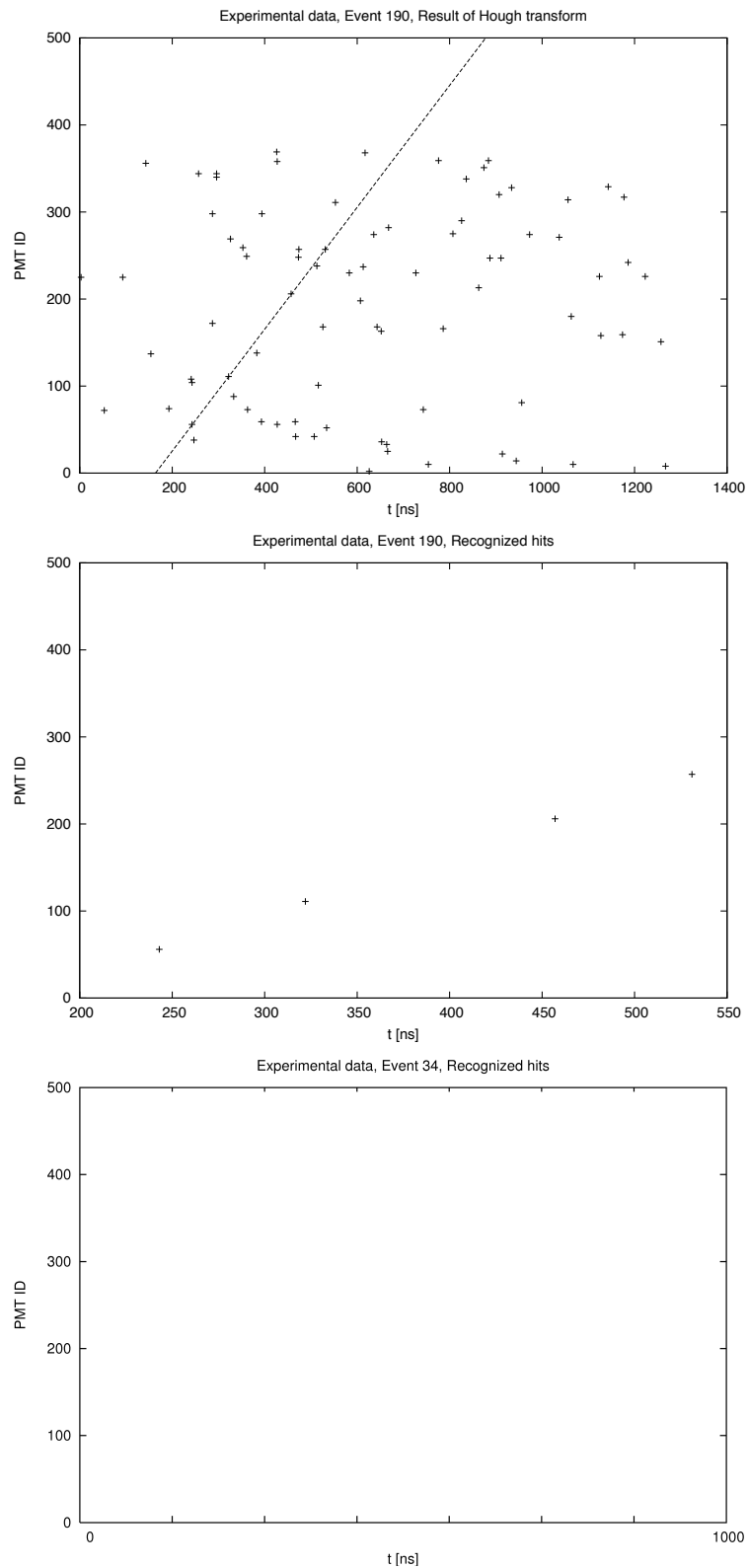


Figure C.23: Raw data (top) and Hough Transform (mid) results of event 190 of run 27955 (recorded on 29.05.2007). The ANTARES trigger did not detect the event.

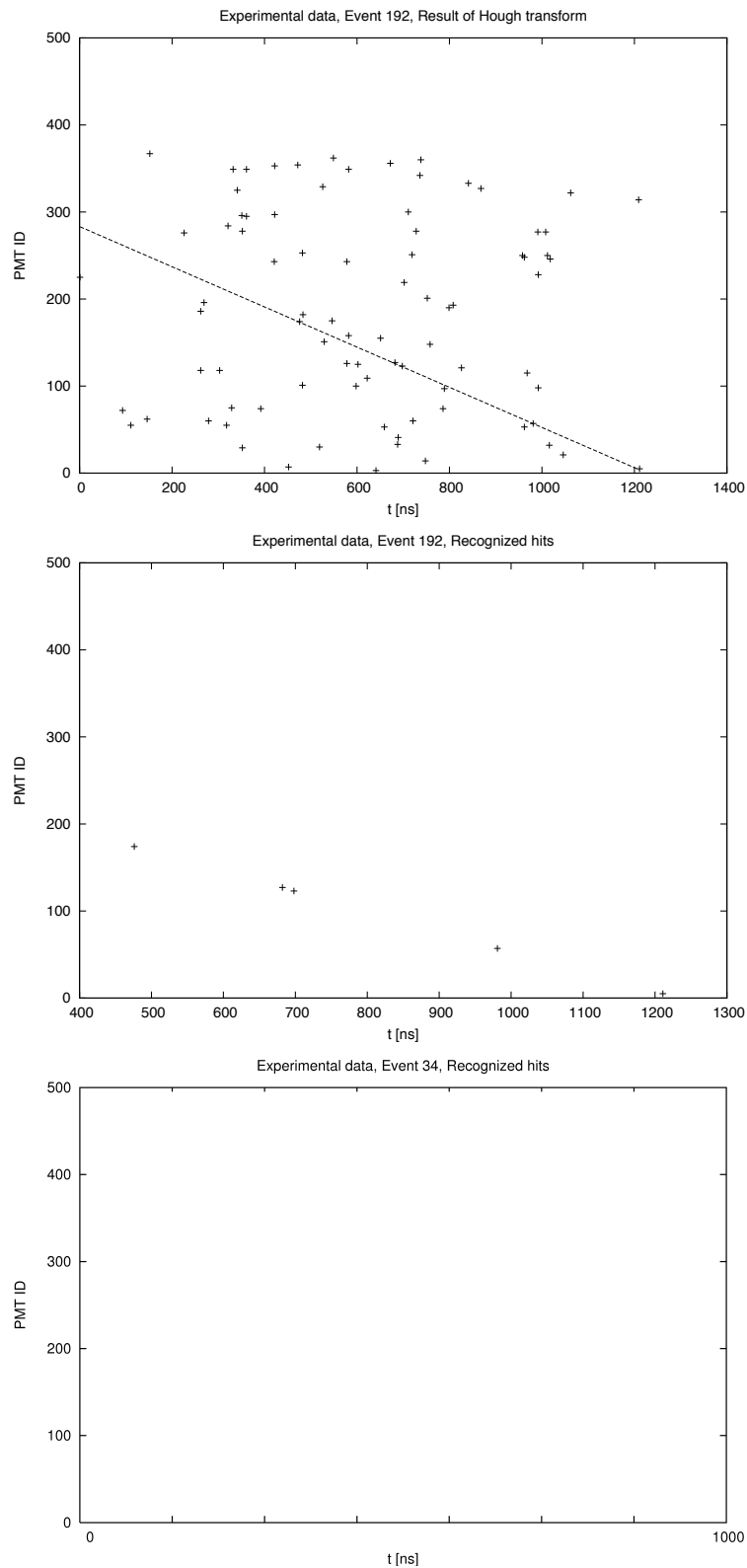


Figure C.24: Raw data (top) and Hough Transform (mid) results of event 192 of run 27955 (recorded on 29.05.2007). The ANTARES trigger did not detect the event.

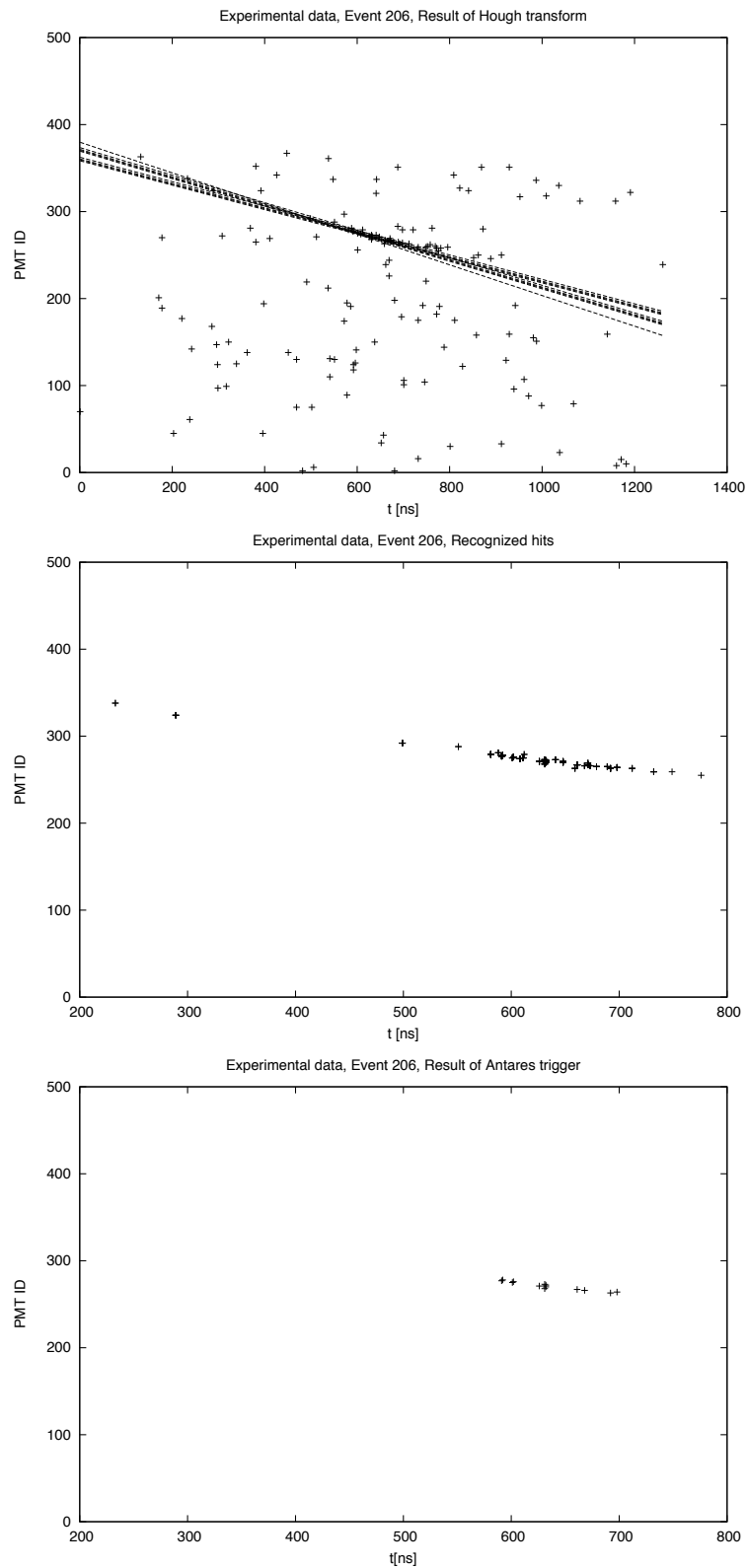


Figure C.25: Raw data (top), Hough Transform (mid) and ANTARES trigger (bottom) results of event 206 of run 27955 (recorded on 29.05.2007).

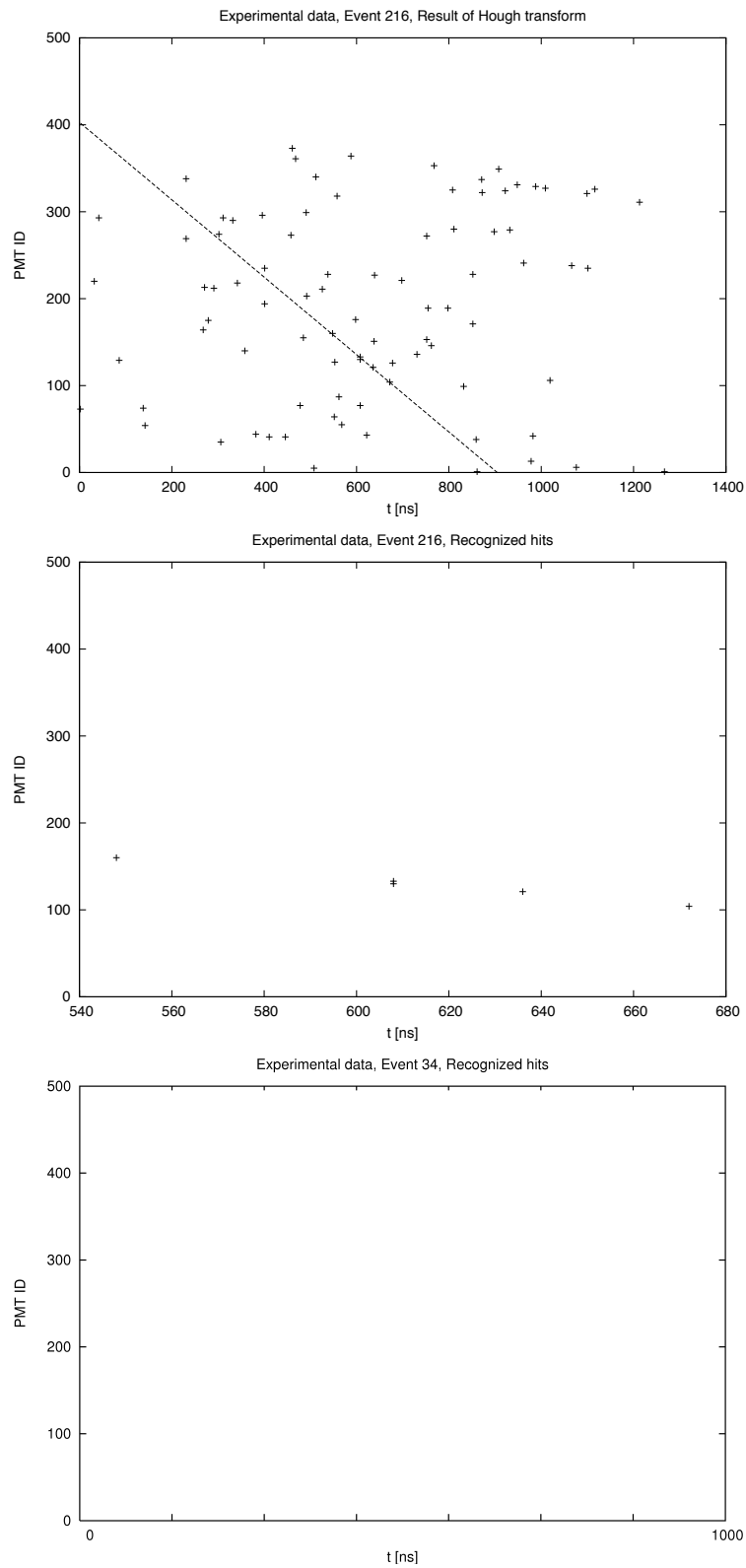


Figure C.26: Raw data (top) and Hough Transform (mid) results of event 216 of run 27955 (recorded on 29.05.2007). The ANTARES trigger did not detect the event.

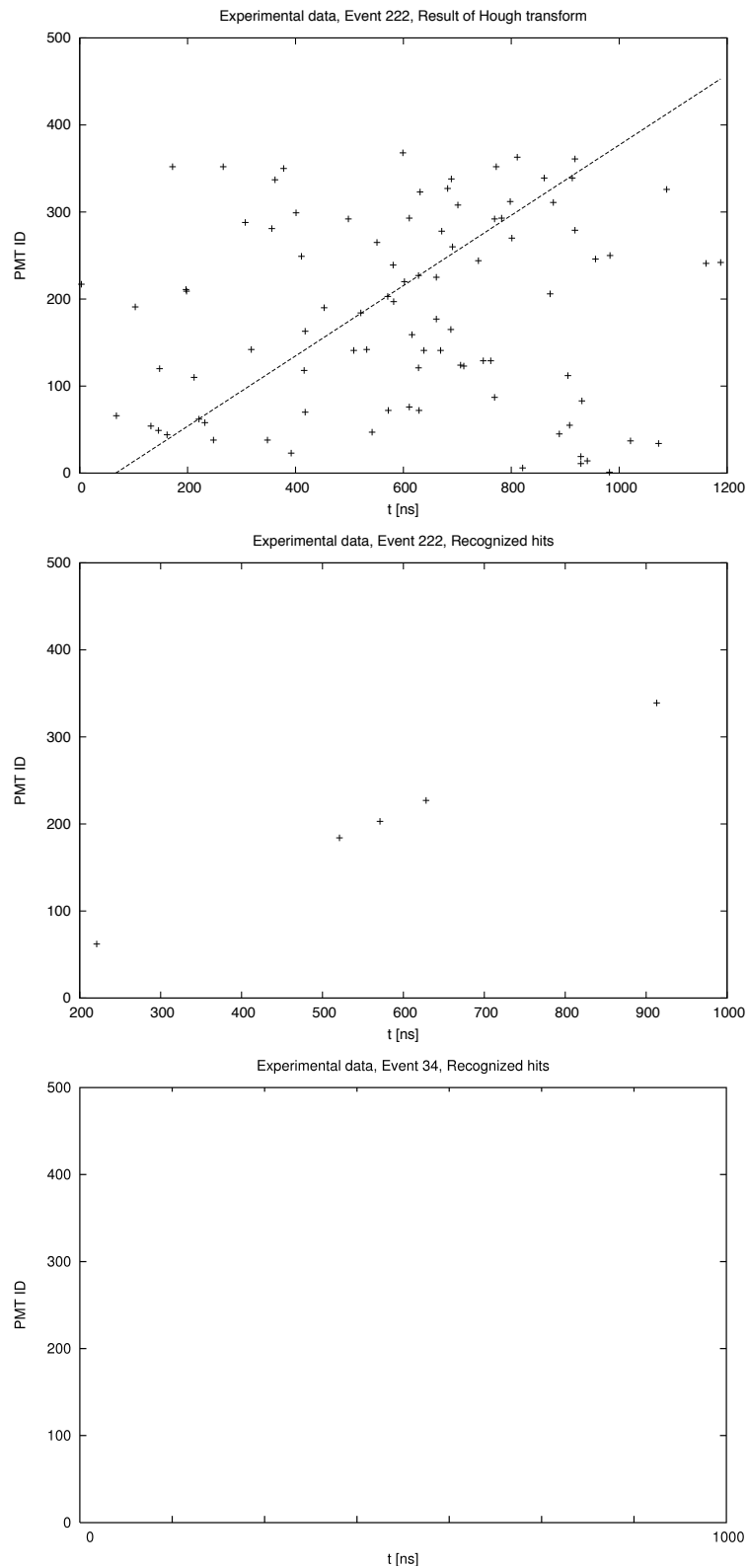


Figure C.27: Raw data (top) and Hough Transform (mid) results of event 222 of run 27955 (recorded on 29.05.2007). The ANTARES trigger did not detect the event.

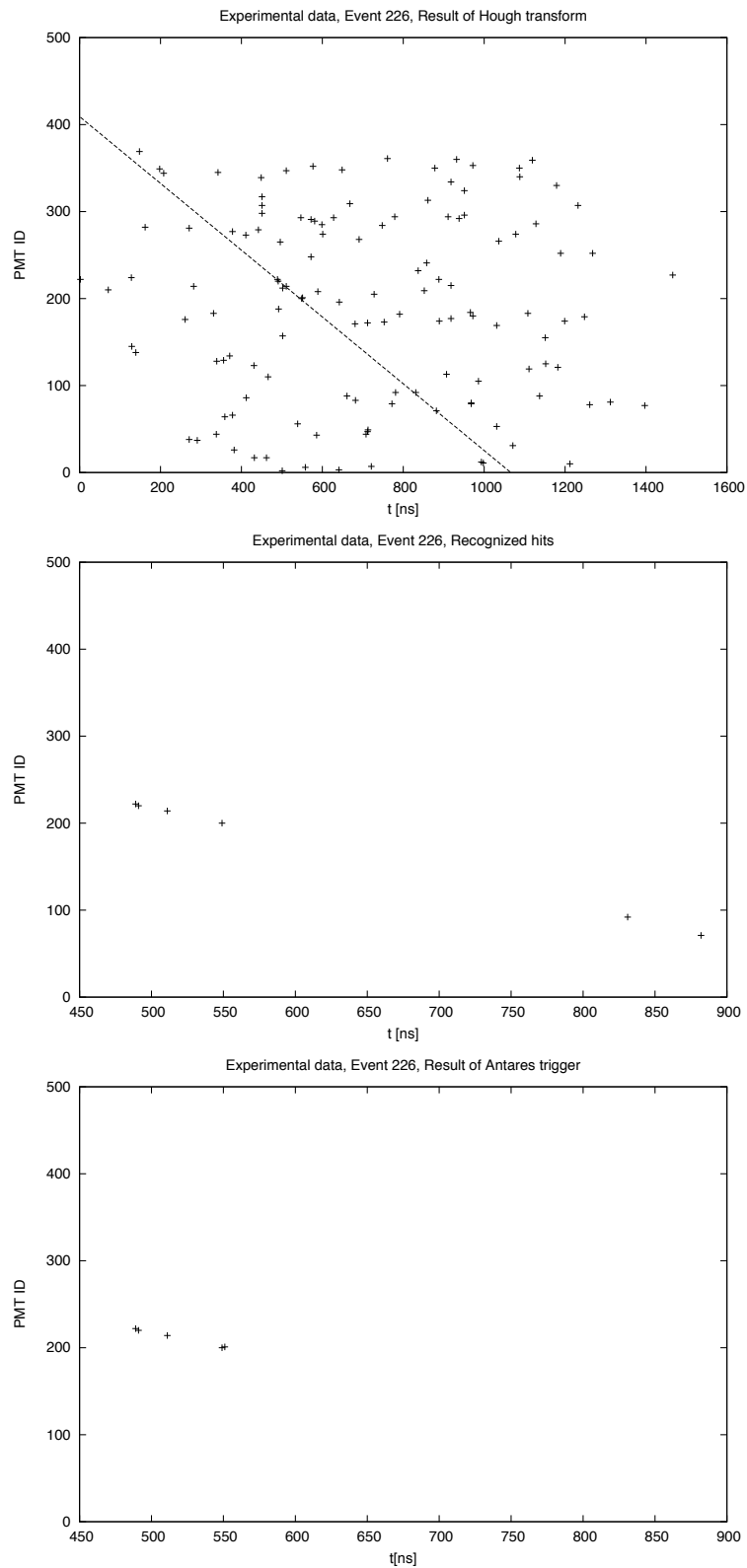


Figure C.28: Raw data (top), Hough Transform (mid) and ANTARES trigger (bottom) results of event 226 of run 27955 (recorded on 29.05.2007).

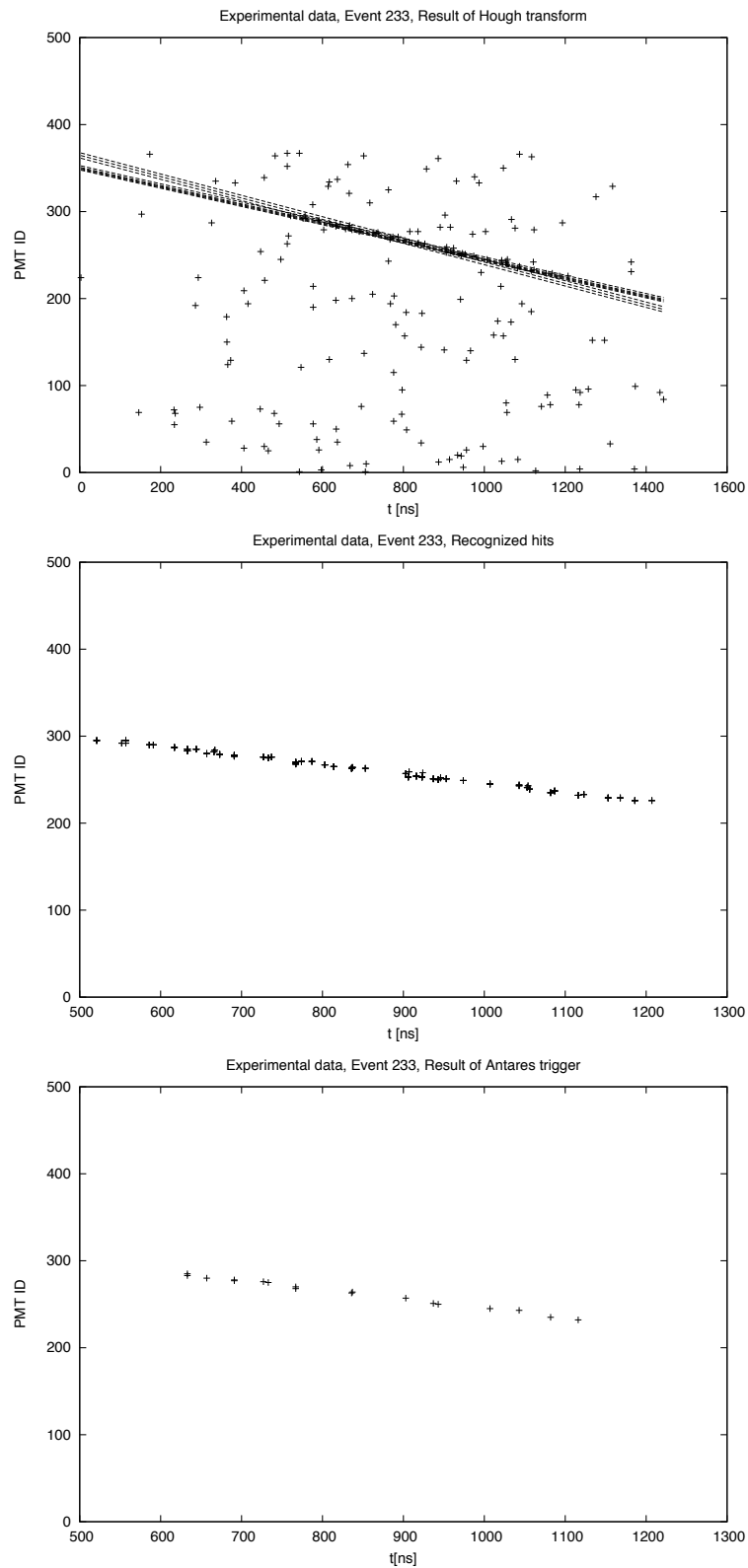


Figure C.29: Raw data (top), Hough Transform (mid) and ANTARES trigger (bottom) results of event 233 of run 27955 (recorded on 29.05.2007).

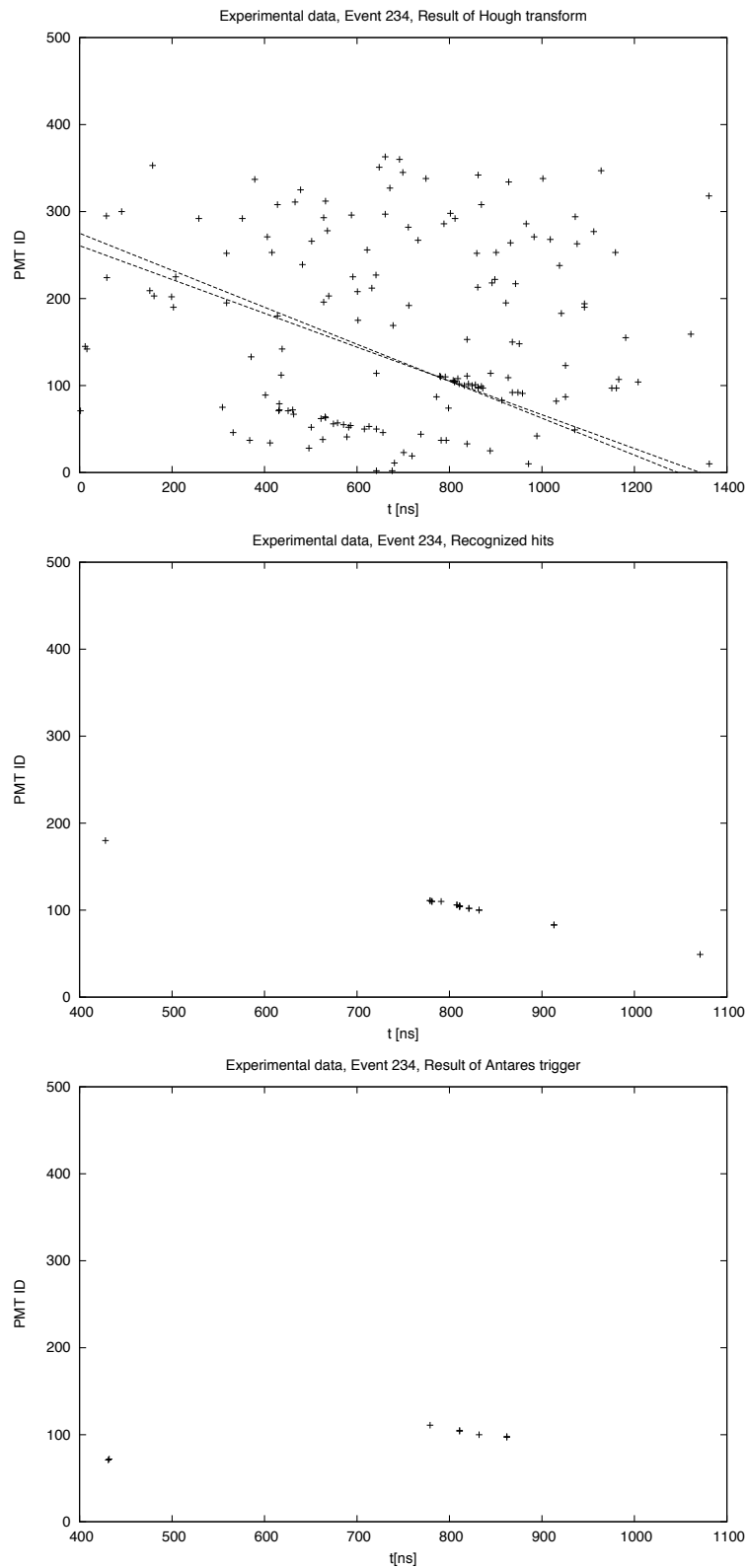


Figure C.30: Raw data (top), Hough Transform (mid) and ANTARES trigger (bottom) results of event 234 of run 27955 (recorded on 29.05.2007).

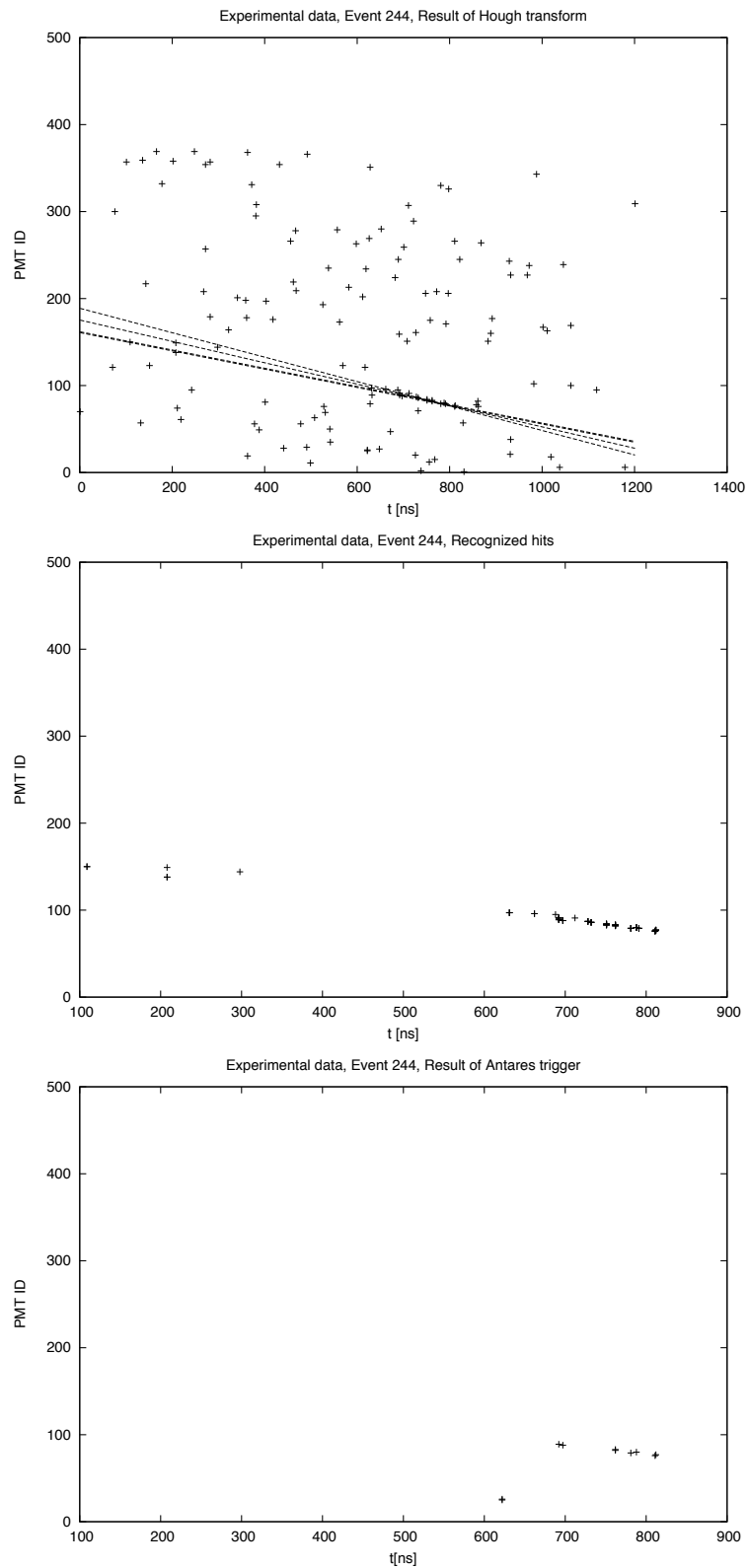


Figure C.31: *Raw data (top), Hough Transform (mid) and ANTARES trigger (bottom) results of event 244 of run 27955 (recorded on 29.05.2007).*

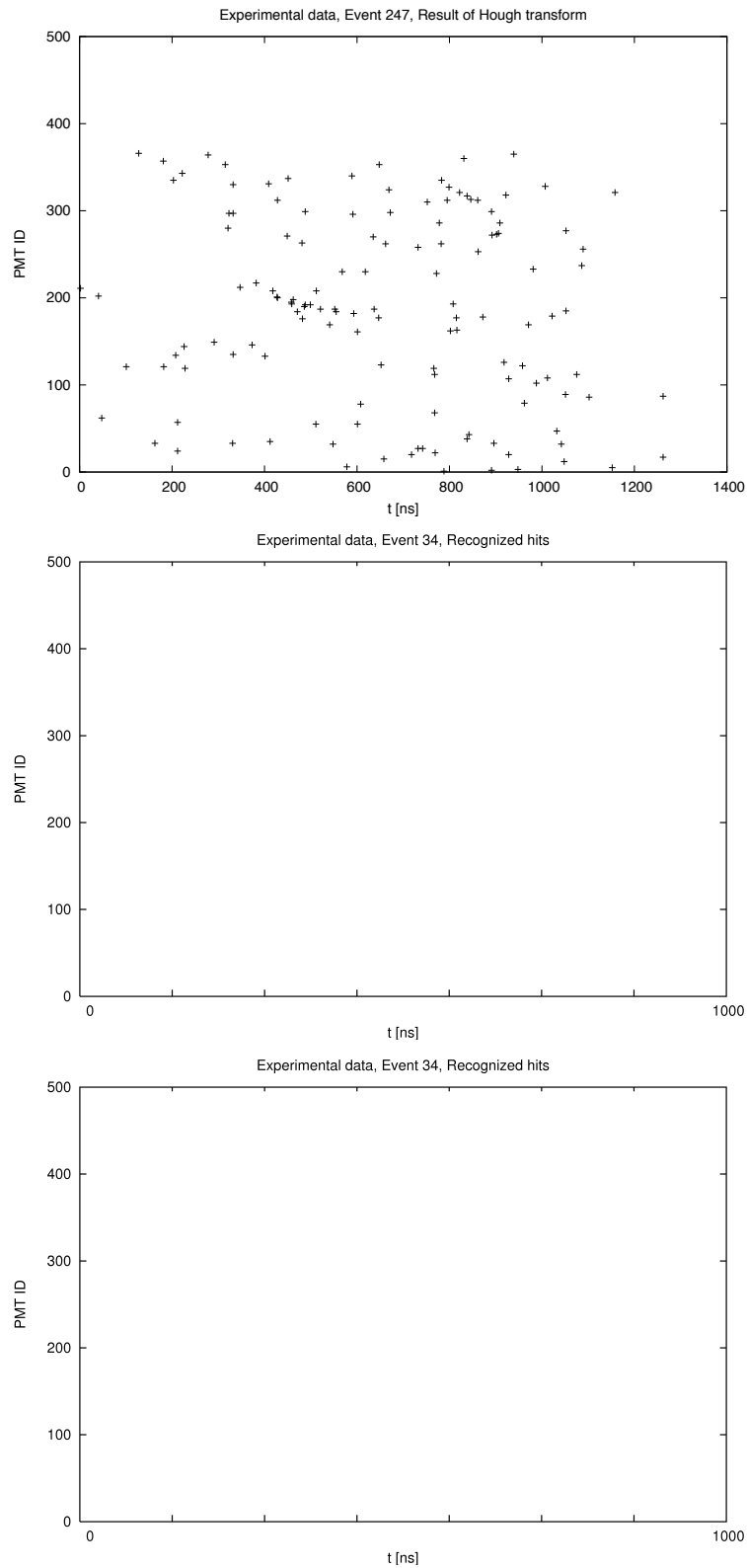


Figure C.32: Raw data of event 247 of run 27955 (recorded on 29.05.2007). Neither the standard trigger nor the the ANTARES trigger detected the event

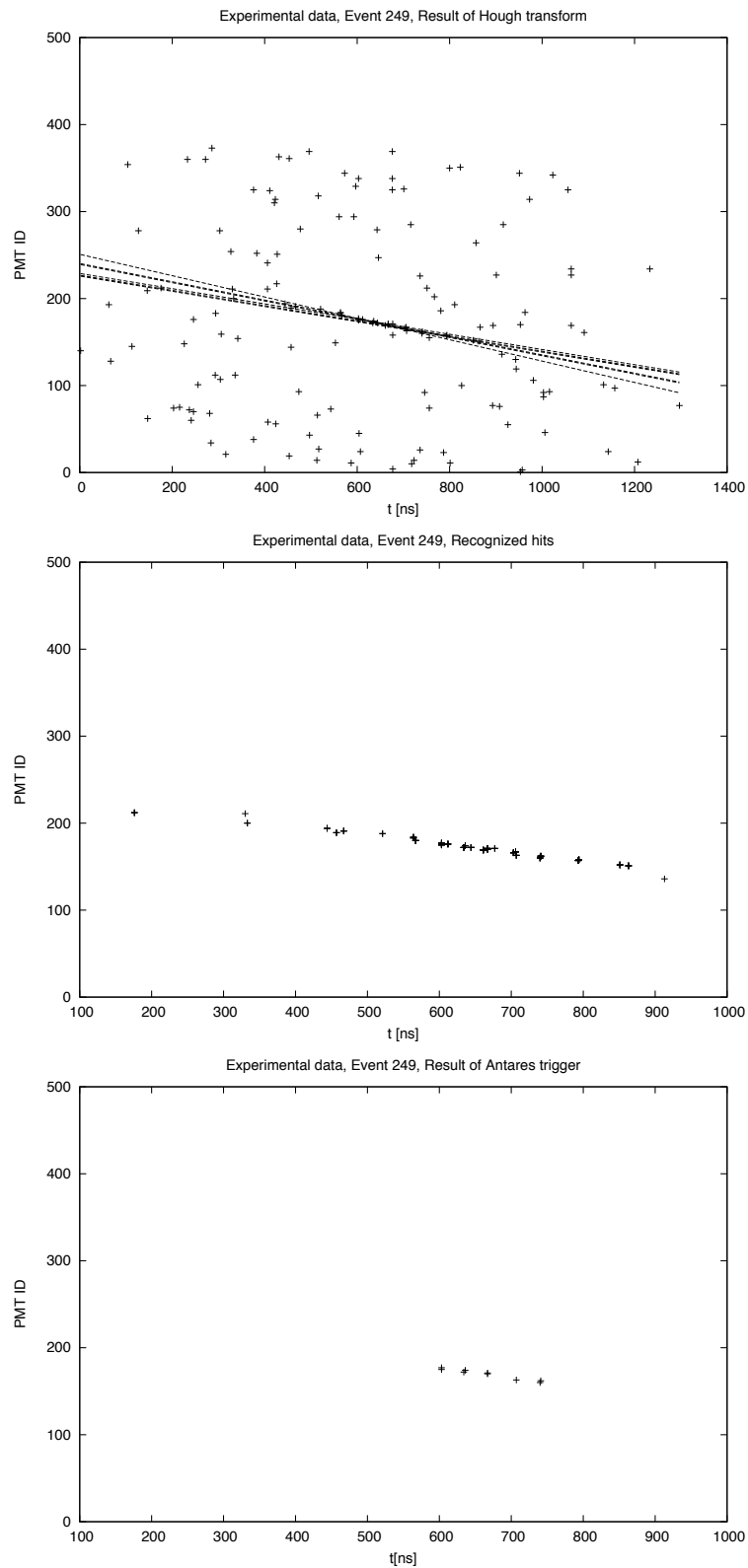


Figure C.33: Raw data (top), Hough Transform (mid) and ANTARES trigger (bottom) results of event 249 of run 27955 (recorded on 29.05.2007).

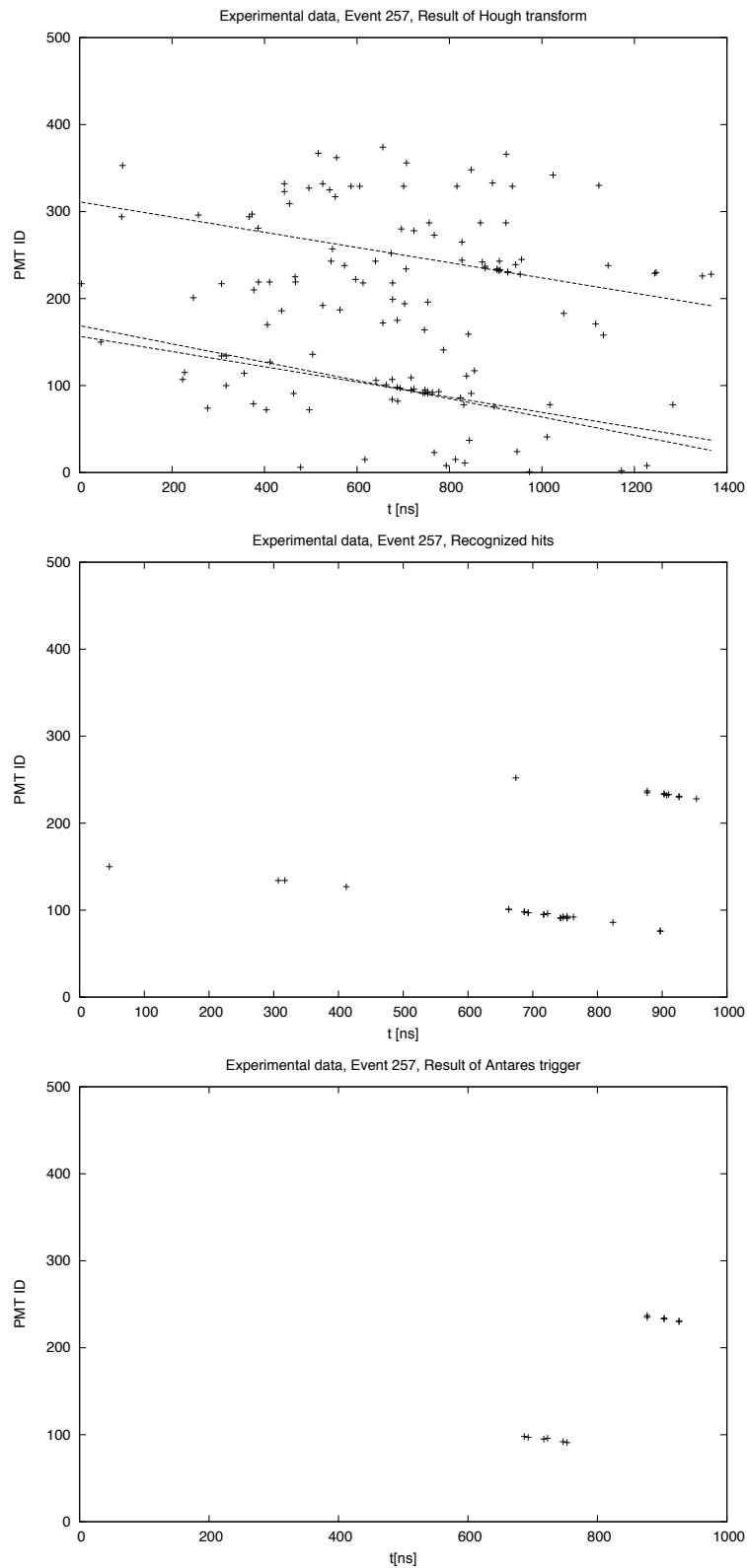


Figure C.34: Raw data (top), Hough Transform (mid) and ANTARES trigger (bottom) results of event 257 of run 27955 (recorded on 29.05.2007).

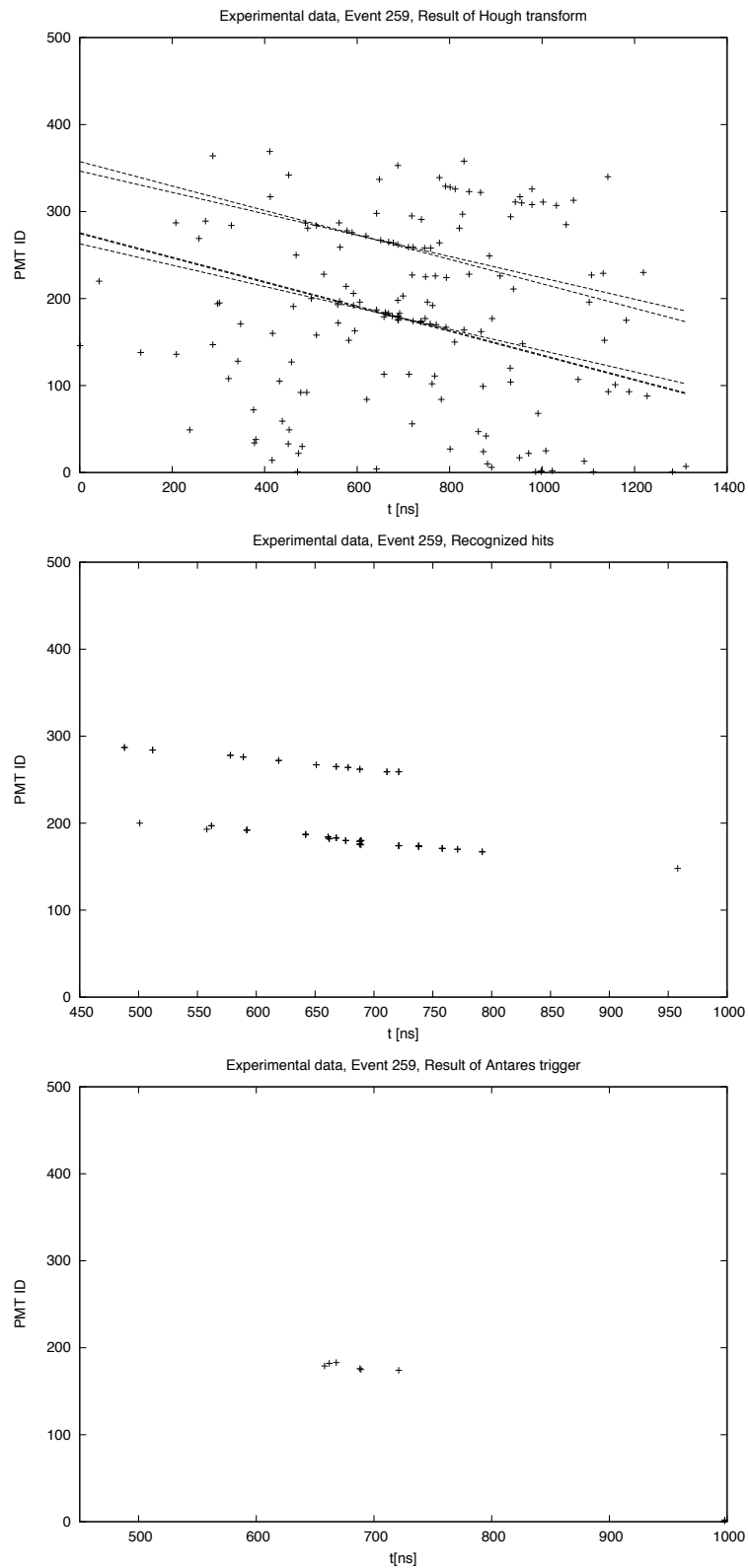


Figure C.35: Raw data (top), Hough Transform (mid) and ANTARES trigger (bottom) results of event 259 of run 27955 (recorded on 29.05.2007).

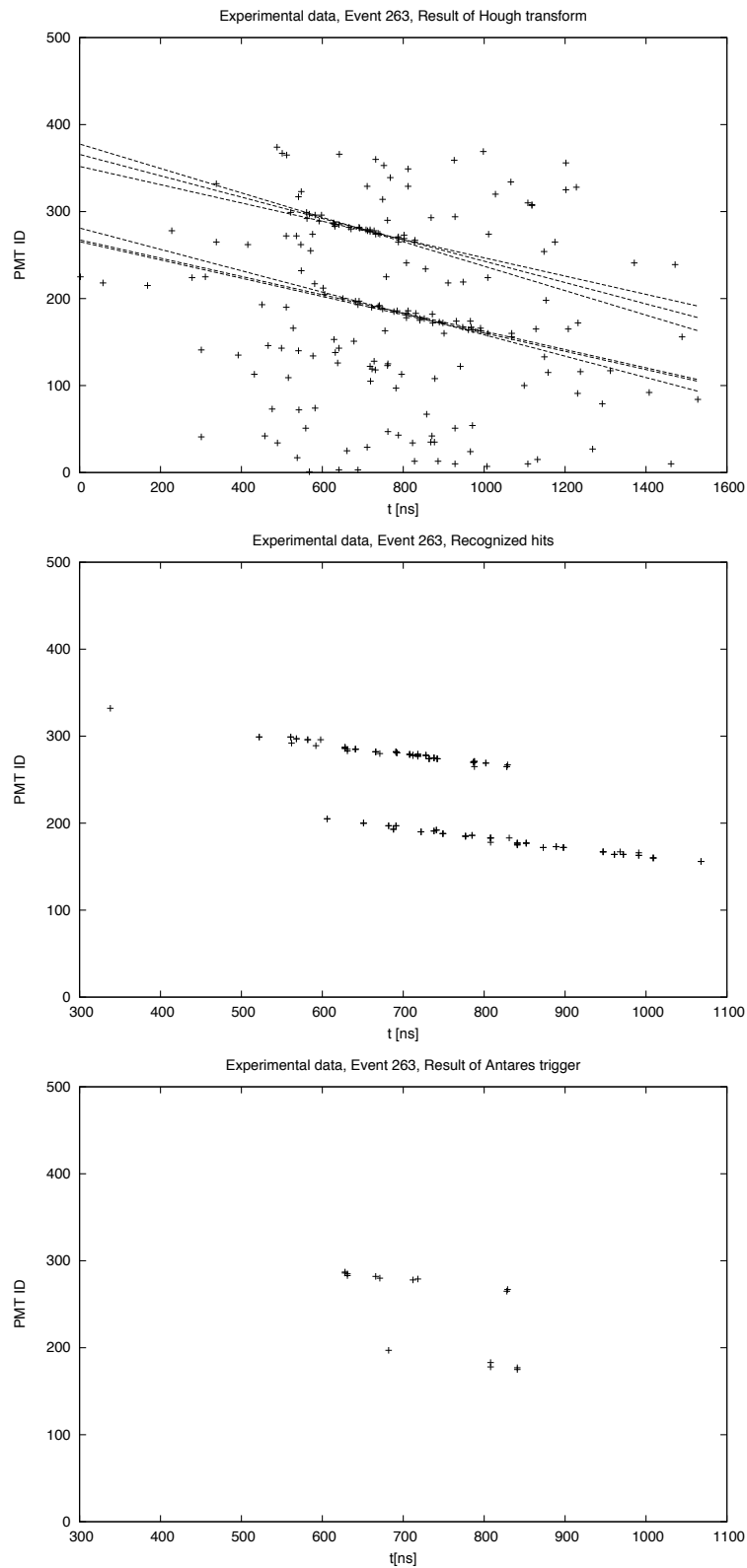


Figure C.36: Raw data (top), Hough Transform (mid) and ANTARES trigger (bottom) results of event 263 of run 27955 (recorded on 29.05.2007).

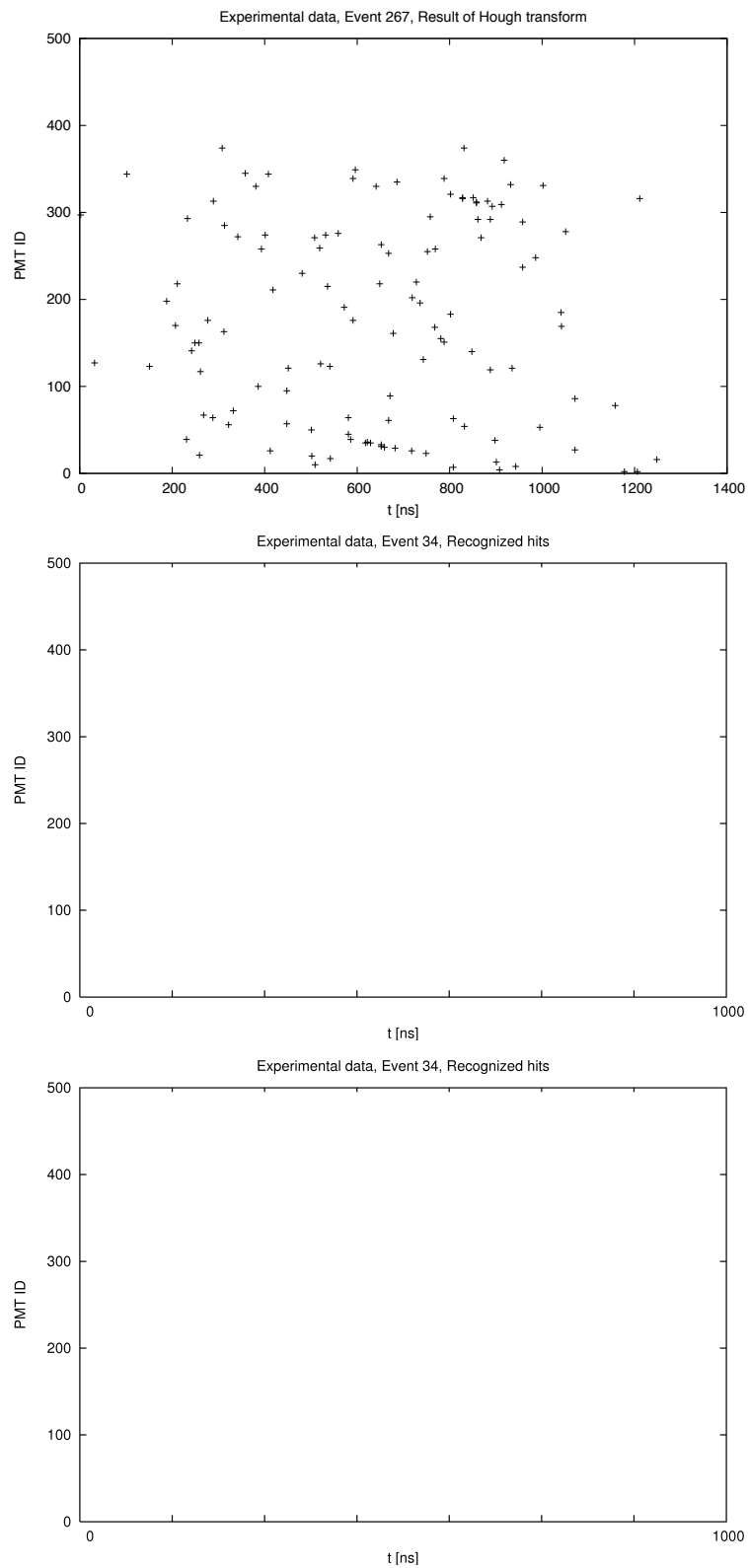


Figure C.37: Raw data of event 267 of run 27955 (recorded on 29.05.2007). Neither the standard trigger nor the the ANTARES trigger detected the event

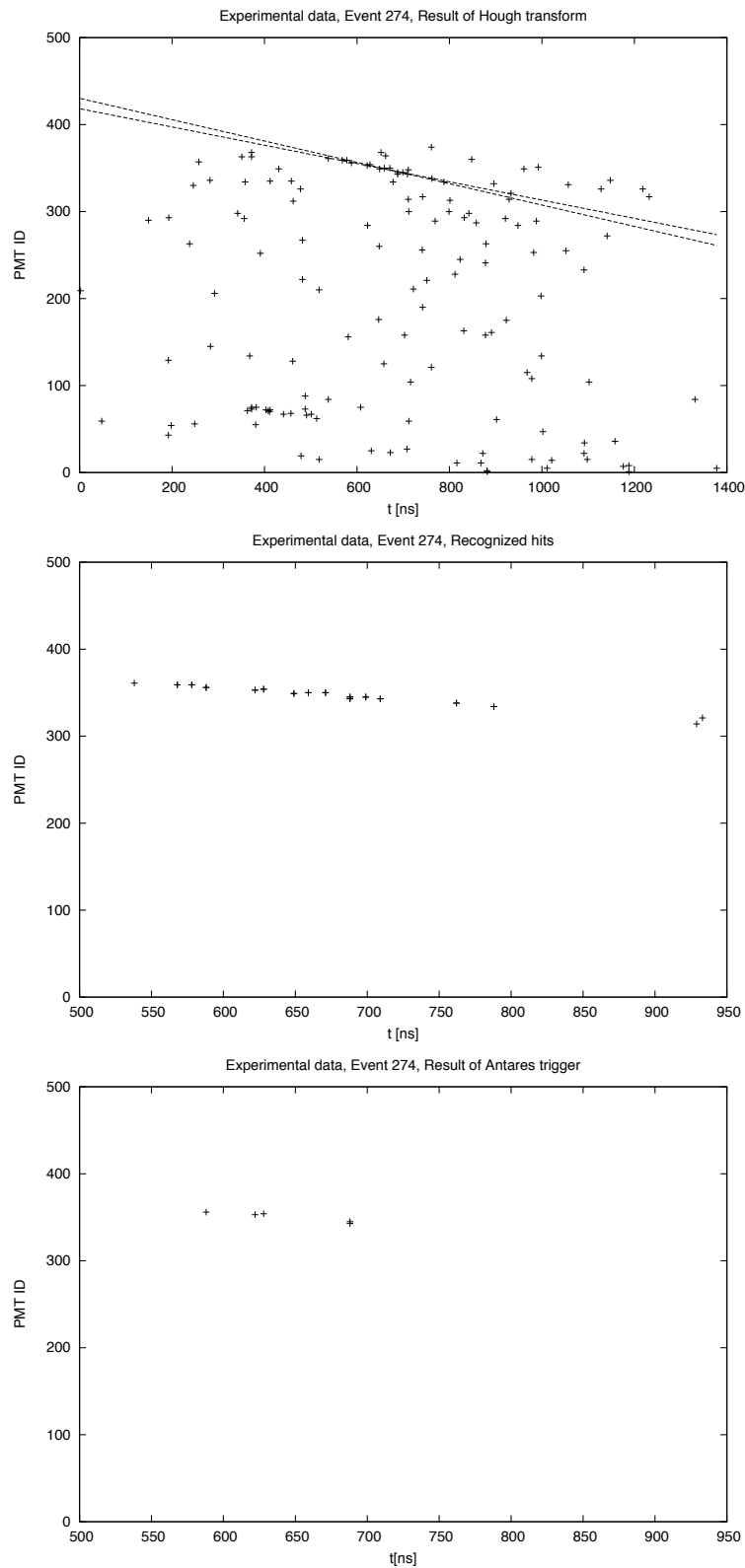


Figure C.38: Raw data (top), Hough Transform (mid) and ANTARES trigger (bottom) results of event 274 of run 27955 (recorded on 29.05.2007).

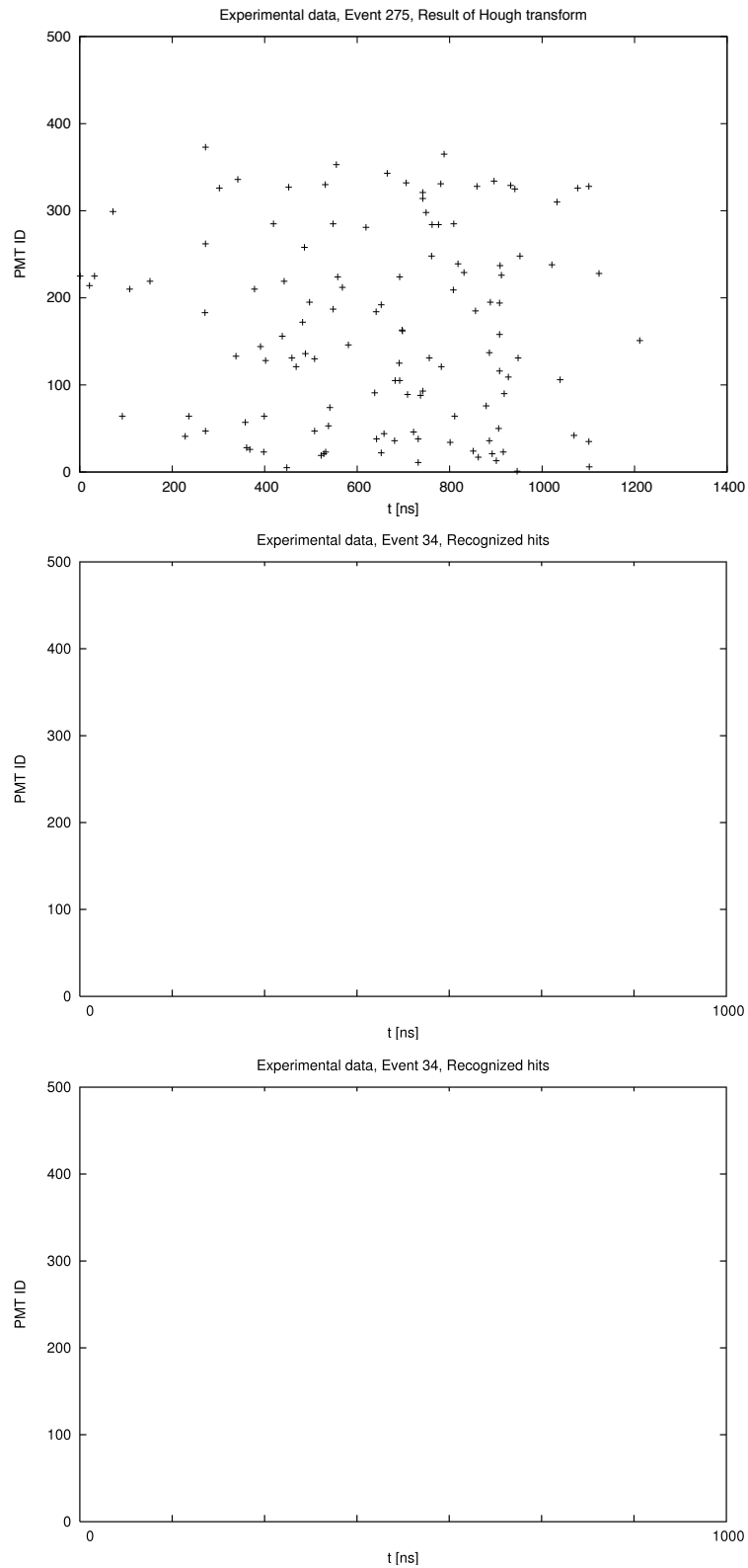


Figure C.39: Raw data of event 275 of run 27955 (recorded on 29.05.2007). Neither the standard trigger nor the the ANTARES trigger detected the event

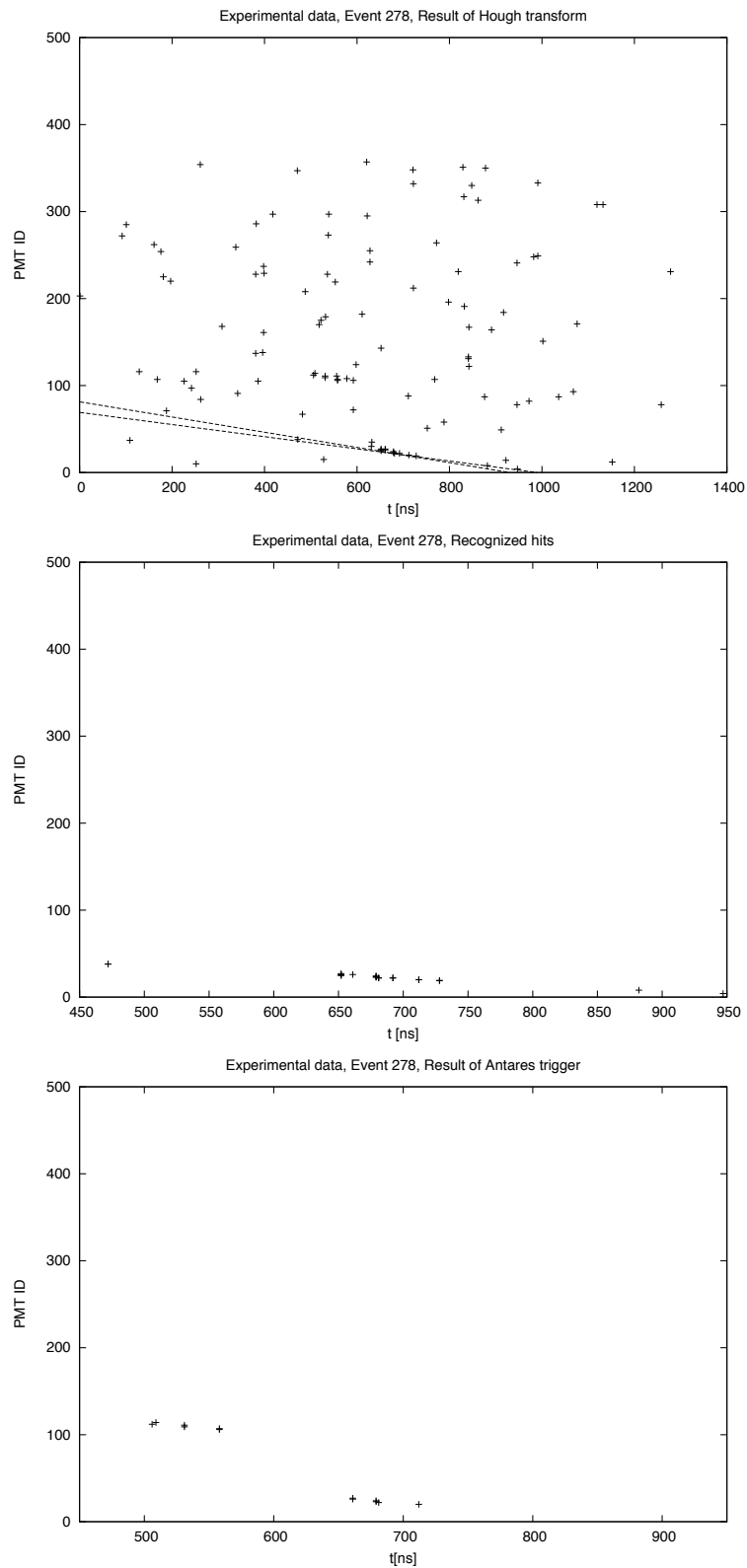


Figure C.40: Raw data (top), Hough Transform (mid) and ANTARES trigger (bottom) results of event 278 of run 27955 (recorded on 29.05.2007).

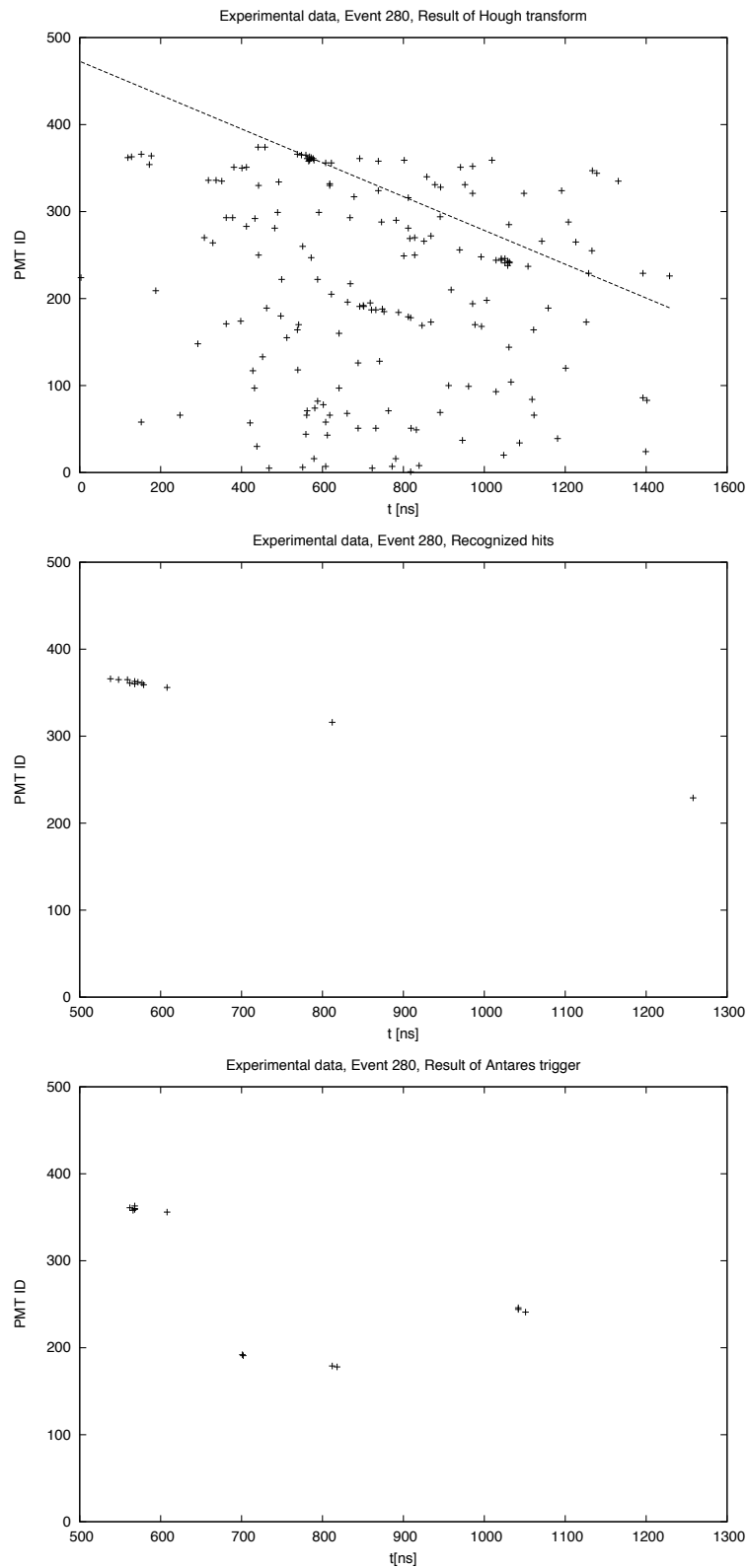


Figure C.41: *Raw data (top), Hough Transform (mid) and ANTARES trigger (bottom) results of event 280 of run 27955 (recorded on 29.05.2007).*

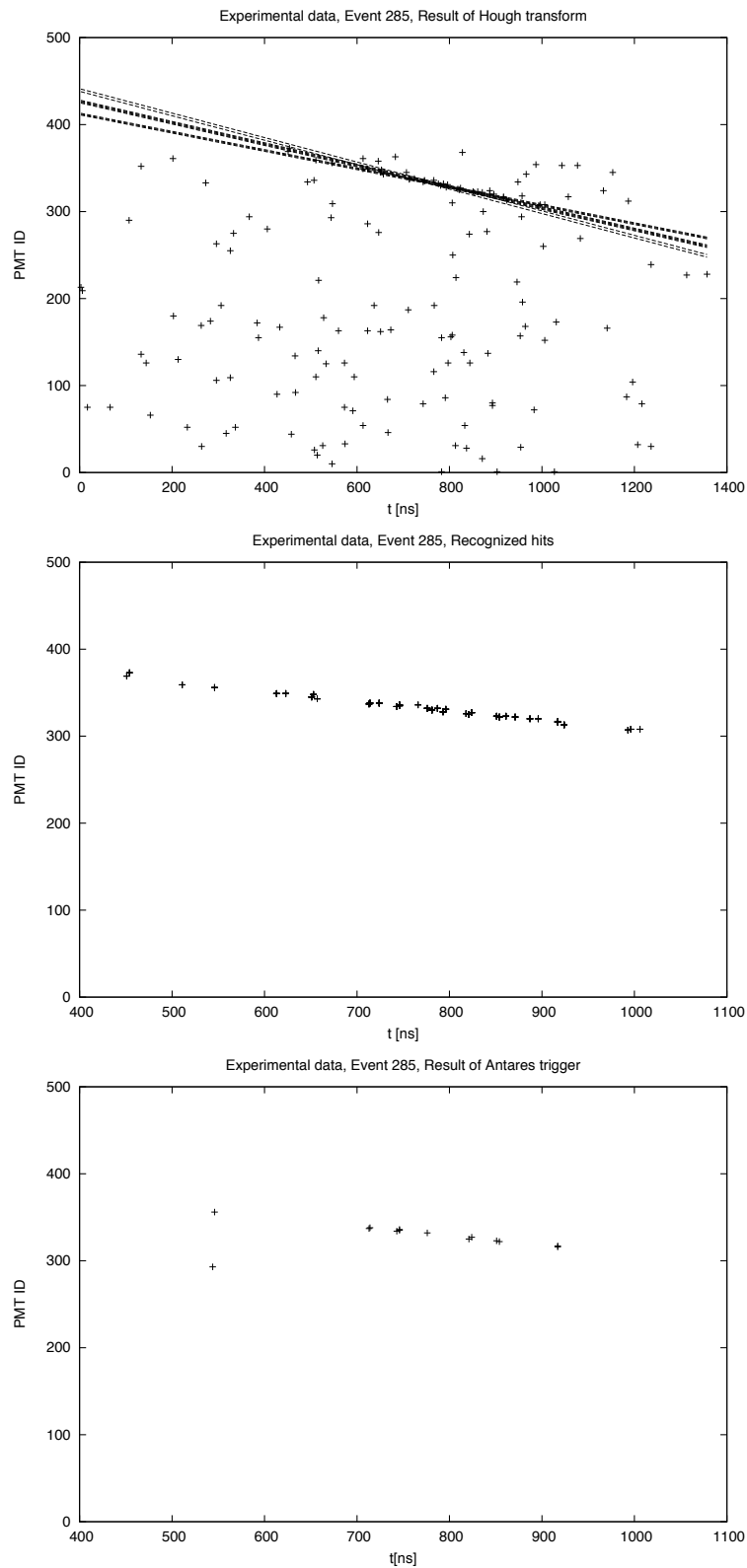


Figure C.42: Raw data (top), Hough Transform (mid) and ANTARES trigger (bottom) results of event 285 of run 27955 (recorded on 29.05.2007).

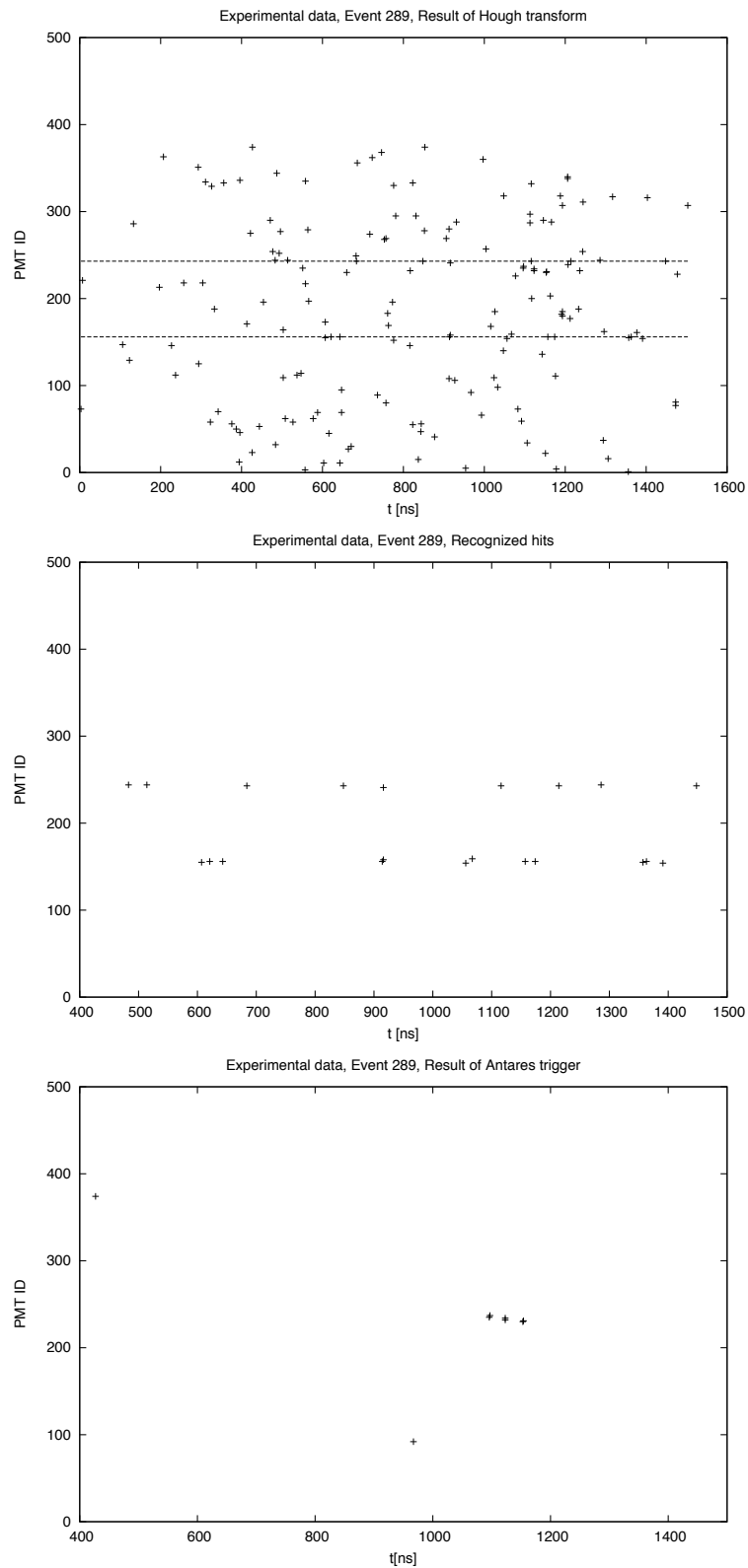


Figure C.43: Raw data (top), Hough Transform (mid) and ANTARES trigger (bottom) results of event 289 of run 27955 (recorded on 29.05.2007).

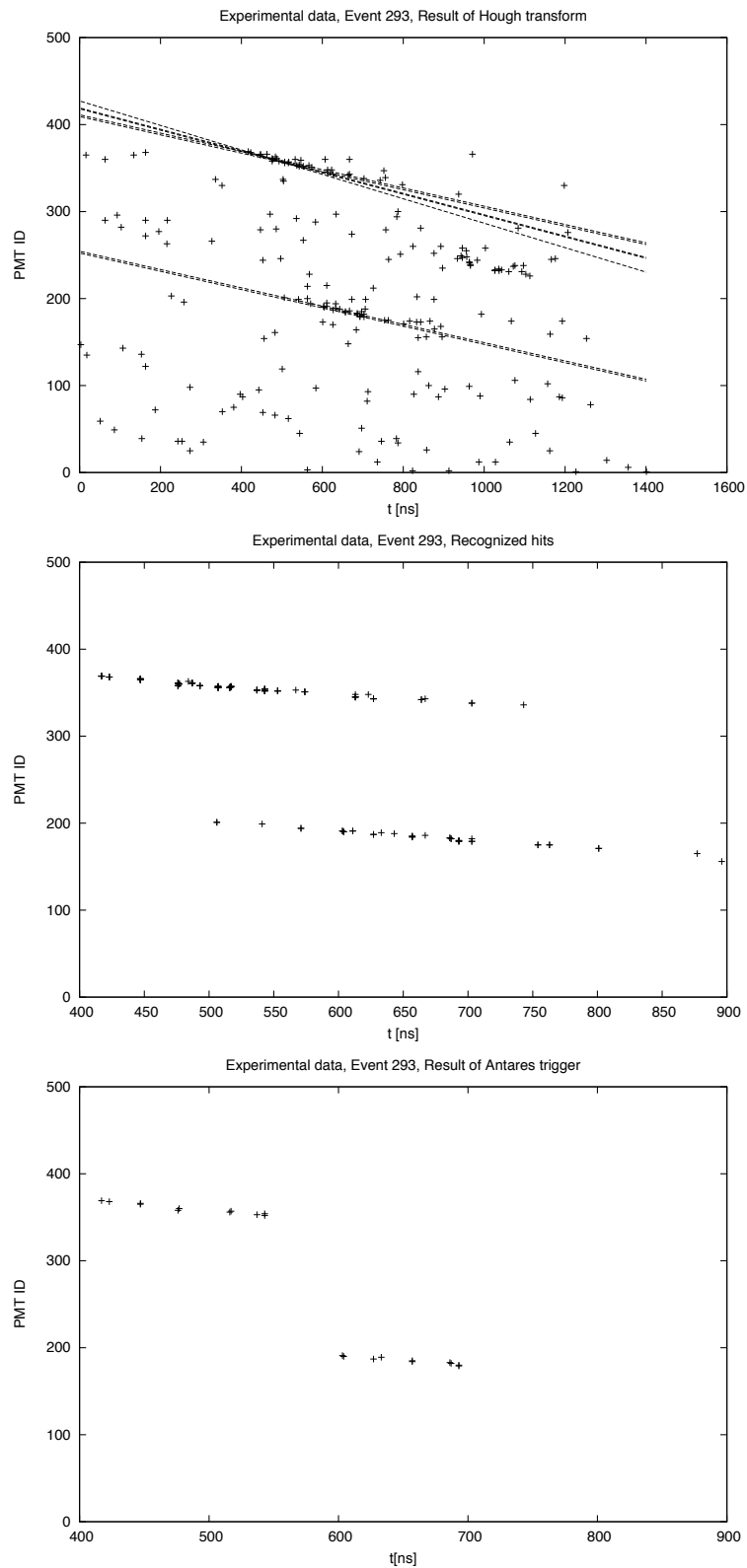


Figure C.44: Raw data (top), Hough Transform (mid) and ANTARES trigger (bottom) results of event 293 of run 27955 (recorded on 29.05.2007).

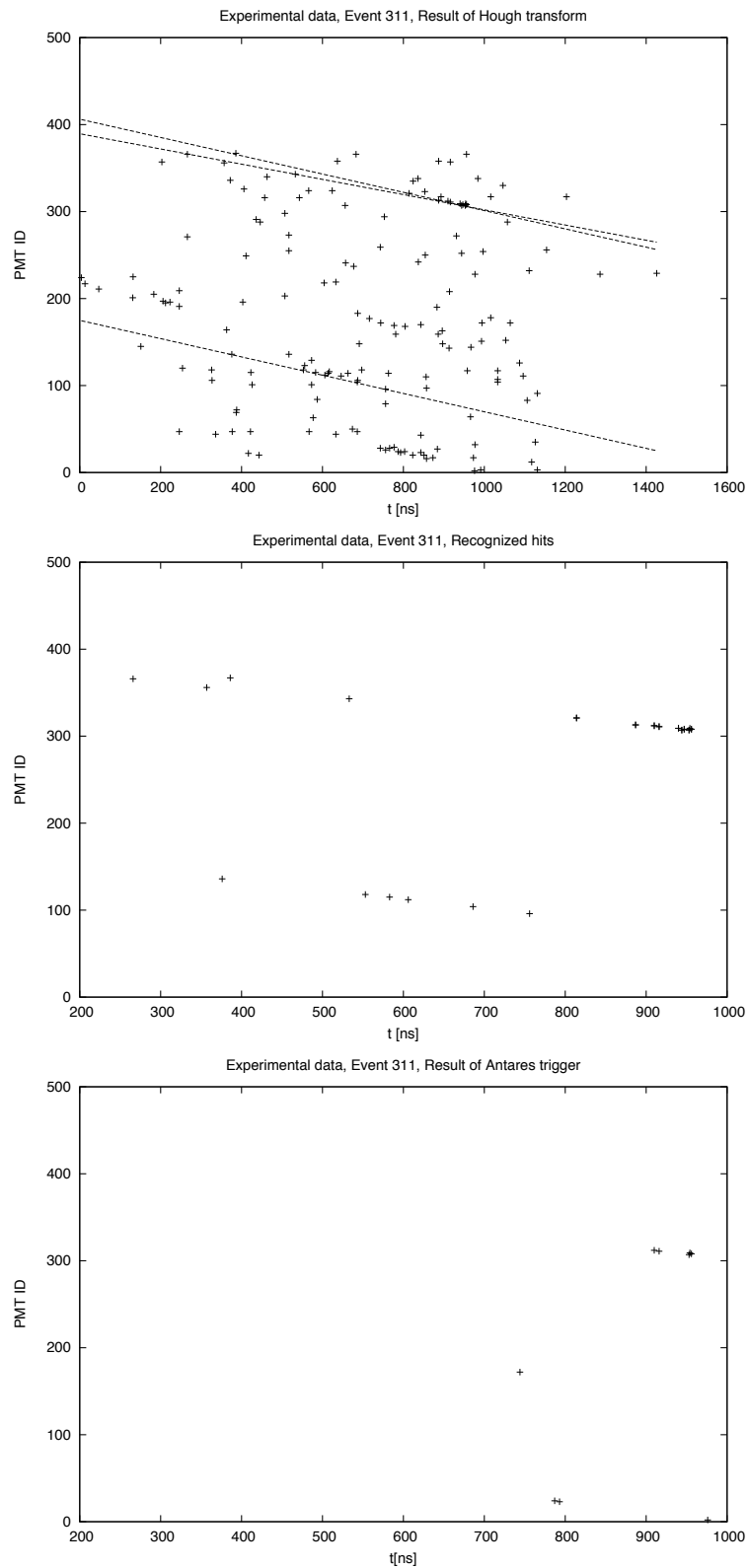


Figure C.45: Raw data (top), Hough Transform (mid) and ANTARES trigger (bottom) results of event 311 of run 27955 (recorded on 29.05.2007).

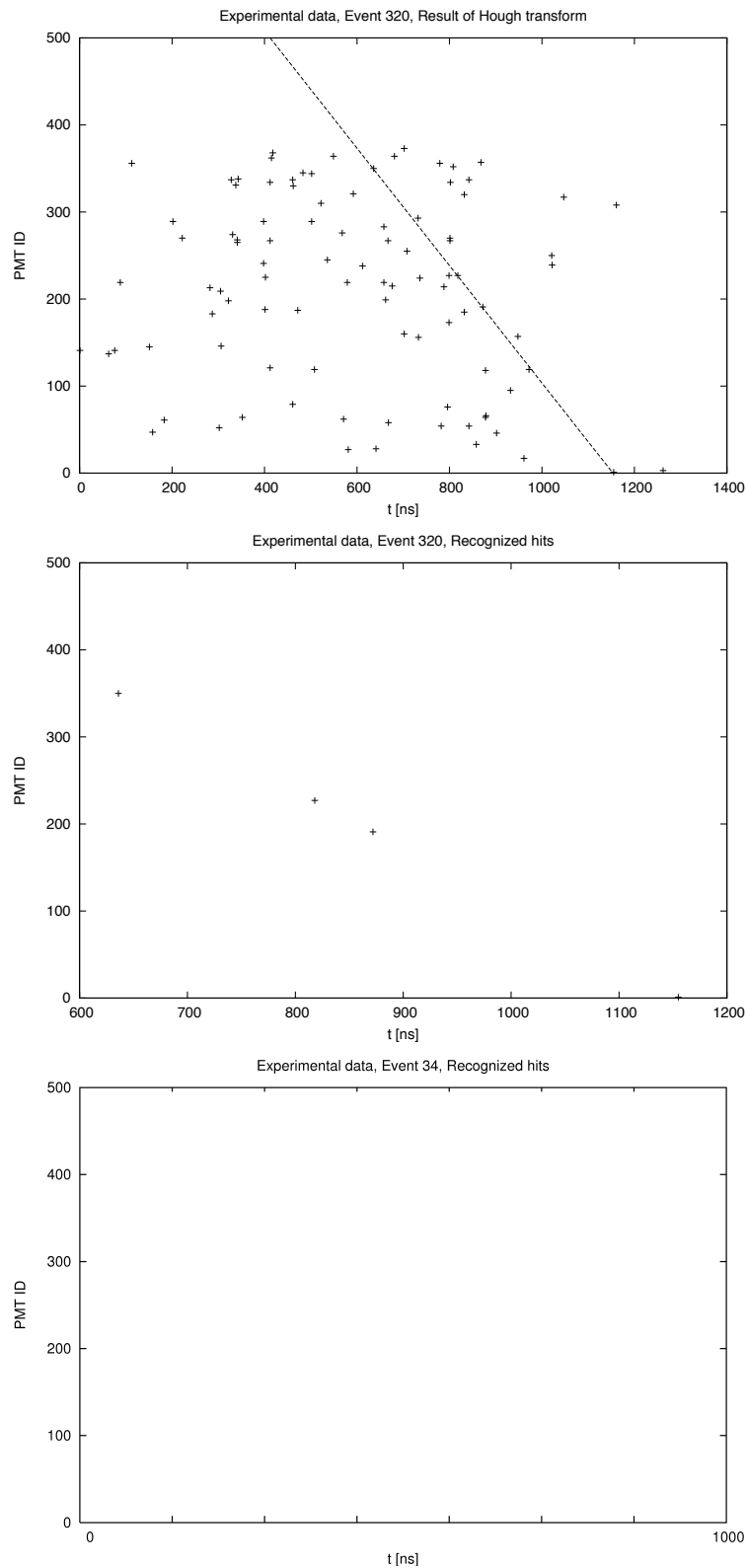


Figure C.46: Raw data (top) and Hough Transform (mid) results of event 320 of run 27955 (recorded on 29.05.2007). The ANTARES trigger did not detect the event.

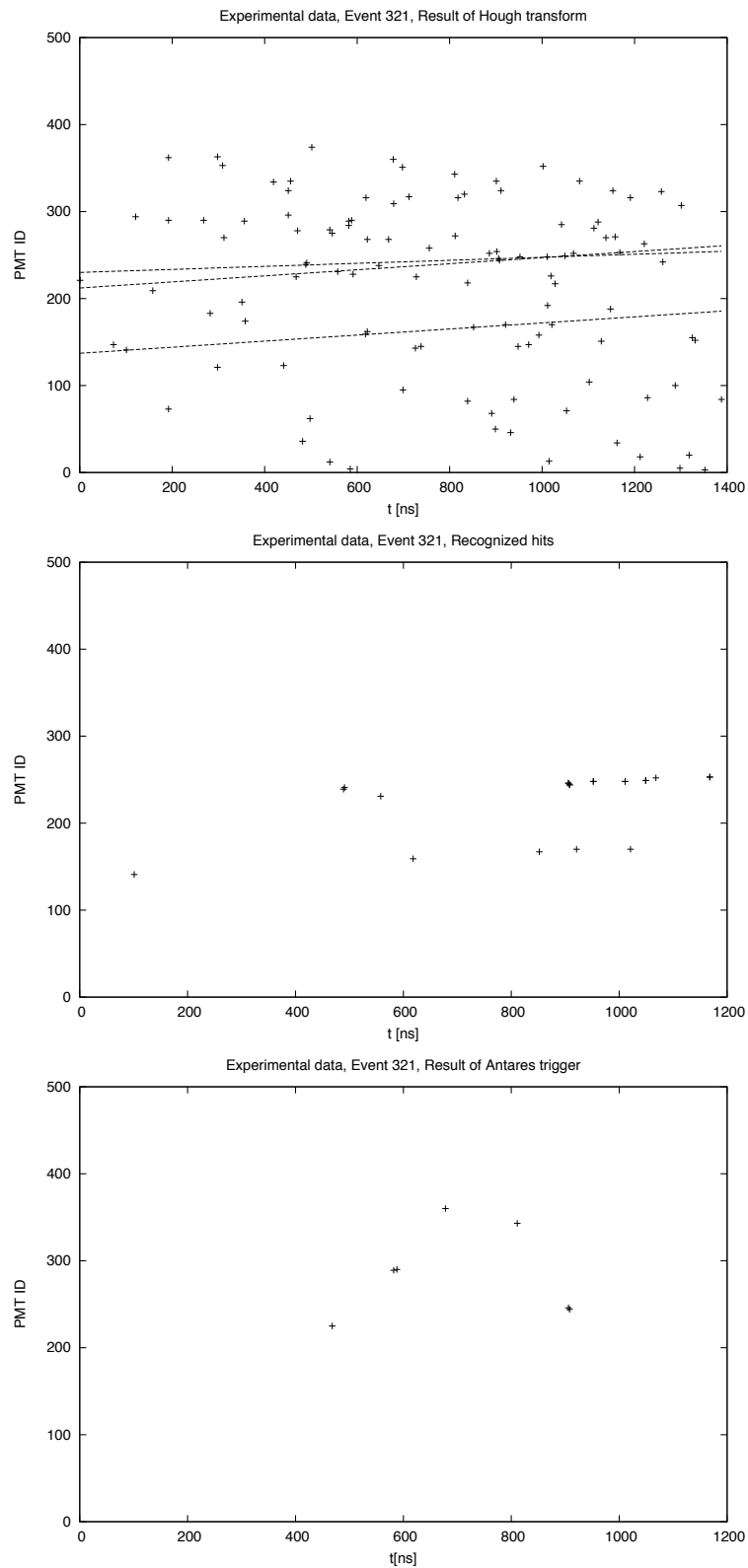


Figure C.47: Raw data (top), Hough Transform (mid) and ANTARES trigger (bottom) results of event 321 of run 27955 (recorded on 29.05.2007).

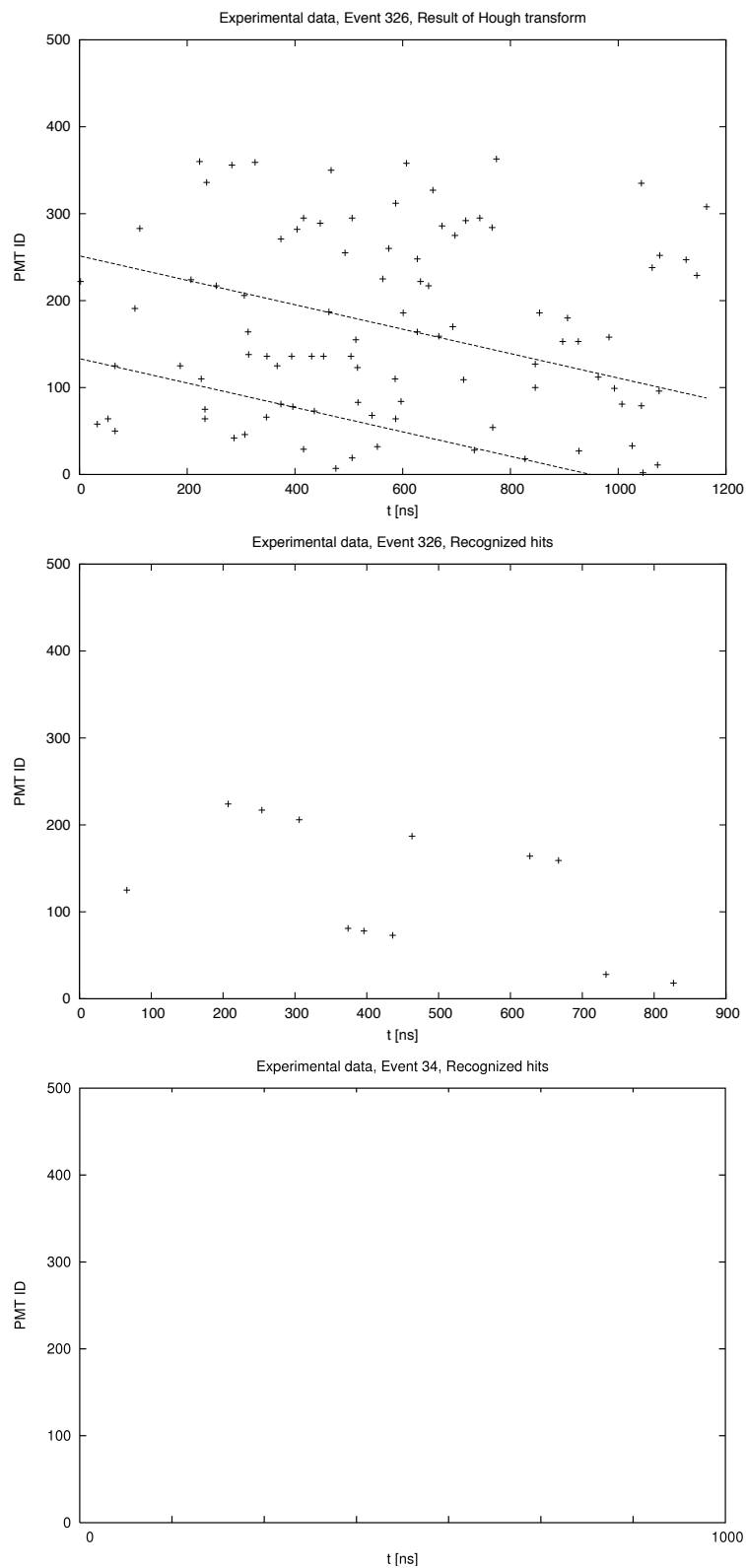


Figure C.48: Raw data (top) and Hough Transform (mid) results of event 326 of run 27955 (recorded on 29.05.2007). The ANTARES trigger did not detect the event.

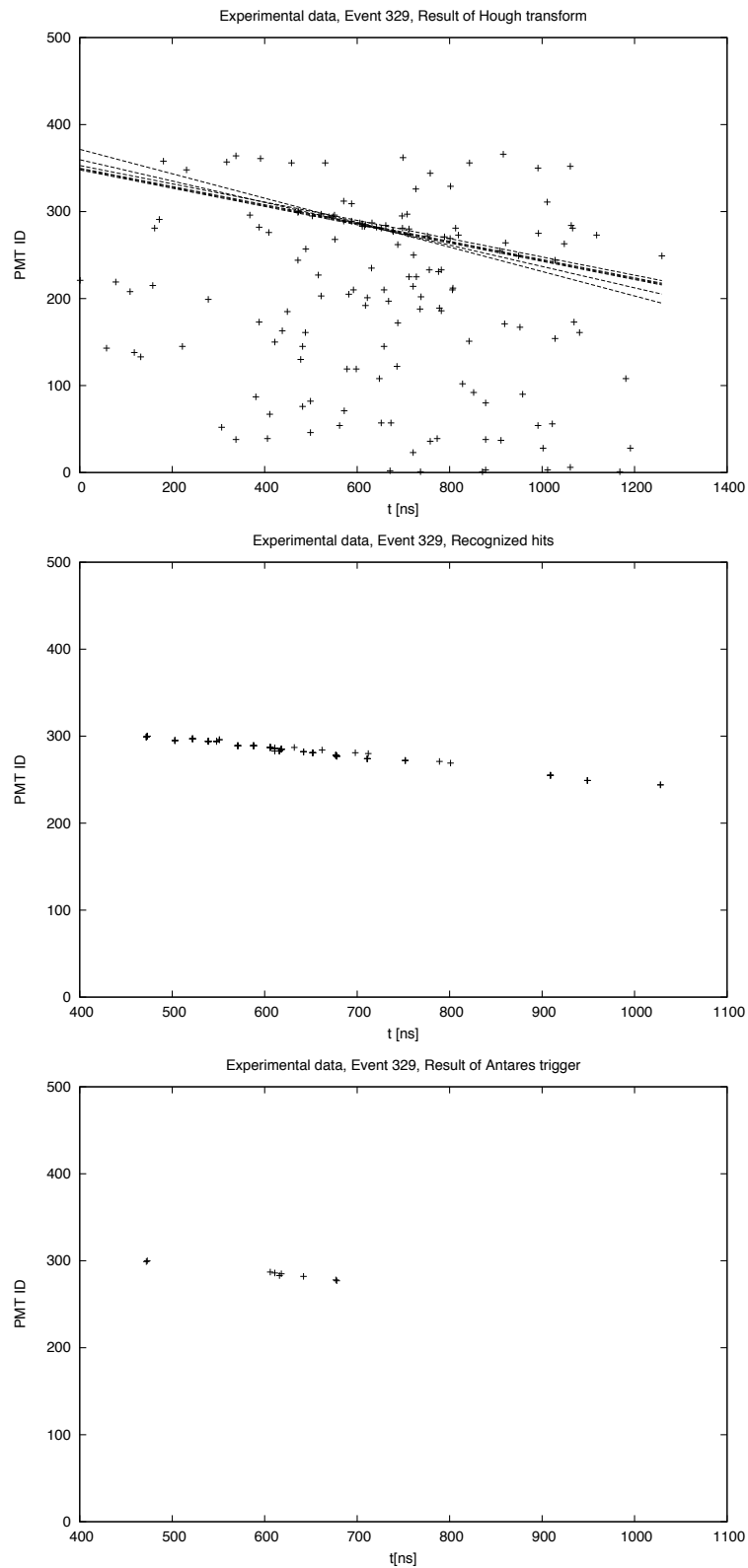


Figure C.49: Raw data (top), Hough Transform (mid) and ANTARES trigger (bottom) results of event 329 of run 27955 (recorded on 29.05.2007).

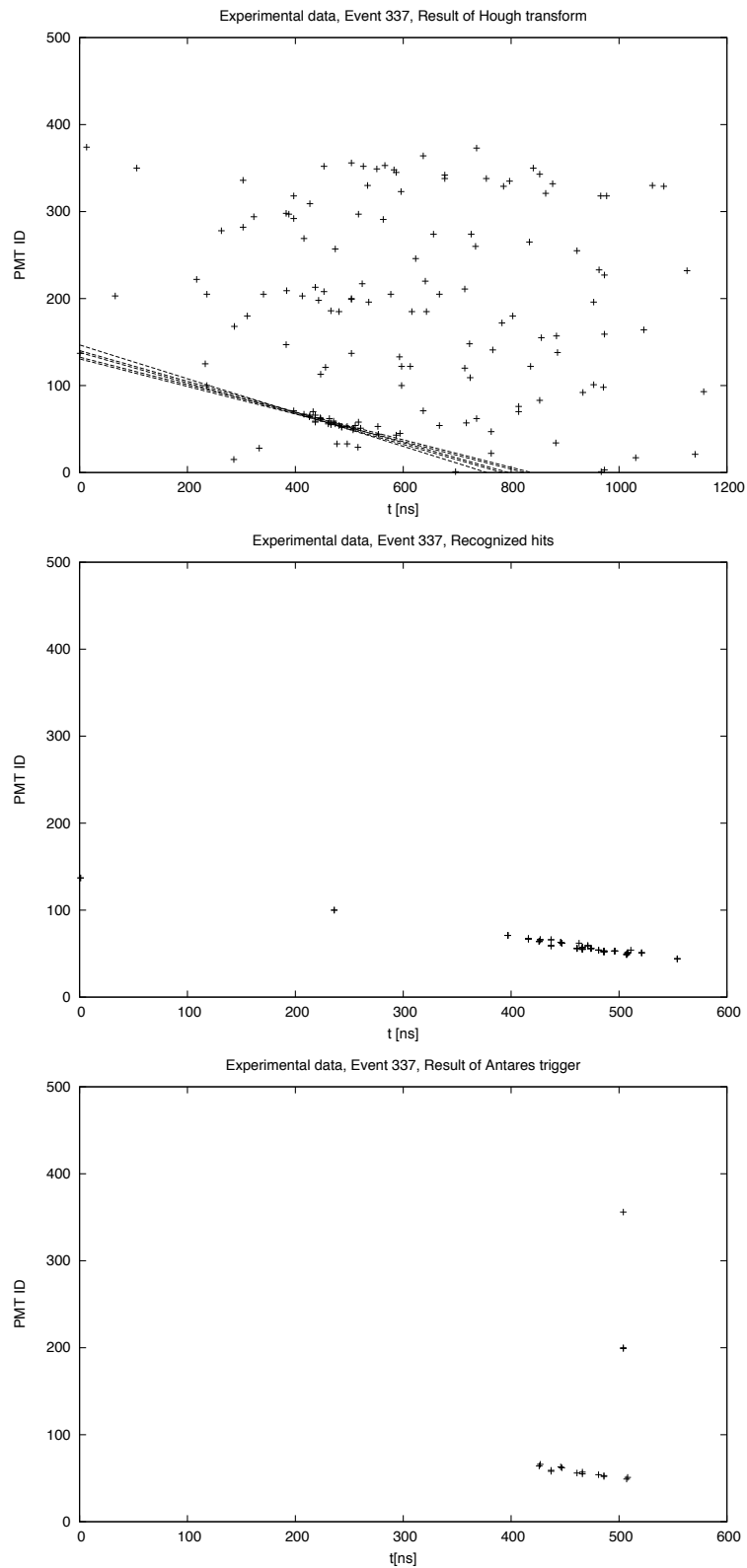


Figure C.50: Raw data (top), Hough Transform (mid) and ANTARES trigger (bottom) results of event 337 of run 27955 (recorded on 29.05.2007).

D Investigations on correlated background photons

D.1 Introduction

One of the first sets of data recorded by one of the ANTARES prototype strings, the Prototype Sector Line (PSL), has been used to investigate possible nanosecond correlations in the persisting background of photons from ^{40}K decays and bioluminescence. This investigation was made because of its possible impact on the ANTARES data filters. One component of this filter system is the so called single photo electron (SPE) value, the amount of charge collected by the PMTs during a certain integration interval. For filtering purposes, this interval as well as the SPE value can be chosen such, that only these hits are recorded, where more than one photon reaches the PMT during the integration interval. This strategy is based on the idea, that the chance for two background photons reaching the same PMT during this time is low in contrast to the chance for (correlated) Čerenkov photons, as explained in chapt. 5.3.8. This idea, however, relies on the assumption that the background photons are uncorrelated. If for some, yet unknown, reason a certain correlation exists on a temporal scale smaller than the integration window, this data filter strategy is effectively abolished.

D.1.1 The single photo electron peak

As stated in chapt. 5.3.8, the ANTARES PMTs use a default integration window of 25ns. This means that the charge created by all photons which arrive at the photo cathode within this certain interval contribute to one single signal read out. Careful measurements of the photoelectric behaviour of the PMTs used for the ANTARES detector at CEA/Saclay [48, 49, 50] lead to a certain signature, the so called SPE peak, of each PMT. This curve is a measure for the probability that a certain charge is detected if exactly one photon hits the PMT during the integration window. An example is shown in fig. D.1. The curve is based on two distributions: thermal background and a statistical distribution of the charge which is finally generated by the electron cascade which is created by the impacting photon. The peak thus signals the most probable charge which is expected from one photon. This value, which is called *PMT threshold*, can then be used as filter criterion in order to distinguish between single photons and correlated photons.

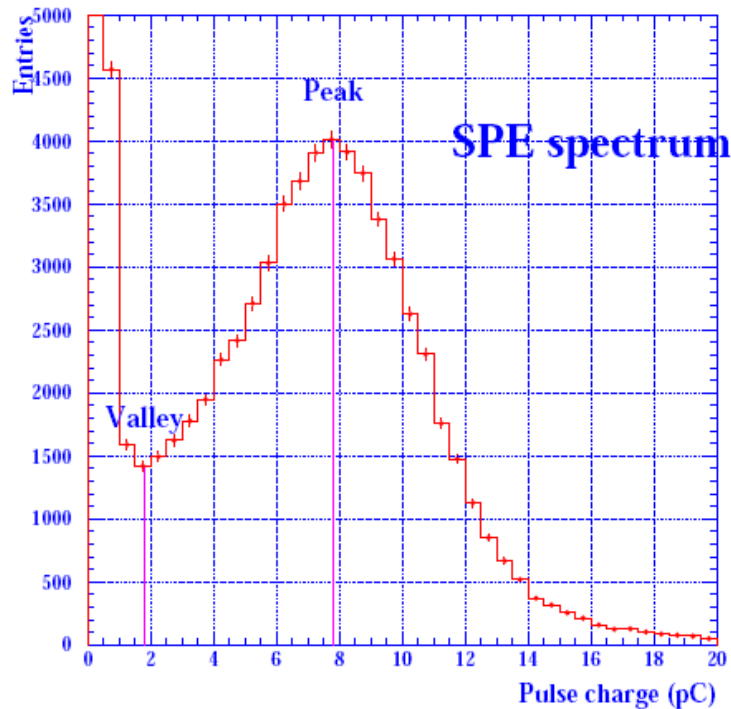


Figure D.1: Charge distribution of a photomultiplier tube with single photoelectron (SPE) peak. The image has been taken from [51].

D.1.2 Correlated photons

Apart from truly random coincidences, mainly two effects contribute to the set of correlated photons:

- Late after-pulses
- "Real" correlations

Late after-pulses are an intrinsic effect of all PMTs: Some of the electrons which are set free by the incoming photons scatter at gaseous remnants within the tube and are then reflected back to the photo-cathode. There they set free new electrons which lead to the same signal as electrons released by photons would do. Since this scattering takes place in a time short compared to the propagation time of the electrons through the tube, the overall signal is identical to a signal of two or more photons detected within this propagation time.

"Real" correlations in contrast are pairs or multiples of photons which are emitted regularly by some source.

The basic idea is now, that the rate of late after-pulses, γ_{ap} , grows linearly with the overall rate of incoming photons, γ . In contrast, the rate of really correlated photons, γ_c , is proportional to the square of the overall photon rate:

$$\gamma_{ap} \propto \gamma \quad (\text{D.1})$$

$$\gamma_c \propto \gamma^2 \quad (\text{D.2})$$

Thus, plotting the relation between rates measured at a high threshold γ_h and those measured at a low threshold γ_l against γ_l yields the curves as depicted in fig. D.2: The contribution from late after-pulses is a constant function in this plot while the contribution from real correlations increases linearly with the overall rate.

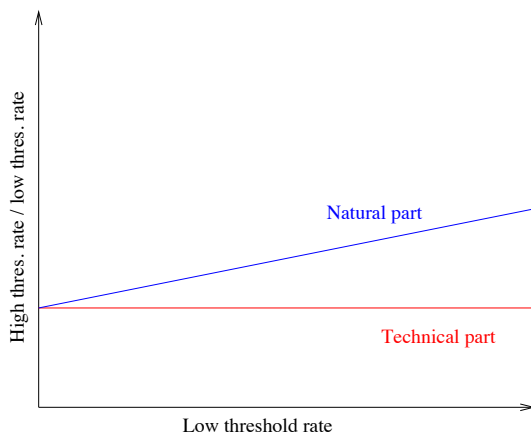


Figure D.2: *Expected contributions of late after-pulses (technical part, red line) and real correlations (natural part, blue line) to the relations of the rates measured by an ARS with high threshold and an ARS with a low threshold.*

This different behaviour of the two components of background noise can now be used to search for correlated background in measured ANTARES data, as will be explained in the next section.

D.2 Prototype Sector Line Data

D.2.1 The prototype sector line

The prototype sector line was one of the first prototypes of the final ANTARES strings. It consisted of 5 full featured storeys, 4 LCMs and 1 MLCM which were connected in

the same way they are now in one sector of an ANTARES string, thus the name „sector“line. The PSL had been deployed in February of 2003 and was recovered in June of the same year. Originally it was intended to remain on the bottom of the sea for a much longer time, but due to oxidation of the supporting frame and the OMC it had to be recovered that early again. Nevertheless it recorded valuable data which significantly increased the understanding of the deep sea conditions as well as for the final detector layout.

D.2.2 Used data-sets

For the investigation of correlated background photons, the required data sets must have offered both: recordings at different SPE threshold settings as well as simultaneous recordings at a constant low threshold. These conditions had been met by the following runs:

- 1233-1243
- 1250-1258
- 1437-1447

In these runs, the SPE threshold of two PMTs in each storey (ARS2 and ARS4) had been increased from run to run, while that of the third PMT (ARS0) had been held at a constant value near the mean SPE peak value.

Unfortunately, runs 1437-1447 had a different high voltage setting of the PMT, thus data from these runs has not been used. Additionally, data from storey 5 has been ignored, since this storey was equipped with a different version of the analogue ring sampler chips, the impact of which was unknown to the data taking process.

D.2.3 Data analysis

The following strategy was applied to the measured data:

- The data sets were divided into intervals of 50000 units length, one unit being $\approx 13\text{ms}$ (a time interval which is internally used by the ANTARES hardware).
- For each unit the baseline was searched, i.e. that rate which is caused by background only. The baseline was defined as that rate where 90% of all data points in the unit were above of, see fig. D.3.

- The arithmetic mean of the baseline in all units was calculated and taken as the mean baseline rate of the interval.
- The results of ARS2/ARS0 and ARS4/ARS0 were plotted against the results of ARS0 alone. The plots are depicted in fig. D.4.

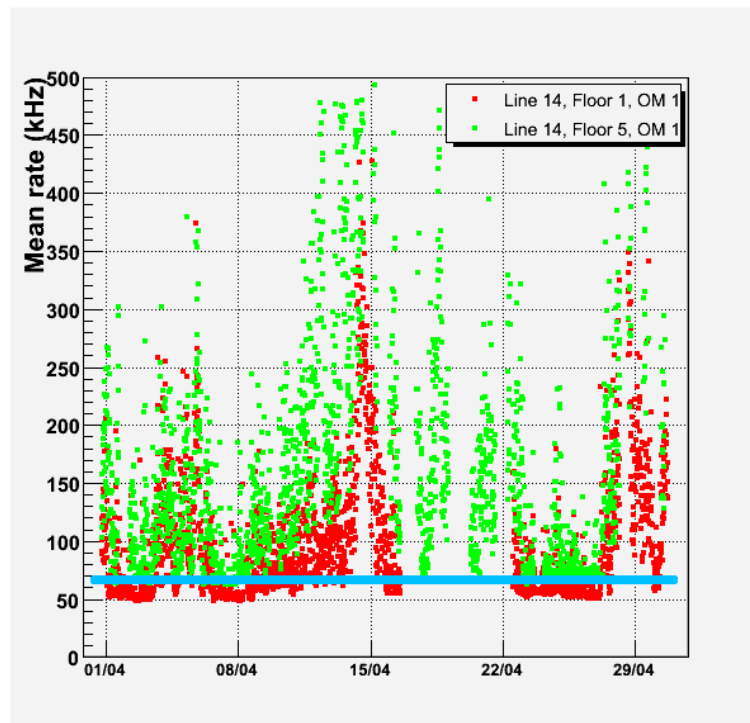


Figure D.3: Example for data recorded by the instrumentation line IL07. The blue line marks the baseline for the data recorded by floor 5 (green dots). The image has been taken from [52].

D.2.4 Results

The plot involving ARS4 shows some strange behaviour, which is not fully understood, but believed to stem from unnaturally high, bioluminescence based background rates, see fig. D.5. In the data set concerning ARS2, however, an increase in the signal seems to be present.

This result has to be taken with care, though. Due to the low amount of only two values per data point, it could quite probably be just a statistical artifact.

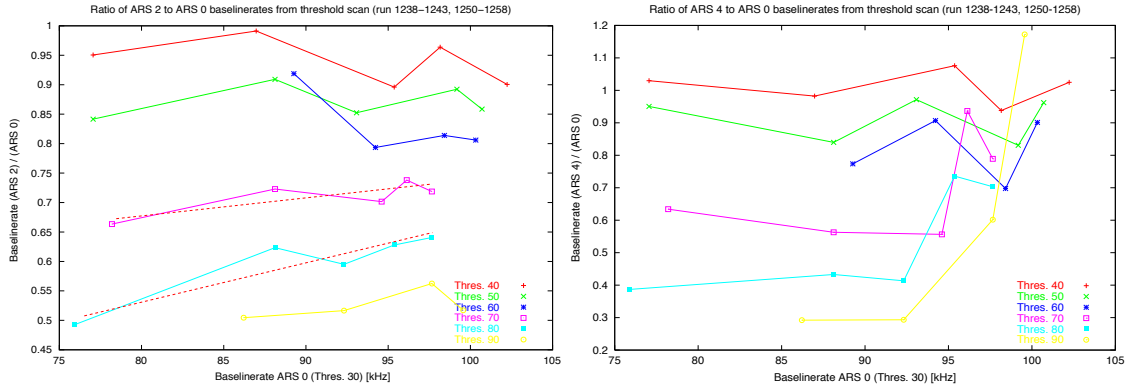


Figure D.4: The ratio of the baseline rates of ARS2/ARS0 (left side) and ARS4/ARS0 (right side) plotted against the baseline rate measured by ARS0 for different SPE threshold settings of ARS2 and ARS4.

D.3 Simulation study

In order to verify the strategy used above, a simulation study was done, which shall now be presented.

Assuming a rate of γ , the probability for the measurement of one photon within a time interval t is $P_1 = \gamma t$. Consequently, the probability for measuring two photons is $P_2 = P_1^2 \propto \gamma^2$.

The probability P for finding a signal above the selected threshold Θ is then

$$P(\Theta) = a_1(\Theta)P_1 + a_2(\Theta)P_2 \quad (\text{D.3})$$

Parametrising the SPE function S as sum of two Gaussians, $S(\Theta) = f_1(\Theta) + f_2(\Theta)$ yields

$$a_1(\Theta) = \int_{\Theta}^{\infty} S(\Theta') d\Theta' \quad (\text{D.4})$$

and

$$a_2(\Theta) \propto \int_{\Theta}^{\infty} \left(f_1(\Theta') + \int_0^{\infty} f_2(\Theta' - \Theta'') f_2(\Theta'') d\Theta'' \right) d\Theta' \quad (\text{D.5})$$

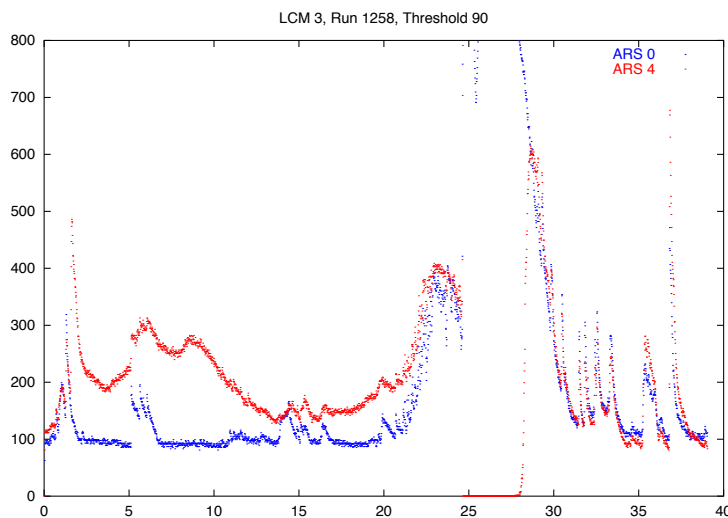


Figure D.5: *Baseline-rate as function of time for ARS0 and ARS4 of LCM 3 (arbitrary units).*

The first term of the sum is the contribution of thermal noise, which is independent of the actual rate and thus has to be integrated over only once.

For certain thresholds Θ_1 and Θ_2 the measured ration R is then

$$R = \frac{P(\Theta_1)}{P(\Theta_2)} = \frac{a_1(\Theta_1) + a_2(\Theta_1)\gamma t}{a_1(\Theta_2) + a_2(\Theta_2)\gamma t} \quad (\text{D.6})$$

Thus, the slope of the curve is indeed a measure for the rate of correlated photons.

Assuming no correlation yields the curves depicted in fig. D.6.

Comparing this result to the result from the SPE data, fig. D.4 shows clear differences.

D.4 Summary

Due to low statistics, no definitive conclusion on the presence or absence of correlated background photons can be drawn with the present data sets. Nevertheless, the data give at least a hint that such correlations exist. This result is also supported by the simulation study. Further investigation of the phenomenon thus seems advisable for two reasons: The existence of correlated background rates would not only be an important result concerning the ANTARES filter strategy, it would also be interesting to discover the cause of this correlations. Are they created by bio-luminescent beings or by radioactive decay of some sort? Which process, chemical or physical, could lead to randomly distributed photons correlated at a nano-second timescale?

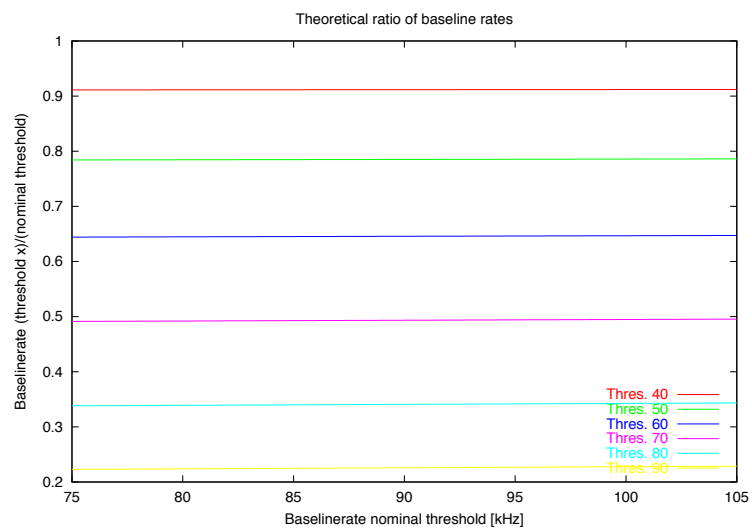


Figure D.6: *Theoretical results for expected baseline rates if no correlation in the background photons is assumed (arbitrary units).*

E The slow control system for acoustic particle detection

Apart from the systems for optical detection of neutrinos, the ANTARES telescope also houses equipment to test a new and quite different detection principle: the detection of particles by means of acoustic signals which they produce when propagating through some medium.

One side project of this thesis was the development of the control unit for the acoustics's hardware, including the on-board software as well as its seamless integration into the existing ANTARES detector control systems, which is described now.

E.1 Acoustic particle detection

The basic detection principle is, that a particle, which propagates through some medium, locally deposits energy in this medium. This energy deposition leads to local heating and in consequence to fast expansion of the medium, resulting in a sound wave originating from the particle's track. If $p(\mathbf{r}, t)$ is the pressure field describing the sound wave, this field is connected to the energy density deposited in the medium, $\varepsilon(\mathbf{r}, t)$, by

$$\frac{1}{c^2} \frac{\partial^2 p}{\partial t^2} - \Delta p = \frac{\alpha}{C} \frac{\partial^2 \varepsilon}{\partial t^2} \quad (\text{E.1})$$

with c the speed of sound in the medium, α the bulk expansion coefficient and C the specific heat capacity. This principle, known as thermo-acoustics model, was developed by Askarian in 1957 [53, 54]. It has since been successfully approved by several experimental setups, for example [55] or [56].

E.2 Acoustics within ANTARES

The idea was to equip the ANTARES neutrino telescope with hydrophones and suitable electronics in order to record acoustic signals created by high energy particles propagating through the surrounding water. These signals could then be used to reconstruct the track of the particle which caused them. Several studies on reconstruction algorithms [57], suitable hydrophones [58, 59] and acoustic background noise [60] preceded the actual development of the acoustic setup used within ANTARES, resulting in the following design:

- As much ANTARES standard hardware as possible shall be used.
- The three optical modules will be replaced by six hydrophones attached to the optical module frame.
- The ARS boards within the LCM container will be replaced by special signal processing boards.
- The signal processor will be realised by an FPGA¹ in order to allow easy adjustment of the signal processing to new requirements.
- Physical data as well as control information will be transmitted in ANTARES standard data formats in order to transparently integrate the setup into the existing data taking system.

Especially the last item showed up as quite complicated, because of certain requirements which were not provided by the ANTARES standard data formats, as for example the possibility to transmit large amounts of data for reprogramming the FPGA. The problem was finally solved by using the ANTARES slow control connection for data transfer, which had to be modified slightly to transmit the required amount of data without affecting the data taking and control of the rest of the detector.

A very detailed description of the acoustic particle detection hardware and its integration into the ANTARES setup can be found in [61].

E.3 The Slow Control

The term "slow control" basically refers to those parts of the communication between the detector and the coast station, which do not contain any physical data but instead control and calibration information. While the physical data are sent over high-speed Ethernet and glass fibre links, the control information uses slow serial links between the different components within an LCM container. Two different slow control systems are in use: One is based on a RS485 serial link[62], which uses Modbus[63] as transfer protocol. This link mainly transmits environmental data, like temperature, compass information or tilt meter data from special sensor boards. The second system is based

¹An FPGA is a special, so called *programmable logic chip*. Such a device is not "programmed" in the usual sense, meaning that a certain program is executed instruction by instruction. Instead, the software reconfigures the wiring and the behaviour of the logical gates of the chip itself. So to say, the software "changes the hardware", or, in other words, the software does not "run" on the hardware, the software *is* the hardware. In general, a programmed FPGA is capable of very few quite special tasks only, but they are done massively in parallel, leading to an increase of performance well beyond any classical processor



Figure E.1: *Illustration of an acoustic storey. The three optical modules, which are part of a standard storey, have been replaced by six hydrophones. The image has been taken from [61].*

on a dedicated five-wire bus which uses some kind of SPI[64] derived transfer protocol. This link transmits configuration data to the electronics controlling the photomultiplier tubes, the so called ARS (Analogue Ring Sampler) main-boards. Since the acoustic boards are designed to replace the ARS boards, this second system had to be adapted to the new requirements.

E.3.1 Existing slow control system

Fig. E.2 gives a schematic overview of the slow control system for optical neutrino detection. Slow control information for the ARS boards is encoded in a string of 239 bits[65]. This string is either stored in a file in `/export/filesystem`² on the on-shore control host and the file-name is passed to the DAQ board during the configuration phase, or the configuration string itself is sent to the DAQ board directly. In the first case, the file system is accessible by the DAQ board via the standard Network File

²`/export/filesystem` is the global directory on the control host which is accessible from any DAQ board and contains all configuration files and software images used by the off-shore hardware.

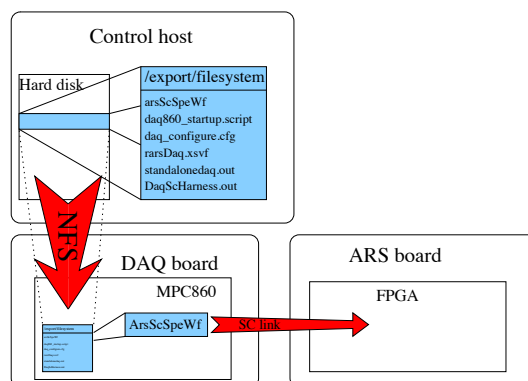


Figure E.2: *Schematic diagram of the slow control system.*

System (NFS). Subsequently, the MPC860 μ C on the DAQ board sends this 239 bit information to the according ARS board using an adapted protocol which is derived from the SPI protocol definition. The physical link between the MPC860 and the ARS board is established by 5 wires, which are controlled by an FPGA on the DAQ board, which, in turn, maps the registers to control these wires into the memory space of the MPC860. The main MPC860 slow control routine is a simple loop over all 239 bits, setting the FPGA registers (and thus the logic state of the wires) to high or low, according to the state of the corresponding bit and the protocol definition. This simple design makes it quite easy to change both the amount of data to be transferred and the transfer protocol itself, by altering the MPC860 software. Since each DAQ board is individually configurable to its very own software version, which is loaded from `/export/filesystem` at power-up, it is possible to use special code for the acoustic modules without affecting data acquisition of the rest of the detector.

E.4 Hardware

E.4.1 Constraints and selected hardware

One of the major constraints when selecting suitable hardware was power consumption. Thus, the main attention was turned to selecting low power components, especially concerning the micro controller which is the endpoint of the slow control communication link.

The product, which has eventually been chosen is the STR-710-F model by ST Microelectronics. It is an ARM 7 based micro controller, which is capable of 5 different low power modes: In the so called *Standby Mode*, the complete processor core is switched off, leading to a guaranteed maximum power consumption of $30\mu\text{A}$ at 3.3V [66] with

certain tests showing a consumption of even $\ll 1\mu\text{A}$ [67]. In *Stop Mode* only the CPU clock is stopped, resulting in a guaranteed maximum power consumption of $50\mu\text{A}$. The other three low power modes, called *Slow Mode*, *Wait For Interrupt Mode* and *Low Power Wait For Interrupt Mode* basically work by slowing down or stopping the clock while keeping the peripherals running, thus resulting in a typical power consumption of the order of a few mA. In normal running mode, the power consumption is of the order of 60mA at 48MHz clock frequency. Further reduction of power consumption can be achieved by individually stopping the clock for unused peripheral systems (as for example the on-chip USB controller) and activating built-in pull-down resistors for each unused I/O port.

The basic idea was, that the micro controller stays in either Standby Mode or Stop Mode (which can be selected at compile time of the software) most of the time, entering running mode only when a slow control transfer is requested. After the transfer has been processed, it returns to the selected low power mode. In order to "wake up" the micro controller from Standby or Stop Mode, one of the physical slow control lines (SC_VALID, see E.5.1) is connected to a dedicated wake-up pin of the chip, so that the micro controller will automatically enter running mode at the beginning of a slow control transfer.

The micro controller will be called μC in the following sections of this work. Additionally, for reasons of simplicity, only Standby Mode is mentioned in the rest of this work, although it could also be Stop Mode. This will make no difference for the basic working principle.

E.5 The slow control protocol

The slow control for acoustic particle detection can be split into two distinct parts. The first part could be seen as the "real" slow control functionality in terms of "control". Its main purpose is to set different parameters of the acoustic detection hardware, for example sample frequency, gain of the amplifiers and the like.

The second part covers the possibility to perform some kind of "firmware update" of the on-board digital signal processor, which is realised in form of an FPGA, thus allowing for (almost) completely free reconfiguration. During the rest of this work, the "real" slow control will be referred to as "acoustic slow control", while the update process will be called "FPGA update".

This section will introduce the slow control protocol in detail. To be more precise, it will introduce the communication protocol between the DAQ board and the acoustic boards. The slow control link between the DAQ board and the coast station has not to be altered. This section is divided into two different topics, namely the link layer (the

realisation in hardware) and the application layer (the software part of the protocol), according to layers 2+1³ and 7 of the ISO OSI model[68] of communication protocols⁴.

E.5.1 Link layer of the slow control protocol

The slow control connection between the DAQ board and the AcouDAQ boards (the boards containing the electronics for the read-out of the hydrophones) is based on the existing bus system for slow control of the ARS boards. This connection consists of 5 dedicated wires:

- 3 SC_VALID lines: One line for each ARS (or AcouDAQ) Board. This line selects the board to which the slow control command is sent.
- 1 SC_CLK line: This line provides a clock for bit synchronisation. It is shared among the ARS/AcouDAQ boards.
- 1 SC_DATA line: Over this line, the actual data are transferred. This line is also shared among the boards.

The ARS SC protocol

A short summary of the protocol is given now. Details, especially concerning timing constraints can be found in [65].

ARS slow control consists of a stream of 239 bits, which are either sent from the DAQ board to a certain ARS board (*write* request) or from a certain ARS board to the DAQ board (*read* request). The basic procedure is:

- The DAQ board rises the SC_VALID line of the corresponding ARS board and starts sending clock pulses over SC_CLK.
- During the first clock cycle, the DAQ board rises SC_DATA in case of a write request or pulls SC_DATA low in case of a read request.
- During the next two clock cycles, the DAQ board specifies the ID of the ARS chip on the selected ARS board by transmitting two bits over SC_DATA. This is necessary, because there are up to three ARS chips per board, which can be configured independently.

³Layers 1 and 2 are quite often commonly referred to as "link layer", although the OSI model treats them separately as "link layer" (layer 2) and "hardware layer" (layer 1). This work follows the commonly accepted denotation for reasons of simplicity.

⁴OSI layers 3 to 6 have no counterpart in this protocol since it is an inter-chip point-to-point protocol only and thus the network and HMI (human machine interface) capabilities covered by these layers are not implemented.

State	Meaning
0	Configuration of hydrophone is transferred During write request: The first 16 bit contain configuration data During read request: Return the configuration which is selected by the first 8 bit of the last write request
1	Upload of FPGA net list: During write request: FPGA net list is transferred During read request: CRC32 check-sum of data is requested

Table E.1: *Meaning of the most significant ID bit for acoustic slow control.*

- During the next 239 clock cycles, either the DAQ board (during a write request) or the ARS board (during a read request) rises and lowers SC_DATA according to the values of the corresponding bits in the 239 bit configuration string.
- The DAQ board releases SC_VALID and stops clock generation on SC_CLK.

Changes for AcouDAQ SC

Two changes occur to the protocol on the link layer.

The first one concerns the amount of data to be transferred. Instead of a fixed length of 239 bit, a stream of arbitrary length can now be transmitted over the bus system.

The second change concerns the SC_VALID line. This line not only selects the destination board, it is also connected to the wake-up-pin of the receiving μ C. Since the μ C needs a certain time for bootstrapping after the wake-up-pin has been triggered, a delay of 1ms has been inserted after the DAQ board has risen the SC_VALID line and before clock generation starts. This delay, however, has no influence on the optical slow control since it is simply ignored by the standard ARS main-boards.

E.5.2 Application layer of the slow control protocol

The application layer defines the interpretation of the data which is sent over the slow control bus system.

The meaning of the most significant ARS ID bit has changed for acoustic boards, according to table E.1.

Acoustic slow control

If the most significant ARS ID was set to 0, 16 bit have to be transferred over the SC_DATA line either by the AcouDAQ board or by the DAQ board, depending if it is a read or a write request. The first eight bit are interpreted as parameter ID, the following eight bit as parameter value. The meaning of these values are described in detail in section E.5.3. In order to avoid further alterations to the DAQ board software, it is possible to use the standard (optical) slow control for the acoustic system. In this case, only the first 16 bits of the 239 bit string are interpreted as acoustic slow control command in a write request, the remaining 223 bits are ignored. Similarly, when 239 bits are requested by the DAQ board in a standard read request, only the first 16 bits contain the slow control information while the remaining 223 bits are set to zero. This allows it to fully integrate the acoustic slow control system into the existing ANTARES run control environment. In this case, the unused bits should be set to zero in a write request, too, because they are also reported back as zero as stated above. Otherwise, the ANTARES run control would falsely detect a transmission error, which could have (unknown) influences on the data taking process.

FPGA update

In order to update the FPGA net list (the data file describing the FPGA configuration), the net list file has to be converted into a so called XSVF file. This is a proprietary file format developed by Xilinx Inc., which does not only contain the FPGA data itself, but also JTAG⁵ commands required to re-program the FPGA or the FPGA flash memory respectively. The net list file itself has to be created by a suitable FPGA development tool, as for example Xilinx ISETM. Software for creating XSVF files as well as for interpreting the included JTAG commands (and subsequently reprogramming the FPGA / flash) is provided as open source C code by Xilinx Inc.[69, 70].

Due to the limited memory capacity of the AcouDAQ board of only 1MB, the XSVF file may be compressed by a simple run length encoding (RLE) algorithm. RLE is a quite suitable algorithm for compressing files which consist of large chunks of identical bytes, which, fortunately, is one of the properties of XSVF files. In this case, compression is reached by alternately storing how often one byte is repeated and then the value of the byte itself. For example RLE compressing the following sequence of bytes

```
0x10 0x10 0x10 0x10 0x10 0x1f 0x1f 0x1f 0x1f 0x1f 0x1f 0xab 0xab 0xab
```

yields

⁵JTAG (Joint Action Test Group) is an industry standard protocol for updating (and debugging) micro controllers and other embedded devices in a "live system", i.e. while the system is powered up and/or even running.

0x05 0x10 0x06 0x1f 0x03 0xab

because the value 0x10 occurs 5 subsequent times, the value 0x1f 6 times and the value 0xab 3 times. Test runs with different FPGA configurations showed that the XSVF files are typically compressed down to 20% of their original size, allowing of up to 5MB of data to be transferred to the FPGA.

In order for the AcouDAQ board to know if the file is compressed or not, a 16 bit header has to be prepended to the data itself, which takes the value 0x0ff0 if the file is compressed and 0x0000 otherwise (a third possible value of 0xf000 tells the μ C to start reprogramming the flash, as described below). A header size of 16 bit has been chosen, because the memory on the AcouDAQ board is 16 bit accessible only.

Both, prepending the header as well as compressing the file, is performed by a special tool (*prepfpga*, described in detail below), which takes the XSVF file as input and creates a (possibly compressed) output file with header as well as a file containing a CRC32 check-sum of the output file. Compression can either be switched on manually or will be done automatically, if the size of the XSVF file exceeds the available memory.

The check-sum can be used to verify, that the file has been transmitted correctly to the AcouDAQ board. CRC32 has been chosen, because it is based on a per-bit algorithm and thus can be computed by the μ C on the fly while receiving the file. The CRC32 algorithm can be summarised as follows[71, 72]:

- Initialise the 32 bit check-sum with 0
- For each bit of the input stream
 - Store the status of the most significant bit of the check-sum
 - Shift the check-sum one bit to the left
 - If the current bit of the input stream and the stored most significant bit of the check-sum differ, XOR the check-sum with 0x04c11db7
- Output the check-sum

In order to re-program the FPGA, the processed XSVF file (including the header) has to be sent to the μ C via SC_DATA. The μ C stores this file in RAM and computes its own check-sum of the received data, which can be retrieved by a subsequent read request. It can then be compared to the check-sum calculated by *prepfpga*. This second step is not necessary but strongly recommended in order to avoid or, at least, detect transmission errors. After the successful transfer has been verified, at least 16 bit containing the value 0xf000 have to be sent to the μ C, which trigger the actual update of the FPGA flash memory. After successful completion of the update, the FPGA is

Value	Name	Meaning
0x0000	SC_UPLD	This packet contains an FPGA file
0x0ff0	SC_COMP	This packet contains a compressed FPGA file
0xf000	SC_RPRG	Start reprogramming the FPGA flash memory (Only the header field is regarded, possible following bits are ignored.)

Table E.2: *Header fields for acoustic slow control and their names as used within the code.*

reset so that it is immediately ready for use. A detailed instruction summary is given in section E.5.4.

Table E.2 summarises the possible header fields.

E.5.3 The μ C-FPGA interface

Acoustic slow control

The amount and meaning of slow control parameters which can be transmitted to the FPGA are dynamical variables. They depend solely on the configuration of the FPGA and can change completely with each new net list version. Therefore, a special, simple protocol was developed, which allows transmission of control sequences independently from their particular meaning. This protocol, which is described now, is related to the SPI protocol, but was designed with regard to easy realisation in VHDL⁶.

Communication takes place via five dedicated wires between the μ C and the FPGA. Table E.3 lists the names of these wires, as they will be used in the rest of this work, together with their meaning and the direction of the data flow from the μ C's point of view. Each slow control request consists of 16 bits, split into two 8 bit sections. The first byte is referred to as "parameter ID", the second one is called "parameter value". The parameter ID determines the type of parameter while the parameter value contains the value which is either sent to or read from the FPGA. The following protocol is applied over the five wire physical link:

- The μ C pulls SER_ATT high and starts generating clock pulses on SER_CLK.
- If ready, the FPGA has to pull SER_RDY high within 10 clock pulses. Otherwise, the μ C releases SER_ATT and returns into Standby Mode.

⁶Very High Speed Integrated Circuit Hardware Description Language, one of a few programming languages in which FPGA net lists are developed.

Name	Direction	Meaning
SER_ATT	out	Attention: Communication request
SER_CLK	out	Clock: Clock for bit synchronisation
SER_DAI	in	Data in: Data from FPGA to μC
SER_DAO	out	Data out: Data from μC to FPGA
SER_RDY	in	Ready: FPGA ready for communication

Table E.3: *Communication link between μC and FPGA.*

- During the next clock cycle, the μC determines the direction of the communication by pulling SER_DAO low (read data) or high (set data).
- During the next 8 clock cycles, the μC transmits the ID of the parameter over SER_DAO.
- The μC sends one extra clock cycle as delimiter between the parameter ID and the parameter value (the so-called *arw-delimiter*, named after one of the developers of the initial FPGA net list).
- During the next 8 clock cycles
 - the FPGA transmits the current value of the parameter to the μC over SER_DAI, in case of a read request, or
 - the μC transmits the new value to the FPGA over SER_DAO, in case of a write request.
- The μC stops clock generation on SER_CLK, releases SER_ATT and returns into Standby Mode.
- The FPGA releases SER_RDY.

Note that the FPGA **must** survey the status of SER_ATT during the communication and abandon received data as well as release SER_RDY if SER_ATT returns to low before the last clock cycle. This is the only possibility for the μC to signal a transmission abort to the FPGA. Additionally, the μC raises each I/O port (including SER_xxx) for about $150\mu\text{s}$ during hardware reset. Thus, checking the status of SER_ATT throughout the whole communication process is mandatory for the FPGA to distinguish between a μC reset and a real slow control transmission.

As mentioned before, the particular meaning of the parameter IDs and the corresponding values is not specified in the protocol, since this depends deeply on the configuration of the FPGA. Furthermore, the only possibility for the FPGA to signal an error is to release the SER_RDY line during the communication process. In this case, the μC

immediately stops clock generation and returns into Standby Mode. Note, that such an error condition **will not** be reported back to the DAQ board! Success or failure of a slow control command can only be detected either by a read request, which will report back the status of the **last** configured parameter (thus, it is strongly recommended to verify the success after each configuration request), or by starting data taking and evaluating the properties of the physical data recorded.⁷

E.5.4 FPGA update manual

The following ten steps provide detailed instructions on how to update the FPGA configuration of the acoustic boards using the tools available at the time this work was written.

1. Create an XSVF file (which will be named 'infile' in this manual) using Xilinx iMPACT or Xilinx svf2xsvf.
2. Create a file with header and the corresponding check-sum with the tool prepfpga:

```
prepfpga [-c] infile
```

If the -c option is specified, the output file will be compressed in size. Compression is automatically done, if the input file exceeds the available memory on the acoustic board. If even the compressed file is too large, a warning message will be issued. The file should **not** be used in this case! Two output files will be created: infile.out and infile.chk

3. Copy infile.out to /export/filesystem on the control host. Make sure, that it is readable by the DAQ board!
4. Use rsh to log in on the DAQ board and load infile.out by typing

```
load_bitArray("infile.out");
```

in the VxWorks command shell.

⁷At the time of this work, the FPGA was configured such, that it included the current slow control configuration in the physical data frames sent to the coast station, allowing easy verification of reconfiguration success or failure. This, however may change in future releases of the FPGA net list.

5. Send the file to the acoustic board number `n` by typing

```
ars_sc_write(n,3);
```

in the VxWorks command shell. Note, that `n` starts from 0, not from 1!

6. Retrieve the check-sum by typing

```
ars_sc_read(n,3);  
d 0x1000000
```

in the VxWorks command shell. This will result in some output similar to

```
01000000: 4bce 663b 0000 0000 0000 0000 0000 0000 ...  
01000010: 0000 0000 0000 0000 0000 0000 0000 0000 ...  
01000020: 0000 0000 0000 0000 0000 0000 0000 0000 ...  
...  
...  
...
```

7. Compare the first two numbers (4bce 663b in this case) to the content of `infile.chk`. If they differ, repeat from step 4.
8. Send the re-program command by typing

```
load_bitArray("reprog.dat");  
ars_sc_write(n,3);
```

in the VxWorks command shell.

9. Repeat typing

```
ars_sc_read(n,3);  
d 0x1000000
```

in the VxWorks command shell, until the first number (which was 4bce in step 6) is `bdbd` (it will be `ffff` during reprogramming the FPGA). `bdbd` is, in fact, the first word of the check-sum of the re-program command.

10. The FPGA is now configured, reset and ready for use.

List of Figures

- 1.1 Verhältnis der Anzahl der vom ANTARES Standard Trigger und von der Hough-Transformation gefundenen Ereignisse für alle vier untersuchten Ereignis-Klassen bei verschiedenen Untergrundraten (kHz pro Photomultiplier), basierend auf Ereignissen aus Monte-Carlo-Simulationen. 7
- 3.1 Feynman graphs of neutral (left) and charged (right) current neutrino-nucleon interactions. The only observable signature of a neutral current reaction is the resulting hadronic shower (X), while a charged current reaction additionally produces a charged lepton (in this case a muon μ). 15
- 3.2 Basic detection principle of the ANTARES neutrino telescope. Taken from [13]. 16
- 3.3 Members of the ANTARES collaboration at the time this work was written. Taken from [13]. 18
- 3.4 Regions of the sky which are in the field of view of a neutrino telescope located in the Mediterranean, like ANTARES. The white area is never in the field of view of ANTARES the dark blue area always. AMANDA/IceCube observes the region north of the "northern hemisphere" border. The centre of the map corresponds to the galactic centre. The image also shows certain interesting neutrino sources. The figure has been taken from [17]. 18
- 3.5 Schematic 3D representation of the ANTARES detector and the arrangement of the 12 strings on the seabed. Taken from [13]. 19
- 3.6 Two storeys of an an ANTARES detector string (MILOM, March 2005) prior to their deployment. The optical module frames (1) with optical modules (2) as well as the LCM containers (3) are clearly visible. Taken from [13]. 20
- 3.7 An optical module as used in the ANTARES detector. The photomultiplier tube (1) and the mesh of mu metal (2) within the pressure resistant glass sphere are clearly visible. The back half of the sphere is coloured black (3) in order to allow light to enter the sphere from front direction only. Taken from [13]. 21

3.8 Schematic representation of the ANTARES instrumentation line and its sensors collecting environmental data: Conductivity and temperature (CT), water velocity (ADCP), water transparency (Cstar), sound velocity (SV), oxygeniety (O₂) and seismological data (Sismo). Storeys 2, 3 and 6 contain equipment for acoustic particle detection (Acou), with storeys 2 and 6 being also equipped with cameras (Cam) monitoring the surrounding water area. 22

5.1 Schematic drawing of a neuron. 1: Dendrites, 2: Soma, 3: Cell nucleus, 4: Axon, 5: Synapses. The drawing is taken from [28]. 31

5.2 A simple three layered neural network for calculating the XOR function (table 5.1). The numbers next to the axons and dendrites represent the conducted activity (in arbitrary units). The numbers within the cell bodies show the threshold value the activity must reach in order to create a new signal. The dendrites labeled with "A" are "amplifying", i.e. they will create a new activity of value 1 in the subsequent neuron. The dendrites with label "I" are "inhibiting", they will create a signal -1.

a) The thresholds in the neural network are initially set to arbitrary values. A (1,0) pattern presented to the input neurons yields the wrong value 0. b) The wrong value is fed back to the neural network (f.b.) and the threshold of the upper intermediate neuron is adjusted. The network now yields the correct value 1. In a living organism, this feedback is achieved e.g. by a pain receptor which is connected to the system by additional neurons (these are not depicted for reasons of simplicity). c) A (0,1) pattern is represented to the network, and again the wrong value 0 is created at the output layer. d) Again, the threshold is adjusted by some feed-back mechanism (f.b.) (that of the lower input neuron this time) so that the correct value 1 is calculated. e) and f) The network now also computes the correct values for input patterns (1,1) and (0,0). It has learned to distinguish between the two pattern classes "both input neurons sense the same value" and "both input neurons sense different values".

For an exact calculation of the XOR function, the threshold values of the two input neurons need to be 0.5 both. This would be achieved by further iterations of the above procedure.

The series of pictures is based on the artificial neural network presented in [29]. 32

5.3 A light cone propagating through an array of strings. Left side: If the angle between the axis of the cone and the strings is smaller than the apex angle (i.e., the cone comes from "below"), each photomultiplier tube on a certain string is illuminated one after the other in equal intervals of time, leading to straight lines in an PMT/t diagram (dashed blue lines). Right side: In cases of angles greater than the apex angle of the light cone (the cone comes from "the side"), the trajectory of the string can be seen as a plane yielding a hyperbola, which is mapped into the PMT/t diagram. 37

5.4 A light-cone crossing one detector string at an arbitrarily chosen angle somewhere between its apex-angle and 90°. Only the conic section (hyperbola resulting from the section between the plane defined by the moving cone and the string) is shown on the left hand side for different, equidistant times t_1 to t_6 . The right hand side shows the resulting signature in an PMT/t diagram. It has the basic shape of a hyperbola opened to the right, however the shape may be distorted, depending on the impact angle, see section 5.2.2. 38

5.5 Data from a shower event, mapped into a PMT/t diagram 38

5.6 Data from a muon event, mapped into a PMT/t diagram. 39

5.7 Path along the hits from a muonic charged current event (blue line). The concentration of the blue line along the collinear point distributions is clearly visible. 43

5.8 Left side: Three points aligned on a line with slope -5 which intersects the y axis at (0,45). Right side: Hough Transform of the points from the left image. The three lines have a common intersection at (-5,45). . . 47

5.9 Illustration of the normal parametrisation of a line 48

5.10 Three Hough planes corresponding to the data points (80,6) (red), (85,11) (green) and (90,1) (blue) which intersect at $a \approx 66$, $b \approx 10$ and $y_0 \approx 7$ (yellow circle). θ had been fixed to 0 and t_0 to 13. 50

5.11 Three data points (80,6), (85,11) and (90,1) and the corresponding hyperbola with parameters $t_0 = 13$, $y_0 = 7$, $a = 66$, $b = 10$ and $\theta = 0$. t_0 and θ had been fixed prior to the transform, a , b and t_0 have been determined by the Hough Transform. 51

- 5.12 The principle of finding intersections: Each line of the Hough plane (left) is "drawn" into a virtual coordinate system by increasing associated memory cells by one (right). Intersections of lines show up as local maxima (red squares). The indexes of these memory cells correspond to the coordinates in Hough space. In this case, the three intersections (m_1, b_2) , (m_2, b_3) and (m_3, b_1) have been found. 53
- 5.13 Left side: Only lines with an angle θ of their normal between -90° and 180° correspond to lines in the physically relevant part of the coordinate system (yellow area). Right side: All other values for θ do not parametrise patterns belonging to physical events. 54
- 5.14 Differently oriented lines in a discrete square coordinate system. As can easily be verified by counting, each line consists of exactly ten pixels, independent from its orientation. 56
- 5.15 A grid of $n \times n$ fields with two fields occupied (black squares). $n^2 - 2$ fields are still free (light and dark grey squares), with $n - 2$ of them aligned on the same line as the occupied ones (dark grey squares). . . . 56
- 5.16 Basic principle of the nearest-neighbour strategy. Hits of a physical event lie quite compact to each other (green area), while background hits are usually much more distinct, although they may also be collinear and thus are falsely detected as belonging to the event (red arrow). . . 59
- 6.1 Example of the detection of an electronic neutral current event at $1.1 \times 10^5 \text{ GeV}$ with 100kHz background noise. Top left: Raw data fed to the Hough Transform. Top right: Lines found by the Hough Transform. Bottom left: Hits extracted from raw data based on the Hough Transform's result. Bottom right: Original data without background noise. . . 63
- 6.2 Found hits as function of real hits for electronic neutral current events at 150kHz background rate. 65
- 6.3 True hits as function of real hits for electronic neutral current events at 150kHz background rate. 66
- 6.4 True hits as function of found hits for electronic neutral current events at 150kHz background rate. The parameters a and b of the linear fit ($ax + b$, green line) have been determined to $a = 0.96$, and $b = -4.98$. . . 67
- 6.5 False hits as function of found hits for electronic neutral current events at 150kHz background rate. 68
- 6.6 Ratio of false and true hits as function of real hits for electronic neutral current events at 150kHz background rate. 69

6.7	Fraction of correctly identified hits as function of background noise for different event types.	70
6.8	Fraction of correctly identified hits as function of background noise for different event types after applying a cut at 25 found hits.	71
6.9	Fraction of correctly identified hits as function of background noise for different event types after applying a cut at 9 found hits, OM clustering and binning with 5ns resolution.	72
6.10	Fraction of correctly identified hits as function of background noise for different event types after applying a cut at 9 found hits, OM clustering and binning with 5ns resolution to data from a single detector string.	73
6.11	Results from standard ANTARES trigger (top) and Hough transform (bottom) applied to an electronic neutral current event. The Hough Transform method correctly identified about 3 times as much hits as the standard trigger (the small deviations in the positions between found hits and input data are a result from the integer arithmetic used for reasons of computing time).	77
6.12	Ratio of hits found by the Hough Transform method and the ANTARES standard trigger at different background rates.	78
6.13	Ratio of true hits found by the Hough Transform method and the ANTARES standard trigger at different background rates.	78
6.14	Number of hits found by the ANTARES standard trigger and the Hough Transform within the first 500 events of run 27955 (recorded on 29.05.2007). 79	
6.15	Raw data (left column), Hough Transform (mid column) and ANTARES trigger (right column) results of event 233 of run 27955 (recorded on 29.05.2007). Both trigger types were of similar efficiency.	79
6.16	Raw data (left column), Hough Transform (mid column) and ANTARES trigger (right column) results of event 289 of run 27955 (recorded on 29.05.2007). Both triggers reported hits which apparently do not seem to be physical hits.	79
6.17	Raw data (left column), Hough Transform (mid column) and ANTARES trigger (right column) results of event 179 of run 27955 (recorded on 29.05.2007). Both trigger types detected the events but the Hough Transform method was more efficient.	80

6.18	Raw data (left column), Hough Transform (mid column) and ANTARES trigger (right column) results of event 321 of run 27955 (recorded on 29.05.2007). The Hough Transform method detected the event, the ANTARES standard trigger failed.	80
6.19	Raw data (left column), Hough Transform (mid column) and ANTARES trigger (right column) results of event 278 of run 27955 (recorded on 29.05.2007). Both trigger types detected the events but the ANTARES standard trigger was more efficient.	80
6.20	Raw data (left column), Hough Transform (mid column) results of event 34 of run 27955 (recorded on 29.05.2007). The ANTARES standard trigger detected the event, the Hough transform method failed (the event does not contain physical data, which has been correctly recognised by the ANTARES standard trigger, whereas the Hough Transform method falsely triggered on background hits).	81
B.1	Example of the detection of an electronic neutral current event at 1.1×10^5 GeV with 100kHz background noise. Top left: Raw data fed to the Hough Transform. Top right: Lines found by the Hough Transform. Bottom left: Hits extracted from raw data based on the Hough Transform's result. Bottom right: Original data without background noise. .	92
B.2	Found hits as function of real hits for electronic neutral current events at different background rates.	93
B.3	True hits as function of real hits for electronic neutral current events at different background rates.	94
B.4	True hits as function of found hits for electronic neutral current events at different background rates. The parameters a and b of the linear fit ($ax + b$, dashed line) have been determined to $a = 0.99, b = -5.52$ (70 kHz), $a = 0.98, b = -4.76$ (100 kHz), $a = 0.96, b = -4.98$ (150 kHz), $a = 0.94, b = -4.79$ (200 kHz), $a = 0.94, b = -4.51$ (250 kHz) and $a = 0.92, b = -4.65$ (300 kHz).	95
B.5	False hits as function of found hits for electronic neutral current events at different background rates.	96
B.6	Ratio of false and true hits as function of real hits for electronic neutral current events at different background rates.	97

B.7	Example of the detection of an electronic charged current event at $1.3 \times 10^5 \text{ GeV}$ with 100kHz background noise. Top left: Raw data fed to the Hough Transform. Top right: Lines found by the Hough Transform. Bottom left: Hits extracted from raw data based on the Hough Transform's result. Bottom right: Original data without background noise. .	98
B.8	Found hits as function of real hits for electronic charged current events at different background rates.	99
B.9	True hits as function of real hits for electronic charged current events at different background rates.	100
B.10	True hits as function of found hits for electronic charged current events at different background rates. The parameters a and b of the linear fit ($ax + b$, dashed line) have been determined to $a = 0.99, b = -4.87$ (70 kHz), $a = 0.98, b = -5.05$ (100 kHz), $a = 0.96, b = -4.50$ (150 kHz), $a = 0.94, b = -4.78$ (200 kHz), $a = 0.94, b = -4.92$ (250 kHz) and $a = 0.92, b = -4.63$ (300 kHz).	101
B.11	False hits as function of found hits for electronic charged current events at different background rates.	102
B.12	Ratio of false and true hits as function of real hits for electronic charged current events at different background rates.	103
B.13	Example of the detection of a muonic neutral current event at $4.6 \times 10^4 \text{ GeV}$ with 100kHz background noise. Top left: Raw data fed to the Hough Transform. Top right: Lines found by the Hough Transform. Bottom left: Hits extracted from raw data based on the Hough Transform's result. Bottom right: Original data without background noise. .	104
B.14	Found hits as function of real hits for muonic neutral current events at different background rates.	105
B.15	True hits as function of real hits for muonic neutral current events at different background rates.	106
B.16	True hits as function of found hits for muonic neutral current events at different background rates. The parameters a and b of the linear fit ($ax + b$, dashed line) have been determined to $a = 0.96, b = -4.69$ (70 kHz), $a = 0.94, b = -4.51$ (100 kHz), $a = 0.90, b = -4.41$ (150 kHz), $a = 0.85, b = -4.10$ (200 kHz), $a = 0.87, b = -4.75$ (250 kHz) and $a = 0.85, b = -4.43$ (300 kHz).	107
B.17	False hits as function of found hits for muonic neutral current events at different background rates.	108

B.18	Ratio of false and true hits as function of real hits for muonic neutral current events at different background rates.	109
B.19	Example of the detection of a muonic charged current event at 3.0×10^3 GeV with 100kHz background noise. Top left: Raw data fed to the Hough Transform. Top right: Lines found by the Hough Transform. Bottom left: Hits extracted from raw data based on the Hough Transform's result. Bottom right: Original data without background noise. . .	110
B.20	Found hits as function of real hits for muonic charged current events at different background rates.	111
B.21	True hits as function of real hits for muonic charged current events at different background rates.	112
B.22	True hits as function of found hits for muonic charged current events at different background rates. The parameters a and b of the linear fit ($ax + b$, dashed line) have been determined to $a = 0.98, b = -4.43$ (70 kHz), $a = 0.965, b = -4.31$ (100 kHz), $a = 0.95, b = -4.56$ (150 kHz), $a = 0.93, b = -4.44$ (200 kHz), $a = 0.93, b = -4.52$ (250 kHz) and $a = 0.91, b = -4.58$ (300 kHz).	113
B.23	False hits as function of found hits for muonic charged current events at different background rates.	114
B.24	Ratio of false and true hits as function of real hits for muonic charged current events at different background rates.	115
C.1	Raw data (top), Hough Transform (mid) and ANTARES trigger (bottom) results of event 13 of run 27955 (recorded on 29.05.2007)	118
C.2	Raw data (top), Hough Transform (mid) and ANTARES trigger (bottom) results of event 15 of run 27955 (recorded on 29.05.2007)	119
C.3	Raw data (top), Hough Transform (mid) and ANTARES trigger (bottom) results of event 22 of run 27955 (recorded on 29.05.2007)	120
C.4	Raw data (top), Hough Transform (mid) and ANTARES trigger (bottom) results of event 23 of run 27955 (recorded on 29.05.2007)	121
C.5	Raw data (top), Hough Transform (mid) and ANTARES trigger (bottom) results of event 32 of run 27955 (recorded on 29.05.2007)	122
C.6	Raw data (top) and Hough Transform (mid) results of event 34 of run 27955 (recorded on 29.05.2007). The ANTARES trigger did not detect the event.	123
C.7	Raw data of event 100 of run 27955 (recorded on 29.05.2007). Neither the standard trigger nor the the ANTARES trigger detected the event.	124

C.8	Raw data (top), Hough Transform (mid) and ANTARES trigger (bottom) results of event 101 of run 27955 (recorded on 29.05.2007).	125
C.9	Raw data (top) and Hough Transform (mid) results of event 106 of run 27955 (recorded on 29.05.2007). The ANTARES trigger did not detect the event	126
C.10	Raw data (top), Hough Transform (mid) and ANTARES trigger (bottom) results of event 110 of run 27955 (recorded on 29.05.2007).	127
C.11	Raw data (top), Hough Transform (mid) and ANTARES trigger (bottom) results of event 117 of run 27955 (recorded on 29.05.2007).	128
C.12	Raw data (top) and Hough Transform (mid) results of event 119 of run 27955 (recorded on 29.05.2007). The ANTARES trigger did not detect the event	129
C.13	Raw data (top), Hough Transform (mid) and ANTARES trigger (bottom) results of event 124 of run 27955 (recorded on 29.05.2007).	130
C.14	Raw data of event 168 of run 27955 (recorded on 29.05.2007). Neither the standard trigger nor the the ANTARES trigger detected the event .	131
C.15	Raw data (top), Hough Transform (mid) and ANTARES trigger (bottom) results of event 173 of run 27955 (recorded on 29.05.2007).	132
C.16	Raw data (top), Hough Transform (mid) and ANTARES trigger (bottom) results of event 174 of run 27955 (recorded on 29.05.2007).	133
C.17	Raw data (top), Hough Transform (mid) and ANTARES trigger (bottom) results of event 179 of run 27955 (recorded on 29.05.2007).	134
C.18	Raw data (top) and Hough Transform (mid) results of event 180 of run 27955 (recorded on 29.05.2007). The ANTARES trigger did not detect the event.	135
C.19	Raw data (top) and Hough Transform (mid) results of event 182 of run 27955 (recorded on 29.05.2007). The ANTARES trigger did not detect the event.	136
C.20	Raw data (top) and Hough Transform (mid) results of event 184 of run 27955 (recorded on 29.05.2007). The ANTARES trigger did not detect the event.	137
C.21	Raw data (top), Hough Transform (mid) and ANTARES trigger (bottom) results of event 185 of run 27955 (recorded on 29.05.2007).	138
C.22	Raw data (top) and Hough Transform (mid) results of event 187 of run 27955 (recorded on 29.05.2007). The ANTARES trigger did not detect the event.	139

C.23 Raw data (top) and Hough Transform (mid) results of event 190 of run 27955 (recorded on 29.05.2007). The ANTARES trigger did not detect the event.	140
C.24 Raw data (top) and Hough Transform (mid) results of event 192 of run 27955 (recorded on 29.05.2007). The ANTARES trigger did not detect the event.	141
C.25 Raw data (top), Hough Transform (mid) and ANTARES trigger (bottom) results of event 206 of run 27955 (recorded on 29.05.2007).	142
C.26 Raw data (top) and Hough Transform (mid) results of event 216 of run 27955 (recorded on 29.05.2007). The ANTARES trigger did not detect the event.	143
C.27 Raw data (top) and Hough Transform (mid) results of event 222 of run 27955 (recorded on 29.05.2007). The ANTARES trigger did not detect the event.	144
C.28 Raw data (top), Hough Transform (mid) and ANTARES trigger (bottom) results of event 226 of run 27955 (recorded on 29.05.2007).	145
C.29 Raw data (top), Hough Transform (mid) and ANTARES trigger (bottom) results of event 233 of run 27955 (recorded on 29.05.2007).	146
C.30 Raw data (top), Hough Transform (mid) and ANTARES trigger (bottom) results of event 234 of run 27955 (recorded on 29.05.2007).	147
C.31 Raw data (top), Hough Transform (mid) and ANTARES trigger (bottom) results of event 244 of run 27955 (recorded on 29.05.2007).	148
C.32 Raw data of event 247 of run 27955 (recorded on 29.05.2007). Neither the standard trigger nor the the ANTARES trigger detected the event .	149
C.33 Raw data (top), Hough Transform (mid) and ANTARES trigger (bottom) results of event 249 of run 27955 (recorded on 29.05.2007).	150
C.34 Raw data (top), Hough Transform (mid) and ANTARES trigger (bottom) results of event 257 of run 27955 (recorded on 29.05.2007).	151
C.35 Raw data (top), Hough Transform (mid) and ANTARES trigger (bottom) results of event 259 of run 27955 (recorded on 29.05.2007).	152
C.36 Raw data (top), Hough Transform (mid) and ANTARES trigger (bottom) results of event 263 of run 27955 (recorded on 29.05.2007).	153
C.37 Raw data of event 267 of run 27955 (recorded on 29.05.2007). Neither the standard trigger nor the the ANTARES trigger detected the event .	154

C.38	Raw data (top), Hough Transform (mid) and ANTARES trigger (bottom) results of event 274 of run 27955 (recorded on 29.05.2007).	155
C.39	Raw data of event 275 of run 27955 (recorded on 29.05.2007). Neither the standard trigger nor the the ANTARES trigger detected the event .	156
C.40	Raw data (top), Hough Transform (mid) and ANTARES trigger (bottom) results of event 278 of run 27955 (recorded on 29.05.2007).	157
C.41	Raw data (top), Hough Transform (mid) and ANTARES trigger (bottom) results of event 280 of run 27955 (recorded on 29.05.2007).	158
C.42	Raw data (top), Hough Transform (mid) and ANTARES trigger (bottom) results of event 285 of run 27955 (recorded on 29.05.2007).	159
C.43	Raw data (top), Hough Transform (mid) and ANTARES trigger (bottom) results of event 289 of run 27955 (recorded on 29.05.2007).	160
C.44	Raw data (top), Hough Transform (mid) and ANTARES trigger (bottom) results of event 293 of run 27955 (recorded on 29.05.2007).	161
C.45	Raw data (top), Hough Transform (mid) and ANTARES trigger (bottom) results of event 311 of run 27955 (recorded on 29.05.2007).	162
C.46	Raw data (top) and Hough Transform (mid) results of event 320 of run 27955 (recorded on 29.05.2007). The ANTARES trigger did not detect the event.	163
C.47	Raw data (top), Hough Transform (mid) and ANTARES trigger (bottom) results of event 321 of run 27955 (recorded on 29.05.2007).	164
C.48	Raw data (top) and Hough Transform (mid) results of event 326 of run 27955 (recorded on 29.05.2007). The ANTARES trigger did not detect the event.	165
C.49	Raw data (top), Hough Transform (mid) and ANTARES trigger (bottom) results of event 329 of run 27955 (recorded on 29.05.2007).	166
C.50	Raw data (top), Hough Transform (mid) and ANTARES trigger (bottom) results of event 337 of run 27955 (recorded on 29.05.2007).	167
D.1	Charge distribution of a photomultiplier tube with single photo-electron (SPE) peak. The image has been taken from [51].	170
D.2	Expected contributions of late after-pulses (technical part, red line) and real correlations (natural part, blue line) to the relations of the rates measured by an ARS with high threshold and an ARS with a low threshold.	171

D.3	Example for data recorded by the instrumentation line IL07. The blue line marks the baseline for the data recorded by floor 5 (green dots). The image has been taken from [52].	173
D.4	The ratio of the baseline rates of ARS2/ARS0 (left side) and ARS4/ARS0 (right side) plotted against the baseline rate measured by ARS0 for different SPE threshold settings of ARS2 and ARS4.	174
D.5	Baseline-rate as function of time for ARS0 and ARS4 of LCM 3 (arbitrary units).	175
D.6	Theoretical results for expected baseline rates if no correlation in the background photons is assumed (arbitrary units).	176
E.1	Illustration of an acoustic storey. The three optical modules, which are part of a standard storey, have been replaced by six hydrophones. The image has been taken from [61].	179
E.2	Schematic diagram of the slow control system.	180

List of Tables

5.1	Truth table of the XOR function.	30
6.1	Percentage of true hits among found hits for different event types at different background rates.	68
6.2	Total number of hits found by the standard ANTARES trigger (ANT Tr) and the Hough Transform (Hgh Tr) in background only events at different rates. Hgh Max is the maximum number of hits found for a single event. Hgh NN is the number of hits found after applying the nearest-neighbour filter strategy and Hgh NN Max the maximum number of hits found for a single event using this strategy.	74
6.3	Number of events belonging to a particular result class. Class 1: Both trigger types detected a similar number of hits. Class 2: Both trigger types failed in detecting the event. Class 3: The Hough Transform method was more efficient than the ANTARES standard trigger. Class 4: The Hough Transform method detected the physical events, the ANTARES standard trigger did not detect the events. Class 5: The ANTARES standard trigger was more efficient than the Hough transform method. Class 6: The ANTARES standard trigger detected the physical events, the Hough Transform method did not detect the events.	75
E.1	Meaning of the most significant ID bit for acoustic slow control.	183
E.2	Header fields for acoustic slow control and their names as used within the code.	186
E.3	Communication link between μ C and FPGA.	187

Abbreviations

ADCP	Acoustic Doppler Current Profiler
AMADEUS	Antares Modules for Acoustic DEtection Under the Sea
AMANDA	Antarctic Muon And Neutrino Detector Array
ANN	Artificial Neural Network
ANTARES	Astronomy with a Neutrino Telescope and Abyss environmental RESearch
ARS	Acoustic Ring Sampler
BSS	Bottom String Socket
CEA	Commissariat à l'Énergie Atomique (et aux énergies alternatives)
CRC32	Cyclic Redundancy Check (32 Bits)
FPGA	Field Programmable Gate Array
GB	GigaByte
GUT	Grand Unified Theory
GZK	Greisen, Zatsepin, Kuzmin (cut-off)
HMI	Human Machine Interface
IL	Instrumentation Line
ISO	International Organization for Standardization
JB	Junction Box
JTAG	Joint Action Test Group
LCM	Local Control Module
LED	Light Emitting Diode
MB	MegaByte
MILOM	Mini Instrumentation Line with Optical Modules
MLCM	Master Local Control Module
MOND	MODified Netwonian Dynamics
NFS	Network File system
NN	Neural Network
OM	Optical Module
OMC	Optical and Mechanical Cable
OMF	Optical Module Frame
OSI	Open Systems Interconnection
PCA	Principal Component Analysis
PMT	PhotoMultiplier Tube
PSL	Prototype Sector Line
RLE	Run Length Encoding
SC	Slow Control
SCM	String Control Module
SPE	Single Photoelectron Peak
SPI	Serial Peripheral Interface
TB	TeraByte
USB	Universal Serial Bus
VHDL	Very high speed integrated Hardware Description Language

Bibliography

- [1] K. Greisen. End to the cosmic ray spectrum? *Phys. Rev. Lett.*, 16:748–750, 1966.
- [2] G. T. Zatsepin and V. A. Kuzmin. Upper limit of the spectrum of cosmic rays. *JETP Lett.*, 4:78–80, 1966.
- [3] M. Milgrom. A Modification Of The Newtonian Dynamics As A Possible Alternative To The Hidden Mass Hypothesis. *The Astrophysical Journal*, 270:365–370, 1983.
- [4] J. Wess and B. Zumino. Supergauge transformations In Four Dimensions. *Nuclear Physics B*, 70:39–50, 1974.
- [5] C. Rovelli and L. Smolin. Loop Space Representation Of Quantum General Relativity. *Nuclear Physics B*, 331, 1990.
- [6] B. Povh et al. *Teilchen und Kerne*. Springer, Berlin, Heidelberg, New York, 2001. Korrigierter Nachdruck.
- [7] K. Nakamura et al. Review of Particle Physics. *Journal of Physics G*, 37(7A):555–556, 2010.
- [8] W. D. Arnett and J. L. Rosner. Neutrino mass limits from SN1987A. *Phys. Rev. Lett.*, 58:1906–1909, May 1987.
- [9] S. Ambrosanio and B. Mele. Neutralino decays in the minimal supersymmetric standard model. *Phys. Rev. D*, 53:2541–2562, Mar 1996.
- [10] H. Stöcker. *Taschenbuch der Physik*. Harri Deutsch, Thun und Frankfurt am Main, 1998.
- [11] B. Hartmann. *Reconstruction of Neutrino-Induced Hadronic and Electromagnetic Showers with the ANTARES Experiment*. PhD thesis, Universität Erlangen-Nürnberg, Institut für Astroteilchenphysik, 2006.
- [12] D. Jackson. *Classical Electrodynamics*. John Wiley & Sons, New York, 1998.
- [13] <http://antares.in2p3.fr>.
- [14] L. Bergström and A. Goobar. *Cosmology And Particle Astrophysics*. John Wiley & Sons, Chichester, New York, Weinheim, 1999.
- [15] Technical Design Report of the ANTARES 0.1 km² project. <http://antares.in2p3.fr/internal/tdr/>. Downloaded on May 3, 2003.

- [16] <http://antares.in2p3.fr/Collaboration/index.html>.
- [17] KM3NeT - Technical Design Report for a Deep-Sea Research Infrastructure in the Mediterranean Sea Incorporating a Very Large Volume Neutrino Telescope. <http://www.km3net.org/TDR/Prelim-TDR-KM3NeT.pdf>. Downloaded on April 12, 2010.
- [18] E. Carmona and J.J. Hernández. A new reconstruction technique for ANTARES. *ANTARES internal note*, ANTARES-Soft/2000-11, 2000.
- [19] A. Romeyer and Th. Stolarczyk. Reconstruction algorithms: A handbook for developers. *ANTARES internal note*, ANTARES-Soft/2001-001, 2001.
- [20] A. Heijboer. An algorithm for track reconstruction in ANTARES. *ANTARES internal note*, ANTARES-Soft/2002-002, 2002.
- [21] H. Niemann. *Klassifikation von Mustern*. Springer, Berlin, 1983.
- [22] P. E. Hart R. O. Duda and D. G. Stork. *Pattern Classification*. John Wiley & Sons, Inc, New York, 2001.
- [23] D. H. Ballard and C. M. Brown. *Computer Vision*. Prentice Hall, New Jersey, 1982. Available as E-Book at <http://homepages.inf.ed.ac.uk/rbf/BOOKS/BANDB/bandb.htm>, downloaded on June 21st 2006.
- [24] R. U. Abbasi et al. Alternative Methods to Finding Patterns in HiRes Stereo Data. *arXiv:astro-ph/0702361v1*, 2007.
- [25] R. Gupta C. A. L. Bailer-Jones and H. P. Singh. An introduction to artificial neural networks. *arXiv:astro-ph/0102224v1*, 2001.
- [26] R. G. Anhangar and M. F. Anhangar. Handwritten Farsi Character Recognition using Artificial Neural Networks. *International Journal of Computer Science and Information Security*, 4(1 & 2), 2009.
- [27] R. Goundar and J. Vanualailai. Convergence Criteria for a Hopfield-type Neural Network. *arXiv:math/0503361v1*, 2005.
- [28] W. Buselmaier. *Biologie*. Bechtermünz, Augsburg, 1997.
- [29] R. Rojas. *Neural Networks A Systematic Introduction*. Springer, Berlin, 1996.
- [30] W. McCulloch and W. Pitts. A logical calculus of the ideas immanent in nervous activity. *Bulletin of Mathematical Biology*, 52:99–115, 1990.

- [31] <http://blogs.techrepublic.com.com/programming-and-development/?p=70>.
Downloaded on January 24, 2009.
- [32] K. Pearson. On Lines and Planes of Closest Fit to Systems of Points in Space. *Philosophical Magazine*, 2:559–572, 1901.
- [33] K. Karhunen. Über lineare Methoden der Wahrscheinlichkeitsrechnung. *Ann. Acad. Sci. Fennicae, Ser. A. I. Math.-Phys.*, 37:1–79, 1947.
- [34] M. Loève. *Probability theory, Vol. II (Graduate Texts in Mathematics)*. Springer, New York, 1978.
- [35] P. J. Francis and B. J. Wills. Introduction to Principal Component Analysis. *arXiv:astro-ph/9905079v2*, 1999.
- [36] I. Bronstein et al. *Taschenbuch der Mathematik*. Harri Deutsch, Frankfurt am Main, Thun, 1997.
- [37] P. V. C. Hough. Methods and means for recognizing complex patterns. U.S. Patent 3,069,654, 1962.
- [38] J. Princen et al. A Formal Definition of the Hough Transform: Properties and Relationships. *Journal of Mathematical Imaging and Vision*, 1:153–168, 1992.
- [39] J. J. Hopfield and C. D. Brody. What is a moment? Cortical sensory integration over a brief time interval. *Proceedings of the National Academy of Sciences of the United States of America (PNAS)*, 97(25):13919–13924, 2000.
- [40] J. J. Hopfield and C. D. Brody. What is a moment? Transient synchrony as a collective mechanism for spatiotemporal integration. *Proceedings of the National Academy of Sciences of the United States of America (PNAS)*, 98(3):1282–1287, 2001.
- [41] R. O. Duda and P. E. Hart. Use of the Hough Transformation To Detect Lines and Curves in Pictures. *Graphics and Image Processing*, 1972.
- [42] C. Aulbert. *Finding Millisecond Binary Pulsars in 47 Tucanae by Applying the Hough Transformation to Radio Data*. PhD thesis, Universität Potsdam, Max-Planck-Institut für Gravitationsphysik, 2005.
- [43] C. F. Olson. Constrained Hough Transforms for Curve Detection. *Computer Vision and Image Understanding*, 73(3):329–345, 1999.
- [44] K.-L. Chung et al. New memory- and computation-efficient hough transform for detecting lines. *Pattern Recognition*, 37:953–963, 2004.

- [45] L. A. F. Fernandes and M. M. Oliveira. Real-time line detection through an improved Hough transform voting scheme. *Pattern Recognition*, 41:299–314, 2008.
- [46] J. Illingworth and J. Kittler. A Survey of the Hough Transform. *Computer Vision, Graphics, and Image Processing*, 44:87–116, 1988.
- [47] <http://antares.in2p3.fr/internal/Eff/fig/2008c.mrd.gif>. Downloaded on April 08, 2010.
- [48] H. Lafoux and S. Basa. Photomultiplier specifications and measurements procedures for the 0.1 km². *ANTARES technical note*, 3-OMS-01-04-A, 2000.
- [49] F. D. Ardellier. PV de recette de la série probatoire (100 PMTs) du marché n° 0028055. *ANTARES technical note*, 3-OMS-01-10-A, 2001.
- [50] F. D. Ardellier. PV de recette du 2ieme batch de 96 PMTs R7081-20. *ANTARES technical note*, 3-OMS-01-12-A, 2001.
- [51] H. Lafoux S. Basa. Photomultiplier specifications and measurement procedures for the 0.1 km². *ANTARES technical note*, 3-OMS-01-04-A, 2000.
- [52] http://antares.in2p3.fr/internal/Eff/fig/IL07_mean_0804.gif. Downloaded on April 08, 2010.
- [53] G. A. Askarian. Hydrodynamic radiation from the tracks of ionizing particles in stable liquids. *At. Energ.*, 3(8):921–923, 1957.
- [54] G. A. Askarian et al. Acoustic detection of high energy particle-showers in water. *Nucl. Instrum. Meth.*, 164:267–278, 1979.
- [55] L. Sulak et al. Experimental studies of the acoustic signature of proton beams traversing fluid media. *Nucl. Instr. Methods*, 161(2):203–217, 1979.
- [56] K. Graf. Teststrahlmessungen zur akustischen Neutrinodetektion: Thermoakustische Schallerzeugung in Wasser. Master’s thesis, Universität Erlangen-Nürnberg, Institut für Astroteilchenphysik, 2005.
- [57] T. Karg. *Detection of ultra high energy neutrinos with an underwater very large volume array of acoustic sensors: A simulation study*. PhD thesis, Universität Erlangen-Nürnberg, Institut für Astroteilchenphysik, 2006.
- [58] K. Salomon. *Simulation und Messung verschiedener Hydrophonkomponenten zur akustischen Teilchendetektion*. PhD thesis, Universität Erlangen-Nürnberg, Institut für Astroteilchenphysik, 2007.

- [59] C. Naumann. *Development of Sensors for the Acoustic Detection of Ultra High Energy Neutrinos in the Deep Sea*. PhD thesis, Universität Erlangen-Nürnberg, Institut für Astroteilchenphysik, 2007.
- [60] F. Deffner. Studie zur akustischen Neutrinodetektion: Analyse und Filterung akustischer Daten aus der Tiefsee. Master's thesis, Universität Erlangen-Nürnberg, Institut für Astroteilchenphysik, 2007.
- [61] K. Graf et al. Towards Acoustic Detection of UHE Neutrinos in the Mediterranean Sea - The AMADEUS Project in ANTARES. *J. Phys. Conf. Ser.*, 60:296–299, 2007.
- [62] Electrical Characteristics of Generators and Receivers for Use in Balanced Digital Multipoint Systems. *International Standard*, TIA-485-A, 2003.
- [63] Modbus Application Protocol Specification V1.1b. 2006.
- [64] Inc. Motorola Inc., Freescale Semiconductor. SPI Block Guide V04.01. S12SPIV4/D, 2004.
- [65] J. P. Pineau. ARS_MB Version 4.0 User's Manual. *ANTARES technical note*, 3LCM_15_08A, 2003.
- [66] STMicroelectronics. *STR71xF ARM7TDMITM 32-bit MCU with Flash, USB, CAN, 5 timers, ADC, 10 communications interfaces*, November 2006.
- [67] *Proceedings, Embedded World Conference 2005, Feb. 22 - 24, 2005, Nuremberg*, 2005.
- [68] Information technology - Open Systems Interconnection - Basic Reference Model: The Basic Model. *International Standard*, ISO/IEC 7498-1:1994(E), 1996.
- [69] Xilinx Inc. *XAPP058 - Xilinx In-System Programming Using an Embedded Microcontroller*, June 2004.
- [70] ftp://ftp.xilinx.com/pub/swhelp/cpld/eisp_hp.tar.Z. Downloaded on February 28, 2007.
- [71] W. H. Press et al. *Numerical Recipes in C*. Cambridge University Press, Cambridge, New York, Port Melbourne, 1992.
- [72] Part 3: Carrier sense multiple access with collision detection (CSMA/CD) access method and physical layer specifications. *International Standard*, IEEE Std 802.3-2002, 2002.
- [73] F. Schöck, personal communication.

-
- [74] J. E. Bresenham. Algorithm for computer control of a digital plotter. *IBM Systems Journal*, 4(1), 1965.
- [75] A. Goldenshluger and A. Zeevi. The Hough Transform Estimator. *The Annals of Statistics*, 32(5):1908–1932, 2004.
- [76] S. R. Deans. *The Radon Transform and Some of Its Applications*. John Wiley & Sons, 1993.
- [77] A. Belkov. Implementation of the Hough Transform for 3D Track Reconstruction in Drift Chambers. *arXiv:physics/0201071v1*, 2002.
- [78] V. A. Rubakov. Superheavy magnetic monopoles and decay of the proton. *JETP Letters*, 33:644–646, 1981.
- [79] G. Börner. *The Early Universe - Facts and Fiction*. Springer, Berlin, Heidelberg, New York, 1993.
- [80] E. W. Kolb and M. S. Turner. *The Early Universe*. Addison-Wesley, Reading, Menlo Park, New York, 1990.

Acknowledgment

In order to show the incompleteness and uncertainty of any kind of science based on maths, the following list is neither ordered alphabetically nor is it in any way politically correct - instead it is ordered according to the associated Gödel numbers. Fortunately, none of the mentioned proved to be unprovable, except the one that states it explicitly - however, this cannot be proved.

- You (for wasting your time reading this thesis)
- Nina (for simply being there, here and now)
- Mr. Bleck (for chicken-bagels and the world's best large cups of extra strong coffee)
- My family (for love, support and all that really matters)
- Irish Castle (for Wilder Pilger concerts, great Newcastle and even greater Irish Stews)
- Cafe Cycles (for unlimited Hetzi supply and sometimes a big, tasteful baguette)
- The unprovable (for... well...)
- Tine (for a lot of hihhi) and Timo (for a lot of hohoho)
- Pummel and Bine (for the spirit of Amsterdam (No! Not what you think!))
- Brasserie Prisma (for unlimited Huppi supply and sometimes a big, tasteful plate of Schinken-Käse-Spätzle)
- Zwergl and Carmen (for company at lonely tuesdays and proofreading this thesis)
- My colleagues at EB (for a great atmosphere and money supply)
- The Suffkopf-Crew (for interesting discussions, a lot of fun and sometimes even inspiration)
- Uli Katz and Gisela Anton (for having enough patience)
- My ex-colleagues at Theorie III and PI1 (for having a great time at the university)
- The MrStrech Girls and Guys (for mjammm-jamm, nice evenings and wonderful WGTs)
- All others for which the black sun will never cease
- Anyone whom I forgot to mention explicitly

Erklärung

Hiermit bestätige ich, dass ich diese Arbeit selbstständig und nur unter Verwendung der angegebenen Hilfsmittel angefertigt habe.

Erlangen, März 2012

Horst Laschinsky

